Freie Universität Berlin

Investigation of nanocarriers as drug delivery systems by electron paramagnetic resonance spectroscopy

Im Fachbereich Physik der Freien Universität Berlin eingereichte
Dissertation zur Erlangung des akademischen Grades
Doktor der Naturwissenschaften (Dr. rer. nat.)

Siavash Saeidpour
aus Teheran

Fachbereich Physik
Freie Universität Berlin
2019

Diese Arbeit entstand in der Arbeitsgruppe von Prof. Dr. Robert Bittl am Fachbereich Physik der Freien Universität Berlin.

To my parents
Fatemeh and Reza

Did I not say to you, "go not there, for I am your friend; in
this mirage of annihilation I am the fountain of life?"
Did I not say to you, "Be not content with worldly forms,
for I am the fashioner of the tabernacle of your contentment?"
Rumi

Summary

Summary

In this thesis, the potential of the electron paramagnetic resonance (EPR) spectroscopic technique is applied to questions at the interface of dermatology, pharmacology, chemistry, and nanotechnology.

The skin as the outermost part of the body is the only organ to which drugs can be administered directly for the treatment of its diseases. However, the skin also acts as the barrier between the surrounding and the internal organs. Consequently, it protects the whole body against xenobiotics of the external environment. Thereby, the skin prevents penetration of administered drugs into its deeper layers or through it. Overcoming this intrinsic barrier is of great importance in dermatology for therapy success. Nanocarriers as drug delivery systems may be a solution for penetration through the skin barrier and are candidates for drug administration. However, efficient nanocarrier fabrication requires detailed knowledge about the interaction of drugs with these nanocarriers, in particular, with respect to the localization and distribution of the drugs within them. The aim of the study presented here is to unravel such interactions for two specific types of nanocarrier, dendritic core-multishell (CMS) nanoparticles and nanostructured lipid particles (NLP), which are both promising nanocarrier candidates.

Since EPR has been established as a useful tool for probing the interaction of a spin probe with its micro-environment, it was chosen here as the method of choice for identifying these interactions. However, EPR requires paramagnetic species, while drugs typically are diamagnetic. Therefore, and in the sense of a pilot study, the small paramagnetic nitroxides 2,2,6,6-tetramethylpiperidinyloxyl (TEMPO) and proxyl carboxylic acid (PCA) were used as model compounds for studying their interactions with their environment. The drug Dexamethasone (Dx), used in dermatology for treating inflammatory diseases, was spin labeled with PCA (DxPCA) and utilized for investigating the interactions in both, NLP and CMS nanoparticles. Using a set of continuous wave (cw) and pulsed EPR methods at X- and W-band enabled the precise extraction of the g- and A-matrices of the paramagnetic species as well as the measurement of their relaxation times. The g- and A-matrices represent specific probes for the polarity/proticity of the micro-environment. Additionally, the spin-lattice relaxation time yields complementary data on the spin probes' micro-environment, which is independently corroborated by the mobility of the spin probes.

This EPR-derived information is then used for the localization of the spin probes within the nanocarriers. Finally, comparing all obtained data enabled presenting an "association model" for the interaction between spin probes and nanocarriers. In short, in NLPs DxPCA is dispersed within the entire lipid matrix, PCA is not loaded, and TEMPO is enriched within the core. Likewise, the evidence obtained from EPR shows that DxPCA is localized at the interface between the hydrophobic and the hydrophilic shells of CMS nanoparticles. This knowledge gained may now be used in order to design more efficient nanocarriers or to select the right ones in dependence of the drug to be delivered.

Zusammenfassung

Zusammenfassung

In der vorliegenden Arbeit wird ein breites methodisches Repertoire der Elektronenspin-resonanz-Spektroskopie (engl. electron paramagnetic resonance, EPR) auf Fragestellungen im Grenz-bereich zwischen Dermatologie, Pharmakologie, Chemie und Nanotechnologie angewendet. Die Haut, als äußere Hülle unseres Körpers ist das einzige Organ, auf das Medikamente zur Behandlung von Krankheiten direkt aufgetragen werden können. Sie ist aber auch die Grenze zwischen der Umgebung und den inneren Organen, und schützt somit den Körper gegen Fremdstoffe aus der Umgebung. Daraus ergibt sich als Konsequenz, dass die Haut die Wanderung von Medikamenten in tiefere Schichten oder durch sie hindurch be- oder sogar verhindert. Deswegen ist es für die Dermatologie von großer Wichtigkeit diese natürliche Barriere zu überwinden. Die Verwendung von Botensystemen, z.B. in Form von Nanoträgern, bietet hierfür einen interessanten Lösungsansatz, da in ihnen Pharmaka über die Hautbarriere transportiert werden könnten. Die effiziente Verwendung von Nanoträgern erfordert jedoch ein detailliertes Wissen über die Wechselwirkung zwischen Träger und Pharmakon, insbe-sondere bezüglich der Verteilung und Lokalisation des Pharmakons im Träger. Das Ziel der hier vorgestellten Studie ist es, genau solche Wechselwirkungen für zwei bestimmte Klassen von Nanoträgern zu charakterisieren, die dendritischen Kern-Vielschalen Nanoträger (engl. core multi-shell, CMS) und die nanostrukturierten Lipidteilchen (engl. nanostructured lipid particles, NLP), beides vielversprechende Kandidaten für Nanoträger.

Um die Wechselwirkungen zwischen Pharmakon und Nanoträger zu studieren, wurde hier die EPR-Spektroskopie ausgesucht, weil sie als Methode etabliert ist, um Wechselwirkungen zwischen einer Spinsonde und ihrer Mikroumgebung zu untersuchen. Allerdings müssen für die EPR-Spektroskopie paramagnetische Zentren vorliegen, während Pharmaka üblicherwei-se diamagnetisch sind. Deswegen, und im Sinne einer Pilotstudie wurden hier die kleinen paramagnetischen Nitroxide TEMPO und PCA als Modellverbindungen genutzt, um deren Wechselwirkungen mit ihrer Umgebung zu untersuchen. Dann wurde das Pharmakon Dexa-methason (Dx), welches in der Dermatologie zur Behandlung von Entzündungen eingesetzt wird, mit PCA spinmarkiert (DxPCA) und genutzt, um Wechselwirkungen in NLP und CMS Nanopartikeln zu studieren. Der Einsatz verschiedener Dauerstrich (engl. continuous wave, cw) und gepulster EPR-Methoden im X- und W-Band ermöglichte die präzise Bestimmung der g- und A-Matrizen sowie der Relaxationszeiten der paramagnetischen Spezies. Die g- und A-Matrizen sind spezifische Sonden für Polarität/Protizität der Mikroumgebung. Die Spin-Gitter-Relaxationszeit liefert darüberhinaus weitere komplementäre Informationen über die Mikroumgebung, die wiederum in unabhängiger Art und Weise durch Informationen über die Mobilität der Spinsonden gestützt wird. Die so mit der EPR-Spektroskopie erhaltenen Informationen wurden dann genutzt, um die Spinsonden in den Nanoträgern zu lokalisieren. Darüberhinaus ermöglichte ein Vergleich aller Daten die Entwicklung eines „Assoziationsmo-dells" für die Wechselwirkung zwischen Spinsonde und Nanoträger. Kurz zusammengefasst, DxPCA ist in der gesamten Lipidmatrix der NLPs verteilt, PCA ist nicht geladen und TEMPO wird im Kern der NLP angereichert. Ganz analog zeigen die EPR-Daten, dass DxPCA an der Grenze zwischen der hydrophoben und außer hydrophilen Schalen der CMS-Nanoträger angereichert wird. Diese Erkenntnisse können nun in der Zukunft dazu verwendet werden, um Nanoträger effizienter zu machen oder in Abhängigkeit vom Pharmakon auszuwählen.

Contents

Contents

List of Figures

List of Tables

1 Introduction

Chapter 1. Introduction

More efficient treatment strategies for diseases are one of the most significant challenges in medical research. Efficient treatment requires carrying a drug to the target position in the body at the optimal concentration [1]. Scientists have tried to find new ways to deliver drugs that are a compromise between the dose taken up and the dosage required at the target [2]. Infused and orally-administered medications may bring unwanted side effects inherent to relatively high dosages to assure the desired efficacy. Finding the optimal dosage of administration is, therefore, of high importance. New ways of drug delivery have to balance the dosage and concentration at the desired point in the body to optimize the therapeutic effect [3]. Recently, nanocarriers were proposed for treating diseases as an alternative solution which has gained new momentum in drug delivery studies [4].

The skin is the most important organ as it protects against external physical and chemical encounters and acts as a penetration barrier for external particles. It consists of three different layers. The epidermis is the outermost layer which in turn encompasses four sub-layers. The top layer of the epidermis, stratum corneum, is responsible for the barrier function of the skin [5]. The unique arrangement of the stratum corneum builds an essential skin permeation resistance blocking the passage of molecules to deeper layers [6]. Recent studies suggested that nanocarriers penetrate into the skin layers, and thus the successful treatment of skin diseases enters a new era [7]. Thus, the advantageous properties of nanocarriers will not only be utilized for the treatment of outer layers, but also for penetration deep into the hair follicles, where free drug molecules in non-particulate form would never be capable to penetrate [8]. Therefore, nanocarriers have become an exciting, new approach for the treatment of skin diseases; for instance, inflammatory diseases [9], atopic dermatitis [10] and psoriasis [11].

Nanocarriers offer a new path for overcoming previously impenetrable barriers in many fields, e.g., medical research [12]. The fabrication of nanocarriers has significantly developed in the last two decades [13]. Nanocarriers are promising candidates for many necessary treatments in dermatology. They have the potential to penetrate into the skin and reach the location affected by the disease and carry the drugs into the deeper and target layers of the skin [14]. Successful loading of drugs into nanocarriers and their transport to the desired location in the patient's skin are the main objectives of current medical studies. Thereby, a significant obstacle is the complexity of the skin, which makes controlled drug transport and releases difficult [15]. A viable drug delivery design should ensure optimum size, function, and selectivity of the transporter for the target point.

Recently, a variety of nanocarriers were developed from various materials with different properties and sizes [16–22]. Of specific interest are responsive nanocarriers, which can change their size upon physical or chemical stimuli making them ideal for different therapeutical application [23–26]. In the present thesis, we investigate the properties of the novel nanocarriers, Core Multi-Shell (CMS) nanoparticles, and Nanostructured Lipid Particles (NLP), for effective therapy of skin diseases. The CMS nanoparticles are a unimolecular structure that has a branched core-unit, e.g. hyperbranched polyglycerol, with amphiphilic polymeric chains attached to it, which at least consist of one hydrophilic block, e.g. polyethylene glycol monomethyl ether, as outer shell and one hydrophobic block (12, 15, 18, 19, and 36 C-atoms) as inner shell. The inner shell is conjugated to the core by ester bonds to reduce the toxicity

of metabolites [27]. NLP were developed as a successor generation for liposomes [28, 29]. A liquid lipid of the nanoemulsion is exchanged by a solid lipid, leading to increased physical stability, increased protection of incorporated drugs, and significantly improved controlled release [30].

The primary goals for a dermal drug delivery system (DDS) are, first, the drug has to be loaded efficiently, second, it has to be transported through the skin, third, it has to be released. To achieve this, knowledge has to be acquired about some properties of the drug, its physico-chemical interaction with the nanoparticle systems and possible release mechanisms. Knowledge about how drugs incorporate into nanocarriers is an essential key to a promising therapeutic approach of nanocarriers for dermal application [31]. Different methods and techniques are used for the characterization of the pharmaceutical system of interest [32, 33]. These methods are light scattering [34], small-angle X-ray scattering [35] and neutron scattering [36], atomic force microscopy [37], ζ-potential measurements [38], electron microscopy [39], fluorescence spectroscopy [40], optical imaging such as confocal laser scanning microscopy [41], infrared spectroscopy and Raman spectroscopies [42] as well as magnetic-resonance-based spectroscopies (nuclear magnetic resonance (NMR) and magnetic resonance imaging (MRI)) [43, 44].

In this investigation, the advantages of electron paramagnetic resonance (EPR) spectroscopy are utilized to determine how a drug associates with a nanocarrier as dermal DDS. EPR spectroscopy, as a candidate technique for the investigation of nanocarriers [32, 45], is a unique, powerful and informative method for studying the interaction of spin probes with their microenvironment [46], providing information about the localization of a drug within a nanocarrier system, and the dynamics of drug loading into a nanocarrier [47]. Here, the drug Dexamethasone (Dx), used in dermatology for treating inflammatory diseases, was spin labeled with PCA (DxPCA) and utilized for investigating the interactions in both CMS nanoparticles and NLP [48, 49]. The EPR technique mostly used throughout this work is dual-frequency EPR spectroscopy, X-(9.4 GHz) and W-(94 GHz) band at cryogenic and ambient temperatures. The dual-frequency approach allows us to distinguish between magnetic field dependent and independent parameters in different micro-environments. High-field EPR (W-band) is used for investigation of the polarity and proticity of micro-environments. Additionally, the mobility of drug analogues is investigated and drug-nanocarrier systems are characterized [50, 51].

This thesis is structured as follows: first, the skin and its function are described. Then, the role of nanocarriers as DDSs in alternative treatment for skin diseases is detailed. The association model of a drug with nanocarriers, which is an essential aspect for our research, is introduced (Chapter 2). An introduction to EPR spectroscopy and its applications and a motivation explaining why EPR spectroscopy is a promising technique for this investigation are later detailed (Chapter 3). The preparation of nanocarriers and the loading procedure of spin probes into them follows. Afterward, EPR spectroscopy techniques which are used in this research are explained, and the extraction of the magnetic and dynamic parameters from the experimental spectra is presented (Chapter 4). Chapter 5 presents a study DxPCA, PCA and TEMPO (Section 5.1). The association of DxPCA within the CMS nanoparticle is investigated (Section 5.2). Finally, in chapter 6, PCA, TEMPO, and DxPCA loaded into NLPs are

characterized and their incorporation into the NLPs is described.

Within the context of this research, several publications spanning from the basic characterization of drug-nanocarrier interaction to drug penetration studies on intact skin have been published and are listed in Appendix C. In the present thesis, unpublished reference experiments and two of the papers (1 and 2 in App. C) reporting on the localization of drug analogs in two different nanocarrier systems will be presented.

2 Skin and drug delivery systems

2.1   The human skin structure

The human skin as one of the largest organs provides the barrier between the surrounding environment and internal organs [52]. However, the skin is not only a simple partition but also has unique lipid composition and complex structural arrangement which generates different functionalities [53]. The essential skin function is to lower water permeability compared to other biological membranes. Also, the skin has a selective mechanism for transporting or preventing penetration of substances into the inner body organs [54]. The skin is composed of three layers: the epidermis, dermis, and subcutis (Fig. 2.1a) [55]. The most important functions of the epidermis as the outermost layer of the skin are protection against the environment, preventing desiccation, and immune surveillance [56]. The epidermis is composed of four sub-layers (Fig. 2.1b). The basal cell layer (stratum basalis, consists of 1-2 cell layers), the spiny cell layer (stratum spinosum, consists of 2-7 cell layers), the granular cell layer (stratum granulosum, consists of 2-3 cell layers), and the cornified cell layer (stratum corneum, consists of more than 25 cell layers) [57, 58].

The stratum corneum, as the outermost layer of the epidermis, is the main target for skin penetration investigations [2, 59, 60]. The structure, properties, and function of the stratum corneum (SC) have been studied for a long time by multiple disciplines, e.g. pharmacology, dermatology, chemistry, and physics, and with ongoing research efforts [61–69]. The thickness of the SC is approximately 5 to 20 μm, and provides barriers to diverse physical and chemical stressors [58]. The main structural components of the SC are represented by the corneocytes, which provide the physical barrier, and the corneodesmosomes, functioning as "spot weldings" or "rivets" to hold the corneocytes together [58]. Lipids are packed in the inter-cellular space of the SC, and provide most of the diffusive resistance [70]. A highly complex mixture of different species of ceramides, cholesterol, and free fatty acids provide the permeability barrier [58]. The chemical properties of the SC are determined by the multiple lipid lamellae of the SC, which are interspersed with enzymes and anti-microbial peptides at the interface of the SC and the stratum granulosum [58]. Additionally, the apolar and polar domains of the lipid bilayer matrix provide optimal protection from a diffusion of apolar and polar materials into the inner layers of the skin. Thereby, the SC controls the crossing of substances in both directions, and is not only responsible for regulating the ingress of exogenous materials but also for preventing excessive water loss from the body [71, 72]. The selective permeability properties of the SC make the skin an immunologically active organ in the body [71, 73]. Currently, the main treatment methods in dermatology are topical application of drugs. Topical application of medication is challenging by the difficulty of penetration due to the complex structure of the SC.

Stratum corneum

Epidermis

Dermis

(a)

Stratum corneum

Granular layer

Spinous layer

Basal layer

Basment membrance

(b)
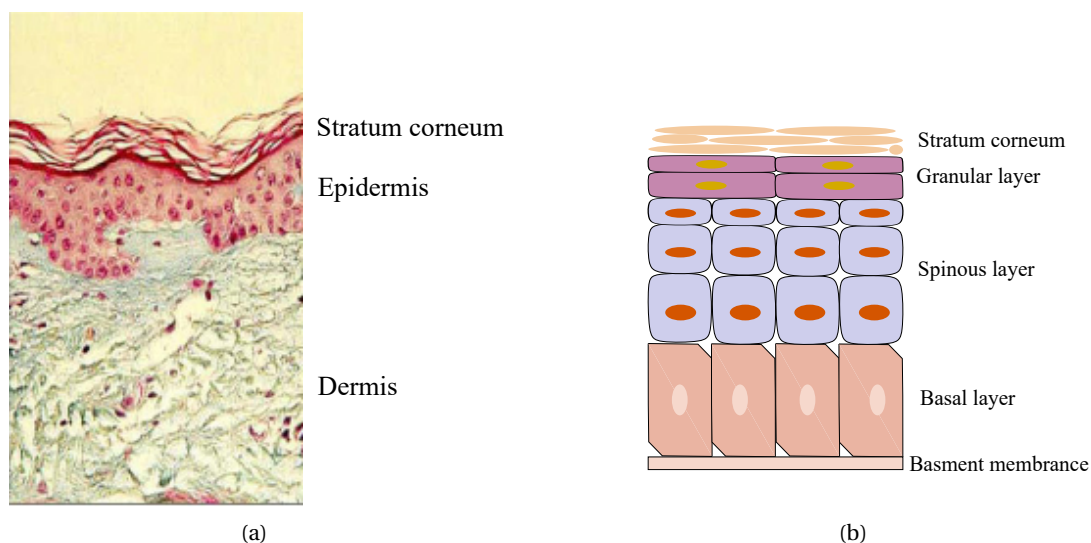
Figure 2.1: Structure of the human skin, a) the stratum corneum is the top layer, and epidermis, dermis, and fat layer are placed towards the body interior. Blood vessels are located within and below the dermis (adopted from [58]). b) The epidermis as upper part of the skin and its four different layers, the stratum corneum, the granular layer, the spinous layer, and the basal layer.

The selective permeability properties for the SC are determined by the structure of the inter-cellular lipids and substance of the keratinocytes provide it [73, 75]. Penetration pathways are demonstrated with the conceptual bricks and mortar model (Fig. 2.2). The bricks symbolize corneocytes, and inter-cellular lipids are shown as mortar [76]. The SC has three possible routes for penetration of external substances. The first one, which is the intra-cellular route for delivery through the SC cells, is one way which allows for substances to penetrate into the skin, especially compounds with small molecular weight (< 500 Da) [77]. The intra-cellular penetration requires transport through the extra-cellular lipid matrix as well as internalization into the cells. The inter-cellular route outside the corneocytes through the extra-cellular lipids is the second possible pathway which is classified as a hydrophobic channel [78]. It is composed of aqueous domains surrounded by polar lipids that construct walls of micro-channels. The inter-cellular penetration route between the SC corneocytes is the pathway by which most compounds penetrate the skin. The transappendageal route is the third route (Fig. 2.2 c). It has great potential for skin treatment by providing deeper penetration and absorption of compounds than the intra- and inter-cellular route. The hair follicles and other skin appendages are examples of the transappendageal route in dermal drug delivery. They are a faster way for small molecules and a more efficient route for delivering drugs into deeper skin layers, and also offer a reservoir for drugs [79]. The knowledge about the structure and permeability properties of the SC enables us to develop and examine new strategies for topical treatment of skin diseases.
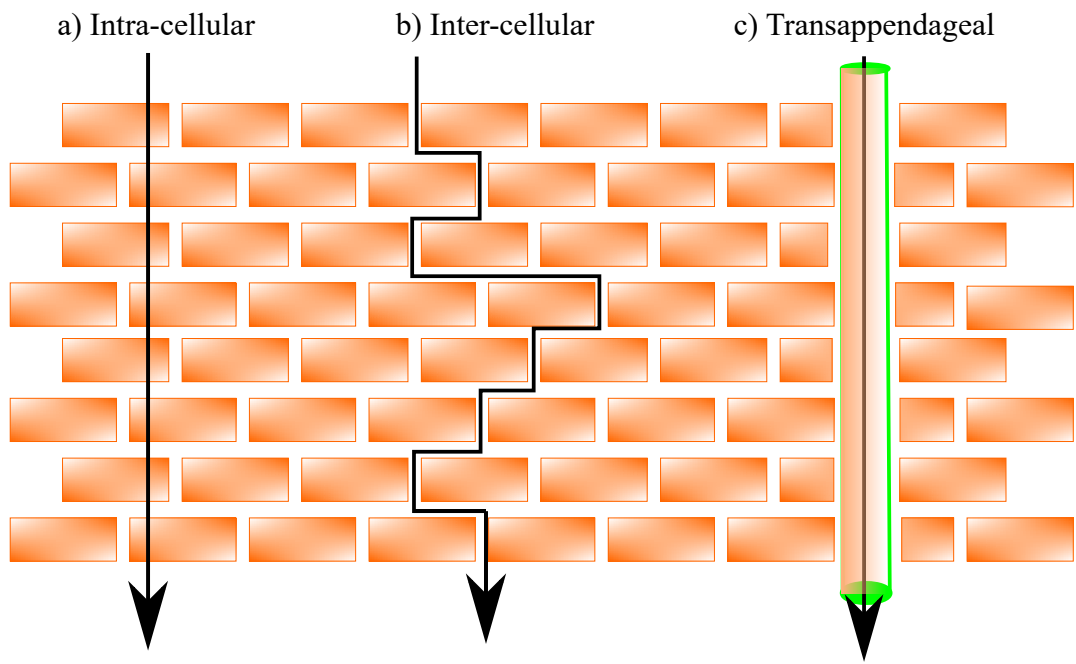
Figure 2.2: a) Intra-cellular b) inter-cellular c) transappendageal penetration route. The green cylinder illustrates the appendages such as hair follicles.

The successful treatment of dermal diseases requires that medication is transported efficiently to the site where it is necessary for treatment. The different physical and chemical approaches available for this purpose are classified in table 2.1.

A drug delivery system is defined as a formulation or a device that enables the introduction of a therapeutic substance into the body and improves its efficacy and safety by controlling the rate, time, and place of release [80]. In recent years, the DDS technique has gained attraction due to the application in pharmaceutical treatments for skin and cosmetics. Nanocarriers as vehicles are promising candidates for DDSs in skin disease therapy. Nanocarriers are used to enhance the percutaneous penetration of drugs as they have numerous advantages in comparison to conventional drug formulations [80, 81].

Table 2.1: Methods for dermal penetration, the table is modifed from [82].

Penetration method	Mode of action
Chemical methods	
Skin hydration	Increased drug solubility and/or disruption of the SC
Chemical penetration enhancers	Increased drug partitioning and/or diffusion in the SC
Vehicles	Drugs are encapsulated into vehicles which interact with the skin
Prodrugs	Chemical modification of the drug
Ion pairs	Permeation is increased by neutralizing the drug charge with an ion of the opposite charge
Salt formation	Drug is changed into a suitable salt form to increase its solubility
Supersaturated solutions	Thermodynamic activity of the drug solution is shifted, thus increasing penetration rate
Eutectic systems	The mixture of drug and another substance lowers the melting point and increases solubility
Physical methods	
Sonophoresis	Creation of microscopic holes for the transport of drugs
Iontophoresis	Cavitational ultrasound generates shock waves that disrupt the SC lipid structure
Electroporation	Electrically driven transport of charged drug molecules
Jet injections	Pore formation with short electrical pulses
Microneedles	High pressure acceleration of drug particles across the SC
Dermabrasion	Selective removal of the SC by applying high pressure microparticles
Thermal ablation	Short intervals of localized skin heating that creates micropores
Laser	Thermal ablation of SC creating pores
Waves (radiofrequency, photomechanical, microwaves, photoacoustic)	Disruption of the structure of SC
Magnetophoresis	Magnetic field is driving drug movement across SC and alters the SC structure
Combination of techniques	
Chemical enhancers and microneedles, sonophoresis and electroporation	
Iontophoresis and other physical methods (electroporation, sonophoresis or microneedles)	
Sonophoresis and other physical methods	

2.2 Nanocarriers as dermal Drug Delivery System

Nanocarriers offer in dermal application an easily accessible route without liver first-pass metabolism, i.e. without significant reduction of drug concentration by transformation to inactive compounds in the liver. They transport drugs efficiently to the diseased location in the skin and can be loaded with a drug which would be very difficult to formulate for effective treatment by other methods. It is an enhanced treatment which brings optimal drug dosage with shorter application period. Controlled drug release then leads to a sufficient local drug concentration without a high systemic drug load. Such a precise application of drugs is highly desirable since this allows one to minimize adverse health effects. Therefore, the topical application based on nanocarriers is an alternative treatment for skin diseases.

As mentioned earlier, the knowledge about the structure and function of the skin and especially the SC is significant. The primary challenge of nanocarriers is to pass the SC and penetrate into the deeper skin layers. The development of particles which are able to penetrate into the SC and diffuse across it is required for successful drug delivery into the deeper layers of the skin [83]. One possible approach is using nanotechnological methods to tailor particles which are able to overcome the skin barrier diffusing across the SC and the lower layers for the delivery of drugs [84]. Different nanocarriers have been developed with the purpose of overcoming the skin barrier property. The nanocarriers are classified by their origin as organic or inorganic substances, their structure and how adequately functionalized they are for facilitating controlled transport and drug release [85]. Various nanocarriers developed for dermal DDS are classified as lipid based nanoparticles [28, 29, 86, 87], polymeric nanoparticles [17], and also different types of inorganic nanoparticles, nanospheres and nanotubes [88].

The investigation of nanocarriers is necessary for accurate targeting, delivery, release, and biocompatibility. The primary challenge for the characterization and development of new nanocarriers is to gain information on how drugs are associated with and get released from them. As a consequence, two different types of nanocarriers were chosen to study in this research; CMS nanoparticles as polymeric defined-structure nanoparticles and NLPs as an example of undefined-structured nanoparticles.

2.2.1 Dendritic core-multishell nanoparticles

Dendritic core-multishell (CMS) nanoparticles represent a class of polymeric nanocarriers used as DDSs [89]. They are inspired by micellar architectures. CMS nanoparticles have undergone substantial development in the last decade and are still an ongoing field of research [90, 91]. Biodegradable [27, 92–95], pH sensitive [96], and hydrophobic hyperbranched polyester based CMS nanoparticles [97, 98] are the types currently being developed. CMS nanoparticles used here consist of a dendritic poly-glycerol (dPG) core with polar properties, surrounded by two layers of different chemical composition, a hydrophobic inner alkyl shell, and a hydrophilic outer poly(ethylene glycol)-methyl-ether (mPEG) shell [92]. They allow the storage and transport of lipophilic or hydrophilic molecules in the inner-shell or outer-shell, respectively [99–101].

CMS nanoparticles as a DDSs have been successfully used for dermal penetration [102]. They exhibit an increased penetration for the lipophilic fluorescent dye nile red loaded into CMS nanoparticles into porcine skin compared to a base cream or SLNs. CMS nanoparticles were proven to be a promising candidate for the delivery of guest molecules more selectively to the desired site of action [103]. Additionally, an increased penetration for 3-carboxy-2,2,5,5-tetramethyl-1-pyrrolidinyloxy (PCA) loaded into CMS nanoparticles was shown in comparison to ultra-flexible vehicles and aqueous solution by EPR spectroscopy [104].
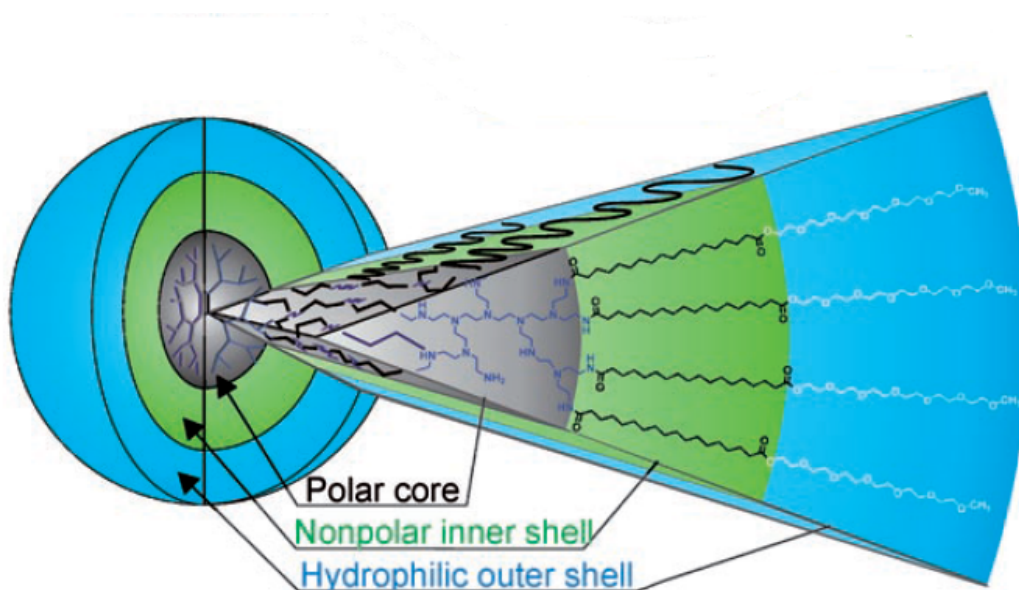
Figure 2.3: Schematic structure of CMS nanoparticles, the polar core is located in the center of CMS nanoparticles and is surrounded by a hydrophobic shell, and the outer shell is a hydrophilic.

Drug localization in the CMS nanoparticles

The location of different markers in the CMS nanoparticles has been investigated. Different techniques such as EPR and fluorescence spectroscopy were used. The localization of 5-doxy stearic acid (5DSA) [101] and PCA [104] was investigated by EPR spectroscopy. PCA is localized on the surface of CMS nanoparticles, while 5DSA is at the boundary between the apolar and the polar regions. Fluorescence spectroscopy revealed a distribution of the cargo nile red within CMS shells that depends on solvent and temperature [100]. By increasing temperature from room temperature to higher than 31°C, a hydrophobic drug model was relocated from the inner shell towards the hydrophilic shell.

2.2.2 Nanostructured lipid particles

Lipid-based nanoparticles for colloidal DDS can be known as solid lipid nanoparticles (SLN) and heterogeneous liquid/solid lipid mixtures, called nanostructured lipid carrier (NLC) [87]. The sizes of lipid-based nanoparticles are in the range of 50-1000 nm. The advantage of NLP over SLN is that more drug is soluble in the liquid lipids than solid lipids [105]. The literature on the distribution of the drug within the aforementioned nanoparticles is very limited [106, 107]. One report made use of model compounds like the fluorescent nile red and reported a localization in the liquid lipid phase of NLPs [108]. Diverging models assume the inclusion of substrates either in the core or the outer shell, colloidal dispersion in the lipid matrix or a homogeneous distribution [29, 87]. The chemical nature of the lipids influences how drugs associated with the NLPs [109]. The mixtures of solid lipids and liquid lipids in preparation of NLP is aimed at avoiding crystallization of a solid compartment and expulsion of the drug, as the particles become solid after cooling but do not crystallize [110]. More complex lipids which are mixtures of mono-, di-, and triglycerides and also contain fatty acids of different chain length exist, which form less perfect crystals with many imperfections offering space to accommodate drugs [87]. Since liquid lipids prevent crystallization the models for describing the incorporation of drugs into SLN has to be modified for NLC [111].

The hydrophobic lipophilic balance (HLB) of lipids plays an important role in NLP fabrication and choice of the right lipids for preparation of NLPs. HLB measures a lipid's degree of hydrophilicity or lipophilicity [112]. HLB is calculated based on identifying various hydrophilic and lipophilic regions in the molecule a scale from 0 to 18. The HLB range of 0-6 shows that it is a hydrophobic agent or it is oil soluble. In the sub-range of 2-3, the lipid is an antifoaming agent and in the sub-range 3-6, it is a water/oil (W/O) emulsifying agent. The HLB range of 6-10 indicates that a lipid is water dispersible. In the sub-range of 7-9, the lipid is a water spreading agent. The HLB range of 12-18 means that the lipid is hydrophilic or water-soluble. In the range of 8-16, the lipid is an oil/water (O/W) emulsifying agent. The range 13-15 encompasses detergents and the sub-range 15-18 solubilizing agents. In general, if the HLB is smaller than 10, then the molecule is lipid-soluble and if larger than 10, it is water-soluble. Two general methods for calculating HLB are used, the first is Griffin's method [113] which is based on the molecular weight and the second method is Davis method [114] which is based on chemical groups in the lipid. Other physical methods have also recently developed [115]. In this research, NLPs which are made of Gelucire®50/13, Witepsol®S55 and Capryol®90 were investigated [116]. A hydrophobic drug has sufficient solubility in these three lipids. Highly purified triglycerides, monoglycerides, complex glyceride mixtures, and hard fats need to be used for the preparation of NLP. Gelucire®50/13 is an amphiphilic lipid and improves the solubility/bioavailability if a poorly water-soluble drug is chosen. Gelucire®50/13 is a water dispersible surfactant forming fine (micro) emulsion with an HLB of 13 [117]. It also, improves wettability [117]. Gelucire®50/13 may act as a stabilizer for lipid nanosuspensions. Witepsol®S55 is a hard fat. It is used for the preparation of vaginal and rectal forms of medicines which require greater wetting of mucous membranes, enhances dispersibility, and is intended to promote absorption. The most important auxiliary is an ethoxylated cetyl-

stearyl alcohol. The HLB of Witepsol[®] S55 has not been determined [118]. Capryol[®]90 is a water-insoluble surfactant (co-surfactant), and has an HLB of 6 [119]. Understanding of the drug/NLP association requires knowledge of how a solvent and a solute interact with each other.

The dissolution of a solute in a solvent is induced by favorable interaction between solute and solvent molecules and strongly depends on their chemical structures. Interactions are characterized by molecular properties such as dipole moment, electronic polarizability, hydrogen bond donor and acceptor capability, and electron pair donor and acceptor capability. Three types of solvent/solute interactions could be described: lipid-lipid solubility, lipid/water solubility, and analog/lipid interaction. The lipid-water interaction is determined by the HLB. The surfactant properties of Gelucire[®]50/13 and co-surfactant properties of Capryol[®]90, determine the formation of the surface of NLPs and the interaction of these lipids and water. In NLP formation, the most relevant interaction is lipid-lipid interaction. The nanoparticles which are made of solid lipids (Gelucire[®]50/13 and Witepsol[®]S55) are characterized by a high order crystalline structure. Inclusion of a liquid lipid such as Capryol[®]90 results in a less organized lipid structure and NLPs which are prepared from two solid lipids and a liquid lipid has a less ordered crystalline state [116].

It was shown that NLPs enhance the amount of a drug in the SC by a factor of 2 compared to base cream and further that NLP provides a reservoir within the SC and the hair follicles allowing slow release of drugs [120].

The targeted design of nanoparticles for efficient drug loading and defined release profiles is even after 25 years of research on lipid-based nanoparticles still not a routine procedure. It requires detailed knowledge about the interaction of the drug with the lipid compounds and about its localization and distribution in the nanoparticle [121]. This is the topic of the current thesis.

Model for drug incorporation into NLPs

Five different models exist in the literature for describing how drugs are associated with NLPs based on SLN (Fig. 2.4) [30, 87, 111]. According to model one, the drug is homogeneously spread in NLPs. Two other models consider compartments containing the drug in the shell or the core of NLPs. The fourth and fifth models consider adhesion to the surface of NLPs. According to the literature, different preparation methods result in different incorporation types for drugs into NLPs. The drug enriched shell model (Fig. 2.4.II) is a model suggested for molten lipid droplets which are cooled rapidly. The drug-enriched core model (Fig. 2.4.III) assumes a recrystallization mechanism. The homogeneous model (Fig. 2.4.I) usually refers to the cold homogenization technique or to the incorporation of highly lipophilic drugs with hot homogenization techniques [111].

NLCs have an imperfect crystal structure in a solid matrix as a consequence of using glycerides composed of different types of fatty acids (Fig. 2.5.I). The loading capacity of a drug in NLC is increased by the number of imperfections. The solubility of a hydrophobic drug in liquid lipids is higher than in solid lipids. In the presence of liquid lipids (oils), separation into a solid

matrix and oily compartments are possible, leading to multiple types (Fig. 2.5.II). The drugs are dissolved during preparation in the liquid-lipid pockets. By using specific lipids to avoid crystallization during preparation, non-crystalline NLCs are formed. This type of NLC is called amorphous type (Fig. 2.5.III).

A number of studies have been performed to characterize the shape and surface of lipid nanoparticles via scanning electron microscope (SEM) [122] and atomic force microscopy (AFM) [123]. These two methods show that the morphology of the surface of different types of lipid nanoparticles is spherical and smooth. These properties are amplified by the presence of a liquid lipid component [105].
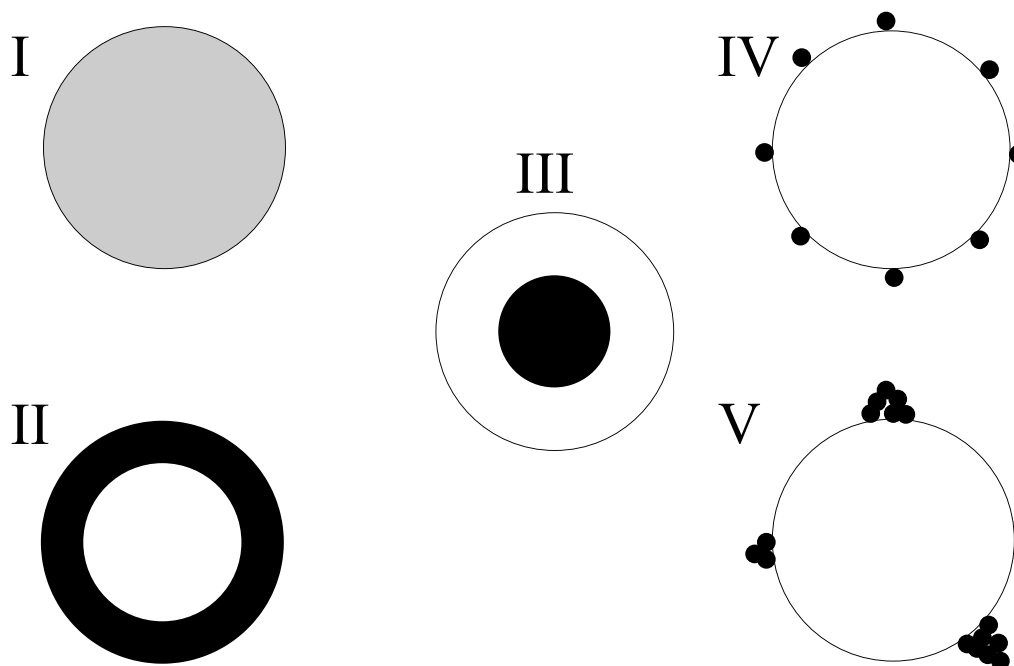
Figure 2.4: Drug incorporation models within nanosized lipid particles, I) homogeneously dissolved drug or drug dispersed within the entire lipid matrix, II) drug enriched within the outer shell (homogeneously or forming clusters); III) drug enriched within the core (homogeneously or forming clusters), IV) drug adhering to the nanoparticle surface and V) clustered compounds adhering to the nanoparticle surface (adopted from [30]).

Figure 2.5: Drug incorporation models of nanostructured lipid carriers, I) The imperfect crystal type NLC II) Multiple type NLC; III) Amorphous type NLC (adopted from [111]). Yellow and green circles depict drug and liquid lipid (oil), respectively.

2.3 The challenge of using nanocarriers as a dermal drug delivery system

Recently, nanocarriers are seen as the DDS of choice for topical application in the treatment of skin diseases. Nanocarriers offer a unique advantage as a pharmaceutical delivery system, as they allow achievement of a much more effective drug dosage ratio compared to other methods. They also provide better protection of drugs against degradation and other destructive factors compared to other DDS, because the carrier wall completely isolates the drug molecules from the environment. Additionally, they provide a better bioavailability for a poorly soluble drug and have a broad potential application. However, they only support a narrow selection of drugs, which needs to be expanded to most types of medications including macromolecules. In principle, nanocarriers are furthermore promising candidates with the potential of more controlled drug release [124]. However, efficient drug release remains a great challenge for nanocarrier based DDS. Different types of nanocarriers were introduced, and are developed in academic and also in industrial research. For developing efficient DDSs, two major questions need to be addressed for future applications of nanocarriers as DDS in topical treatment: 1) how can a pharmaceutical be efficiently loaded into the DDS and 2) how is it transported through the SC and released upon arrival at the target? Drug incorporation models play the main role in the evaluation of the available nanocarriers and the design of new nanocarrier systems for future use [125]. A prerequisite for answering both questions is to gain knowledge about the loading location of the drug within the nanocarriers. In the current work, we address these questions via EPR spectroscopy.

3 Electron Paramagnetic Resonance spectroscopy

Electron paramagnetic resonance (EPR) is a technique based on the absorption of electromagnetic radiation by a paramagnetic sample placed in a magnetic field. EPR is a spectroscopic method for determining the structure, dynamics and the spatial distribution of paramagnetic species. Also, EPR spectroscopy is a non-destructive method for studying properties of the surrounding micro-environment of paramagnetic molecules such as polarity/proticity and viscosity [50]. It is a promising method for achieving a better understanding of DDS and characterizing the drug loading into nanocarriers. Multi-frequency EPR in combination with different modes (cw and pulse mode) is a powerful tool for probing and investigating nanocarriers as micro-environment of drugs.

In this chapter the principles of EPR are presented. Electrons are characterized by their intrinsic spin angular momentum, as described in quantum mechanics [126]. The two eigenstates of a spin in a magnetic field are usually indicated by up $|\uparrow\rangle$ and down $|\downarrow\rangle$. A magnetic moment μ_e is associated with the electron spin [50].

The static spin Hamiltonian ($\widehat{H_0}$) of an unpaired electron describes the time-independent spin interactions (Eq. 3.1). The following terms of the Hamiltonian $\widehat{H_0}$ of a paramagnetic molecule inside a magnetic field are considered: the electron Zeeman interaction, nuclear Zeeman interaction and hyperfine interaction [50].

$$\frac{\widehat{H_0}}{\hbar} = \mu_B \vec{B_0} \widehat{g} \frac{\widehat{\vec{S}}}{\hbar} - \sum_i \frac{g_{ni} \cdot \mu_k}{\hbar} \vec{B_0} \widehat{\vec{I_i}} + \sum_i \widehat{\vec{S}} \widehat{A_i} \widehat{\vec{I_i}} \tag{3.1}$$

- $\widehat{g}$ factor (electron Zeeman interaction matrix)

- $\widehat{A}$, hyperfine coupling matrix

- μ_B and μ_k, Bohr and nuclear magneton

- g_n, nuclear g-factor

The first term of the Hamiltonian describes the electron Zeeman interaction, which is based on the classical magnetic dipole moment induced by the angular momentum of a charged particle. The spin magnetic moment $\widehat{\vec{\mu_e}}$ stems from the spin angular momentum $\widehat{\vec{S}}$ given by

$$\widehat{\vec{\mu_e}} = -\mu_B \widehat{g} \frac{\widehat{\vec{S}}}{\hbar} \tag{3.2}$$

The proportionality constant $\widehat{g}$ between the spin and the magnetic moment is given by the factor $g_e = 2$ in the Dirac equation and according to quantum electrodynamics, g_e for a free electron is 2.002319.

This spin magnetic moment interacts with an external magnetic filed $\vec{B_0}$ like a classical moment:

$$\widehat{H} = -\widehat{\vec{\mu_e}} \cdot \vec{B_0} \tag{3.3}$$

It is referred to as the Zeeman interaction and it is described by the following equation:

$$\widehat{H}_{EZ} = \mu_B \vec{B_0} \widehat{g} \widehat{\vec{S}}$$ (3.4)

When electrons interact with other particles, e.g nuclei, the effect of spin-orbit coupling causes a deviation of the *g*-factor from that of the free electronn, i.e. $g \neq g_e$ [50]. For an unpaired electron in a molecule, the proportionality constant becomes a matrix representing a deviation from collinearity of spin and magnetic moment [127]. The strength of the interaction is dependent on the orientation of $\widehat{\vec{S}}$ in regard to $\vec{B_0}$. This is described by introducing an orientation-dependent *g*-matrix in place of the *g*-factors. Determining and analyzing this coupling matrix is one of the central objectives of EPR spectroscopy. Nitroxide radicals, as spin probe candidates of this study, have an unpaired electron bound to light nuclei (nitrogen, oxygen, carbon, and hydrogen), thus the spin-orbital interaction is small, and the deviation of the *g*-factor from the free electron is small [128]. Nevertheless, the deviations can give important structural information, as well as information about the radical's micro-environment.

The second term of the Hamiltonian is the nuclear Zeeman interaction in analogy to the electron Zeeman interaction as discussed above. Similar to electrons, nuclei are characterized by a spin angular momentum as well. It is described by $\vec{I}$ [129], resulting in a total magnetic moment $\widehat{\vec{\mu_N}}$:

$$\widehat{\vec{\mu_N}} = -\mu_k g_n \widehat{\vec{I}}$$ (3.5)

The energy of nuclear spins in an external static magnetic field is influenced by the magnetic field strength is following:

$$\widehat{H}_{NZ} = \widehat{\vec{\mu_N}} \cdot \vec{B_0} = \mu_k \vec{B_0} g_n \widehat{\vec{I}}$$ (3.6)

Due to the difference in mass between an electron and a nucleus, the nuclear Zeeman interaction is by orders of magnitudes smaller than the electron Zeeman interaction. Nuclear spins in principle also exhibit spin-orbit coupling according to the nuclear shell model but this effect is negligible.

The third term of the Hamiltonian is the hyperfine interaction, which is caused by the interaction of the electron spin magnetic moment with the nuclear spin magnetic moments and is expressed by:

$$\widehat{H}_{HF} = \sum_i \widehat{\vec{S}} \widehat{A_i} \widehat{\vec{I_i}}$$ (3.7)

where *i* indexes the nucleus under consideration [130]. The Hamiltonian of the magnetic interaction between the electron and nuclear spins is split into two parts, the singular part, $\widehat{H}_{iso}$, and the non-singular part ,$\widehat{H}_{aniso}$, of the dipole-dipole interaction between electron and

nucleus:

$$\widehat{H}_{HF} = \widehat{H}_{iso} + \widehat{H}_{aniso} \tag{3.8}$$

The isotropic, or Fermi contact part is the singular contribution to the magnetic dipole-dipole interaction arising from the probability of finding the electron at the coordinate of the nucleus. The Fermi contact interaction is given by:

$$\widehat{H}_{iso} = a \cdot \widehat{\vec{S}} \cdot \widehat{\vec{I}} = \frac{2}{3}\mu_0 g_e \mu_B g_n \mu_k \, | \, \Phi_0(0) \, |^2 \, \widehat{\vec{S}} \cdot \widehat{\vec{I}}, \tag{3.9}$$

where a is the hyperfine coupling constant and $| \, \Phi_0(0) \, |^2$ is the probability of finding the electron at the nuclear coordinate. Since the latter is zero for orbitals other than s-orbitals, those do not contribute to the isotropic part of the interaction.

The anisotropic part of hyperfine interaction is the non-singular part of the dipole-dipole interaction between the electron and nucleus. Due to the non-spherical symmetry of p-, d-, f-orbitals, unpaired electrons in these orbitals show dipolar coupling to the nucleus and are, therefore, responsible for the anisotropic contribution to the hyperfine interaction [131].

$$\widehat{H}_{aniso} = \widehat{\vec{S}} A_{aniso} \widehat{\vec{I}} = -g_e \mu_B g_n \mu_k \{ \frac{(\widehat{\vec{I}} \cdot \widehat{\vec{S}})r^2 - 3(\widehat{\vec{I}} \cdot \vec{r})(\widehat{\vec{S}} \cdot \vec{r})}{r^5} \}, \tag{3.10}$$

where $\vec{r}$ is the electron nuclear distance vector.

The anisotropic part of hyperfine interaction is important for the interpretation of powder sample spectra. The anisotropic hyperfine coupling matrix has zero trace and averages out under rapid tumbling [127].
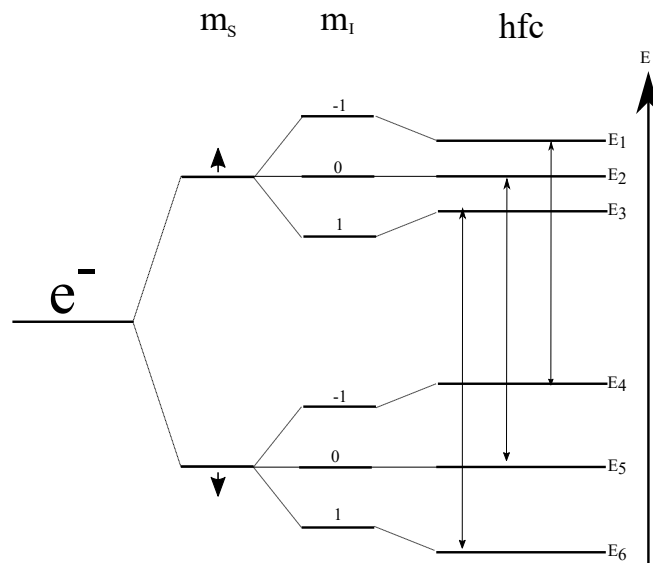
Figure 3.1: Energy levels and allowed transition for a nitroxide, $\widehat{S} = \frac{1}{2}$ and $\widehat{I} = 1$.

The usual effect of the isotropic hyperfine interaction with a single nucleus ($I \neq 0$) is to split the electron energy into $2I + 1$ levels, one for each value of m_I. For a system of one unpaired electron interacting with a nitrogen atom (^{14}N, $I = 1$), the electron energy splits into three levels.

There are now six spin states, which are represented by $| m_s, m_I >$ (Fig. 3.1). There are three allowed EPR transitions (Fig. 3.1). The transition selection rules are:

$$\Delta m_S = \pm 1, \Delta m_I = 0 \tag{3.11}$$

In case of high nitroxide spin probe concentration the effect of Heisenberg exchange by bimolecular collisions has to be taken into account. Heisenberg spin exchange, in which two free radicals exchange their spins during an encounter, may in a larger sense be regarded as a very simple chemical reaction requiring no rearrangement or transfer of masses. Depending on condition it will affect EPR spectra differently, e.g. linewidth broadening or narrowing and saturation effects of exchange [132].

3.1 Micro-environment polarity and proticity from EPR

The magnetic parameters of spin probes are influenced by the polarity and proticity[1] of their micro-environment. This environmental effect is described here for the case of a nitroxide probe. In figure 3.2 two limiting formal structures of a NO group bound to a molecule are depicted. These extreme structures are helpful to understand environmental effects. The neutral structure (Fig. 3.2a) localizes the unpaired electron on the oxygen atom ($\rho_\pi^O \simeq 1$, $\rho_\pi^N \simeq 0$), whereas the ionic structure (Fig. 3.2b) localizes the unpaired electron on the nitrogen atom ($\rho_\pi^O \simeq 0$, $\rho_\pi^N \simeq 1$). In this picture the unpaired spin is localized either on the oxygen (ρ_π^O) or the nitrogen atom (ρ_π^N) and the assumption is that the total unpaired spin is found on these two atoms, i.e. ($\rho_\pi^O + \rho_\pi^N \simeq 1$) in any micro-environment. This immediately leads to the conclusion that the nitroxide spin probe will tend to the neutral structure (Fig. 3.2a) in very apolar/aprotic solvents and will be shifted towards the ionic structure (Fig. 3.2b) in highly polar/protic solvents.

Even though the term polarity and proticity do not have unique definitions, they are commonly used to describe solvent properties. Polarity is characterized by the relative permittivity of the medium (ε_r), the permanent dipole moment of the compound and the sum of all specific and non-specific interactions between the solvent and solute molecules [133]. Taking into account the various intermolecular fields acting, such as polarity, and proticity, on the nitroxide in a solvent, the effective electronic structure is in between the neutral and ionic structure. In the absence of proticity, the electric dipole moment of a nitroxide is affected by the relative dielectric permittivity of its micro-environment. Additionally, in the presence of H-bonding chemical exchange takes place between the nitroxide and a proton donor [134].

---

[1]Characterization of a substance capability to make a hydrogen bond
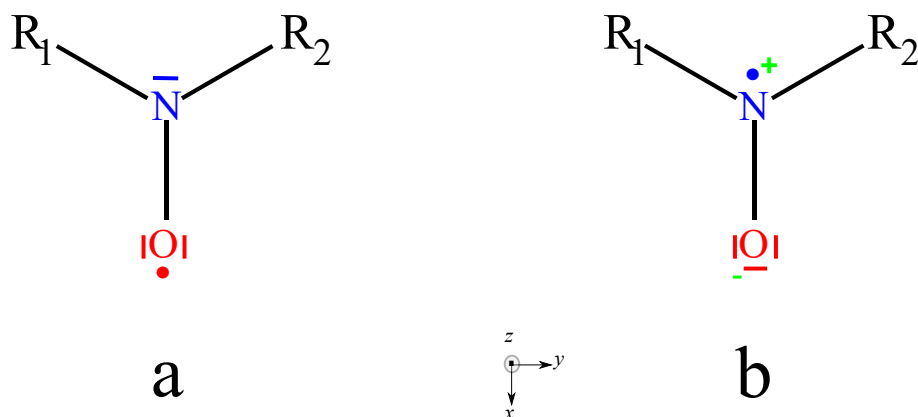
Figure 3.2: Two mesomeric structures of nitroxide, a) the neutral structure and b) the ionic structure. R_1 and R_2 represent methyl groups.

Consequently, polarity and proticity of the solvent induce shifts in the spin density at the nitrogen (ρ_π^N) and the oxygen atoms (ρ_π^O). Accordingly, polar and protic solvents tend to stabilize the ionic structure (Fig. 3.2b), and will increase the unpaired spin density on the nitrogen. Therefore, the polarity/proticity of an unknown micro-environment can be studied by the magnetic parameters reporting on the changes of ρ_π^O and ρ_π^N of the nitroxide. In this study, the magnetic parameters are obtained from EPR.

The redistribution of the spin density between the oxygen and the nitrogen atoms affects the hyperfine coupling experienced by the unpaired spin to the nitrogen nucleus. The hyperfine coupling is determined by the electron spin density on the nitrogen (ρ_π^N) atom in the π molecular orbital of NO, see equation 3.7. When the polarity/proticity of micro-environment of the nitroxide increases, the ρ_π^O decreases and accordingly, the ρ_π^N increases [135]. A large spin density on the nitrogen in polar/protic solvents yields a large hyperfine coupling to the nitrogen atom and the hyperfine coupling value increases linearly with increasing unpaired electron density on the nitrogen (ρ_π^N) (Eq. 3.12). The isotropic term of the nitrogen hyperfine coupling arises from an admixture of the nitrogen s-orbitals into the singly occupied molecular orbital [136]. Thus, the semi-empirical value Q_N represents the hyperfine splitting of nitrogen [137, 138].

$$a_{iso} = Q_N \rho_\pi^N \tag{3.12}$$

The ρ_π^N is the dominant parameter, and the ρ_π^O has a negligible contribution to the hyperfine coupling value.

The anisotropic term of the hyperfine coupling arises from the electron-nuclear dipolar

interaction between the redistributed unpaired electron and the nitrogen nucleus, which depends on the unpaired spin density on the nitrogen ρ_π^N as well (Eq. 3.9) [136]. The A-matrix of a nitroxide has almost axial symmetry, $A_{xx} \simeq A_{yy} < A_{zz}$. Thus A_{zz} produces the largest observable hyperfine splitting. A similar trend for A_{zz} is expected for the A_{iso}. In summary, A_{iso} and A_{zz} can be used as an indicator of the polarity/proticity of the micro-environment of the spin probe.
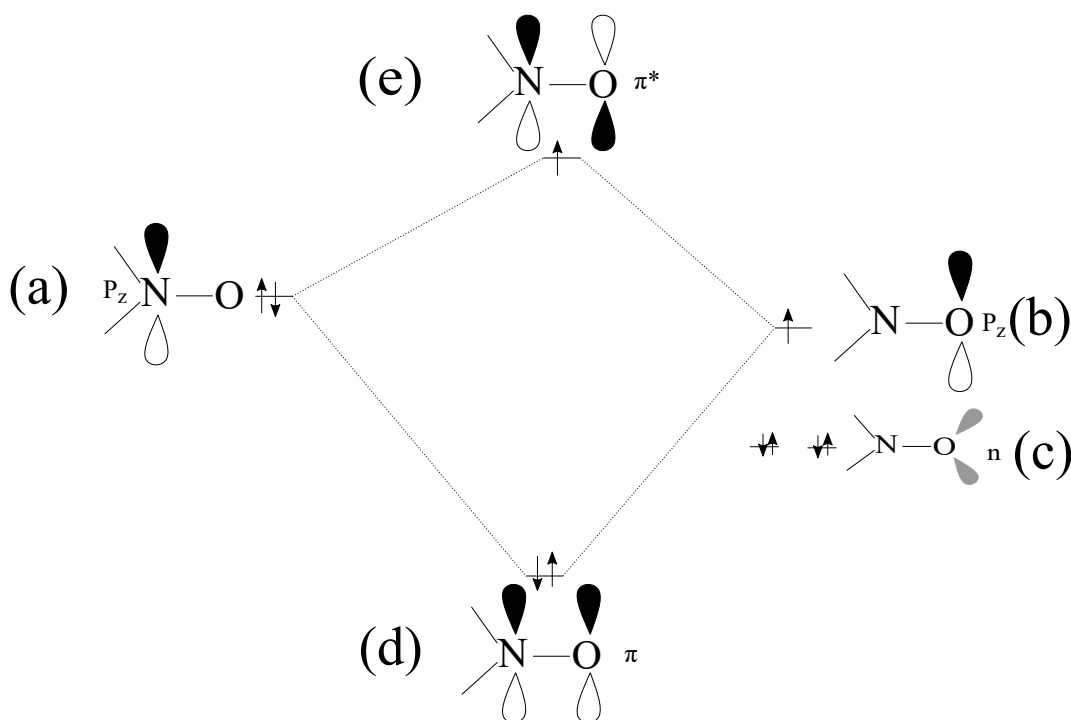
Figure 3.3: Schematic representation the orbital of NO group, based on molecular orbital (MO) theory. On the left, the $2P_z$-orbital on the nitrogen (a); on the right, $2P_z$-orbital on the oxygen (b) and the non-bonding n-orbital on the oxygen (c), on the down, the double occupied bonding π molecular orbital (d), and on the up, the single occupied anti-bonding π^* molecular orbital (e), obtained from [139].

While the hyperfine coupling is largely determined by the spin density on the nitrogen of the NO group, the main source for the deviation of the nitroxide g-matrix from the free electron g-value, g_e, comes from the spin density on the oxygen. This is due to the fact that the spin-orbit coupling parameter of oxygen is significantly larger than the spin-orbit coupling parameter of nitrogen [139]. As we discussed previously, the neutral structure (Fig. 3.2a) is energetically favored in apolar/aprotic solvents and carries the unpaired electron on the oxygen atom, whereas the ionic structure (Fig 3.2a), with the unpaired electron on the nitrogen atom, is energetically favored in a polar/protic solvent. Therefore, a larger deviation of the g-matrix from g_e is expected for nitroxides in apolar/aprotic solvents than in polar/protic solvents.

Thus, the hyperfine coupling in the same direction and the g-matrix in the opposite direction report the changing the polarity properties of the environment. The solvent influence on the nitroxide g-matrix can be well explained by Stone's theory, which calculates the g-matrix using perturbation theory [140]. Thereby, the singly occupied π^* molecular orbital of the NO bond (Fig. 3.3 e) plays together with the oxygen lone pair orbitals (Fig. 3.3 c) the essential roles for understanding the g-matrix of the odd electron [141]. The double occupied bonding π orbital (Fig. 3.3 d) and the single occupied anti-bonding π^* orbital are linear combinations of the two $2P_z$ orbitals of nitrogen and oxygen (Fig. 3.3 a and b), respectively. The character of the π^* orbital (more or less contribution of the oxygen and nitrogen $2P_z$ orbitals) and its orbital energy in comparison to the other orbitals is determined by the environment. Fig. 3.2 shows a representation of the NO group with the x- and y-axes spanning the plane of the nitroxide with the x-axis along with the NO bond and the view direction along the direction of the $2P_z$ orbitals. The lone pair orbitals make an angle φ of roughly $30°$ with y-axis and thus have a larger projection on the y than the x-axis. Since promotion of an electron from an orbital aligned along the y-axis into another aligned along the z-axis involves an angular momentum around the x-axis, the mixing of the lone pair orbitals with the π^* orbital along the z-axis in perturbation theory has a larger influence on the x component of the g-matrix than on its y component and the z remains unaffected close to g_e. The g_x component is given according Stone's approximation by

$$g_x = g_e + \frac{2\xi_O (C_{O,y}^{(n)})^2 \rho_\pi^O}{\Delta E_{n \to \pi^*}} \tag{3.13}$$

with

- g_e the free electron value

- ξ_O the spin-orbit coupling constant of oxygen

- $C_{O,y}^{(n)}$ the coefficient of the oxygen $2p_y$-orbital in lone pair orbital

- ρ_π^O the spin density on the oxygen atom

- $\Delta E_{n \to \pi^*}$ the excitation energy from the lone pair to the π^* orbitals

From equation it is obvious that g_x has a linear dependence on the spin density ρ_π^O on the oxygen. The explicit dependence of g_x on the energy difference between the lone pair to the π^* orbital ($\Delta E_{n \to \pi^*}$) yields a significant influence of hydrogen bonding on g_x, which is beyond the polarity effect. In summary, the nitroxide g_x in apolar/aprotic environment is shifted further away from g_e than in polar/protic environments. Protic environments are expected to yield smaller g_x values than aprotic environments of the same polarity. The g_y component is affected qualitatively in the same way by polarity/proticity, but to a smaller extent as the projection of the lone pair orbital onto the molecular x-axis, which is smaller than onto the y-axis.
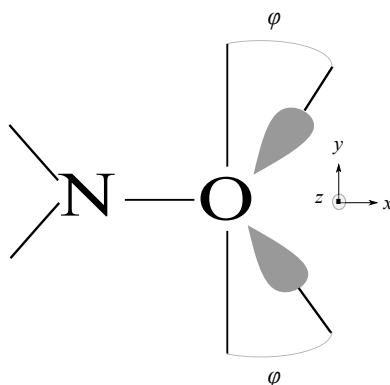
Figure 3.4: Scheme representing the geometry of the non-bonding lone pair orbitals at the oxygen atom with respect to the molecular form of a nitroxide. The lone pairs make an angle φ of approximately 30° with the molecular y-axis and approximately 60° with the molecular x-axis.

Taken together, the linear dependence of the g_x component on the unpaired electron spin density at the oxygen atom (ρ_π^O) and of the hyperfine coupling A_{zz} on the unpaired electron spin density at the nitrogen atom (ρ_π^N) of the nitroxide group yields a decrease of g_x and an increase of A_{zz} with increasing environment polarity/proticity, respectively. This effect is used in this thesis as an indicator for studying the polarity and proticity experienced by spin probes in nanoparticle DDS.

3.2 Anisotropic interaction and spin probe mobility

Spin probes are excellent tools to study dynamic processes via cw EPR. The (anisotropic) dynamics of a spin probe yields valuable information to characterize environment properties. The rotational correlation time [2] (τ_{corr}) of a spin probe can be determined from cw-EPR spectra by simulation. This correlation time is affected not only by solvent viscosity effects but also gives information on e.g. the immobilization of the probe molecule by binding to macromolecules [142].

If the timescale for reorienting the molecule is comparable to the inverse of the spectral width, the shape of the EPR spectrum will be affected by g- and A-matrix. The shape of EPR spectra of partially-immobilized spin probes is dependent on the magnetic field in which the resonance occurs [143]. The effect of the anisotropic g- and A-matrix for the immobilized case of a spin label at X-band frequency are described in the following. The m_I=0 transition simply is broadened by the g-matrix, since the g-anisotropy is smaller than the inhomogeneous linewidth (Fig. 3.5, red line). For the high field transition ($m_I = -1$) the g- and A-matrix elements add and result in the largest spectral width (Fig. 3.5, yellow line). In contrast, for the

---

[2]τ_{corr} is the average time required for rotation through 1 radian about a principal axis

low field transition ($m_I = 1$) the electron Zeeman and hyperfine term in the spin Hamiltonian have different signs and thereby cancel each other partially and yield a smaller spectral width (Fig. 3.5, blue line) then for the $m_I = -1 line$. On the other hand, if the free nitroxide radical is dissolved in a low-viscosity solvent, then the very fast molecular reorientations due to thermal motion averages out the anisotropic terms of the spin Hamiltonian. The position of the spectrum in the field and the magnitude of the hyperfine splitting are thus determined by the average values of the diagonal elements of the g- and A-matrix.
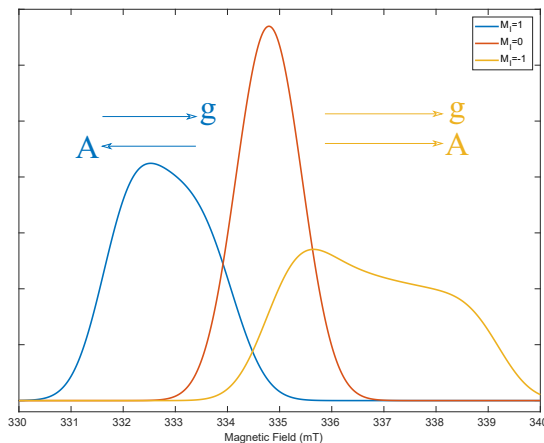
Figure 3.5: The transitions associated with m_I=1, 0, -1 of the g-matrix [2.01 2.006 2.002] and A-matrix [15 15 105] MHz at X-band in powder samples.

The dynamics of spin probes is classified by the relation of the rotational correlation time (τ_{corr}) and the spectral width ($\triangle\omega$). In the very fast limit $\tau_{corr}\triangle\omega \ll 1$, the anisotropic interactions are averaged out and one observes only the isotropic mean of the magnetic interactions (see Fig. 3.6 for τ=0.05 ns). When the ratio is changed to $\tau_{corr}\triangle\omega < 1$, the spectrum can be considered as fast motion regime (see Fig. 3.6 for τ=0.25 ns). Here the high field transition (m_I=-1) starts to broaden due to the larger width (electron Zeeman and hyperfine term add). With increasing rotational correlation time also the low field transition (m_I=+1) becomes broader. When ($\tau_{corr}\triangle\omega \simeq 1$), the dynamics of the spin probe is referred to be in the slow-motion regime for the given EPR frequency. For very long rotational correlation times $\tau_{corr}\triangle\omega \gg 1$, a static distribution of all orientations of the spin probes is observed (Fig. 3.6, τ=25 ns).
The rotational correlation time is obtained from fitting the cw spectra. For spherical particles and low viscosity the Stokes-Einstein equation is a good approximation to relate the size of the particle, the solvent viscosity, and the temperature to the rotational correlation time (Eq. 3.14). By this relation one can deduce a surrounding viscosity η in an unknown environment [144].

$$\tau_{corr} = \frac{8\pi\eta R_{eff}^3}{6k_T T} \tag{3.14}$$

- τ_{corr}, rotational correlation time [s]

- η, viscosity [Pas]

- R_{eff}, effective radius [m]

- k_T, Boltzmann constant [JK^{-1}]

- T, temperature [K]
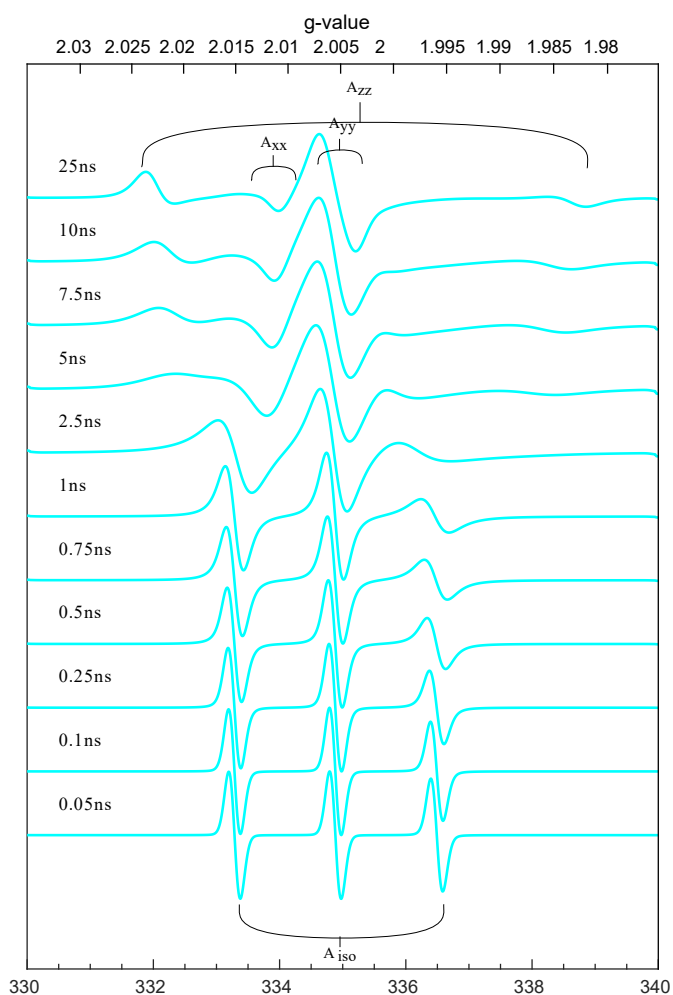
Figure 3.6: Simulation X-band EPR spectra of a nitroxide with different rotational correlation time, according to the *g*- and *A*-matrix of DxPCA (water) based on *chili* function Easyspin to follow the dynamics of the spin probe.

3.3   Electron spin relaxation

A spin system is described by the macroscopic magnetization $\vec{M}$ as the sum of all individual molecular magnets. The time evolution of this magnetization is described by the Bloch equations [145]. A quantitative description of any paramagnetic center's magnetization behavior in a static magnetic field is given by:

$$\vec{M_0} = \chi_0 \vec{B_0} \tag{3.15}$$

where χ_0 is the static magnetic susceptibility.

By convention, the external magnetic field is always assumed to be along the z-axis of the laboratory frame. Then, the change of the magnetization of the paramagnetic center along the z-axis is defined as:

$$\frac{d\vec{M_z}}{dt} = \frac{\vec{M_0} - \vec{M_z}}{\tau} \tag{3.16}$$

The relaxation time τ is the characteristic time for the energy flow from the spin system to the environment. Thus, τ reflects the degree to which the spin system is connected to its environment.

In the dynamic case, the laboratory frame of reference can be picked arbitrarily. There is a Larmor or resonance frequency $\omega_0 = \gamma \vec{B_0}$ at which the paramagnetic spin precesses around B_0 [146]. The magnetization will obey the following equation:

$$\frac{d\vec{M_0}}{dt} = \gamma \vec{M_0} \times \vec{B_0} \tag{3.17}$$

where γ is the gyromagnetic ratio.

Taking relaxation into account, the Bloch equation 3.17 can be written as follows:

$$\frac{d\vec{M}}{dt} = \gamma \vec{M} \times \vec{B_0} + R(\vec{M_0} - \vec{M}) \tag{3.18}$$

where $\vec{M} \times \vec{B_0}$ describes the interaction of the magnetization with the external magnetic field and R describes the relaxation of the magnetization back to the equilibrium state $\vec{M_0}$.

$$R = \begin{bmatrix} \frac{1}{T_2} & 0 & 0 \\ 0 & \frac{1}{T_2} & 0 \\ 0 & 0 & \frac{1}{T_1} \end{bmatrix} \tag{3.19}$$

$\vec{M_x}$ and $\vec{M_y}$ relax with the same rate, which is characterized by T_2, the transversal relaxation time. $\vec{M_z}$ relaxes with T_1, the longitudinal relaxation time. In the presence of an external magnetic field, the net magnetization ($\vec{M}$) precesses around the direction of the external magnetic field (z-axis) with the Larmor frequency.

The time-dependent solution of equation 3.18 is:

$$\vec{M}(t) = R_z(\omega_0 t)\exp^{-Rt}\vec{M}(0) + (1 - \exp^{-Rt})\vec{M_0} \tag{3.20}$$

with R as defined above and

$$R_z(\omega_0 t) = \begin{bmatrix} \cos \omega_0 t & -\sin \omega_0 t & 0 \\ \sin \omega_0 t & \cos \omega_0 t & 0 \\ 0 & 0 & 1 \end{bmatrix} \tag{3.21}$$

is the rotation matrix describing a rotation around the z-axis at the Larmor frequency $\omega_0 = \gamma \vec{B_0}$. In summary, this solution describes a precession of the magnetization around the z-axis that, over time, spirals back towards the equilibrium orientation $\vec{M_0}$.

As described in this section, the relaxation of the magnetization back to the ground state $\vec{M_0}$ is governed by two parameters, the longitudinal or spin-lattice relaxation time (T_1) and transversal or spin-spin relaxation time (T_2). We will discuss their origin in the next two following sections.

3.3.1 Spin-lattice relaxation

Longitudinal or spin-lattice relaxation T_1 causes the magnetization to return to the preferred orientation along of the z-axis. The mechanism of T_1 relaxation depends on the electronic structure of the paramagnetic center. The analysis of T_1 relaxation can provide insight into the molecular interaction of the paramagnetic center with its environment.

Electron spin-lattice relaxation mainly occurs due to the transition between spin states by a process that involves the transfer of energy to the lattice. The T_1 relaxation processes may be discussed in terms of individual quantum events. A wide variety of transition types contribute to the spin-lattice relaxation [144]. The main processes that contribute to T_1 in immobilized samples are direct, Raman and Orbach processes [146]. In these samples, the spin probes are tightly coupled to the vibrations of the surrounding micro-environment. These T_1 processes are based on the orbital-lattice energy transfer involving electronic states and lattice phonons.

3.3.2 Spin-spin relaxation

In contrary to spin-lattice relaxation, the spin-spin relaxation describes a loss of coherence in the spin system. The origin of T_2 the spin-spin interaction where no exchange of energy between the spin system and its surrounding environment is required. Fluctuations in the local magnetic field experienced by the spins cause variations in their Larmor frequencies, leading to the dephasing of the coherent spin ensemble. The spin-spin relaxation time T_2 is defined by the Bloch equation as the time needed for dephasing of different spin packet's magnetization in the x- and y- plane and is the rate for mutual $\vec{S_{1+}}$, S_{2-} electron spin flips. The spin-spin relaxation depends on the physical properties of a paramagnetic center or chemical

properties of its environment and is determined by processes that take spins off resonance or affect the phase of the electron spins in the rotating frame.

3.3.3   Spin diffusion

Spin diffusion corresponds to a spatial propagation of spin magnetization through flip-flop processes of nearby spins [146]. The spectral diffusion as an additional process needs to be considered for an appropriate investigation of relaxation times. The spins that are excited by a microwave pulse are not necessarily the spins that are observed in the relaxation time measurement. The excited spins can be converted into non-observed spins outside of the detection bandwidth and this process will appear as relaxation. Spin diffusion takes into account the effect of all non-resonant processes that transfer magnetization from one paramagnetic center to another. Spin diffusion encompasses all processes that move spin magnetization between positions in the EPR spectrum, including the motion of an anisotropic paramagnetic center, electron-electron exchange, electron-nuclear cross relaxation and nuclear spin flip-flops [147].

3.3.4   Characterization of the micro-environment by spin-lattice relaxation

A comparative study based on relaxation times T_1 and T_2 for characterizing different known and unknown micro-environments can be performed. The electron spin relaxation time reflects the electronic structures of paramagnetic species and the dynamics of these species and their environment [148]. This study focuses on how to utilize the spin-lattice relaxation (T_1) for the characterization of spin probes environments. The different mechanisms contributing to the relaxation, i.e the direct, Raman and Orbach process, are considered [149]. For small molecules, the direct process is more dependent on solvent and less dependent on the characteristics of the molecule [148]. Additionally, the size of spin probes influences the rate of relaxation but does not change the mechanism [150]. The Raman process depends on g-anisotropy and the rigidity of the molecules. When the experimental temperature is below 100 K, the Raman process makes significant contributions to the spin-lattice relaxation process and is the dominant relaxation mechanism [148].

Additionally, T_1 depends on the spin-orbit angular momentum. Spin-orbital coupling influences the relaxation time in different orientations. T_1 is also dependent on the modulation of anisotropic interactions by vibrations and is in that case orientation-dependent [151]. For example, in case of on axial ^{14}N hyperfine interaction, T_1 is the longest along the parallel direction and shortest in the perpendicular plane [151]. The relaxation time also is a function of the number of H-bonds and more H-bonding results in lower relaxation time [151]. Also, T_1 depends on the viscosity and rotational correlation time, both of which are functions of the experimental temperature [152]. In the following, we make use of the well-resolved nitroxide EPR spectrum at W-band frequency at low temperature. Under these conditions, the trend of changes in relaxation time is influenced by spin-orbital coupling and proticity of surrounding micro-environment. Then, it is achievable to differentiate between various media based on the relaxation time.

3.4 Advantages of dual-frequency EPR spectroscopy

Finally, the potential of dual-frequency EPR will be described for the study of the surrounding micro-environment and dynamics of different molecules. The first order energy eigenvalues of equation 3.1 are written in terms of the magnetic spin quantum numbers, m_s and m_I, for one electron and one nucleus:

$$\frac{E(m_s, m_I)}{\hbar} = g\frac{\mu_B}{\hbar}B_0 m_s - g_n\frac{\mu_k}{\hbar}B_0 m_I + Am_s m_I \qquad (3.22)$$

The Hamiltonian consists of two different types of terms, the field-dependent, and the field-independent terms. The electron and nuclear Zeeman interactions are magnetic field-dependent terms. They represent the interaction between spin and magnetic fields. On the other hand, the hyperfine coupling term is based on electron-nuclear interaction and is a field-independent term. The field-dependent terms of the spin Hamiltonian become the dominant terms over the field-independent terms when the external magnetic field and microwave frequency are increased. Then, dual-frequency EPR spectroscopy is advantageous to separate field-dependent and field-independent parameters [51]. If the g-anisotropy of the sample is small (e.g., organic free radicals), features of the EPR spectrum can be hidden in the linewidth. In this situation, it is helpful to use high-frequency EPR spectrometers to resolve the g-anisotropy better, and enhance the resolution due to magnetic field-dependent interactions allowing to extract the g-matrix of spin probes at cryogenic temperatures (Fig. 3.7). Additionally, the change of g_x values of a spin probe in the different micro-environments are observed with better resolution at high-field EPR according to

$$\Delta B_0 = \frac{h\nu}{\mu_B}(\frac{1}{g_1} - \frac{1}{g_2}) \qquad (3.23)$$

On the other hand, the hyperfine interaction, described by the A matrix, is a field-independent process. By choosing dual-frequency, it is possible to study a particular process in the EPR spectrum. The factors that govern the EPR linewidth, such as unresolved hyperfine structure, relaxation, and g-anisotropy, should be taken into account when choosing dual-frequency band. A greater resolution of the EPR spectrum can be achieved by going to higher frequencies for moderate fields to observe the same transition, from X - to W-band. In this context, it should be noted that resolved overlap of different spectral features occurring at a particular microwave frequency will render dual-frequency advantageous (Fig. 3.7) [51].

The rotational correlation time τ_{corr} is another field-independent parameter, the mobility changes the orientation of the molecule with respect to the external magnetic field. Then, the Hamiltonian of the spin system becomes time-dependent. The Hamiltonian of the spin consists of isotropic and anisotropic parts. While the isotropic part of the spin Hamiltonian is invariant to the mobility of the molecule the anisotropic part of Hamiltonian fluctuates in time.
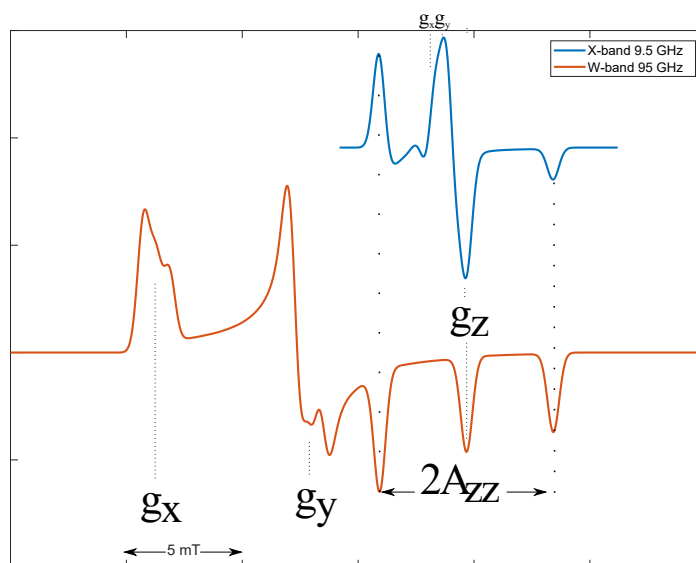
Figure 3.7: Simulated powder spectra of a nitroxide at X- and W-band show the increased Zeeman resolution from X-band to W-band. The g and A values, which are completely resolved at W-band, are indicated in the figure.

The EPR spectra at W-band exhibit very high sensitivity to the g-anisotropy, the spectra provide excellent orientational resolution as compared to that achieved at X-band. Thereby, spectral lines at higher frequency become broader. Thus, the rotational motion modulates the energy levels and the transition frequencies. Since the effect of motional averaging in the EPR spectrum depends on the spectral width, high frequency EPR provides the capability for a different time window of spin probe mobility. EPR can then be used in a dual-frequency EPR approach at the same temperature to probe fast internal modes of motion and to discriminate them from the slow restricted motion of a macromolecule in solution. At low frequencies, one can clearly observe the motions at a slower time-scale with the faster motions averaged out. On the other hand, high frequency EPR provides increased sensitivity to dynamics on the sub-nanosecond time scale. The motional processes that appear fast at lower (X-band) frequencies appear slow at higher (W-band) frequencies (see Fig. 3.6 in comparison to Fig. 3.8) [142].
Finally, this technique also allows to distinguish small g-value difference for mixtures of micro-environments and study them beside the fast and slow motions of the spin probe at room temperature. It was described how magnetic and dynamic parameters influence the shape of room temperature spectra at a different frequency. As discussed before, the fast motion spectrum in one frequency is not necessarily fast in the other frequency. Dual-frequency EPR gives the opportunity to investigate complex motional dynamics.
The sensitivity of the relaxation time measurements is increased from X-band (9.4 GHz) to W-band (94 GHz) [152]. With the higher spectral resolution, one can measure relaxation times at selected orientations to the g-axes of the spin probe. This can yield additional information

about anisotropic motions of a spin probe [153].
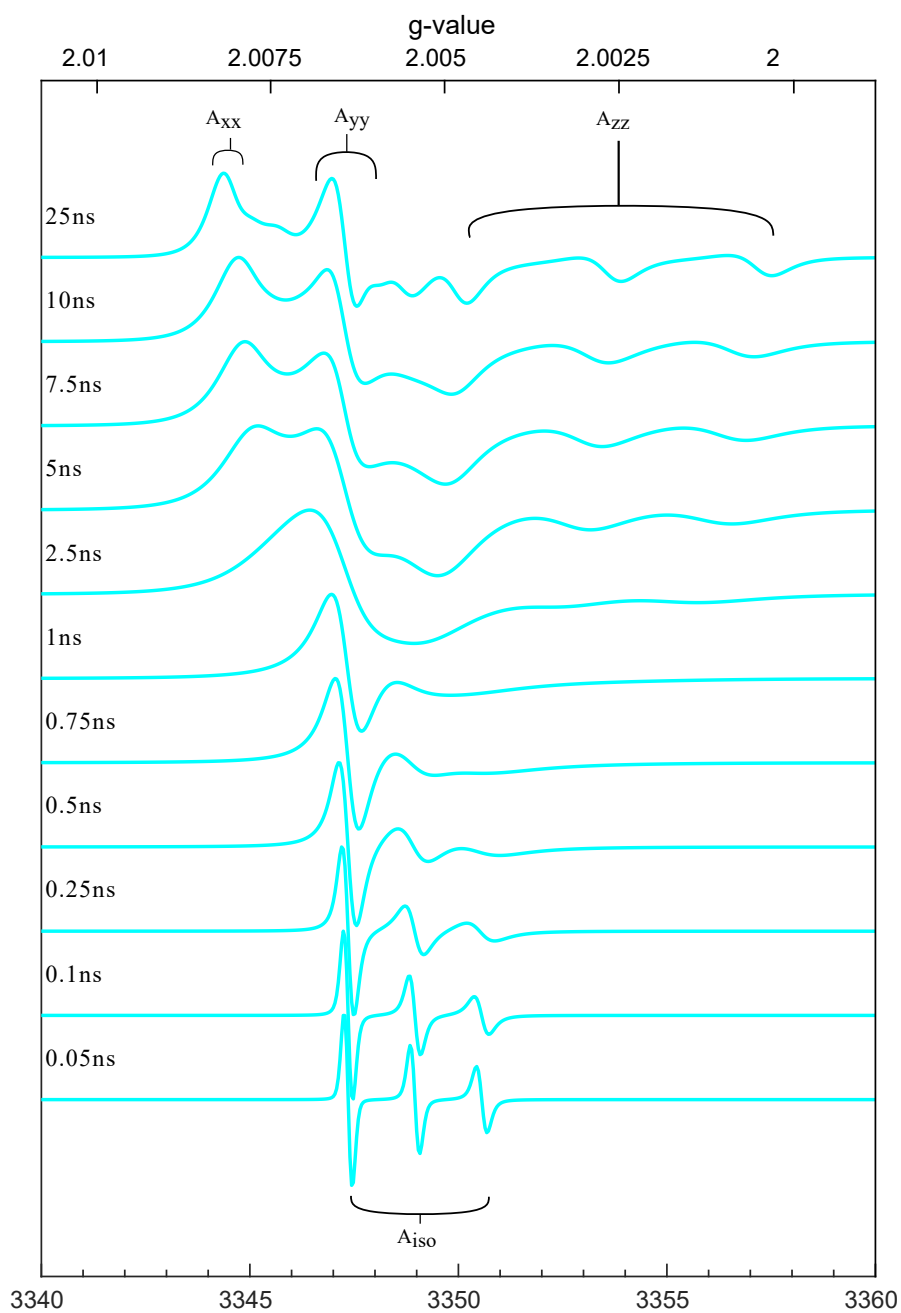
Figure 3.8: Simulation W-band EPR spectra of a nitroxide with different rotational correlation time, according to the *g*- and *A*-matrix of DxPCA (water) based on *chili* function EasySpin to follow the dynamics of the spin probe.

4 Materials and Methods

4.1 Drug, Spin probes, and Spin labeled drugs

This section presents the materials used in this thesis. It starts with the drug dexamethasone which is considered for transport by nanocarriers as DDS. Since this drug is diamagnetic it can not be directly observed by EPR. Therefore paramagnetic spin labels are introduced as well. The section ends with the description of the specific spin labeled drug used in this study.

4.1.1 Dexamethasone

Dexamethasone (Dx) is a potent anti-inflammatory and immune suppressive glucocorticoid used for the treatment of inflammatory and autoimmune conditions such as rheumatoid arthritis and for nasal and eye allergies [154]. It is used to treat some forms of skin disease, among them atopic dermatitis and psoriasis, which are two of the most common inflammatory diseases of the skin. Both skin disorders are complex inherited diseases involving genes that encode immune components and structural proteins that are involved in proliferation and differentiation of epidermal cells [55]. Dx is chosen as the model drug for this research (Fig. 4.1a).

4.1.2 Spin probes

Dx is a diamagnetic drug. Therefore we need a practical way to use the advantage of EPR spectroscopy for studying DDS. Stable nitroxide radicals have proven to be effective tools in solving many problems in chemistry, physics, and biomedicine at the molecular level. Recently, they have started to be used for pharmaceutical and drug delivery system investigations beyond the traditional application [155]. Spin probes provide precious information about the structure of nanocarriers and micro-environment as well as dynamics of nanocarriers and drugs loaded into them.

The first stable nitroxide spin probe was introduced in 1961 [156]. Different nitroxide spin probes for various applications have been developed since then, bringing different functionalities and structures appropriate for studying different systems such as proteins, nucleic acids, lipid membranes and oxidative reactions [157].

3-Carboxy-2,2,5,5-tetramethyl-1-pyrrolidinyloxy (PCA)

3-Carboxy-2,2,5,5-tetramethyl-1-pyrrolidinyloxy (PCA) (Fig. 4.1b) is a five ring nitroxide spin probe with a carboxylic acid group, with molecular weight of $186\,\mathrm{g\,mol^{-1}}$. PCA is a hydrophilic spin probe with partition coefficient[1] (logP) of -1.7 [158], which is used for studying how its micro-environment influences the magnetic parameters. It was chosen as spin probe for investigating association of lipophobic drug to NLP.

The concentration of PCA in different solvents used as reference samples was $50\,\mu\mathrm{M}$ (Table A.1).

---

[1] the ratio of concentrations of a compound in a mixture of two immiscible phases at equilibrium

All solvents (purity ≥ 98%) used were purchased from Sigma-Aldrich.

(a) Dexamethasone

(b) 3-Carboxy-2,2,5,5-tetramethyl-1-pyrrolidinyloxy (PCA).

(c) 2,2,6,6-Tetramethylpiperidin-1-yl oxyl (TEMPO).

(d) Dexamethasone labeled by PCA
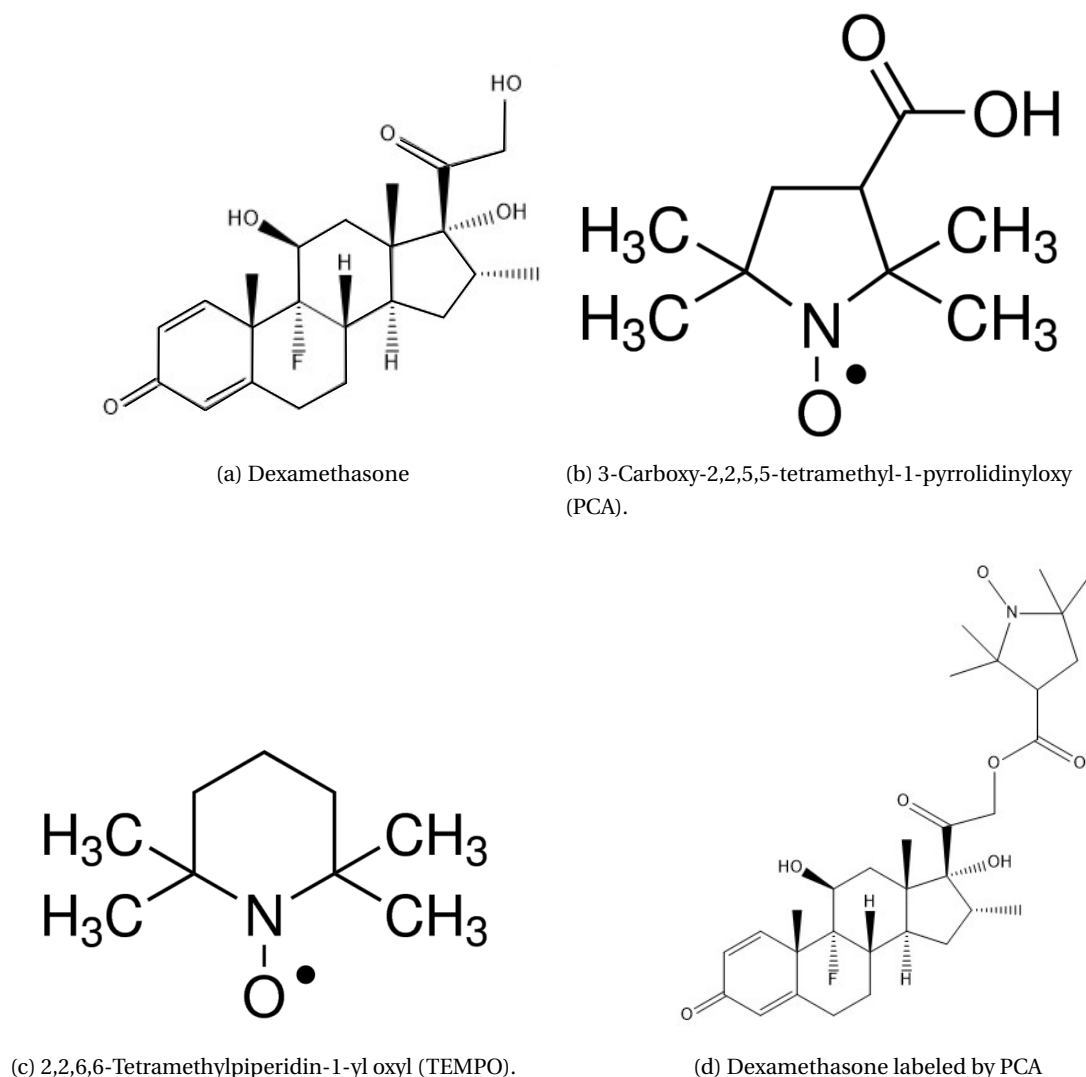
Figure 4.1: Spin probes and a spin labeled drug.

2,2,6,6-Tetramethylpiperidin-1-yl oxyl (TEMPO)

2,2,6,6-Tetramethylpiperidin-1-yl oxyl (TEMPO) (Fig. 4.1c) is a six ring nitrioxide. The proper-ties of TEMPO in different micro-environments, especially in liposomes was studied in [159]. The partition coefficient of TEMPO (logP) is 2.3 [160], but it shows amphiphilic properties [161]. On the other hand, Nilsson and *et al.* reported a partition coefficient of TEMPO 1.8 [162]. In the other research was reported 1.8 for logP [163]. In the thesis, we measured the logP of TEMPO via quantitative EPR method as well to find an accurate value for our investigation (Sec-tion 5.1.3). TEMPO was chosen as the spin probe for investigating how small amphiphilic probes association with NLP.

4.1.3 Dexamethasone labeled by PCA

Dexamethasone labeled by PCA (DxPCA) (Fig. 4.1d) is a modified drug for investigation by EPR spectroscopy. Dexamethasone is specifically labeled by PCA for this research. The reduction rate of five-ring nitroxides is lower than for six-ring nitroxides (e.g TEMPO) after topical application on the skin [164]. This is the main reason for choosing PCA for labeling. DxPCA was synthesized by refluxing Dx with PCA, 4-(Dimethyl)-aminoprrydidine and 1-Ethyl-3-(3-dimethylaminopropyl) carbodiimide in dicholoromethane for 3 h with subsequent column-chromatographic purification. The labeling procedure is comprehensively described by K. A Walker, *et al* [48].

4.2 Sample preparation

4.2.1 DxPCA

The solubility of DxPCA in water is low (~ 89 mg/l at 25°C) [165]. Thus, for achieving the desired DxPCA concentration in water, the solution was sonicated and heated up to 70°C for thirty minutes and afterward diluted. Finally, this solution was centrifuged and aggregated parts were removed by taking the supernatant.

The concentration of DxPCA in the other solvents used as a reference sample, for polarity/proticity investigation, was 50 μM, except for the solvent toluene where it was 25 μM (Table 5.3).

4.2.2 Dendritic core-multishell nanoparticles

DxPCA was loaded in CMS nanoparticles by an entrapment film method. First, DxPCA was dissolved in ethanol, and afterward, the solvent was evaporated and dried under vacuum yielding a thin drug film on the surface of the glass container. Second, the CMS nanoparticles in aqueous solution (5 g/L) were added to the thin DxPCA film. The solution was stirred for 22 h at 1200 rpm. In the end, the solution was filtered through a 0.45 μm regenerated cellulose filter [166].

4.2.3 Nanostructured lipid particles

For the preparation of NLPs the lipid components Gelucire®50/13 (Ge) (stearoyl macro-golglyceerides, GATTEFOSSE GmbH, Bad Krozingen, Germany), Witepsol®S55 (Wi) (solid triglycerides containing hydrogenated coco-glycerides, beeswax, and cetearth-25, CREMER OLEO GmbH & Co. KG, Hamburg, Germany), and Capryol®90 (Ca) (propylene glycol mono-caprylate, GATTEFOSSE GmbH, Bad Krozingen, Germany) were mixed in different ratios, (NLP-Ge [100:0:0], NLP-Ge/Wi [75:25:0], NLP-Ge/Ca [80:0:10], NLP-Ge/Wi/Ca [50:30:10]) and melted at 60°C together with 0.5% (w/w) spinprobes (DxPCA or PCA or TEMPO). The 10% (w/w) lipid nanosuspension was prepared from a nanoemulsion by pouring ultrapure water of the same temperature into the lipid melt followed by high-shear-homogenization for 5 min.

Finally, the nanoemulsion was cooled to room temperature to solidify the lipid phase and thus, to obtain the lipid nanosuspension. The lipid nanosuspension was filtered through 0.7 μm glass fiber filter (Whatmann GF/F; Sigma-Aldrich Chemie GmbH, Steinheim, Germany) to eliminate precipitated drug crystal from the water phase [116, 121].

4.3 EPR Methods

In this section, the schematic of an EPR spectrometer is shown and the instruments used in this study are described. Then, the measurement technique is discussed.

4.3.1 EPR spectrometer equipment

In general, an EPR spectrometer is built from three major components (Fig. 4.2)

- A microwave bridge, containing a microwave source and a detection system

- A magnet and magnet power supply for generation of the magnetic field B_0

- A cavity and a resonator

The microwave source contains a microwave generator, phase shifter and attenuator (Fig. 4.2). Two measurement conditions: cw and pulse mode. In cw mode, a continuous microwave is applied to the sample. For pulse mode, an additional pulse shaper and microwave amplifier are used. The magnetic field is created by a set of a resistive magnet for X-band (9.4 GHz) and a superconductive magnet for the W-band (94 GHz) spectrometer. The resonator fulfills two tasks. First, by its geometry the magnetic component of the microwave B_1 is enhanced and, it minimizes the electric component of the microwave within the sample, which would otherwise tend to be absorbed by the sample, damping the microwave and thus reducing the sensitivity. Second, by tuning the resonator to be critically coupled by iris (i.e. impedance matched) to the transmission line, microwave reflection from the cavity in the absence of EPR transitions is eliminated.

Cryogenic temperature (80 K) and the room temperature measurements at high-field (W-band) were performed on an Elexsys E680 EPR spectrometer equipped with a Teraflex EN600-1021H probe head (both Bruker Biospin, Karlsruhe, Germany). The temperature was controlled by an ITC503 (Oxford Instruments, Oxfordshire, United Kingdom).

Room temperature measurements in an X-band spectrometer were performed at lab built X-band spectrometer. The lab built X-band spectrometer consisting of a Bruker (Rheinstetten, Germany) ER 041 MR microwave bridge controlled by a Bruker ER 048 R microwave bridge controller, a Bruker E088 100-controlled AEG electromagnet, and a Bruker 4122 SHQE-W1 microwave resonator (Bruker Biospin, Karlsruhe, Germany). Lock-in amplification was done by a Stanford Research Systems SR810 DSP lock-in amplifier and the microwave frequency was measured by an Agilent 53181A frequency counter. The temperature was controlled by an ITC

502 (Oxford Instruments, Oxfordshire, United Kingdom). The spin quantification experiments and mobility investigation of DxPCA in CMS as well as loaded in NLPs have been performed at this X-band spectrometer.

The magnetic field was calibrated by using an N in C60 reference sample [167]. In the high-field spectrometer, the magnetic field was calibrated by taking three calibration frequencies around 94 GHz (less, equal and more than 94 GHz) and finding the best linear fit for the frequency-dependent offset.
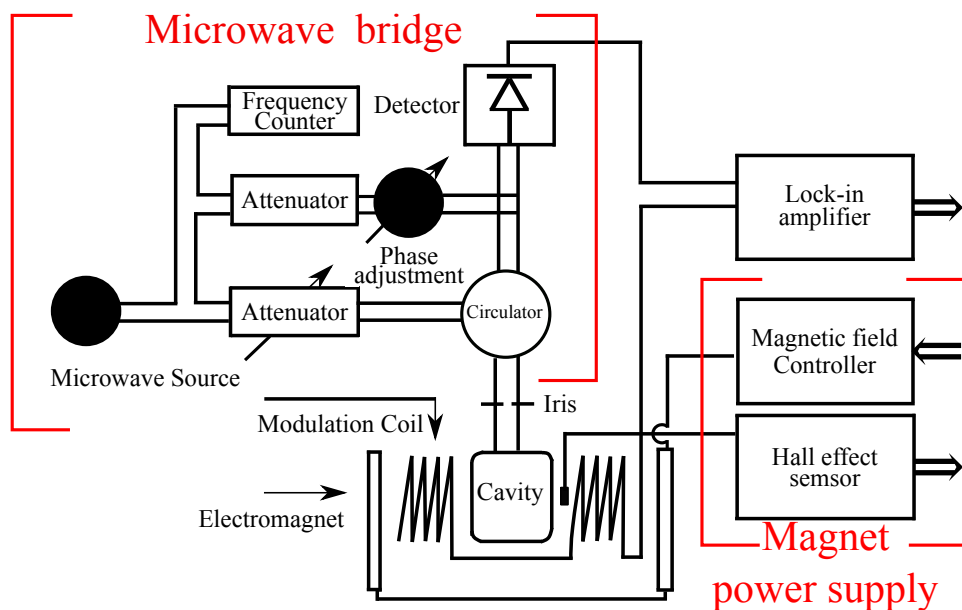
Figure 4.2: Schematic diagram of an electron paramagnetic resonance (EPR) spectrometer: the microwave source, resonator, electromagnet, modulation coils, detector, and lock-in amplifier. Adopted from [168].

4.3.2 Sample tubes

Quartz capillaries with 0.87 mm/0.7 mm outer/inner diameters (OD/ID) (VitroCom Inc. Mountain Lakes, NJ, USA) were used for the cryogenic W-band measurements. Quartz capillaries with 0.25 mm/0.15 mm OD/ID (VitroCom Inc. Mountain Lakes, NJ, USA) were used for the room temperature W-band measurements for liquid samples. Quartz capillaries with 0.55 mm/0.4 mm OD/ID (VitroCom Inc. Mountain Lakes, NJ, USA) were used for the room temperature W-band measurements of lipid samples. The samples were placed in 2 mm/1 mm OD/ID quartz capillaries (QSIL GmbH, Langewiesen, Germany) for room temperature X-band.

4.3.3 Continuous wave measurement

In continuous wave EPR (cw EPR) spectroscopy, the microwave field is applied to the sample over the entire period of time, while the EPR signal is recorded. For a cw experiment, the

resonator is critically coupled (impedance matched) to the microwave transmission line. This means that a) the resonator operates at maximum quality factor Q and b) that the incoming microwave is fully coupled into the resonator, the reflected signal, and therefore the signal reaching the detector, is zero. When an EPR transition is excited, the sample will absorb microwave, detune the resonator and thus cause some microwave to be reflected again. This signal is read out at the detector [51, 169].

4.3.4 Pulse EPR Spectroscopy

In pulse EPR, microwave pulses are applied to the sample over selected finite intervals of time, so that the orientation of the precessing magnetic moment with respect to the external magnetic field (Larmor precession) can be turned by chosen angles about the x-, y-, z-axes. To this end, it is possible to use two or more pulses with chosen intervals of time in between and to record a signal that is proportional to the sample at appropriate intervals following the application of the last pulse [131].

Hanh echo and field sweep echo experiment

The Hanh echo experiment (Fig. 4.3a) is based on the nonlinear behavior of an ensemble of spins with different Larmor frequencies [170]. At thermal equilibration the magnetization vector is aligned along the z-axis (Fig. 4.3a.I). The micro-wave field is then applied (Fig. 4.3b). The $\frac{\pi}{2}$ pulse along the x-axis rotates the magnetization to the y-axis (Fig. 4.3a.II). After the pulse, the different spins begin to precess with their individual Larmor frequencies around the z-axis, resulting in a defocussing of the transverse magnetization (Fig. 4.3a.III). After, a time τ, a π pulse along the x-axis turns all the magnetization vectors by $180°$ around this axis (Fig. 4.3a.IV). After another time τ, all the vectors are again aligned with the -y-axis (Fig. 4.3a.V). The refocusing and defocussing is called an electron spin echo [152].

Measurement of the echo amplitude as a function of the external magnetic field B_0 yields the absorption EPR spectrum (Fig. 4.3c) [161]. Instead of the cw EPR technique, the FSE is a useful alternative technique to record absorption spectra with strong anisotropic line broadening. For comparison of the cw EPR spectra and the FSE one needs to apply a numerical pseudo modulation technique to drive the derivative spectra [171].

The setup of an FSE experiment is more time-consuming than for a cw experiment. The FSE experiment further needs post-processing to produce the modulated spectrum. That is another disadvantage of this technique compared to cw EPR. On the other hand, in the situation when the Heisenberg exchange broadening contributes to cw spectra, the FSE was used to filter out the contribution of aggregated part the sample. Then, the spectrum was analyzable and the magnetic parameters were extracted. In the situations, where the aggregated part was recorded by the cw technique, for convenience we replaced the FSE technique to record the spectra.
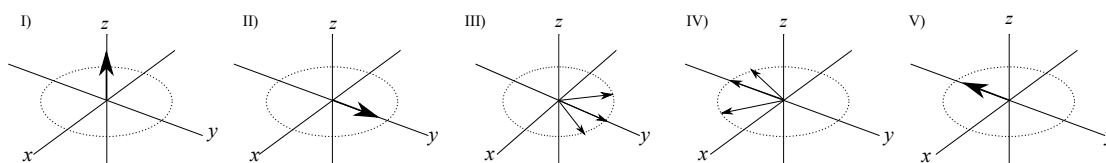
(a) a) Initially the net magnetic moment vector is in its equilibrium position parallel to the direction of the strong external field. b) at the end of a $\frac{\pi}{2}$ pulse the net magnetic moment is in the equatorial plane. c) after the pause, vectors begin to fan out slowly. d) the π pulse flips the vector by 180°. This implies that at the end of the pulse all the incremental moment vectors begin to re-cluster slowly. e) Because of the inverted relative positions following the 180° pulse and because each incremental vector continues to precess with its former frequency, the incremental vectors will be perfectly reclustered at a delay of τ after the π-pulse. Adopted from [146].

(b) The Hahn echo sequence.

(c) Field sweep echo detection
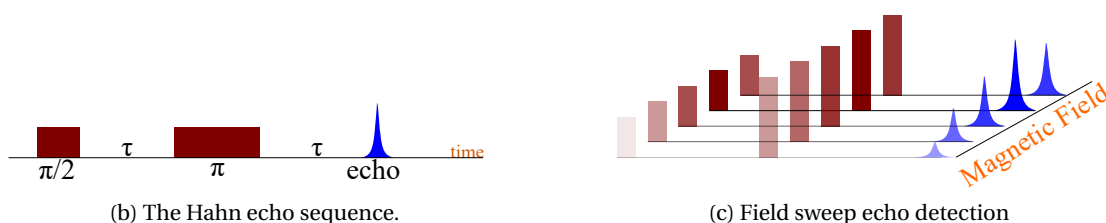
Figure 4.3: a)The formation of an echo b) The spin system is initially excited using a $\pi/2$ pulse, followed by a π-pulse after a delay τ. After a further delay of τ, an echo is observed. π and $\pi/2$ pulses can be achieved by either varying the pulse length or pulse power. c) By repeating this sequence at different magnetic fields, the spectrum of the sample can be recorded.

Inversion recovery measurement technique

The spin-lattice relaxation times have been measured by the inversion recovery technique. For inversion recovery, the Hahn echo sequence is preceded by a π pulse inverting the magnetization. The inversion recovery sequence is $\pi - t - \pi/2 - \tau - \pi -$ echo (Fig. 4.4). The first pulse inverts the population of down and up spin. Relaxation occurs during the time interval of t, which is stepped in the experiment. The second and third pulses generate a spin Hahn echo, that monitors the magnetization that remains along the z-axis. If the initial pulse inverts the spins, the echo starts out inverted and recovers through zero to the equilibrium value equal to that of the standard 2-pulse Hahn echo at that time. This sequence is very susceptible to the effects of spectral diffusion because of the inverting pulse. On the other hand, an intense short pulse is capable of exciting the maximum number of spins. In estimating T_1, one must also take into account the effect of diffusion time [144].

The relaxation time can be dependent on the magnetic field orientation as a result of anisotropy of the spin system [151]. The orientation-dependence can be investigated by measurements at different magnetic field [151]. The spin-lattice relaxation mechanism depends on the frequency and temperature. Therefore all measurements were performed under identical conditions at W-band at 80 K [172].
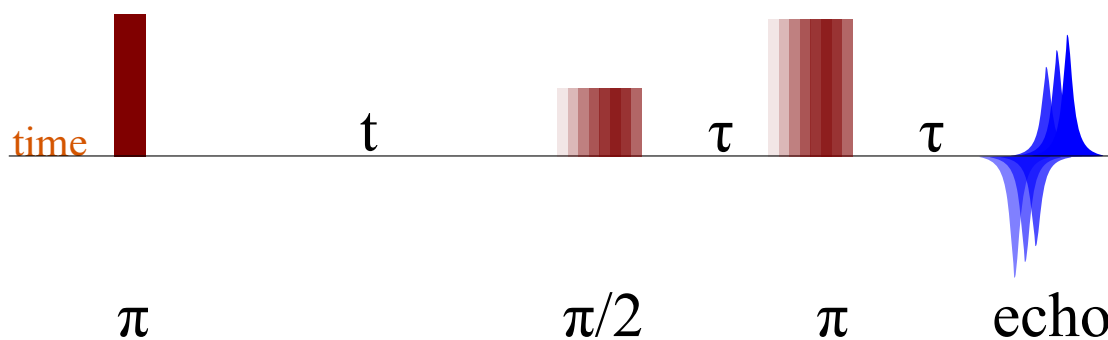
Figure 4.4: Inversion Recovery pulse sequence, T_1 measurement technique.

4.3.5 Partition coefficient measurement by EPR technique

Quantitative EPR provides the opportunity to count the spins in a sample and calculate the ratio of spins in different phases [173]. Therefore it is an alternative to ultraviolet-visible (UV-Vis) spectroscopy. EPR spectroscopy gives the possibility to determine the number of spins in a sample from recorded cw spectra [169]. The basis of the spin quantification is the double integrated intensity of the unsaturated experimental spectrum. 200 μM solutions of TEMPO and DxPCA in 1-octanol and PCA in water were prepared and respectively, water and 1-octanol were added in the same amount as the initial volume of the solution. 1-octanol and water were mixed for 10 minutes. Afterward, the solution was left for rest for 30 minutes. The two solvents separate into two phases. We took 10 μL of each phase.

4.4 Spectra analysis and simulation methods

All EPR spectra were analyzed with the EasySpin [174] Matlab (The MathWorks, Natick, MA, USA) toolbox. The powder spectra are simulated by the perturbation method to estimate the spin Hamiltonian parameters [175]. Two approaches exist for simulating the slow-motion spectra. The first one is the trajectory method which utilizes the time-dependent trajectories of the axis that are fixed in the nitroxide frame to calculate the EPR spectra directly. The second approach is based on stochastic Liouville equation (SLE) which can be regarded as a generalized semi-classical master diffusion equation [176].

The convenient and acceptable simulation is based on the different aspects of EPR spectra. The theoretical background of the interaction of an electron and its micro-environment leads us to select the right function and value for the simulation. Then, the appropriate spin Hamiltonian model needs to be chosen. The parameters of a Hamiltonian are defined based on the experiment, and the structure of the spectrum. In this research, the spin Hamiltonian is defined based on electron Zeeman interaction, and a hyperfine coupling term. The dynamics regime also needs to be identified; this can be defined according to the mobility of spin probes and nanocarriers. The dynamics regime is categorized into rigid limit (EasySpin function *pepper*), slow-motion regime (EasySpin function *chili*) and fast-motion regime (EasySpin

function *garlic*). The proper functions for simulation are chosen according to the condition of each experiment.

The magnetic parameters of all investigated spin probes were obtained by W-band EPR spectroscopy at 80 K because there the dynamics of the spin probe contribute little to the Hamiltonian. For the simulation of the EPR spectrum of a rigid limit sample, the orientational distribution needs to be considered. None of the samples is crystalline or partially ordered, all of them are in a disordered state comparable to a powder sample. Each orientation of the molecule with respect to the external field occurs with equal probability, and the line positions in the EPR spectrum depend on the relative orientation between the spin probe and the laboratory frame. The experimental parameters of the measurements also affect the simulation, such as field modulation and microwave power or the presence of saturation [177]. For our system, the magnetic parameters such as g_y, g_z and A_z can be extracted directly from magnetic field points of the different transitions in the powder spectrum (Fig. 4.5). In contrast, the line-width and shape of the peaks need to be considered for extracting the g_x, A_x and A_y values.

The fast or slow tumbling spectrum can be simulated with the magnetic parameters obtained from high field spectra at cryogenic temperature [178, 179]; and the essential field dependent and independent parameters are retrieved. Two motions influence the slow-motion spectra in the DDS investigation. The first one depends on the motion of the spin probe which is loaded into the nanocarriers and the second one is the motion of the nanocarriers. If one motion is fast, it affects the averaging process. A rotational correlation time of less than 1 ns leads to isotropic spectra. The τ_{corr} is adjusted according to the effective g and A matrix. The line shape and broadening are other parameters that need to be considered for τ_{corr} [180].

In some cases, two or more signals can contribute to the spectrum with different weights. The extraction of magnetic parameters by simulation allows separating components. Thus, studying the interaction of the paramagnetic center with a complex micro-environment is possible.

The relaxation time measurements are fitted by a bi-exponential function using the curve fitting toolbox in MATLAB. The spin-lattice relaxation time (T_1) and spectral diffusion time (T_D) will obtained from a fitting function.
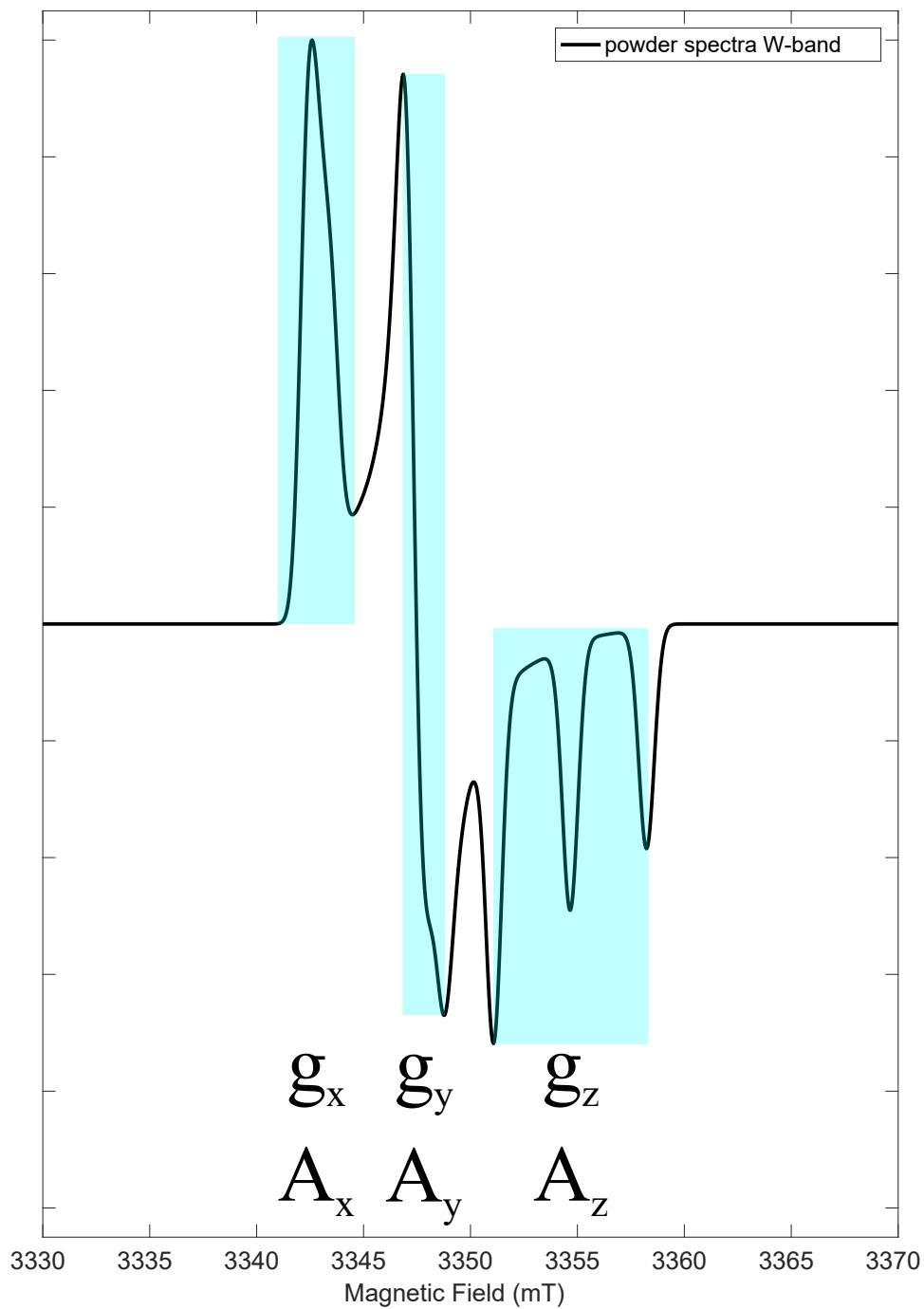
Figure 4.5: Analysis rigid limit spectra of a nitroxide at W-band, the shadow parts illustrate the part of spectrum are related to each magnetic parameters.

5 Localization of spin labeled dexamethasone in core multi-shell particles

In this chapter, the interaction of spin probes with their micro-environment was studied to obtain information on the association of DxPCA with CMS. In the first step, the magnetic and dynamic parameters of the spin probes PCA, TEMPO, and DxPCA in different solvents were investigated by dual-frequency EPR spectroscopy at ambient and cryogenic temperatures. The magnetic (Section 5.1.1 and 5.1.2) and dynamic (Section 5.1.4) parameters have been extracted from the EPR spectra by simulations. The partition coefficient of the spin probes was determined by quantitative EPR at room temperature (Section 5.1.3). Furthermore, the spin-lattice relaxation times (Section 5.1.5) of the different spin probes have been obtained, and their dependence on the environment has been analyzed. This study gives insight into the interaction between a paramagnetic center and its micro-environment, which is essential for understanding the behavior of spin probes loaded in nanocarriers. Finally, the micro-environment of DxPCA loaded to the CMS nanoparticles has been investigated and the results are presented in section 5.2. The magnetic and dynamic parameters together with the spin-lattice relaxation time lead to a model for the DxPCA location in the CMS nanoparticles.

5.1   Characterization of spin probes and spin labeled drug by dual-frequency EPR

The magnetic and dynamic parameters of the small spin probes PCA and TEMPO were studied in order to reveal how they are influenced by polarity/proticity and viscosity in well-known media. Then, the effect of solvent polarity and proticity on the magnetic parameters of the spin labeled drug DxPCA was studied using high-field EPR (W-band) at cryogenic temperature (80 K), which was followed by investigating the mobility at ambient temperature. Finally, the spin-lattice relaxation times for PCA, TEMPO, and DxPCA were measured at W-band at 80 K. The properties of the three spin probes are then compared.

These reference experiments enable us to deduce the spin probe's interaction with media of unknown polarity, proticity, and viscosity. This study provides insight into the interaction between the spin labeled drug and CMS nanoparticles (Section 5.2) as well as NLPs, which will be discussed in chapter 6.

5.1.1   The magnetic parameters of PCA and TEMPO

The hydrophilic PCA has very poor solubility in toluene and the lipophilic TEMPO is poorly soluble in water. Therefore, PCA in toluene and TEMPO in water have not been used in EPR experiments at cryogenic temperatures. In the first step, the magnetic parameters of PCA in water and TEMPO in toluene were studied (Fig. 5.1).

Figure 5.1: High-field spectra EPR of PCA in water and TEMPO in toluene at 80 K; green PCA in water and red TEMPO in toluene. Microwave power 5 μW, modulation amplitude 5 G, dashed black lines are the simulations.

The two spectra show clear differences. The main difference is the range of the magnetic field of the low field peak which corresponds to different g_x values for the two spin probes. Furthermore, the g_x peak of TEMPO shows, besides the central maximum, an additional feature on the high field side (marked with ∗ in figure 5.1), which represents a larger hyperfine splitting than for PCA. The g_y peak of TEMPO is similarly split as g_x. The simulation of the spectra yields the magnetic parameters. The g principle values and the A principle values for TEMPO in toluene are g:[2.0100(3), 2.00633(2), 2.00213(1)] and A:[19, 19, 98(1)] MHz; for PCA in water they are g:[2.00805(3), 2.00596(2), 2.00212(2)] and A:[15, 15, 105(1)] MHz. The magnetic parameters of these two samples do not reflect the properties of the two compared nitroxide as a result of the two very different solvents.

Therefore, the magnetic parameters were investigated in protic ethanol and aprotic DMSO since both nitroxides dissolve sufficiently in them (Fig. 5.2). The g_x peak of TEMPO is located at a lower magnetic field range as compared to PCA. Both spectra of TEMPO have a similar shape in the g_x and g_y range as the spectrum of TEMPO in toluene. The magnetic parameters extracted from the spectra are summarized in table 5.1. TEMPO has larger g_x values in both solvents compared to PCA, the values for g_y and g_z are almost identical and similar to most other nitroxide spin probes. The hyperfine coupling value along the z-axis is in a similar range for all samples. TEMPO has a visible splitting along the x- and y-directions, which means TEMPO has larger hyperfine coupling along with these directions than PCA. Each value is approximately 4 MHz larger than the corresponding value for PCA. The g_x peak of TEMPO in EtOH shows, besides the central maximum, a shoulder on the low field side in addition to the hyperfine splitting visible on the high field side. The additional low magnetic field feature of the g_x peak of TEMPO in EtOH occurs at a similar magnetic field as the g_x peak of TEMPO in toluene and corresponds to the similar value as g_x value of TEMPO in toluene. TEMPO, as an amphiphilic nitroxide, partially interacts with a hydroxyl group of EtOH and an apolar/aprotic micro-environment. The smaller, approximately thirty-five percent fraction of TEMPO in ethanol with the larger g_x value similar to that of TEMPO in toluene represents a situation without H-bond and, thus, an aprotic/apolar micro-environment

Table 5.1: Magnetic parameters of PCA and TEMPO in EtOH and DMSO (error margins in the last digit given in parenthesis), together with proticity of the used solvents.

Spinprobes/Solvent	g-matrix	A-matrix (MHz)
	g_x, g_y, g_z	A_x, A_y, A_z
PCA in Water(p)	2.00805(3), 2.00596(2), 2.00212(2)	15, 15, 105(1)
PCA in DMSO(a)	2.00835(3), 2.00610(2), 2.00218(2)	13, 13, 101(1)
PCA in EtOH(p)	2.00850(3), 2.00615(3), 2.00222(2)	13, 13, 101(1)
TEMPO in DMSO(a)	2.00922(2), 2.00615(2), 2.00210(1)	16, 19, 105(1)
TEMPO in EtOH(p)	2.00935(5), 2.00622(3), 2.00212(2)	17, 20, 103(1)
	2.01000(3), 2.00622(3), 2.00212(2)	17, 20, 98(1)
TEMPO in Toluene(a)	2.01000(3), 2.00633(2), 2.00213(1)	19, 19, 98(1)
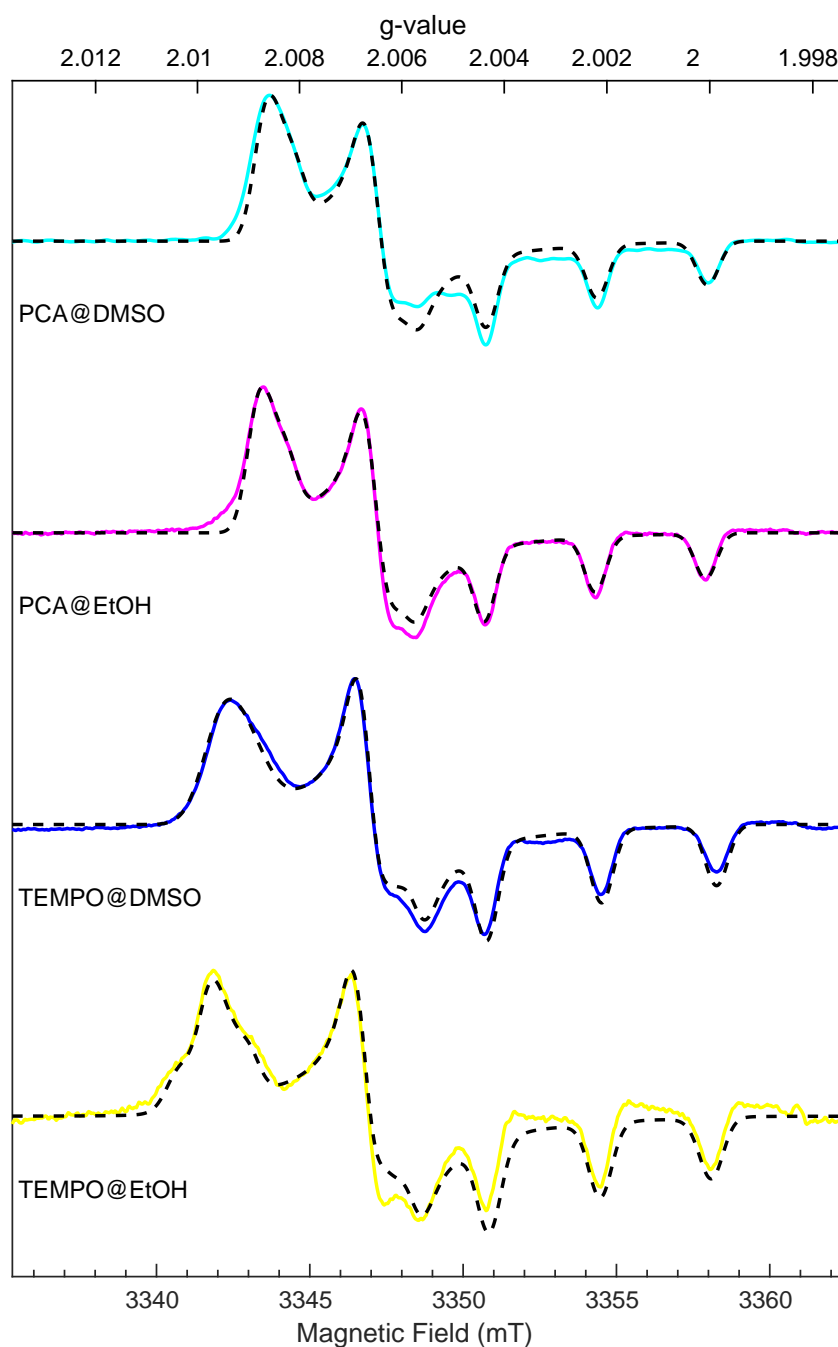
Figure 5.2: High-field EPR spectra of PCA and TEMPO in DMSO and EtOH solvents at 80 K; cyan is PCA in DMSO (FSE, π pulse 76 ns and τ: 300 ns, and pseudo modulated) and magenta is PCA in EtOH (microwave power: 10 μW); blue is TEMPO in DMSO (microwave power: 5 μW) and yellow is TEMPO in EtOH (microwave power: 50 μW). Modulation amplitude of all experimental spectra is 5 G. Dashed black lines are the simulations corresponding to the experimental spectrum.

5.1.2 The magnetic parameters of Dexamethasone labeled with PCA in different solvents

The theoretical background for the influence of polarity and proticity on magnetic parameters was described in section 3.1. The g_x value is shifted down and the A_z value is shifted up as the polarity increases. As also discussed before, the solvent polarity does not have an absolute definition. We chose to characterize the solvents according to their relative permittivities (ε_r) and interaction forces between solvent and solute based on the hydrogen-bonding. Water and toluene were chosen as utmost polar/protic and apolar/aprotic solvents to understand how the magnetic parameters are affected by the extreme conditions. Also, water is used as the primary solvent and surrounding environment for both types of investigated nanocarriers. Ethanol and DMSO were chosen as two different solvents with polar properties. However, they differ however in the origin of their polarity and have different ε_r. While EtOH is protic/polar, DMSO is aprotic/polar. Additionally, two other pairs of solvents were chosen with similar relative permittivities for further investigation of proticity effects. The first pair is 1-propanol and acetone with $\varepsilon_r \simeq 20$ where 1-propanol is a protic solvent. The second pair consists of the protic 1-decanol and aprotic methyl formate with $\varepsilon_r \simeq 10$ [181]. In table 5.2 the polarity indices of different solvents are reported [1].

Table 5.2: Different solvents are used for polarity investigation, E_T^{30} is an empirical solvent polarity parameter from [133] based on the intermolecular charge-transfer absorption of the negatively solvatochromic pyridinium N-phenolate betaine dye at 25 °C and 1013 hPa, E_T^N is the polarity index normalized to E_T^{30}.

Solvent	relative permittivity (ε_r)	proticity	E_T^{30}	E_T^N
Water	80.1	protic	63.1	1
Ethanol	24.5	protic	51.9	0.654
DMSO	46.7	aprotic	45.1	0.444
1-propanol	20.1	protic	50.7	0.617
Acetone	20.7	aprotic	42.2	0.355
1-decanol	8.1	protic	47.5	0.519
Methyl formate	8.5	aprotic	41.9	0.346
Toluene	2.38	aprotic	33.9	0.099

---

[1] E_T^N values are defined according to $\dfrac{E_T(\text{solvent}) - E_T(\text{TMS})}{E_T(\text{water}) - E_T(\text{TMS})}$, using water ($E_T^{30}$=63.1) and tetramethylsilane (TMS) (E_T^{30}=30.7) as extreme reference solvents.
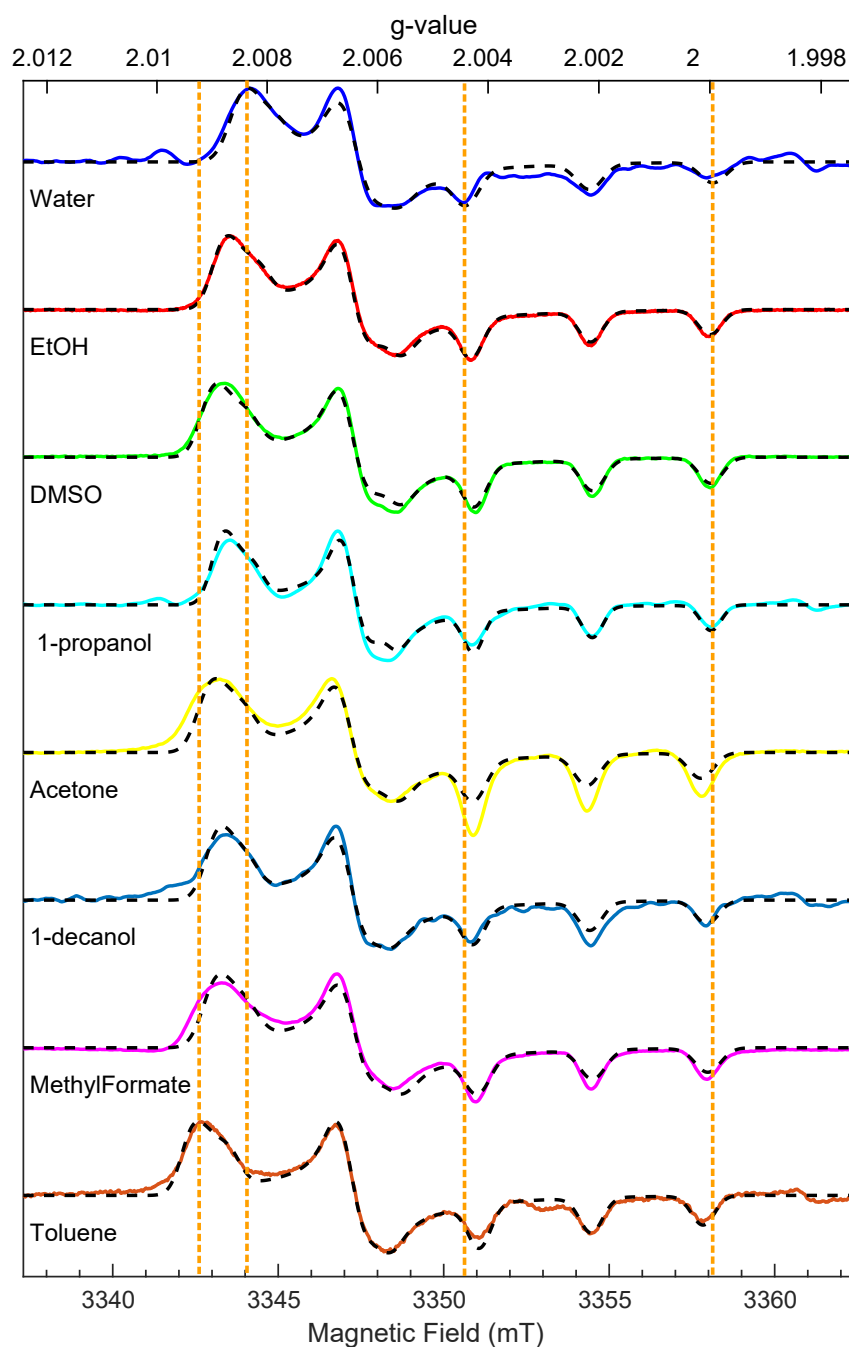
Figure 5.3: Spectra of DxPCA in different solvents obtained at W-band at 80 K via cw, and FSE, Water (blue, FSE π-pulse 108 ns and τ: 300 ns), DMSO (green, microwave power 0.02 μW), EtOH (red, microwave power 0.04 μW), Acetone (yellow, microwave power 5 μW), 1-proponal (cyan, FSE π-pulse 100 ns and τ: 400 ns), Methyl formate (magenta, microwave power 0.05 μW), 1-decanol (dark blue, FSE π-pulse 80 ns and τ: 300 ns) and Toluene (orange, microwave power 1 μW). Modulation amplitude of all experimental spectra are 5 G. Dash black lines are simulations corresponding to each experimental spectrum.

The EPR spectra of DxPCA in the different solvents were recorded at W-band (94 GHz) at 80 K (Fig. 5.3). The g_x peak of DxPCA in toluene (Fig. 5.3-orange spectrum) occurs at the lowest magnetic field position compared to the other spectra. This shows that DxPCA dissolved in toluene has the highest g_x value in this solvent series. The other extreme is DxPCA in water (Fig. 5.3-blue spectrum) with the most upshifted g_x peak and thus the lowest g_x value. The gradual change in the field position for g_x from water to toluene demonstrates the influence of the polarity and proticity on the g_x value of DxPCA in the solvent series. The hyperfine splitting along the z-direction is shifted up from toluene to water. DxPCA in water has the largest hyperfine splitting and DxPCA in toluene has the smallest one. DxPCA solved in the other solvents has intermediate hyperfine splittings between toluene and water.

The anisotropic magnetic parameters of DxPCA in the different solvents are extracted from the W-band EPR spectra at 80 K (Table 5.3). The value of g_x from the most polar solvent (water) to an apolar solvent (toluene) is shifted up and the value of A_z is shifted down. The value of g_z for all solvents are constant. The value of g_y has only a small shift down from toluene to water. The A_x and A_y almost remain constant for all solvents. Thus, the change of g_x and A_z are the essential parameters for the investigation of DxPCA in nanocarriers. The g_x values change in the range of ±0.001 (fifth digit of g_x Table 5.3, column three). The A_z changes in the range of 10 MHz (Table 5.3, column four).

Table 5.3: Magnetic parameters of DxPCA in different solvents (error margins in the last digit given in parenthesis), with normalized empirical solvent polarity parameter E_T^N of the used solvents; the solvents are marked as protic (p) or aprotic (a) respectively.

Solvent	E_T^N	g-matrix	A-matrix (MHz)
		g_x, g_y, g_z	A_x, A_y, A_z
Water (p)	1	2.00810(2), 2.00600(2), 2.00210(4)	15, 15, 104(1)
Ethanol(p)	0.654	2.00844(4), 2.00600(2), 2.00210(5)	15, 15, 101(1)
1-propanol(p)	0.617	2.00853(3), 2.00600(5), 2.00210(1)	13, 13, 101(1)
1-decanol(p)	0.519	2.00860(2), 2.00610(3), 2.00210(3)	13, 12, 99(1)
DMSO(a)	0.444	2.00864(4), 2.00600(3), 2.00210(1)	15, 15, 100(1)
Acetone(a)	0.355	2.00870(3), 2.00610(2), 2.00220(1)	15 15, 96(1)
Methyl formate(a)	0.346	2.00865(5), 2.00600(2), 2.00210(1)	15, 15, 98(1)
Toluene(a)	0.099	2.00900(5), 2.00610(3), 2.00210(3)	15, 15, 95(1)

The g_x of DxPCA in toluene has the largest value in this series of experiments. It indicates a highest spin density on the oxygen atom in the NO bond. On the other hand, the g_x in aqueous solution has the smallest value. This shows that the spin density is shifted from the oxygen atom to the nitrogen atom, which is caused by the electric dipole moment of the surrounding medium. Comparing the g_x in two polar solvents, ethanol and DMSO, it is seen that the change in a spin density in the NO bond is influenced rather by the proticity than by the polarity of a solvent. The g_x in acetone is shifted up compared to the 1-proponal. A similar effect occurs for g_x in methyl formate compared to the 1-decanol. The g_x is lower in protic than aprotic in

solvents with similar relative dielectric permittivities.

The hyperfine coupling along the z-direction is the other most sensitive parameter with respect to the polarity/proticity properties of the solvents. In general, A_z of DxPCA in different micro-environments has an inverse pattern as compared to g_x. DxPCA has the lowest A_z value in toluene and the highest A_z value in water. The z-component of the hyperfine coupling in ethanol is larger than DMSO. In both pairs, the comparison of protic and aprotic solvents with similar relative permittivities corroborates the finding that proticity has more influence than the polarity, e.g. going from 1-propanol to 1-decanol changes ε_r from 20 to 8 but g_x changes by only 0.00007 while going from 1-propanol to acetone with identical ε_r changes g_x by 0.00017.

The dependence trend of g_x and A_z based on the polarity index E_N^T is visualized in figure 5.4. The best fits for both sets of experimental data are calculated and are plotted (Fig. 5.4-red and blue lines). The trend of changing the magnetic parameters is in a good agreement with the theory as discussed in theory section 3.1.

The interpretation of DxPCA magnetic parameters in different solvents clarifies that the solvent proticity outweighs other parameters. In other words, in two solvents with the identical relative permittivity, the magnetic parameters of DxPCA are affected more by the protic solvents.
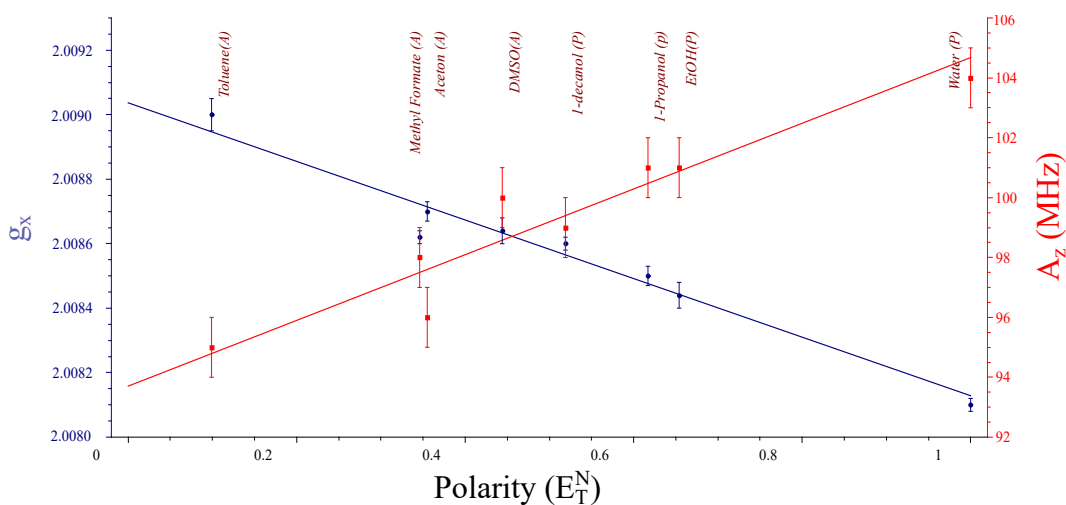
Figure 5.4: Experimental dependence of g_x and A_z of DxPCA on different solvents and linear fits (lines). The g_x values decrease from toluene to the water while A_z increases from toluene to water.

5.1.3 Partition coefficient of spin probes

In the previous sections, the magnetic parameters of DxPCA by EPR spectroscopy have been investigated. Spin quantification is another advantage of EPR spectroscopy (Section 4.3.5). This feature is used to calculate the partition coefficients of PCA, TEMPO and DxPCA (Fig. 5.5).
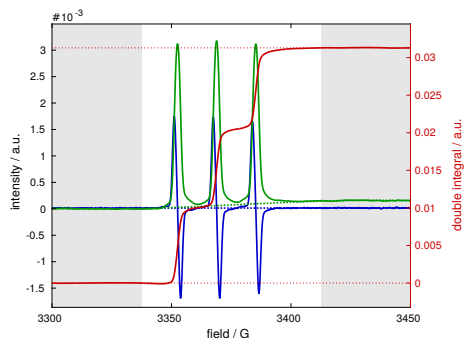
(a) PCA at water in water/1-octanol solution, microwave power 0.2 mW and modulation amplitude 3 G, number of spins: ~1.434e15.
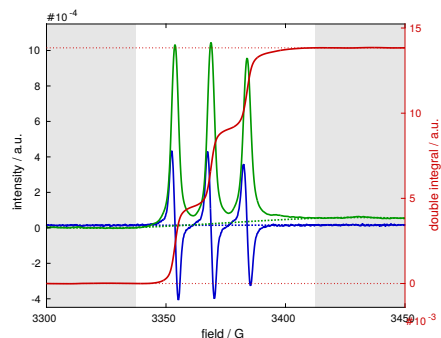
(b) PCA at 1-octanol in water/1-octanol solution, microwave power 20 mW and modulation amplitude 3 G, number of spins: ~2.736e13.
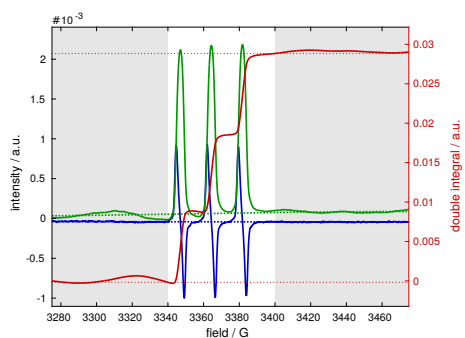
(c) TEMPO at water in water/1-octanol solution, microwave power 0.25 mW and modulation amplitude 3 G, number of spins: ~1.625e14
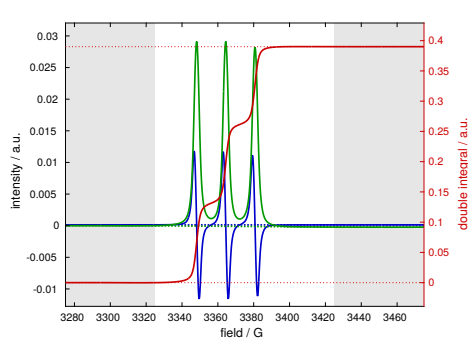
(d) TEMPO at 1-octanol in water/1-octanol solution, microwave power 1.5 mW and modulation amplitude 5 G, number of spins: ~1.056e16.
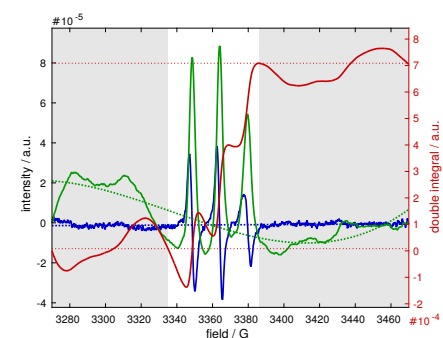
(e) DxPCA at water in water/1-octanol solution, microwave power 1 mW and modulation amplitude 3 G, number of spins: ~7.65e12.
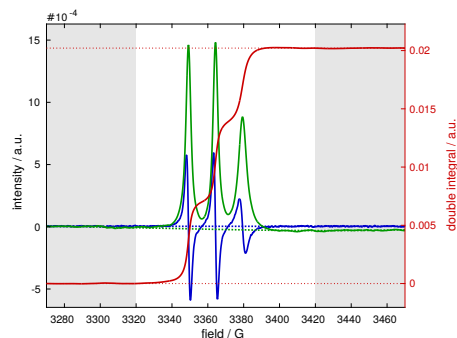
(f) DxPCA at 1-octanol in water/1-octanol solution, microwave power 0.1 mW and modulation amplitude 1 G, number of spins: ~7.305e14.

Figure 5.5: Spectra of PCA, TEMPO and DxPCA in water and 1-octanol at X-band at rt, blue spectra are experiment spectra, the green spectra are first integral and the red spectra are second integral.

56

The number of spins of each nitroxides in both solvents, water and 1-octanol, was obtained by quantitative EPR as discussed in section 4.3.5. Quantitative EPR yields the logP values of -1.6, $+1.82$, and $+1.89$ for PCA, TEMPO, and DxPCA. Literature values exist for PCA and TEMPO. The only published value of logP for PCA is -1.7 [158] and agrees well with the value determined by quantitative EPR. Two different logP have been published for TEMPO, $+1.85$ [182] and $+2.3$ [160]. The EPR derived logP of $+1.82$ for TEMPO confirms the value given in [182]. DxPCA has been prepared for this study for the first time and, no logP value was published before. However, Dexamethasone is a hydrophobic drug with a reported logP=$+1.83$ [183]. The value of $+1.89$ found here can be well rationalized by the composition of DxPCA. In the condensation reaction of the hydrophilic PCA with the lipophilic Dx, PCA loses its hydroxyl group and the resulting DxPCA is a lipophilic substance as Dx. Thus, the spin labeling of Dx by PCA leaves the partition coefficient of DxPCA almost unaltered from Dx, making DxPCA a very good model compound for investigating the association of Dx in nanoscale DDS.

5.1.4   Spin probe mobility in different media

As previously described in the theory section 3.2 the shape of room temperature EPR spectra depends on the g- and A-matrix, as well as the microwave frequency and, is strongly determined by the mobility of the spin probe [184, 185]. Variations in the mobility due to different spin probe environments manifest themselves clearly in the line shape, linewidth and effective hyperfine splitting for the spectra recorded at ambient temperatures, which are shown in following.

In the first step, three different spin probes have been studied in water at room temperature at W-band EPR frequency. In figure 5.6 all three compounds show three line spectra. However, they differ in the relative peak amplitudes and linewidths. The differences in the heights of the peaks and line-widths represent different tumbling rates of the spin probes in water. TEMPO in water spectrum (Fig. 5.6-red line) consists of three sharp lines with almost the same heights with narrow line-widths. The PCA spectrum (Fig. 5.6-green line) consists of three lines. The amplitudes of the 2nd and the 3rd lines of PCA spectrum are lower than of the 1st line. Also, the linewidth of the PCA spectrum is larger than the TEMPO spectrum. Each line of the DxPCA spectrum has a different amplitude, and furthermore, the amplitudes of the 2nd and the 3rd peaks are smaller than the 1st line. The linewidth of the DxPCA spectra (Fig. 5.6-blue line) is larger than for the two other nitroxides. The impact of the effective radius of the spin probes, temperature and viscosity of their environment on the spin probes' rotational correlation time τ_{corr} have been described in the theory section 3.2. The τ_{corr} of each measurement has been extracted from these spectra by simulation, for TEMPO 8 ps, for PCA 30 ps and for DxPCA 80 ps. The effective radius R_{eff} of the spin probes according to the τ_{corr} has been calculated based on the Stokes-Einstein equation (Eq. 3.14). The viscosity of water at 25°C is $\eta_{\text{Water}} = 0.89$ mPas. Then, the R_{eff} of TEMPO is 2.2 Å. Accordingly, the R_{eff} of PCA is 3.2 Å. Likewise, the R_{eff} of DxPCA is 4.4 Å. Additionally, g_{ave}=2.0057 and A_{ave}=49.3 MHz of TEMPO in water have been extracted by simulation from the room temperature EPR spectrum.
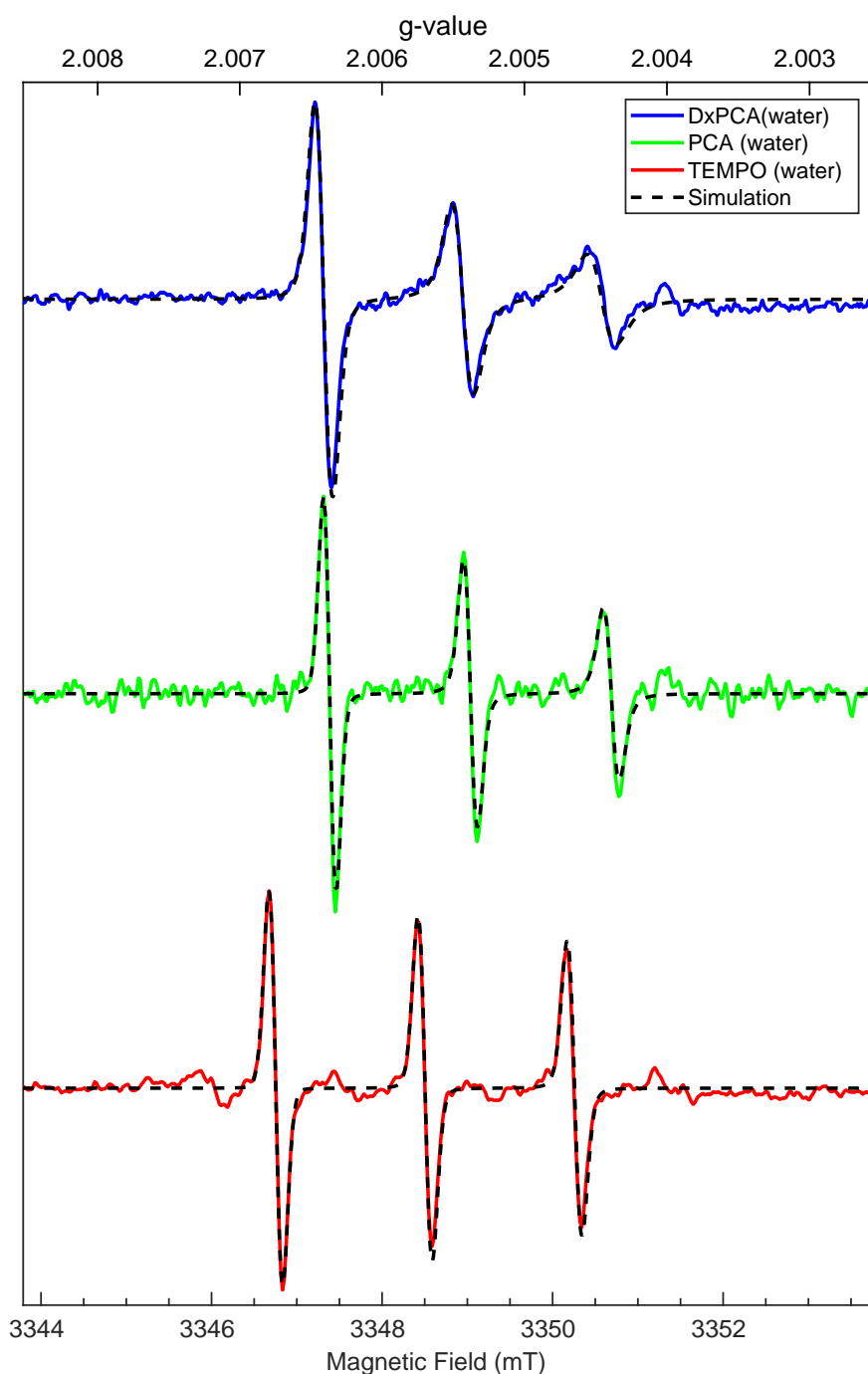
Figure 5.6: Spin probes with different mobilities are investigated at W-band at room temperature, blue is DxPCA in water (microwave power 0.02 mW), green is PCA in water (microwave power 0.005 mW) and red is TEMPO in water (microwave power 0.005 mW), and the modulation amplitude of all spectra is 1 G. Dashed black lines are simulations corresponding to the experimental data.

The mobility study of these three spin probes in the solvents DMSO and ethanol was performed as described previously for the polarity investigation. The viscosity η at 25°C for EtOH, and DMSO are η_{ethanol}=1.061 mPa.s and η_{DMSO}=1.99 mPa.s, i.e the viscosity of DMSO at this temperature is around twice the viscosity of EtOH. Additionally, the viscosity of EtOH is similar to the viscosity of water but slightly higher. A nitroxide has in EtOH a higher rotational correlation time τ_{corr} than in more viscous solvent DMSO. Furthermore, TEMPO has the smallest effective radius compared to PCA and DxPCA. Accordingly, TEMPO has the fastest, DxPCA has the slowest and PCA has an intermediate tumbling rate.

In figure 5.6, all the spectra consist of three lines. The difference in the relative amplitudes of the peaks for the same nitroxides in these two solvents is the result of the different viscosities of the solvents and the effective radius of the nitroxides as described before. The peaks of the TEMPO spectra have almost similar relative amplitudes (Fig. 5.6-yellow and blue spectra). The relative amplitude of each line of PCA spectra is changed compared to the TEMPO spectra and the height of the lines becomes smaller for the 2$^{\text{nd}}$ and 3$^{\text{rd}}$ lines (Fig. 5.6-purple and cyan spectra). Similar as in water, the relative amplitudes for the 2$^{\text{nd}}$ and 3$^{\text{rd}}$ peaks of the DxPCA spectra in EtOH and DMSO are smallest (Fig. 5.6-red and green spectra) as compared to PCA and TEMPO. The increasing broadening of the line from TEMPO to DxPCA in each solvent represents the contribution of τ_{corr} and R_{eff} in the width of the rt-EPR spectrum. The spectra corresponding to the DMSO solvent consist of three narrow lines. In contrast, the spectra of nitroxides in EtOH have a broader linewidth due to the methyl group. The main point is the linewidth of all spin probes dissolved in EtOH are different from the linewidth of the spin probes dissolved in DMSO and water. The methyl group of ethanol influences the spin-spin relaxation time [186]. Dephasing is much faster in solvents that contain methyl groups than in solvents without methyl groups. According to the T_2 relaxation time behavior in ethanol, we needed to consider a Lorentzian line for the simulation instead of the Gaussian line. The rotational correlation time clearly contributes to the line shape of the spin probes in ethanol. It affects relative amplitude and linewidth in the transition at higher magnetic fields.

Table 5.4: Rotational correlation time τ_{corr} for PCA, TEMPO and DxPCA and isotropic g_{ave} and A_{ave} values in the solvents water, EtOH and DMSO.

Composition	τ_{corr} (ps)	g_{ave}	A_{ave} (MHz)	linewidth function	linewidth (mT)
DxPCA in water	80	2.0054	46	Gaussian	0.2
DxPCA in EtOH	112	2.0055	43	Lorentzian	0.45
DxPCA in DMSO	250	2.0056	43	Gaussian	0.3
PCA in water	30	2.0054	46.3	Gaussian	0.15
PCA in EtOH	50	2.0056	42	Lorentzian	0.45
PCA in DMSO	80	2.0054	42	Gaussian	0.2
TEMPO in water	8	2.0057	49.3	Gaussian	0.17
TEMPO in EtOH	10	2.0059	46	Lorentzian	0.45
TEMPO in DMSO	20	2.0058	45	Gaussian	0.18
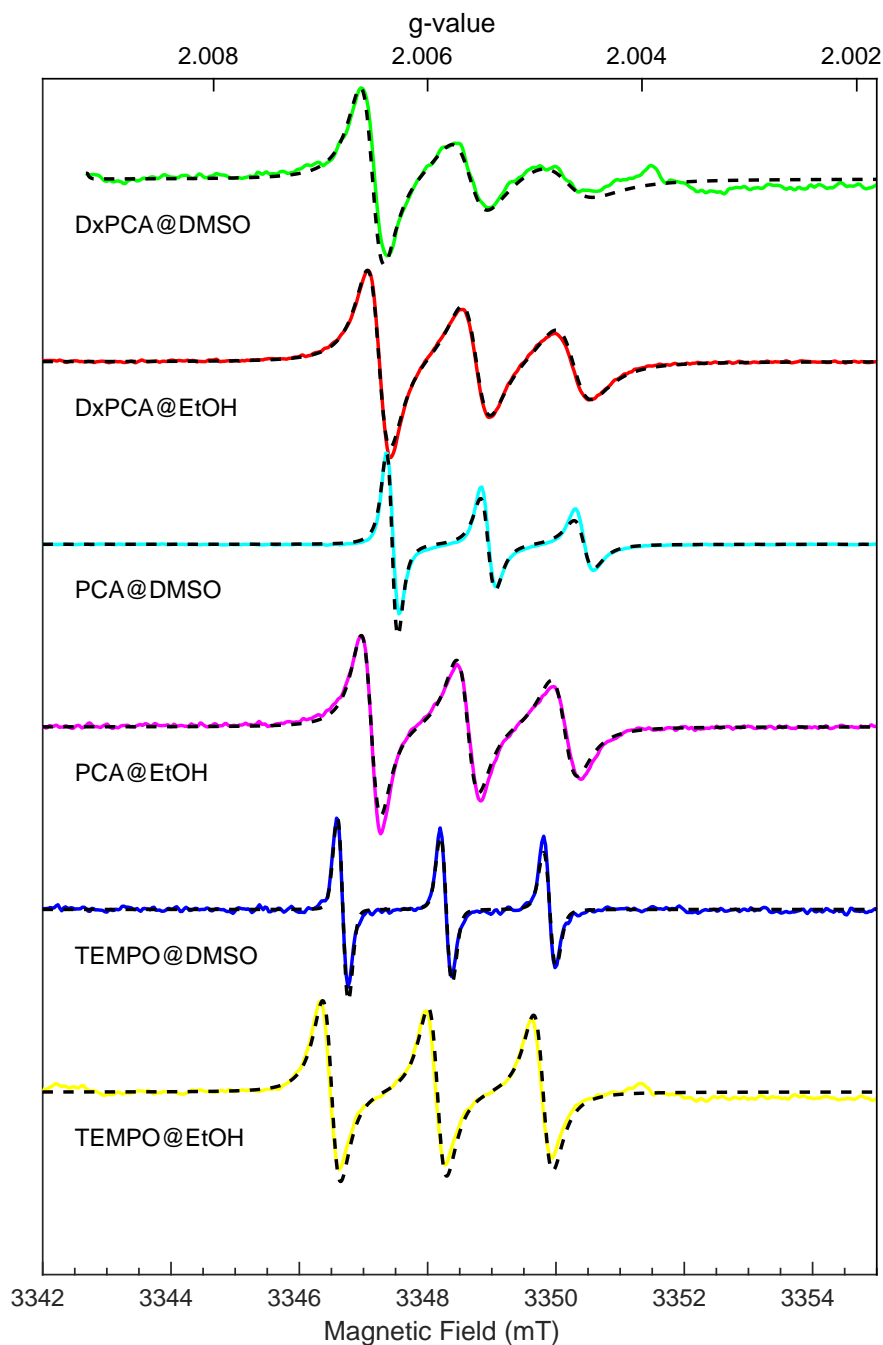
Figure 5.7: The high field spectra of DxPCA, PCA and TEMPO in DMSO and EtOH solvents at 25 °C, green is DxPCA in DMSO (microwave power 0.5 mW), red is DxPCA in EtOH (microwave power 2.5 μW), cyan is PCA in DMSO (microwave power 0.5 μW) and magenta is PCA in EtOH (microwave power 2.5 μW), blue is TEMPO in DMSO (microwave power 5 μW) and yellow is TEMPO in EtOH (microwave power 50 μW), and modulation amplitude is 1 G. The dashed black line is a simulation corresponding to the experimental data.

5.1.5 Spin-lattice relaxation time measurement

The spin-lattice relaxation time can depend on the environment of a spin probe. Therefore, the relaxation time of DxPCA was measured in water and toluene. Water is chosen as a polar/protic solvent and toluene as an apolar/aprotic solvent to study how polarity and proticity influence the relaxation time. Additionally, the T_1 was measured for PCA dissolved in water and for TEMPO in toluene. Inversion recovery traces were recorded at 80 K at W-band (Fig. 5.8). A bi-exponential function $(1 - 2(A_1 e^{(-\tau/\tau_1)} + A_2 e^{(-\tau/\tau_2)}))$ fits the time traces (Table 5.5). Thereby, τ_1 is the relaxation time T_1, and τ_2 represents the spectral diffusion time T_D (Sec 3.3.3). A short, intense pulse excites the maximal number of spins [149]. Then, the inversion recovery sequence is most susceptible to the effects of spectral diffusion because the inverting pulse is so short. The relaxation time traces for different field positions are shown in the table 5.5. We see the shortest relaxation time in the x-direction and the longest in the z-direction (Fig. 5.8b). As described in the section 3.3.1 about the A_z effect on the spin-lattice relaxation time the T_1 of DxPCA in water is smaller than for DxPCA in toluene (Table 5.5). The T_1 of PCA and DxPCA in water are very similar to each other. Both spin centers relax equally in water and can be described by the same relaxation process. The T_1 for TEMPO in toluene is comparable to that for DxPCA in toluene; however, the latter is slightly longer. On the other side, the τ_2 values are independent of the environments of PCA and DxPCA. Thereby, the τ_2 determines spectral diffusion time T_2.

These studies on the three spin probes TEMPO, PCA and DxPCA in different solvents enable now an analysis of the micro-environment seen by DxPCA in DDS. The remainder of chapter 5 will focus on DxPCA in CMS and DxPCA in NLP will be discussed in chapter 6.

Table 5.5: Spin lattice relaxation time (T_1) of spin probes obtained by bi-exponential fitting of inversion recovery time traces at different field positions.

$1 - 2(A_1 e^{(-\tau/\tau_1)} + A_2 e^{(-\tau/\tau_2)})$					
Composition	field position	A_1	τ_1 (us)	A_2	τ_2 (us)
DxPCA in Water	g_x	0.64	390	0.36	35
	g_y	0.66	420	0.34	40
	g_z	0.65	490	0.35	30
DxPCA in Toluene	g_x	0.69	230	0.31	38
	g_y	0.70	240	0.30	41
	g_z	0.68	360	0.32	43
PCA in water	g_x	0.69	390	0.31	32
	g_y	0.67	450	0.33	35
	g_z	0.66	660	0.34	35
TEMPO in Toluene	g_x	0.63	180	0.37	18
	g_y	0.63	190	0.37	17
	g_z	0.64	320	0.36	23
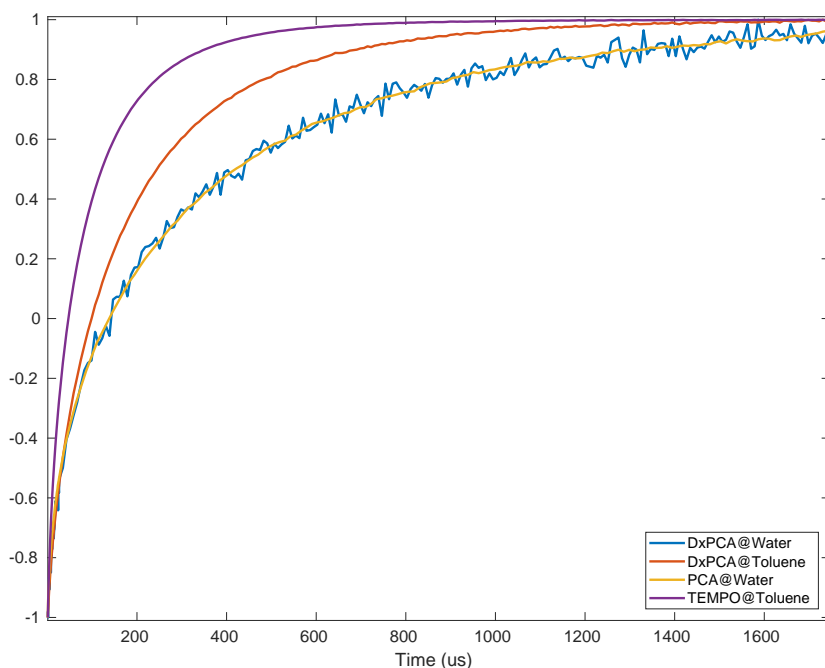
(a) Inversion recovery time trace of DxPCA and PCA dissolved in water as well as DxPCA and TEMPO dissolved in toluene at 80 K, the spectra were recorded at the g_y field position.
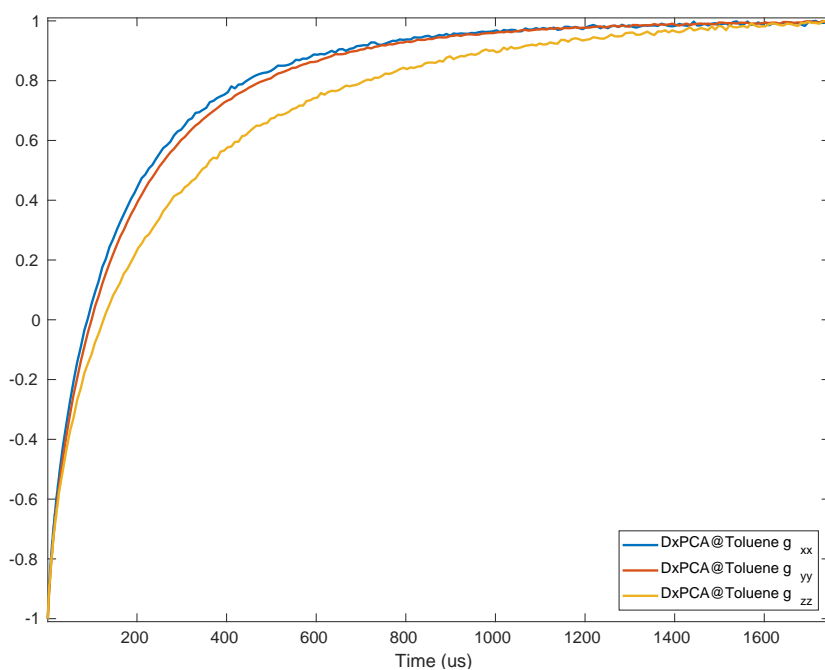
(b) Inversion recovery time trace of DxPCA in toluene for different field position, g_x, g_y, and g_z, W-band, 80 K.

Figure 5.8: Inversion recovery time trace at W-band at 80 K.

5.2 Investigation of spin labeled dexamethasone loaded into core multi-shell particles

The location of the spin-labeled drug (DxPCA) loaded into CMS was investigated by analyzing the effects of the micro-environment on the DxPCA magnetic parameters and dynamic properties. The micro-environment polarity and proticity affect the g and A parameters, the viscosity influences the rotational correlation time, and the coupling between the probe molecule and its environment determines the spin-lattice relaxation time.

5.2.1 Characterization of CMS nanoparticles by probing polarity and proticity

The spectra of DxPCA loaded into the CMS nanoparticles (DxPCA in CMS) were obtained at the cryogenic temperature at W-band frequencies. We used the FSE technique and afterward applied pseudo modulation for obtaining the spectra displayed in Fig. 5.9. As previously discussed (Section 5.1.2), the g_x peak of DxPCA in toluene arises at lower field compared to DxPCA in water. Moreover, the splitting along the z-axis for DxPCA in water is larger than for DxPCA in toluene. The spectral features of DxPCA loaded in CMS, g_x peak and A_z splitting, are located in the region between those of the polar/protic and the apolar/aprotic solvents. The magnetic parameters of DxPCA in CMS were extracted by simulation. The g-matrix is: [2.00865(2), 2.0061(2), 2.0021(4)] and A-matrix is: [14 14 98(1)] (MHz). The comparison of the magnetic parameters of DxPCA loaded in CMS shows that they represent an intermediate case between a polar/protic (water) and apolar/aprotic (toluene) micro-environment (Fig. 5.9).

The structure of CMS nanoparticles is well-known (Section 2.2.1). The magnetic parameters were extracted from loaded DxPCA, are a signature of micro-environments. The relation between the magnetic parameters of DxPCA and the structure of CMS nanoparticles conducts us to the location of the loaded DxPCA in CMS nanoparticles. This relation is addressed by investigating the behavior of DxPCA in different micro-environments. The magnetic parameters of DxPCA and how this modification influences the magnetic parameters were studied, and are presented in the previous section 5.1.1.

The dependence of the g_x and A_z components on E_T^N is plotted in figure 5.10. This shows that when the solvent changes from apolar/aprotic to polar/protic, the well-known trend of a g_x shifts towards lower values, and, on other hands, a shift of nitrogen (^{14}N) hyperfine coupling (A_z) towards higher values [136]. The changes in g_x and A_z are governed by the proticity in polar micro-environments while in absence of hydrogen bonding the relative dielectric constant ε_r is the main governing parameter [187]. When we compare two protic and aprotic solvents with approximately the same ε_r, e.g. acetone and 1-propanol, the dominate proticity parameter on g_x and A_z becomes evident as reported previously in section 5.1.2.

The unmodified PCA -when loaded to CMS nanoparticles suspending in water- is located on the surface of the CMS nanoparticles [104]. The magnetic parameters of PCA (g:[2.00890, 2.00600, 2.0012], A:[30, 35, 72] (MHz)) show a highly polar micro-environment.
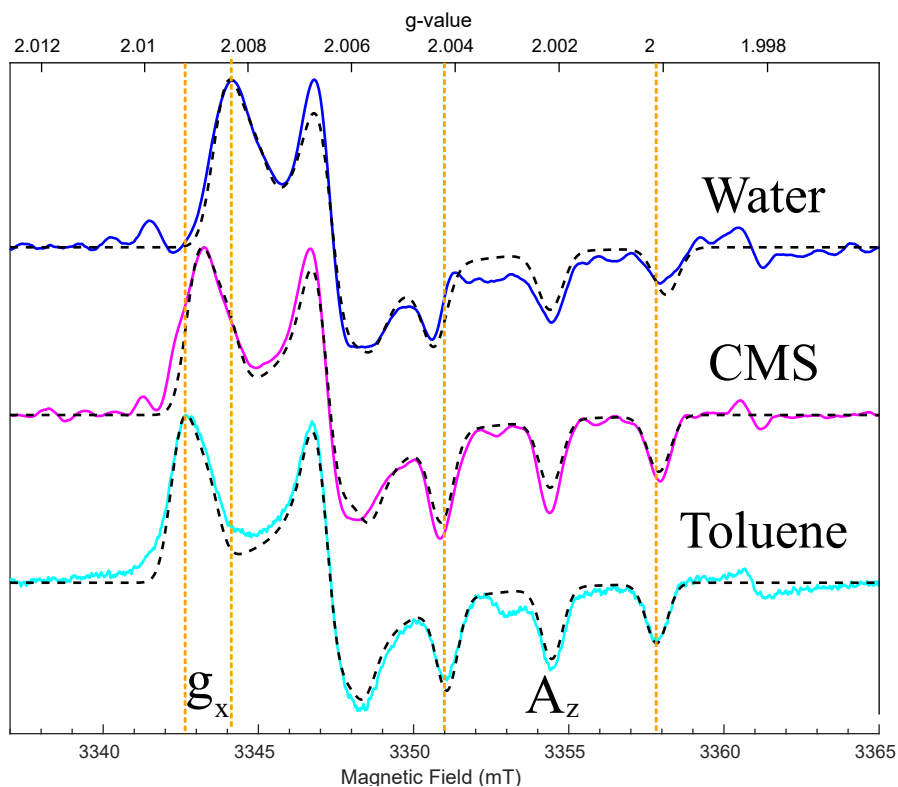
Figure 5.9: W-band EPR spectra of DxPCA in different environments at 80 K; DxPCA in water (blue), DxPCA loaded to CMS (magenta) and DxPCA in toluene (cyan), dashed lines: simulations. All spectra were normalized to a frequency of 94 GHz.

The magnetic parameters of DxPCA while loaded in CMS nanoparticles suspended in water (DxPCA in CMS) determined here (*g*-matrix principle values (2.00865, 2.0061, 2.0021) and *A*-matrix principle values (14, 14, 98) MHz) clearly, deviate from those found for PCA in CMS [104]. The parameters for DxPCA in CMS represent a micro-environment of intermediate polarity as visualized in Fig. 5.10. According to the structure of the CMS particles, the core is polar and protic, the inner shell is apolar and aprotic, and the outer shell is a polar and aprotic environment. The transition region between the core and the inner shell and the transition region between the inner shell and outer shell are an environment of intermediate polarity. However, these two regions differ with respect to their polarity. The identification in which of the two transition regions of intermediate polarity is the location of DxPCA needs further characterization of the proticity experienced by DxPCA. This can be achieved by analysis of the T_1 relaxation time (see section 5.1.5).
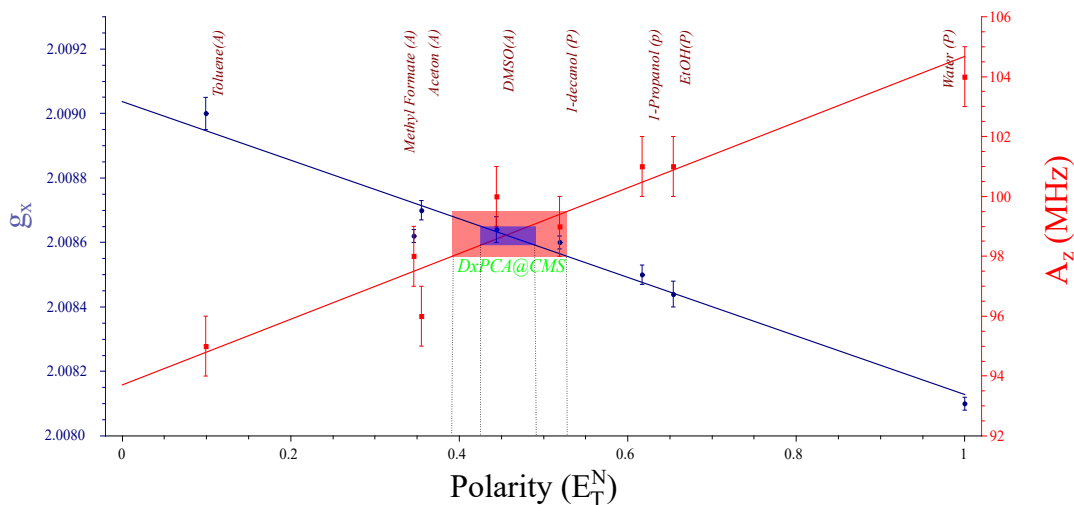
Figure 5.10: Dependence of g_x and A_z of DxPCA on different solvents and linear fits (lines). The areas filled in blue and red mark the polarity range compatible with the DxPCA in CMS g_x and A_z parameters, respectively.

5.2.2 Investigation of micro-environment by relaxation time measurements

Investigating the spin-lattice relaxation time (T_1) is a complementary method for characterizing the micro-environment properties additional to the making use of the g and A dependence on these parameters. T_1 is sensitive to molecular vibrations and, thereby, provides information on mechanical properties of the micro-environment [151, 172]. The corresponding time traces of relaxation time measurements on DxPCA in CMS are shown in figure 5.11. The time traces were fitted by a bi-exponential function ($f(\tau) = 1 - 2(A_1 e^{\tau/\tau_1} + A_2 e^{\tau/\tau_2})$). The obtained fit parameters are given in table 5.6. The larger time constant τ_1 has an amplitude, which is two times larger than that of the shorter time constant τ_2 and it was considered as the relevant T_1 time while τ_2 represents a spin diffusion time constant [151].

Comparison of the T_1 (i.e. τ_1 in table 5.5) for PCA and DxPCA in water shows very similar T_1 times for both samples, which are clearly distinct from the T_1 time for DxPCA in CMS. This corroborates the previous finding that DxPCA experiences an environment different from the water phase and is within the CMS. The OH bonding between the NO and the surrounding environment is the primary parameter, which influences the relaxation time. DxPCA in water has a slower relaxation time than DxPCA in CMS. Thus DxPCA in CMS is not affected by OH bonding.

The comparison of the relaxation time of DxPCA in CMS with the DxPCA in toluene (Table 5.5) additional to water shows that DxPCA in CMS experiences the aprotic micro-environment. Since the transition region between the polar core and the inner shell is partially protic, this interface can be excluded. Therefore one can conclude that DxPCA is located in the border

between the inner shell and the outer shell based on the intermediate polarity and a protictiy of its micro-environment.
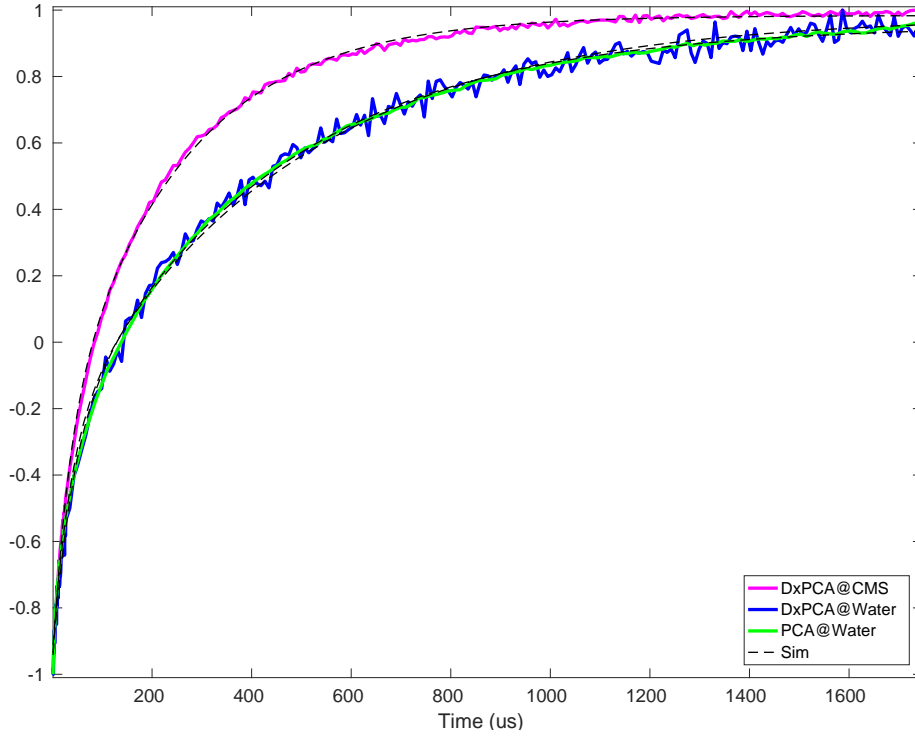
Figure 5.11: Determination of the spin-lattice relaxation time (T_1) from inversion recovery measurement for DxPCA loaded into the CMS by a bi-exponential fit. Relaxation time measurement of DxPCA loaded into the CMS (magenta), DxPCA in water (blue) and PCA in water (green) at W-band, g_y field position, 80 K, simulation black thin dashed line.

Table 5.6: Spin-lattice relaxation time of DxPCA loaded in the CMS, W-band, measurement at 80 K, at the field positions g_x g_y and g_z. The spin-lattice relaxation time T_1 was obtained by bi-exponential fitting of the inversion recovery time traces to the function $f(\tau) = 1 - 2(A_1 e^{\tau/\tau_1} + A_2 e^{\tau/\tau_2})$ with τ_1 identical as T_1 and τ_2 as T_D.

field position	A_1	τ_1 (μs)	A_2	τ_2 (μs)
g_x	0.63	250	0.37	35
g_y	0.67	240	0.33	31
g_z	0.66	402	0.34	34

5.2.3   Mobility of spin probes loaded to the CMS nano particles

Further information on the attachment of DxPCA to the CMS can be gained by analysis of the DxPCA mobility (Fig. 5.12).

The spectrum of small free nitroxide spin probes in isotropic solution with low viscosity, corresponding to rotational correlation times τ_{corr} 100 ps at X-band frequency, consists of three sharp lines. For slower tumbling due to a more viscous environment or anisotropic, the three lines become broader. The characteristic rotational correlation time for this regime is in the range of 300 ps $< \tau_{corr} <$ 1000 ps at X-band frequencies. The spectra become significantly broadened for further immobilized spin probes, where particularly the low field peak (1st line) and high field peak (3rd line) are sensitive to broadening (Fig. 3.6). Values for τ_{corr} can be extracted from the spectra by simulation [184]. The optimum EPR frequency band for monitoring spin label dynamics depends on the relevant rotational correlation times. Here, experiments at X-band frequency were found to be adequate.

Both the spectra of PCA and DxPCA show three sharp lines in aqueous solution with approximately equal height (Fig. 5.12a, top and middle spectra) in agreement with the small effective radius and the low viscosity solvent (see section 5.1.4). The slightly larger effective radius of DxPCA compared to PCA results in a slower rotation and, in consequence, yields a slightly broadened and less intense high field peak for DxPCA. Spectral simulation reveals rotational correlation times of about 30 ps and 80 ps for PCA and DxPCA, respectively. These numbers are in good agreement with the rotational correlation times calculated for both molecules using the Stokes-Einstein equation (Eq. 3.14) according to the effective radius of PCA and DxPCA and viscosity of water at room temperature. The broad line underneath of narrow peaks in the DxPCA spectrum is an unresolved and stunning component of DxPCA spectrum. This contribution is due to the low solubility of Dx in water (approx. 2 μmol/l at rt), causing a partial aggregation of DxPCA. These aggregates are likely to contain a high DxPCA concentration with distances between DxPCA molecules giving rise to a substantial spin-spin coupling, which in turn results in a strongly broadened spectrum (Fig. 5.12a) devoid of the otherwise characteristic hyperfine structure.

The spectrum of DxPCA in CMS (Fig. 5.12a bottom spectrum) clearly consists of two components. The first component consists of the characteristic three narrow and sharp lines. The second component is, in this case a broad signal well visible to the left of the first sharp line. Again, the sharp lines represent a highly mobile fraction of DxPCA, indicative of the presence of free DxPCA in solution not loaded to CMS. The broad spectral contribution (Fig. 5.12b-bottom spectrum) was extracted by subtracting the free DxPCA component from the DxPCA in CMS spectrum. The resulting spectral component is representative of the intermediate mobility range between the fast tumbling and the solid-state regime and can be qualitatively simulated under the assumption of a rotational correlation time $\tau_{corr} \approx$ 7 ns.
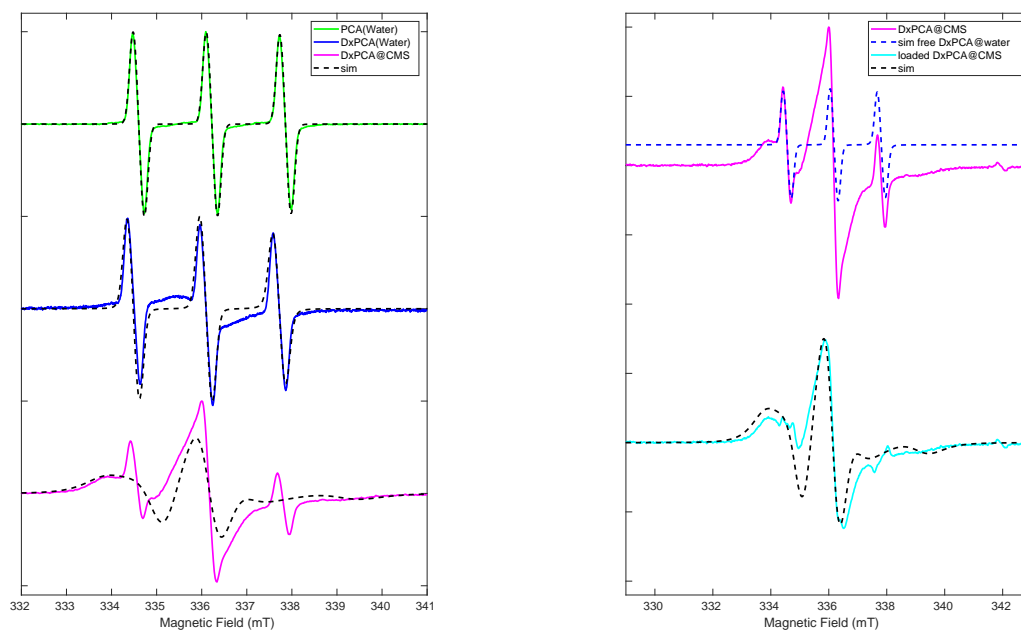
(a) Spectra of DxPCA loaded to the CMS (magenta) in comparison with PCA (green) and DxPCA (blue) in water.

(b) Deconvolution of DxPCA in CMS spectrum into the free DxPCA spectral contribution and a partially immobilized DxPCA spectral contribution. The resulting spectrum after subtraction is given by the solid cyan bottom line.

Figure 5.12: Spectra of DxPCA loaded to the CMS, the dashed blue and black lines show a qualitative simulation of this spectrum, obtained at X-band and room temperature, all spectra normalized to 9.4 GHz. All the simulations were done with one set of parameters.

This number clearly shows a severely slowed rotational motion of DxPCA loaded to CMS compared to DxPCA in aqueous solution. An interpretation of the rotational correlation time in terms of DxPCA mobility within CMS is possible when first considering the rotational correlation time of the CMS nanoparticles. Their average diameter was determined by dynamic light scattering (DLS) as $D_{CMS} \simeq 19$ nm. Again, using the Stokes-Einstein equation (Eq. 3.14), rotational correlation time $\tau_{corr} \simeq 1$ μs of DxPCA for completely immobilized in the CMS nanoparticles is calculated. The corresponding simulated spectrum for this rotational correlation time is demonstrated in figure 3.6.

Such a very slow rotational correlation time yields in simulations spectra virtually indistinguishable from the solid-state limit. Thus, we can conclude that the rotational motion of the whole CMS nanoparticles has no influence on the observed spectral shape and the $\tau_{corr} \approx 7$ ns derived from DxPCA in CMS exclusively reports the residual mobility of DxPCA within the CMS.

The deconvolution of the DxPCA in the CMS spectrum allows a further conclusion on the rela-

tive amounts of free DxPCA in solution and DxPCA loaded to CMS. In figure 5.13, even though the peak amplitudes of the narrow three lines for the free DxPCA component are substantially larger than that of the broad DxPCA in CMS component, the ratio between free and loaded DxPCA amounts to 1:19 (5%:95%). This shows that the equilibrium between DxPCA in CMS and free DxPCA in the aqueous solution is strongly shifted to DxPCA loaded to the CMS.
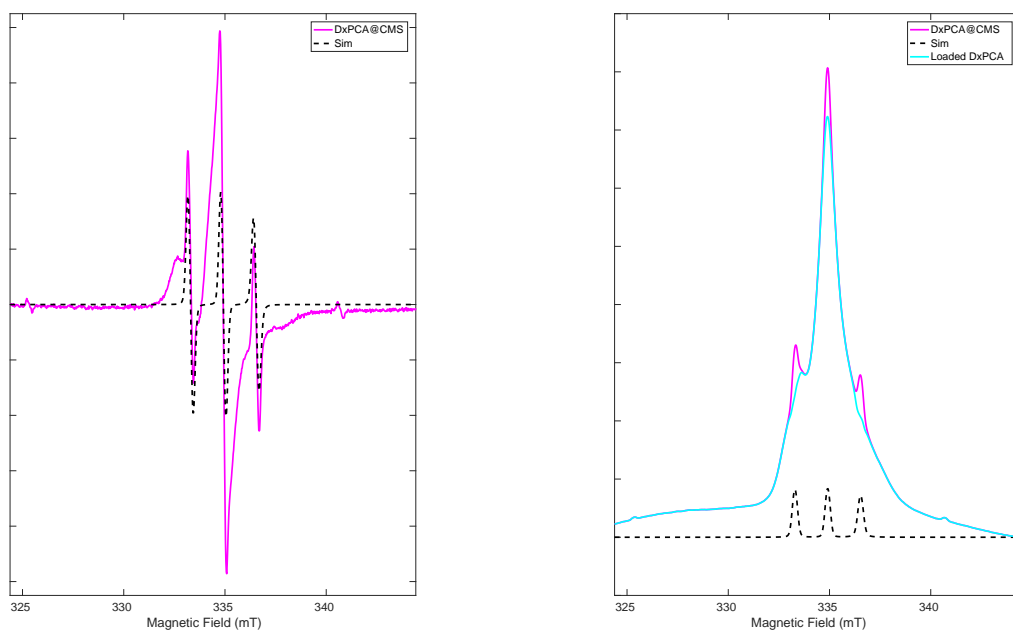
(a) Simulation free DxPCA in aqueous solution Dx-PCA in CMS(magenta) and simulated free DxPCA (black dash line).

(b) subtracting free DxPCA from DxPCA in CMS spectrum (magenta); the free DxPCA in water spectrum (black dashed line) is a simulation of the corresponding spectrum. The resulting spectrum after subtraction is given by the solid cyan line.

Figure 5.13: Loading efficiency of CMS by subtracting free DxPCA from the experimental spectrum.

Taken together, the EPR data collected on DxPCA loaded to CMS yield a localization of DxPCA at the interface between the inner and the outer CMS shell, with a DxPCA rotational correlation time substantially longer than in the aqueous phase. Furthermore a $19:1$ ratio between DxPCA incorporation into the CMS and in the aqueous solvent for the CMS was found.

6 Drug distribution in nanostructured lipid particles

Nanostructured lipid particles (NLPs) are smooth spherical particles for which the exact lipid distribution is unknown. Even less is known about the loading and distribution of drugs within the NLPs. In this chapter, the advantage of dual-frequency EPR is utilized to find the location of spin probes with different partition coefficients loaded into NLPs and this information is used to define a drug/NLP association model. The small nitroxides PCA, TEMPO, and the spin-labeled drug DxPCA are examined as model drugs, in different pure and mixed lipids as well as NLPs, made thereof (Section 6.1). To reach this end, the magnetic parameters of the spin probes were determined in the aforementioned lipids (Section 2.2.2) by W-band EPR at cryogenic temperature. Additionally, the dynamics of the spin probes inside the lipids and NLPs were characterized using X- and W-band cw spectra recorded at room temperature. This information was used for deducing the location of the loaded spin probes in NLPs (Section 6.2) and, along with the results of spin-lattice relaxation times, for unrevealing the incorporation mechanism of spin probes and spin-labeled drugs into NLPs. This made it possible to postulate association models for drugs in NLPs (Section 6.3).

6.1 Characterization of spin probes loaded to nanostructured lipid particles

6.1.1 Spin probe magnetic parameters in lipids and NLPs

In this step, the magnetic parameters of three spin probes, PCA, TEMPO, DxPCA, dissolved in pure and mixed lipids as well as loaded to NLPs were investigated. The spin probes were dissolved in the following lipid preparations:

- Gelucire (Ge) as the main lipid used in NLPs investigated here along with NLPs made purely from Gelucire (NLP-Ge).

- Witepsol (Wi), Capryol (Ca), and also in the mixture of the two. Due to the intrinsic chemical properties of Witepsol and Capryol, NLPs can neither be made out of these lipids individually nor out of a mixture of both.

- Gelucire/Witepsol and Gelucire/Capryol mixtures, as well as NLPs, NLP-Ge/Wi and NLP-Ge/Ca, made from these mixtures.

- Gelucire/Witepsol/Capryol mixture and an NLP made from this mixture (NLP-Ge/Wi/Ca).

The results of these investigations are grouped into three subsections for the respective spin probes PCA, TEMPO, and the spin-labeled drug DxPCA.
It should be mentioned that in the case of spin probes loaded to NLPs, the aqueous solvent surrounding the NLPs has to be considered besides the pure and mixed lipids since water has a substantially higher polarity and proticity compared to pure or mixed lipids. The g-matrix principal value g_x and the ^{14}N hyperfine coupling parameter A_z of the respective

spin probe were utilized as sensitive reporters for the polarity and proticity of the micro-environment [181, 188].

Magnetic parameters of PCA in lipids and NLPs

The spectra of PCA dissolved in bulk lipids and loaded in NLPs recorded at W-band at 80 K to evaluate the polarity/proticity properties of different micro-environments are shown in Fig. 6.1. These spectra were recorded at W-band frequencies and a temperature of 80 K in cw mode except for the samples involving lipid Witepsol and the Witepsol/Capryol mixture. For these spectra the cw spectra showed a broad unresolved background attributed to aggregated PCA. In spectra recorded by the FSE technique (see Section 4.3.4) this broad background is absent, likely due to very fast relaxation of the aggregated PCA fraction. Qualitatively, the structure of the PCA spectra in the lipid preparations (apart from Wi and Ca) is very similar to that of PCA in well-known environments (Fig. 5.1) without any sign of spectral broadening, indicating that PCA only interacts with one micro-environment in all mixtures. However, they show a clear variation of the g_x-peak position and ^{14}N hyperfine splitting, hfs, along the g_z direction (indicated by vertical lines) in the different lipid preparations with the clear trend of all g_x peaks in the NLP samples being high-field shifted compared to those of the corresponding bulk lipid mixtures. Consistent with the g_x shift, the ^{14}N hfs along the z-axis A_z is larger in the NLP spectra than the bulk lipids. Quantitatively, the g_x peaks in the solid lipids Gelucire and Witepsol (Fig. 6.1–1$^{\text{st}}$ and 3$^{\text{rd}}$ spectrum from top, respectively) are found at a g-value around 2.009, which is significantly larger than observed in the reference solvent EtOH with $g_x = 2.0085$. The g_x peak for the mixture of these two lipids (Fig. 6.1-6$^{\text{th}}$ spectrum) occurs at an even slightly larger g-value. In contrast, the PCA spectrum in the liquid lipid Capryol (Fig. 6.1-4$^{\text{th}}$ spectrum) shows a g_x peak position at a clearly lower g-value than in the solid lipids, but still significantly larger than in EtOH ($g_x = 2.0085$). The g_x peaks for PCA dissolved in the two mixtures Gelucire/Capryol (Fig. 6.1-8$^{\text{th}}$ spectrum) and Witepsol/Capryol (Fig. 6.1-5$^{\text{th}}$ spectrume) occur roughly at the positions of the solid lipids. PCA in the bulk mixture of all three lipids (Fig. 6.1-10$^{\text{th}}$ spectrum) shows again a g_x-value as in the solid lipids. It is interesting to note that the g_x value seen for all NLP preparations is in the range of the value seen for PCA in Capryol even though the bulk lipid mixtures containing Capryol show the significantly larger g_x value observed for the solid lipids. The magnetic parameters which have been extracted from these experimental spectra by simulation are reported in table 6.1. When comparing the magnetic parameters of PCA dissolved in pure lipids and different solvents (Table 5.1 and A.1), one can conclude, that the g_x and A_z values of all solid pure lipids and all lipid mixtures demonstrate an apolar/aprotic environment surrounding PCA. The only exception is found for PCA in the liquid lipid Capryol showing a smaller g_x and larger A_z. This simultaneous decrease of g_x and increase of A_z is consistent PCA experiencing a more polar or protic environment in Capryol than in the solid lipids. Since Capryol contains a hydroxyl group (Fig. 6.2) and can form an H-bond with PCA we assign the reported change of both magnetic parameters to this feature. Thus both investigated magnetic parameters report a protic PCA environment in pure Capryol.
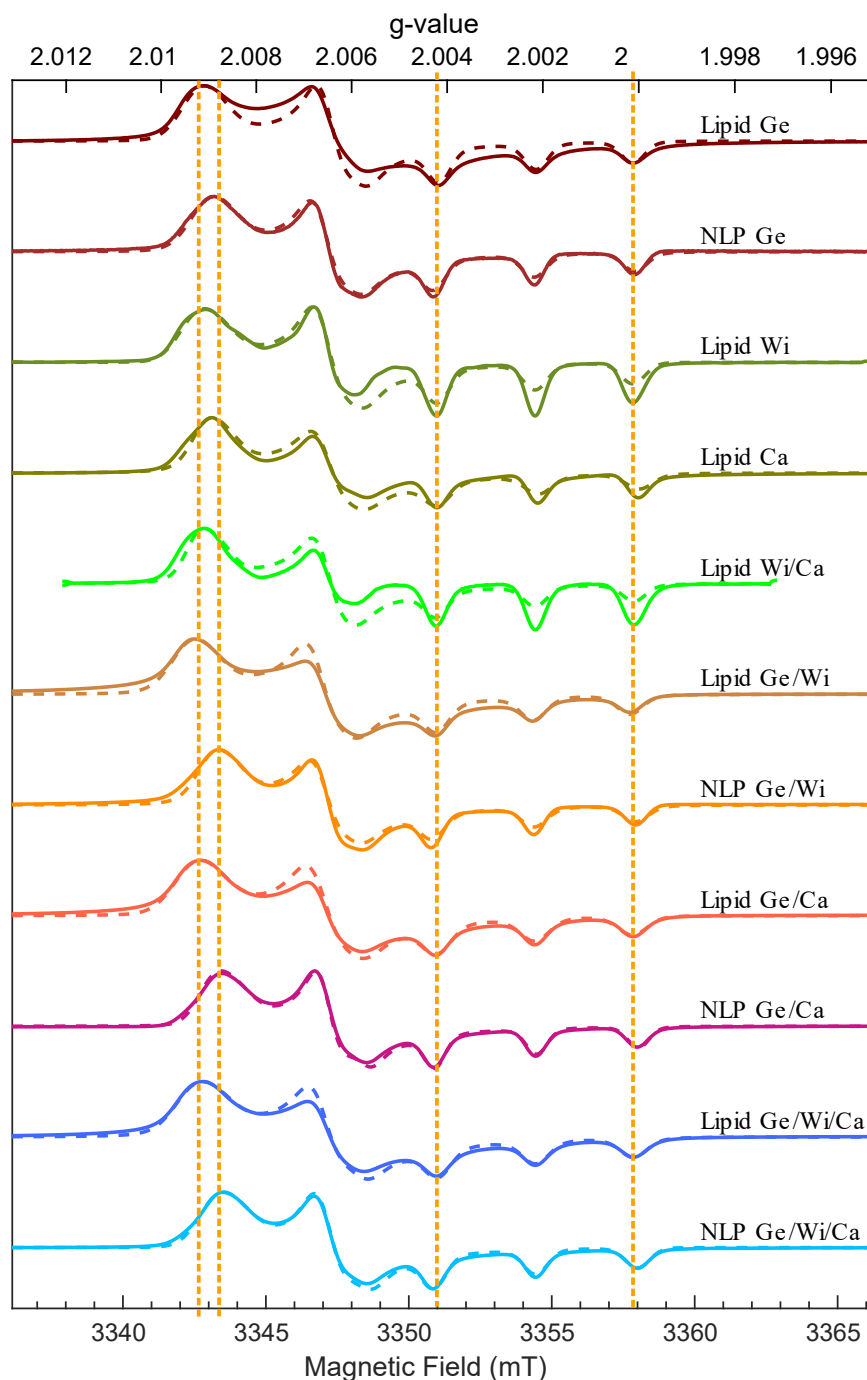
Figure 6.1: Spectra of PCA dissolved in lipids and loaded to NLPs recorded at W-band and 80 K. All spectra were taken at a microwave power of 0.5 μW and a modulation amplitude of 5 G with the exception of Witepsol and Witepsol/Capryol, which have been recorded by FSE and 5 G pseudo modulation. Dashed lines are simulated spectra. To guide the reader's eye, the magnetic field position of g_x peaks and the A_z hyperfine coupling are illustrated by four vertical dashed lines.

PCA loaded into NLPs interacts with a different medium than when dissolved in pure and mixed lipids. When the bulk lipids change to dispersed NLPs, the A_z value of PCA increases from 96 to 100 MHz. The g_x value is reduced in NLPs compared to bulk lipids. The shifted g_x and A_z illustrate a change of the medium surrounding PCA from an apolar/aprotic micro-environment in lipids to a more polar or protic in NLPs. Since the NLP are dissolved in water, we attribute this change in the magnetic parameters of PCA in NLPs as an effect of the aqueous surrounding of the NLPs. However, the magnetic parameters of PCA loaded to NLPs represent an environment significantly less polar/protic than pure water indicating a predominant interaction with the lipids (Table 6.1). Therefore, we interpret the g_x and A_z changes as reporting a change in the effective polarity of the surrounding medium.
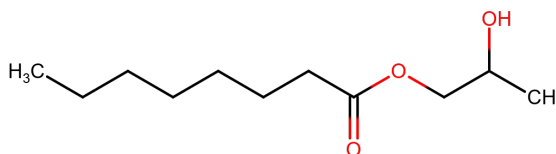
Figure 6.2: Chemical structure of Capryol 90 [189].

Table 6.1: Magnetic parameters of PCA dissolved in lipids and loaded NLPs.

Composition	g-matrix	A-matrix (MHz)
	g_x, g_y, g_z	A_x, A_y, A_z
Gelucire	2.00901(1), 2.00610(5), 2.00214(2)	13, 13, 96(1)
NLP-Ge	2.00880(3), 2.00620(2), 2.00218(1)	13, 13, 99(1)
Witepsol	2.00900(3), 2.00617(1), 2.00216(1)	15, 13, 96(1)
Capryol	2.00880(5), 2.00615(1), 2.00209(1)	13, 13, 99(1)
Witepsol/Capryol	2.00895(3), 2.00622(1), 2.00216(1)	13, 10, 97(1)
Gelucire/Witepsol	2.00920(5), 2.00631(3), 2.00220(2)	13, 13, 95(1)
NLP-Ge/Wi	2.00867(2), 2.00620(2), 2.00218(1)	13, 13, 100(1)
Gelucire/Capryol	2.00910(3), 2.00623(2), 2.00217(2)	15, 15, 96(1)
NLP-Ge/Ca	2.00860(3), 2.00608(2), 2.00213(2)	15, 15, 100(1)
Gelucire/Witepsol/Capryol	2.00905(5), 2.00618(2), 2.00215(1)	16, 16, 96(1)
NLP-Ge/Wi/Ca	2.00858(2), 2.00608(2), 2.00215(1)	15, 15, 100(1)
Water	2.00805(3), 2.00596(2), 2.00212(2)	15, 15, 105(1)

Magnetic parameters of TEMPO in lipids and NLPs

In this step, the hydrophilic spin probe PCA has been replaced by the amphiphilic probe TEMPO. The spectra of TEMPO, recorded at W-band and 80 K, are shown in figure 6.3. All spectra are presented in the same order as those of PCA before (Fig. 6.1). In analogy to the PCA

spectra, the magnetic field range of the TEMPO g_x peak and the hfs along z-axis is discussed. A first inspection of these spectra immediately yields two observations: i) the g_x peaks of TEMPO in the NLPs are located at a similar magnetic field range as for TEMPO in bulk lipids, from which the NLPs were fabricated and ii) the g_x peaks for TEMPO are all broadened and different in shape compared to those for TEMPO in most of the reference solvents presented in figure 5.1 and 5.2. The unaltered g_x peak position for the bulk lipids and the NLPs is in contrast to the situation observed for PCA, where the g_x peaks are shifted to higher magnetic field when moving from bulk lipids to NLPs. This difference in the g_x positions was used as an argument for environments with different polarity properties experienced by PCA in the NLPs than in the bulk lipids. However, the qualitative finding that the position of the g_x peaks remains unchanged for TEMPO cannot be used as evidence for an identical environment of TEMPO in the bulk lipids and NLPs since the the g_x line shapes show clear differences between the spectra.

The g_x peak of TEMPO dissolved in Gelucire (Fig. 6.3-1$^{\text{st}}$ spectrum) is clearly broadened and has a flat line shape. The flat top shapes of the g_x peaks for TEMPO in Witepsol (Fig. 6.3-3$^{\text{rd}}$) and the Gelucire/Witepsol mixture (Fig. 6.3-6$^{\text{th}}$ spectrum) closely resemble the Gelucire case. Thus, TEMPO shows in the two solid lipids and their mixture spectra of similar shape and position of a broadened g_x peak. In contrast, the g_x peak of TEMPO loaded into the liquid lipid Capryol (Fig. 6.3-4$^{\text{th}}$ spectrum) shows a more asymmetric peak shape with a shoulder in the low-field range and the main maximum on the high-field side (Fig. 6.3-2$^{\text{nd}}$ spectrum). All the other spectra resemble those of TEMPO in Capryol as well in the position of their g_x peak as the g_x peak shape.

A certain broadening of the TEMPO g_x peak was observed before in section 5.1.1 for TEMPO with an additional shoulder arising on the high-field side of the main g_x peak. This splitting has been assigned to larger hfs of TEMPO along the g_x axis than of PCA, leading to partially resolved hyperfine splitting. However, simulations with a wide parameter set have shown that a shoulder on the low-field side of the g_x peak cannot be due to partially resolved hfs. A second interpretation for the low-field shoulder is a heterogeneous interaction of TEMPO with its surrounding micro-environment in the bulk lipids and NLPs giving rise to two distinct g_x values, as observed before for TEMPO dissolved in ethanol (Fig. 5.2). There, the larger g_x value, which corresponds to the g_x for TEMPO in toluene, has been assigned to a situation with absent H-bond between TEMPO and the OH group of ethanol, while the lower g_x value corresponds to the presence of a H-bond. For studying this hypothesis, g_x peak simulations based on a single g_{x1} value and simulations assuming the same g_{x1} and a second g_{x2} value were performed. Representative results of this approach are shown in figure 6.4 with the high-field shoulder arising from hfs indicated by ($*$) and the low-field-shoulder due to the second g_{x2} value marked by ($\otimes$). The g_x peak shapes observed of TEMPO in the bulk lipids and NLPs could overall be well reproduced by this approach of considering two different g_x values representing two different interactions between the spin probes and their surrounding micro-environments as shown in figure 6.5. Thereby variable weights for the contribution of the two g_x values were included. The simulation results for the complete spectra are shown as dashed lines in figure 6.3 together with the experimental spectra.
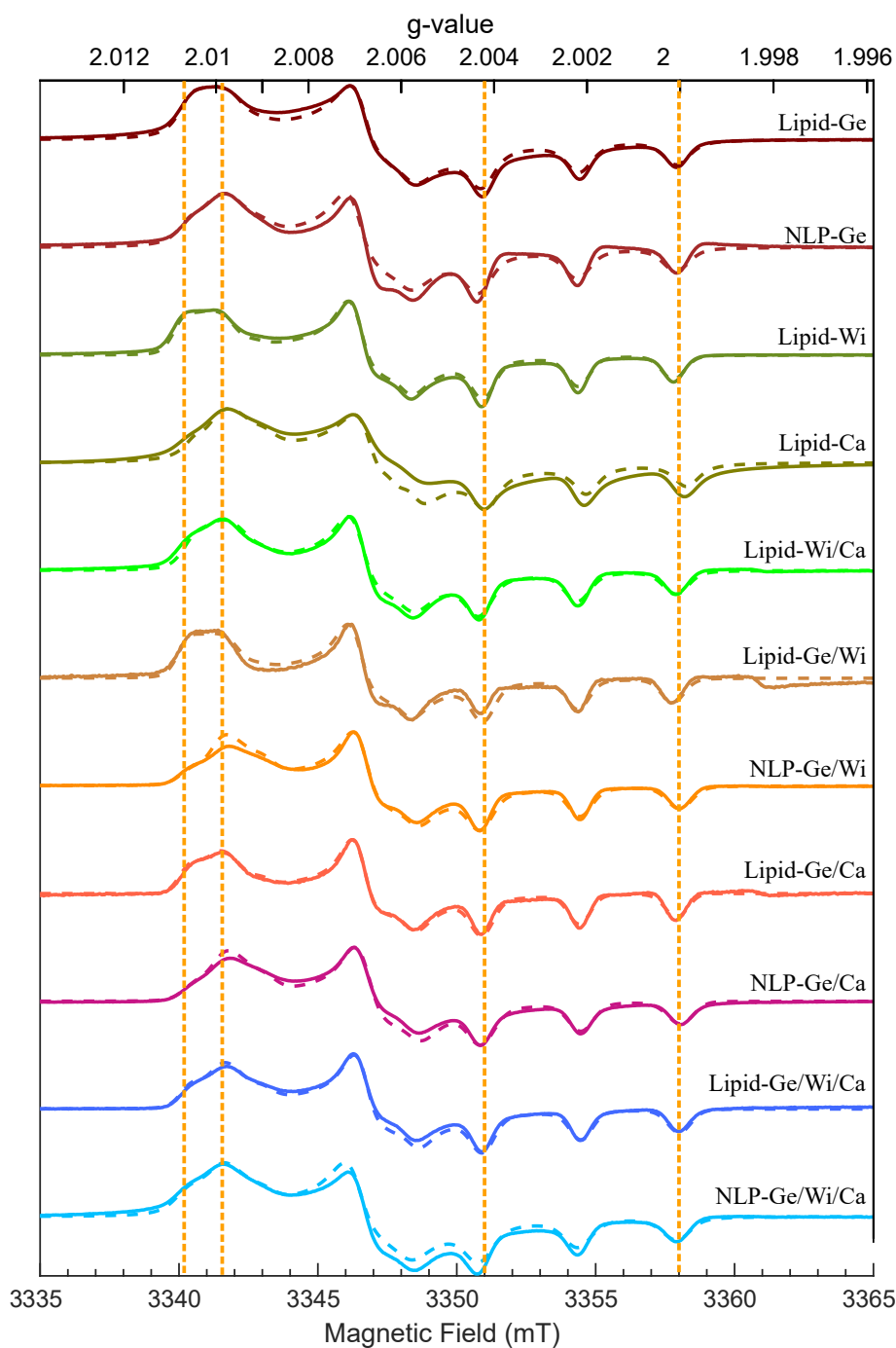
Figure 6.3: Spectra of TEMPO dissolved in lipids and loaded to NLPs recorded at W-band and 80 K. All spectra were taken at a microwave power of 0.5 μW and a modulation amplitude of 5 G with the exception of Witepsol/Capryol and Gelucire/Witepsol, which were recorded at a microwave power of 5 μW. Dashed lines are simulated spectra (see section 4.4). To guide the reader's eye, the magnetic field position of g_x peaks and the A_z hyperfine coupling are illustrated by four vertical dashed lines.
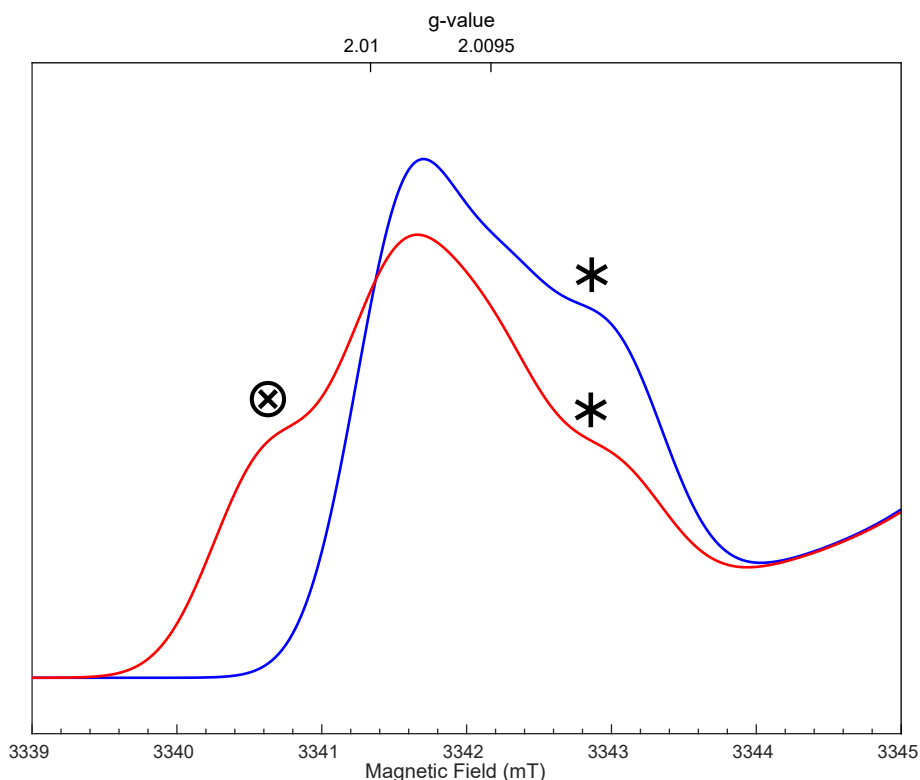
Figure 6.4: Simulation of a g_x peak based on one g_x value (2.0095, blue line) and two g_x values (2.0095 and 2.0100, red line) of identical weight. For both simulated spectra A_x is 20 MHz and the line width is 0.8 mT.

The necessity of including two distinct g_x values to account for the g_x peak shape immediately leads to the consequence of also including two different sets of hfs parameters, since the spin probe micro-environment influence on the g_x value is (anti-)correlated to a change in the hfs A_z value (see section 3.1). The necessary two sets of magnetic parameters together with the variable weight for the two sets rendered the simulation of the TEMPO spectra significantly more challenging than those of PCA. To restrict the simulation complexity, the values for g_y, g_z, A_x, and A_y were chosen equal for the individual two sets for the different bulk lipids and NLPs, respectively, as they show much less dependence on the specific environment than the g_x and A_z values. The two A_z values were extracted from each experimental spectrum by minimizing the residual root-mean-square deviation (RMSD) between the experimental and the simulated spectrum upon keeping all other parameters constant.
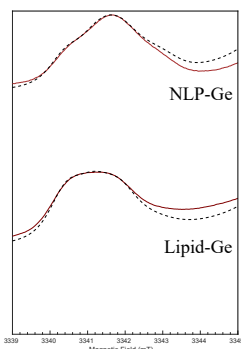
(a) Gelucire g_x 2.01010, 2.00950 (85:15) and NLP g_x 2.01010, 2.00945 (60:40)
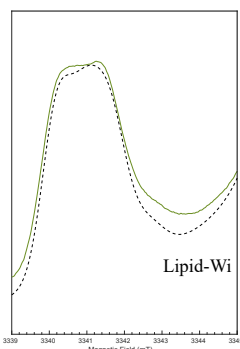
(b) Witepsol g_x 2.01025, 2.00950 (85:15)
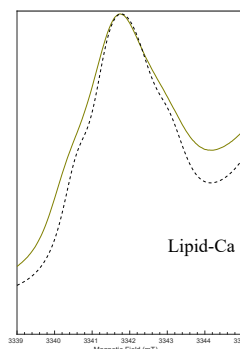
(c) Capryol g_x 2.01000, 2.00938 (40:60)
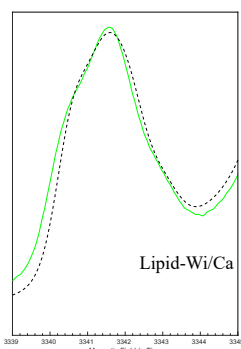
(d) Witepsol/Capryol g_x 2.01000, 2.00940 (70:30)
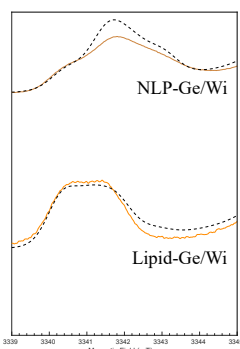
(e) Gelucire/Witepsol g_x 2.01015, 2.00950 (85:15), NLP g_x 2.01010, 2.00940 (35:65)
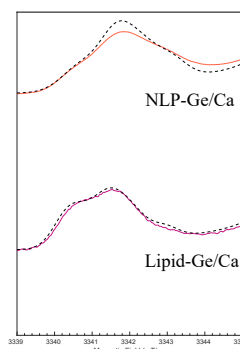
(f) Gelucire/Capryol g_x 2.01012, 2.00945 (70:30), NLP g_x 2.00999, 2.00935 (55:445)
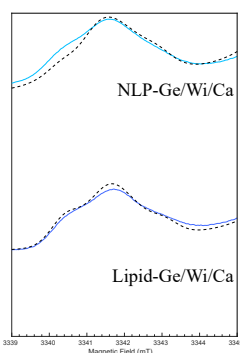
(g) Gelucire/Witepsol/-Capryol g_x 2.01010, 2.00940 (45:55), NLP g_x 2.01015, 2.00940 (60:40)

Figure 6.5: Magnification of the g_x peak of the TEMPO spectra demonstrate better visage of the additional shoulder and corresponding simulation. The g_x values and relative weight are presented.

79

Table 6.2: Magnetic parameters of TEMPO dissolved in lipids and loaded NLPs. The ratio gives the relative weight of the apolar/aprotic and the more polar/protic micro-environment.

Composition	g-matrix	A-matrix (MHz)	ratio
	g_x, g_y, g_z	A_x, A_y, A_z	%
Gelucire	2.01010(5), 2.00630(3), 2.00216(1)	20, 20, 98(1)	85:15
	2.00950(5), 2.00630(3), 2.00216(1)	20, 20, 101(1)	
NLP-Ge	2.01010(5), 2.00640(2), 2.00220(1)	20, 20, 98(1)	60:40
	2.00945(5), 2.00640(2), 2.00220(1)	20, 20, 102(1)	
Witepsol	2.01025(2), 2.00638(3), 2.00218(2)	20, 20, 95(1)	85:15
	2.00950(2), 2.00638(3), 2.00218(2)	20, 20, 101(1)	
Capryol	2.01000(2), 2.00610(5), 2.00200(5)	20, 20, 99(1)	40:60
	2.00938(2), 2.00610(5), 2.00200(5)	20, 20, 103(1)	
Witepsol/Capryol	2.01000(1), 2.00634(1), 2.00219(1)	20, 20, 99(1)	70:30
	2.00940(2), 2.00634(1), 2.00219(1)	20, 20, 100(1)	
Gelucire/Witepsol	2.01015(5), 2.00638(2), 2.00218(2)	20, 20, 95(1)	85:15
	2.00950(5), 2.00638(2), 2.00218(2)	20, 20, 100(1)	
NLP-Ge/Wi	2.01010(2), 2.00625(2), 2.00214(1)	20, 20, 96(1)	35:65
	2.00940(2), 2.00625(2), 2.00214(1)	20, 20, 103(1)	
Gelucire/Capryol	2.01012(3), 2.00629(1), 2.00215(1)	20, 20, 96(1)	70:30
	2.00945(5), 2.00629(1), 2.00215(1)	20, 20, 103(1)	
NLP-Ge/Ca	2.00999(1), 2.00620(2), 2.00212(1)	20, 20, 96(1)	55:45
	2.00935(5), 2.00620(2), 2.00212(1)	20, 20, 103(1)	
Gelucire/Witepsol/Capryol	2.01010(5), 2.00624(1), 2.00212(1)	20, 20, 97(1)	45:55
	2.00940(2), 2.00624(1), 2.00212(1)	20, 20, 102(1)	
NLP-Ge/Wi/Ca	2.01015(5), 2.00640(3), 2.00219(1)	20, 20, 97(1)	60:40
	2.00940(5), 2.00640(3), 2.00219(1)	20, 20, 102(1)	

The two distinct sets of magnetic parameters represent two different interaction scenarios for TEMPO with its surroundings corresponding to the presence or absence of a H-bond. The origin of this different interactions can be straight forward discussed for the lipid Capryol, which consists, in addition to the main hydrophobic sections, of H-bond donating carboxyl and hydroxyl groups (Fig. 6.2) [189]. Together with the amphiphilic property of TEMPO this can explain the observation of g_x values for TEMPO in Capryol, which are very similar to those found for TEMPO in ethanol. Interestingly, also the relative proportion of the aprotic with respect to the protic contribution are very close for ethanol (35:65) and Capryol (40:60). Also for all other lipids and lipid mixtures, two sets of magnetic parameters with a rather aprotic/apolar and a more protic character are found with varying proportions of the two. In all cases, the two sets of g_x values are rather close to those found for TEMPO in ethanol. The two solid lipids Gelucire and Witepsol and their mixture show the least contribution of a protic environment

with only about 15%, which stems from hydroxyl groups of the solid lipids (hydroxyl value of Gelucire (OHV) 36-56, and OHV of Witepsol 50-65). This contribution increases to 30% for the binary mixtures of Capryol with Gelucire and Witepsol, respectively. The weight of the more protic environment increases further 55% for the ternary Gelucire/Witepsol/Capryol mixture. When moving from the lipid mixtures to the corresponding NLP an increase of the protic environment contribution is observed for NLP-Ge/Wi and NLP-Ge/Ca with weights of 65% and 45%,respectively, which are 50% and 15%, respectively, larger than for the lipid mixtures. For NLP made from the ternary mixture Gelucire/Witepsol/Capryol a slight decrease of the protic environment contribution by 15% is observed. Interestingly, TEMPO experiences even when dissolved in the solid lipids Gelucire, Witepsol and the Gelucire/Witepsol mixture an environment resulting in magnetic parameters similar to those when dissolved in ethanol. Taken together, the amphiphilic TEMPO experiences environments giving rise to two different sets of magnetic parameters in all lipids, lipid mixtures and NLP made out of them. The type of lipid and whether TEMPO is added to the the bulk lipids or NLPs changes the relative weights of these environments.

Magnetic parameters of DxPCA in lipids and NLPs

The model drug DxPCA was examined in the same way as the other spin probes (PCA, TEMPO) by W-band measurements at 80 K to characterize the polarity/proticity properties of its micro-environments. Figure 6.6 shows EPR spectra of DxPCA dissolved in pure or mixed lipids and loaded into NLPs. Some of the spectra contain extra lines not stemming from DxPCA and are indicated by (∗). They arise from a Mn(II) contamination of the samples, which is most prominent for all four NLP samples, but is also clearly visible for the Gelucire/Witepsol mixture and less prominent to virtual absence in the other samples.

Similar to the spectra of PCA and as a general trend, a shift of the DxPCA g_x peaks to higher magnetic fields occurs when the lipids are converted into NLPs. The g_x peaks of DxPCA in Gelucire, Witepsol and the Gelucire/Witepsol mixture have symmetric shape and no significant additional features are visible (Fig. 6.6-1st, 3rd and 6th spectrum). However, the g_x peaks of DxPCA in Capryol and in all Capryol containing mixtures as well as in all NLPs have asymmetric structure, and an extra feature occurs on the low-field side of the g_x peaks, similar to the TEMPO spectra. The magnetic field position of these extra features in the NLP spectra are at the same positions as the g_x peaks of DxPCA in the lipids from which the NLP were made of, respectively (see e.g. Fig 6.6-1st, 2nd and 6th, 7th spectra). The g_x peak of DxPCA dissolved in Witepsol is in position and shape very similar to that of DxPCA dissolved in Gelucire (Fig. 6.6-3rd spectrum). However, the g_x peak of DxPCA dissolved in the liquid lipid Capryol occurs at significantly larger magnetic field than for the solid lipids (Fig. 6.6-4th spectrum). Similar to the finding for PCA, the g_x peak of DxPCA dissolved in the Witepsol/Capryol mixture is located between the peaks of DxPCA in Witepsol and Capryol (Fig. 6.6-5th spectrum). Consistent with the highly similar spectra for the two solid lipids Gelucire and Witepsol, also the spectrum of DxPCA dissolved in the Gelucire/Witepsol mixture is very similar (Fig. 6.6-6th spectrum). However, the spectrum for DxPCA loaded into NLP-Ge/Wi shows a clear high-field shift of

g_x compared to the situation in the bulk Gelucire/Witepsol mixture (Fig. 6.6-7th spectrum). The spectrum of DxPCA dissolved in the Gelucire/Capryol mixture is a superposition of the spectra seen for the individual lipids with a low-field shoulder at the position of the g_x peak seen for DxPCA in Gelucire and the main maximum at the position of the g_x peak of DxPCA in Capryol (Fig. 6.6-8th spectrum). Again, the g_x peak of DxPCA loaded into NLP-Ge/Ca is further up-shifted compared to the bulk Gelucire/Capryol mixture (Fig. 6.6-9th spectrum).

The g_x peak of DxPCA dissolved in the Gelucire/Witepsol/Capryol mixture is very similar to that seen in the Gelucire/Capryol mixture with a low-field shoulder fitting to the Gelucire spectrum and the main maximum fitting to the Capryol spectrum (Fig. 6.6-10th spectrum). Finally, the g_x peak of DxPCA loaded to NLP-Ge/Wi/Ca is again up-shifted compared to the Gelucire/Witepsol/Capryol mixture (Fig. 6.6-11th spectrum).

The simulation strategy for the DxPCA spectra was the same as for the TEMPO spectra, described in the previous section (Section 6.1.1). The simulations have been mainly carried out using two sets of magnetic parameters. The resulting g-matrices and ^{14}N hyperfine coupling matrices of DxPCA in the different lipids and NLPs are presented in table 6.3. The spectra for the two solid lipids Gelucire and Witepsol and their mixture can be well simulated assuming only one parameter set with a g_x value of 2.00905 and an A_z value 95 MHz. They correspond to the parameters seen for DxPCA in the apolar/aprotic solvent toluene (Table.5.3). These g_x and A_z values reflecting an apolar/aprotic environment arise also for all other samples, however in some cases only as a minority contribution, e.g. in the DxPCA in NLP-Ge/Wi. The second, smaller g_x and larger A_z vary between the different samples as well in their magnitude and proportion. They are even the 35:65 majority component for the pure liquid lipid Capryol with $g_x = 2.0086$ and $A_z = 100$ MHz. As discussed before, Capryol contains a hydroxyl group (Fig. 6.2) and exhibits more protic properties than Gelucire and Witepsol. Thus, the second set of magnetic parameters for DxPCA dissolved in Capryol likely reflects the possible H-bonding between the spin probe and this liquid lipid.

DxPCA dissolved in a Witepsol/Capryol mixture displays magnetic parameters as for Capryol with a slightly modified 40:60 ratio between the apolar/aprotic and the more protic components, respectively. Both parameter sets occur with equal weight for the Gelucire/Capryol mixture where the smaller $g_x = 2.00865$ is again close to the value found for Capryol, and the larger $A_z = 100$ MHz as found for Capryol alone and for the Witepsol/Capryol mixture. This behavior is also found for the Gelucire/Witepsol/Capryol mixture with the smaller $g_x = 2.0086$ and the larger $A_z = 99$ MHz in good agreement with the Capryol values, and 65:35 ratio.

Upon the change from the bulk lipid to NLPs which are made out of them, the smaller g_x value of DxPCA decreases and the larger A_z value increases. While DxPCA shows in the bulk solid lipids Gelucire and Witepsol and their Gelucire/Witepsol mixture only one set of magnetic parameters, two sets of these parameters are necessary to describe the spectra for DxPCA in NLP made of these lipids and their mixture. Since the first parameter set is also for the NLP samples identical to all other samples only the smaller g_x and larger A_z values of the second set are discussed in the following.
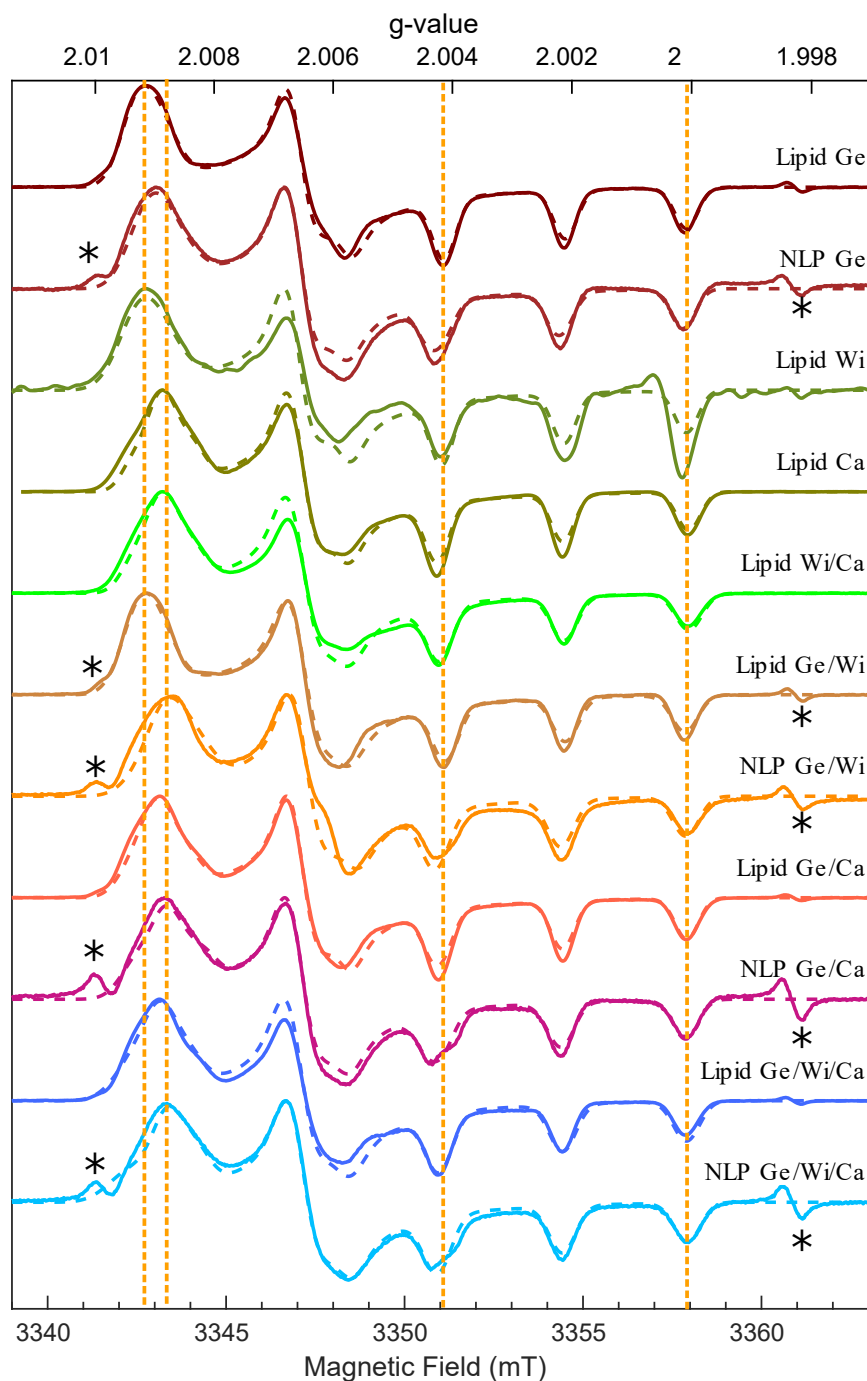
Figure 6.6: Spectra of DxPCA dissolved in lipids and loaded to NLPs recorded at W-band and 80 K. All lipid spectra were recorded by the FSE (τ=300 ns, except Ge/Ca τ=400 ns) technique and pseudo modulation 5 G. The NLPs spectra have been recorded in cw mode at a microwave power of 125 nW with a modulation of 5 G. Dashed lines represent simulated spectra. Additional peaks indicated by ($*$) represent Manganese(II).

The $g_x = 2.0087$ for DxPCA in the NLP-Ge is slightly larger than all other second set g_x values, but the larger $A_z = 99$ MHz is equal to the second A_z value seen for the other samples, with a 50:50 ratio of the two sets. DxPCA in NLP made from Gelucire/Witepsol shows a $g_x = 2.00852$, which is even slightly smaller than for Capryol, and the typical $A_z = 99$ MHz is equal. This sample shows the most extreme ratio of 20:80 in favour of the the second magnetic parameter set reflecting a more polar/protic environment. In the case of DxPCA loaded into NLP-Ge/Wi/Ca the $g_x = 2.0085$ and $A_z = 99$ MHz values are within the error margin identical to those in Capryol or in NLP-Ge/Wi.

Table 6.3: Magnetic parameters of DxPCA dissolved in lipids and loaded to NLPs. The ratio gives the relative weight of the apolar/aprotic and the more polar/protic micro-environment.

Composition	g-matrix	A-matrix (MHz)	ratio
	g_x, g_y, g_z	A_x, A_y, A_z	%
Gelucire	2.00905(5), 2.00617(2), 2.00211(1)	12, 15, 95(1)	-
NLP-Ge	2.00905(5), 2.00617(2), 2.00211(1)	12, 15, 95(1)	50:50
	2.00870(5), 2.00623(3), 2.00230(5)	13, 12, 99(1)	
Witepsol	2.00905(5), 2.00620(3), 2.00213(3)	12, 15, 96(1)	-
Capryol	2.00905(5), 2.00616(2), 2.00214(1)	13, 13, 96(1)	35:65
	2.00860(2), 2.00616(3), 2.00214(1)	13, 13, 100(1)	
Witepsol/Capryol	2.00905(5), 2.00616(3), 2.00212(2)	13, 13, 96(1)	40:60
	2.00860(5), 2.00616(3), 2.00212(5)	13, 13, 99(1)	
Gelucire/Witepsol	2.00905(5), 2.00617(2), 2.00211(1)	11, 13, 94(1)	-
NLP-Ge/Wi	2.00905(5), 2.00617(2), 2.00211(1)	11, 13, 94(1)	20:80
	2.00852(2), 2.00605(5), 2.00220(4)	14, 15, 99(1)	
Gelucire/Capryol	2.00905(5), 2.00617(2), 2.00211(1)	12, 15, 95(1)	50:50
	2.00865(1), 2.00614(2), 2.00220(5)	13, 13, 100(1)	
NLP-Ge/Ca	2.00905(5), 2.00617(2), 2.00211(1)	12, 15, 95(1)	40:60
	2.00845(5), 2.00618(2), 2.00225(5)	15, 12, 101(1)	
Gelucire/Witepsol/Capryol	2.00905(5), 2.00620(3), 2.00213(3)	12, 15, 96(1)	65:35
	2.00860(2), 2.00616(3), 2.00218(3)	13, 13, 99(1)	
NLP-Ge/Wi/Ca	2.00905(5), 2.00615(2), 2.00213(3)	12, 15, 96(1)	50:50
	2.00850(2), 2.00614(2), 2.00218(2)	13, 13, 99(1)	

In summary, the simulations yield a consistent picture of the polarity and proticity experienced by DxPCA in the various lipids:

i) The DxPCA micro-environment in the solid bulk lipids Gelucire, Witepsol, and Gelucire/Witepsol is characterized by one set of magnetic parameters.

ii) The liquid lipid Capryol provides a micro-environment giving rise to two different sets

of magnetic parameters similar to the case seen for TEMPO in EtOH, which can be interpreted as one scenario with and one without a H-bond between the spin probe an the lipid.

iii) The magnetic parameters of DxPCA in the two mixtures Witepsol/Capryol and Gelucire/Capryol are very similar to the Capryol case. However, the ratio between the two sets shows a slight increase of the fraction reflecting an apolar/aprotic environment as seen for the solid lipids.

iv) When NLP are fabricated from Gelucire and Gelucire/Witepsol, the micro-environment of DxPCA drastically changes as evidenced by the occurrence of a second set of magnetic parameters, which reflects the contribution of a significantly more polar/protic environment than bulk lipids.

A similar phenomenon is seen for NLP fabricated from the Gelucire/Capryol and Gelucire/Witepsol/Capryol. The change of the DxPCA micro-environment upon transforming these Capryol containing bulk lipids into dissolved NLPs are reflected by a clear decrease in the magnitude of the second g_x value, again reflecting a more polar/protic second contribution than in the bulk lipids. Furthermore, the proportion of the more polar/protic environment of DxPCA is increased for all NLP samples compared to their corresponding bulk lipid samples. However, it is necessary to note that all g_x and A_z values obtained from the simulations are distinctly different from those found for DxPCA in aqueous solution. This implies that no partitioning of DxPCA between the NLP and the aqueous phase occurs to a detectable amount and leads to the conclusion that all observed DxPCA is located within the NLPs. Thereby, a fraction of DxPCA , which displays the unchanged larger g_x seen in all samples, remains unaffected by the transformation of bulk lipids into NLPs and another fraction, which shows the reduced smaller g_x in the NLPs, experiences a micro-environment influenced by the aqueous phase surrounding the NLP.

In summary, the magnetic parameters of each spin probe provide information about the surrounding environment in lipids and the NLP. The magnetic parameters of PCA dissolved in lipids represent the apolar/aprotic environment while when loaded in NLPs report on a more protic environment clearly distinct from a pure lipidic environment, likely evidencing the influence of the aqueous surrounding of the NLP. The magnetic parameters of TEMPO show an apolar, liphophilic environment in the bulk lipids, however with the simultaneous presence of both aprotic and protic character. When moving to NLPs made out of Gelucire, Gelucire/Witepsol and Gelucire/Capryol the environment of TEMPO appears to become somewhat more protic than in the bulk lipids as evidenced by a further reduction of the small g_x value and an increase of the proportion of this component. NLP made from the Gelucire/Witepsol/Capryol mixture behave differently with virtually no change of the g_x and A_z but a slight increase of the proportion representing the liphophilic environment. The magnetic parameters of DxPCA show the most complex behavior of all three spin probes. DxPCA loaded in the liquid lipid Capryol and any lipid mixtures with Capryol shows two sets of magnetic parameters as seen for TEMPO in contrast to PCA while it shows in the solid lipids Gelucire,

Witepsol and Gelucire/Witepsol only one set as seen for PCA but different from TEMPO. When loaded into NLPs, the magnetic parameters of DxPCA consistently report on the presence of two distinct micro-environments, one with apolar/aprotic character and one with more polar or protic character than experienced in the bulk lipids. Thus, as in the case of the CMS particles, knowledge about the micro-environment polarity/proticity alone is insufficient to localize the spin probes inside the complex NLP. Therefore, additional experiments have been performed and are presented in the following section.

6.1.2 Dynamics of spin probes in lipids and NLPs

The study of spin probe dynamics adds valuable information to the polarity/proticity investigations described above towards an incorporation model for the spin probes within the NLPs. The mobility of the spin probes was determined as in section 5.1.4 using X- and W-band cw EPR measurements at room temperature, and simulation of the spectra as a function of the spin probe rotational correlation time and extraction of the viscosity for the different micro-environments by virtue of the Stokes-Einstein relation (Section 3.2). High-frequency (W-band) cw EPR at room temperature provides high resolution for fast rotational dynamics and was used to probe fast modes of motion of the small PCA and TEMPO spin probes to distinguish them from slow motions of the whole NLPs in solution. The larger DxPCA dissolved in lipids and loaded into NLPs was investigated at X-band frequency at room temperature, since this lower frequency band is better suited for the relevant rotational correlation time window.

Mobility of PCA in lipids and NLPs

The spectra of PCA dissolved in bulk lipids and loaded in NLPs recorded at W-band at rt to evaluate the nitroxide rotational dynamics in the different micro-environments are shown in figure 6.7. These spectra can be divided into three clearly distinct groups. The first group contains the three bulk solid lipid samples with PCA dissolved in Gelucire, Witepsol, and the Gelucire/Witepsol mixture (Fig. 6.7-1st, 3rd, 6th spectrum, respectively). They are characterized by an overall broad and weakly structured line shape. Comparison of, e.g., the PCA in Gelucire spectrum (Fig. 6.7-1st spectrum) with the dependence of nitroxide spectra on the rotational correlation time τ_{corr} presented in figure 3.8 immediately indicates slow rotational motion of PCA in these samples with a τ_{corr} around 1 ns. Within this group the spectrum of PCA in Witepsol shows the particularity of a weak three line spectrum characteristic of fast rotations nitroxides superimposed on the broad main spectrum. However, the integrated intensity of this narrow spectral contribution is very small and amounts to only roughly 0.2 % of the overall spectrum. The magnetic field positions of these lines clearly tell that they originate from a highly apolar/aprotic environment of PCA. This extremely weak spectral contribution can safely be neglected in the further discussion and has in addition no relevance for the preceding discussion of the low temperature spectra in section 6.1.1 since a 0.2 % fraction is invisible under frozen solution conditions.
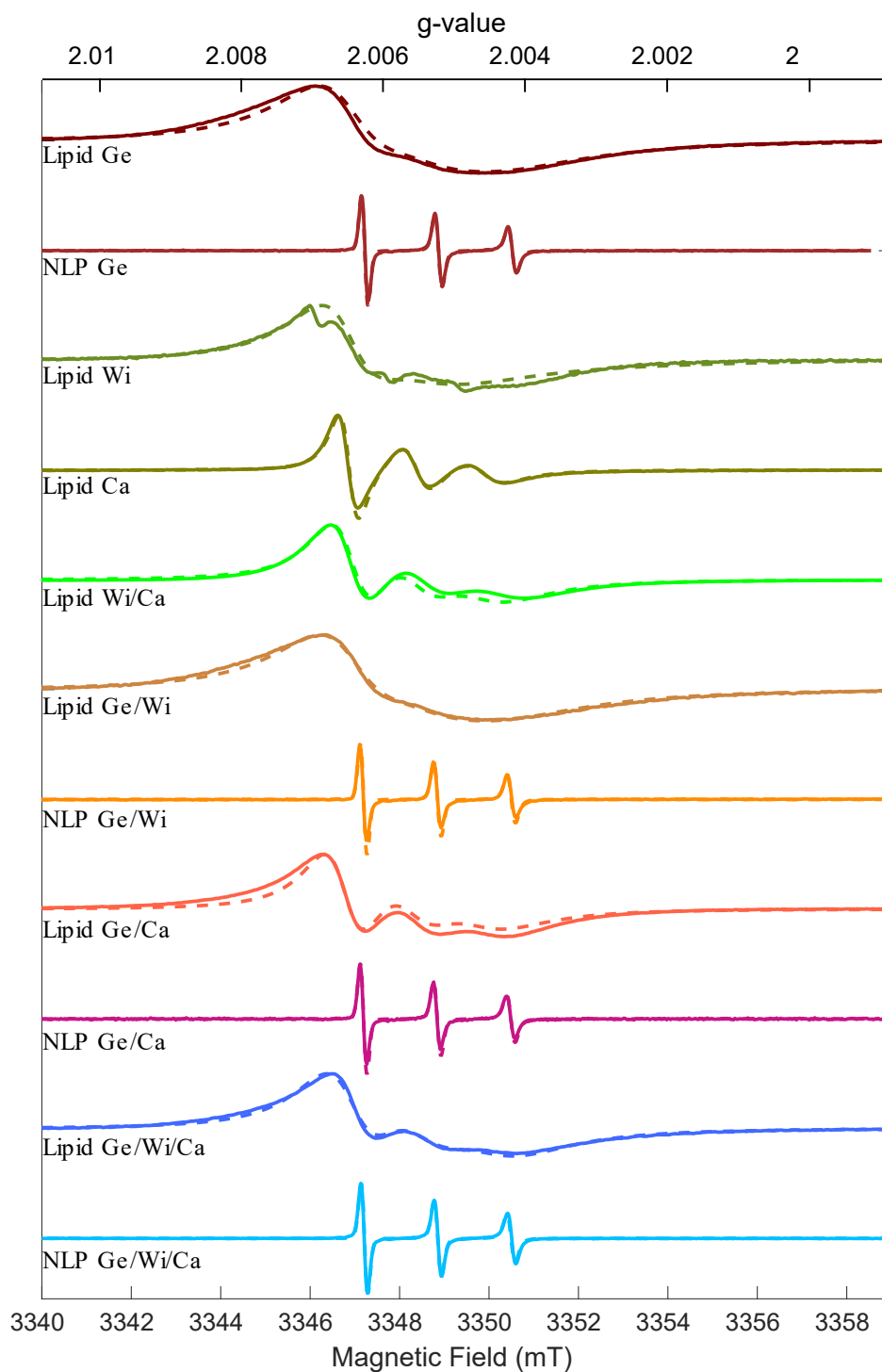
Figure 6.7: W-band spectra of PCA dissolved in lipids and NLP recorded at room temperature. A microwave power of 0.005 mW and a modulation of 1 G was used for all of the spectra.

The second group contains all NLP samples, i.e. PCA in NLP-Ge and NLP-Ge/Wi, NLP-Ge/Ca, and NLP-Ge/Wi/Ca (Fig. 6.7-2nd, 7th, 9th, 11th spectrum, respectively). These spectra are all narrow three-line spectra characteristic for very fast, isotropic limit, tumbling nitroxides.

The third group comprises all four bulk lipid samples containing the liquid lipid Capryol, i.e. PCA in Capryol, Witepsol/Capryol, Gelucire/Capryol, and Gelucire/Witepsol/Capryol (Fig. 6.7-4th, 5th, 8th, 10th spectrum, respectively). These spectra show relatively broad, but significantly better resolved lines than in the case of the bulk solid lipids. The width of the individual lines differs substantially within this group and a comparison with the qualitative dependence on the rotational correlation time in Figure 3.8 shows that these spectra fall into the range of τ_{corr} values between 200-500 ps. The shortest τ_{corr} occurs within this group for PCA in Capryol, while the longest is seen for PCA in Gelucire/Capryol, and Gelucire/Witepsol/Capryol.

The quantitative extraction of the correlation times was performed by spectral simulation with the EasySpin [174] routine *chili* (see section 4.4) using the g and A matrices for PCA in the various samples as listed in table A.2 as starting point. The narrow three-line spectra of the PCA in NLP sample group could be simulated very well and the dashed lines for the simulations are hardly recognizable in figure 6.7. The rotational correlation time is $\tau_{corr} = 30$ ps for all these spectra. Also the spectra of the third group, i.e. PCA in the bulk lipids containing Capryol can be simulated quite well with the best simulation quality occurring for the Capryol only sample with the fastest correlation time $\tau_{corr} = 250$ ps, while the Witepsol/Capryol sample shows a slightly reduced simulation quality at a $\tau_{corr} = 400$ ps as do the Gelucire/Capryol and Gelucire/Witepsol/Capryol samples with a $\tau_{corr} = 450$ ps.

The simulation quality for the bulk solid lipid group is substantially lower than for the other two groups. Nevertheless, meaningful rotational correlation times can be deduced with $\tau_{corr} \approx 700$ ps for PCA in both the Gelucire and the Gelucire/Witepsol and $\tau_{corr} \approx 1.0$ ns in the Witepsol sample. These rotational correlation times τ_{corr} deduced from the spectra simulations are summarized in table 6.4 together with the average g values g_{ave} from the simulations, the g_{ave} obtained from the 80 K EPR measurements (Tab. 6.1), the average A values A_{ave} form the simulations, and the residual linewidth used in the simulations. The obtained τ_{corr} values can be compared with rotational correlation time of PCA in water $\tau_{corr} \approx 30$ ps and correlation times estimated by the Stokes-Einstein equation using the effective gyration radius of $R_{eff} \approx 3.2$ Å for PCA derived from the spectrum of PCA in water at ambient temperature (Fig. 5.6) together with literature values for the lipid viscosities. It is immediately obvious that the τ_{corr} deduced for PCA in NLP exactly matches the value found for PCA in water.

Table 6.4: Rotational correlation time (τ_{corr}) and magnetic parameters of PCA dissolved in lipids and loaded to NLPs. The linewidth values reported as Gaussian and Lorentzian respectively (All anisotropic magnetic parameters are given in table A.2).

Composition	τ_{corr} (ps)	g_{ave}	g_{ave} at 80 K	A_{ave} (MHz)	A_{ave} (MHz) at 80 K	Linewidth (mT)
Gelucire	700	2.00575	2.00575	40.7	40.0	[0.00, 0.18]
NLP-Ge	30	2.00547	2.00572	46.3	41.7	[0.15, 0.00]
Witepsol	1000	2.00577	2.00577	41.3	41.3	[0.00, 0.50]
Capryol	250	2.00576	2.00568	42.7	40.0	[0.00, 0.30]
Witepsol/Capryol	400	2.00577	2.00577	40.0	40.0	[0.00, 1.00]
Gelucire/Witepsol	700	2.00575	2.00590	40.7	40.3	[0.00, 1.80]
NLP-Ge/Wi	30	2.00549	2.00568	46.3	42.0	[0.15, 0.00]
Gelucire/Capryol	450	2.00583	2.00586	42.0	42.0	[0.00, 0.80]
NLP-Ge/Ca	30	2.00549	2.00560	46.3	43.3	[0.15, 0.00]
Gelucire/Witepsol/Capryol	450	2.00571	2.00579	42.7	42.7	[0.00, 1.50]
NLP-Ge/wi/Ca	30	2.00548	2.00560	46.0	43.3	[0.15, 0.00]

Mobility of TEMPO in lipids and NLPs

Spectra of TEMPO in bulk lipids and NLPs, as in the preceding section for PCA, were recorded at W-band at room temperature and are presented in figure 6.8. The spectra are characterized by much better resolution than in the cases of PCA in the bulk lipids, but all show much larger line widths than seen for the PCA in aqueous solution. Furthermore, a clear difference between the bulk lipid spectra and those for the NLP samples is visible. All bulk lipid spectra show three lines while the NLP spectra consist of pairs of three-line spectra with a strong line width difference between them. In each case, the sub-spectrum occurring at lower field carries a larger line width than the up-field shifted sub-spectrum. The low-field sub-spectrum in each of the NLP spectra occurs at the field position and with very similar line width as in the spectrum of the corresponding bulk lipid mixture. The three spectra for TEMPO in Gelucire, in Gelucire/Witepsol and in the Gelucire/Witepsol/Capryol mixture deviate in their overall shape from the other spectra as their three-line spectrum is superimposed on a very broad unstructured line with largest intensity in the Gelucire case and lower intensity in both of the Gelucire/Witepsol and the Gelucire/Witepsol/Capryol mixtures. This broad component can be attributed to a fraction of aggregated TEMPO in these samples. Again resorting to the qualitative rotational correlation time dependence of nitroxides (Fig. 3.8) yields estimates for the respective rotational correlation times characterizing the spectra in figure 6.8.

The relative intensity ratio of the lines in the TEMPO in Witepsol spectrum point to a τ_{corr} in the 100 ps range. Neglecting the broad background of the TEMPO in Gelucire spectrum, a similar intensity ratio and thus a similar τ_{corr} in the 200 ps range has to be assigned to this spectrum as well. Also all the other bulk lipid spectra as well as the low-field three-line sub-spectra for the NLP samples share a similar intensity ratio of the individual lines and are qualitatively characterized by a τ_{corr} in the 100 ps range. The high-field three-line sub-spectra

for the NLP samples show a more even intensity of the individual lines and are sharper. This indicates a shorter τ_{corr} in the 10 ps range.

Further information can be taken from the position of the central line of the bulk lipid spectra and the low field sub-spectra for the NLP samples. This position provides the average g value g_{ave} occurring by the rotational averaging of the g-matrix. A clear high-field shift is visible for the TEMPO in bulk Capryol spectrum compared to the three spectra of the samples containing only solid lipids. The three spectra for TEMPO in the bulk lipid mixtures containing Capryol are found at a field position roughly half way in between the Capryol spectrum and the solid lipid spectra. This can be correlated with the presence of the protic properties of Capryol. The low-field sub-spectra for the NLP samples occur largely at the field position of the corresponding bulk lipids with the exception of NLP-Ge/Ca, which is slightly low-field shifted. This low-field shift is in contradiction to the expectation form the low-temperature measurements in section 6.1.1 where smaller g_x values were determined for the NLP sample than for the bulk lipid sample. The quantitative evaluation of the magnetic field positions of the (sub)spectra and their associated τ_{corr} was again performed by spectra simulations shown by dashed lines in figure 6.8. In general all spectra could be simulated well and the discrepancies visible for the three spectra for TEMPO in lipid-Ge, in lipid-Ge/Wi and in the lipid-Ge/Wi/Ca mixture are solely due to the broad background omitted in the simulations. The integral of the experimental spectrum versus the simulated spectrum clearly shows an underlying broad spectral contribution (Fig. A.2). The obtained parameters are summarized in table 6.5. The g_{ave}, A_{ave} indicate apolar/aprotic environments for all solid and mixed lipids. The combination of magnetic and dynamic parameters reveals a lipidic environment for TEMPO in bulks lipids. The parameters obtained for the high-field shifted sub-spectra for the NLP samples can be interpreted immediately. The g_{ave}, A_{ave}, and τ_{corr} of the high-field fast tumbling three-line sub-spectra for the NLP samples are all identical, respectively, and coincide with the values observed for TEMPO in water (see Section 5.1.4). Thus, these sub-spectra can be immediately be interpreted as reporting a fraction of TEMPO in the aqueous phase but not embedded in the NLP. It should be noted that the low-temperature spectra for TEMPO in NLP showed no indication of a fraction in the aqueous phase. However, this is no contradiction as the partition coefficient for TEMPO in a water/1-decanol mixture also can only be determined by room temperature experiments and the TEMPO in water fraction gives no detectable signal. The interpretation of the bulk lipid spectra and the low-field shifted sub-spectra of the NLP is more complex. At 80 K, the g-values indication the interaction of TEMPO with the surrounding lipidic micro-environment but provide no identical for an interaction of TEMPO with the aqueous solution. However, the g-values of isotropic limit and slow-motion reveal the interaction of TEMPO with water and lipidic micro-environment, respectively. The magnetic parameters of slow-motion TEMPO are identical with magnetic parameters of TEMPO in bulk lipids. These similarity in magnetic and dynamic parameters between slow-motion fraction of TEMPO in NLPs and TEMPO in lipids leads us to conclude, that the slow-motion fraction of TEMPO is embedded inside NLPs.
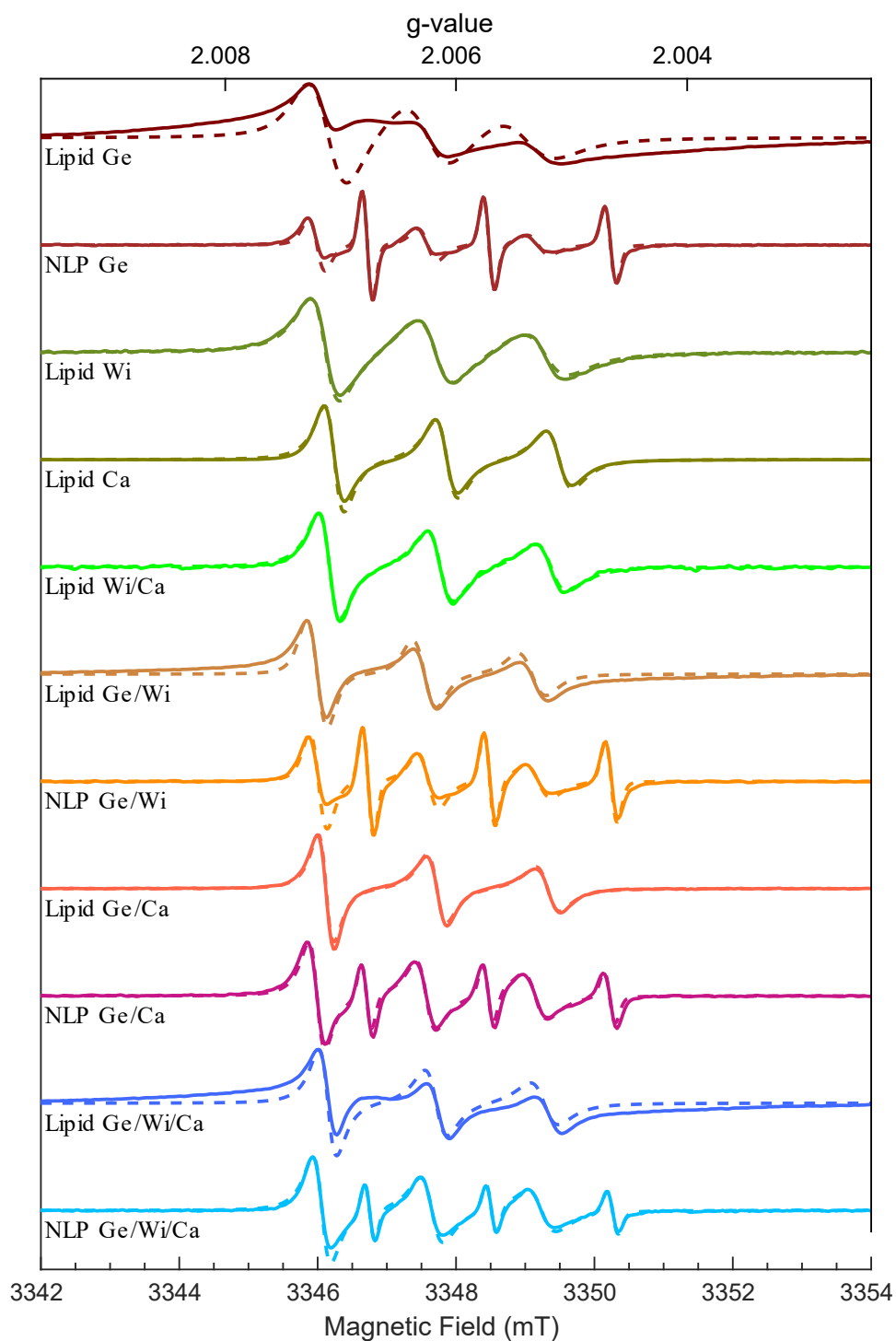
Figure 6.8: W-band cw EPR spectra of TEMPO dissolved in lipids and loaded to NLP at room temperature, Microwave power 0.005 mW and modulation amplitude 1 G.

Table 6.5: Rotational correlation time (τ_{corr}) and magnetic parameters of TEMPO dissolved in lipids and loaded to NLPs. The linewidth values reported as Gaussian and Lorentzian respectively for slow-motion. The linewidth values of fast-motion are Gaussian (All anisotropic magnetic parameters are given in table A.3).

Composition	fast				slow						
	τ_{corr} (ps)	g_{ave}	A_{ave} (MHz)	Linewidth (mT)	τ_{corr} (ps)	g_{ave}	g_{ave} 80 K	A_{ave} (MHz)	A_{ave} 80 K (MHz)	Linewidth (mT)	Ratio (f:s) (%)
Gelucire	-	-	-	-	200	2.0062	2.0061	40.7	46.1	[0.40, 0.00]	-
NLP-Ge	12.5	2.0057	49.3	0.16	65	2.0062	2.0061	45.6	46.5	[0.20, 0.00]	35:65
Witepsol	-	-	-	-	125	2.0062	2.0062	44.7	45.3	[0.00, 0.40]	-
Capryol	-	-	-	-	50	2.0061	2.0059	45.7	47.1	[0.00, 0.30]	-
Witepsol/Capryol	-	-	-	-	80	2.0061	2.0061	45.0	46.3	[0.00, 0.30]	-
Gelucire/Witepsol	-	-	-	-	80	2.0063	2.0062	43.7	45.2	[0.25, 0.00]	-
NLP-Ge/Wi	10	2.0057	49.3	0.17	80	2.0062	2.0060	44.7	46.8	[0.20, 0,00]	20:80
Gelucire/Capryol	-	-	-	-	65	2.0062	2.0061	45.0	46.0	[0.00, 0.20]	-
NLP-Ge/Ca	10	2.0057	49.3	0.16	65	2.0063	2.0060	45.3	46.4	[0.00, 0.20]	10:90
Gelucire/Witepsol/Capryol	-	-	-	-	80	2.0062	2.0060	45.3	46.6	[0.00, 0.20]	-
NLP-Ge/wi/Ca	10	2.0057	49.3	0.17	80	2.0062	2.0061	44.7	46.3	[0.00, 0.20]	5:95

Mobility of DxPCA in lipids and NLPs

Figure 6.9 shows a comparison of X-band spectra of DxPCA in different lipids and NLPs recorded at room temperature. All spectra of DxPCA dissolved in lipids and also loaded into NLPs represent slow tumbling motion (see for comparison Fig. 3.6), with the main difference that the spectra for DxPCA in the bulk lipids, except Capryol and the Witepsol/Capryol mixture, clearly show an underlying broad spectral contribution. Such a broad, unresolved spectrum was already observed for DxPCA dissolved in water. There the three lines of fast tumbling DxPCA are accompanied by a broad unstructured spectrum (see for comparison Fig. 5.12a), which has been assigned to aggregated DxPCA in water and aggregation is also considered as the origin of the broad component seen here for DxPCA in the bulk lipids.

It should be noted that the aggregated fraction contributes differently to the spectral shape at X- and W- band frequencies and thus to the shape of the spectra of PCA and TEMPO spectra acquired at W-band discussed above and the DxPCA spectra acquired at X-band discussed here. While the unresolved spectrum of the aggregated fraction is broadened far beyond the width of the three line spectrum at W-band it is much less broad at X-band and mainly affects the spectral shape around the center of the three lines. The extent of the broad signal is highest for the solid lipids Gelucire and Witepsol and their mixture, but is significantly lower in the mixtures containing the liquid lipid Capryol.

DxPCA in NLPs shows besides the main spectral contribution a faint signal of very fast tumbling DxPCA weakly visible at 336.5 mT and indicated by (∗) in figure 6.9 and for the Gelucire and Gelucire/Witepsol NLP also at about 333 mT (also indicated by ∗). This free DxPCA component in aqueous phase accounts for only at most 2% of the overall intensity [192] and is neglected in the following.
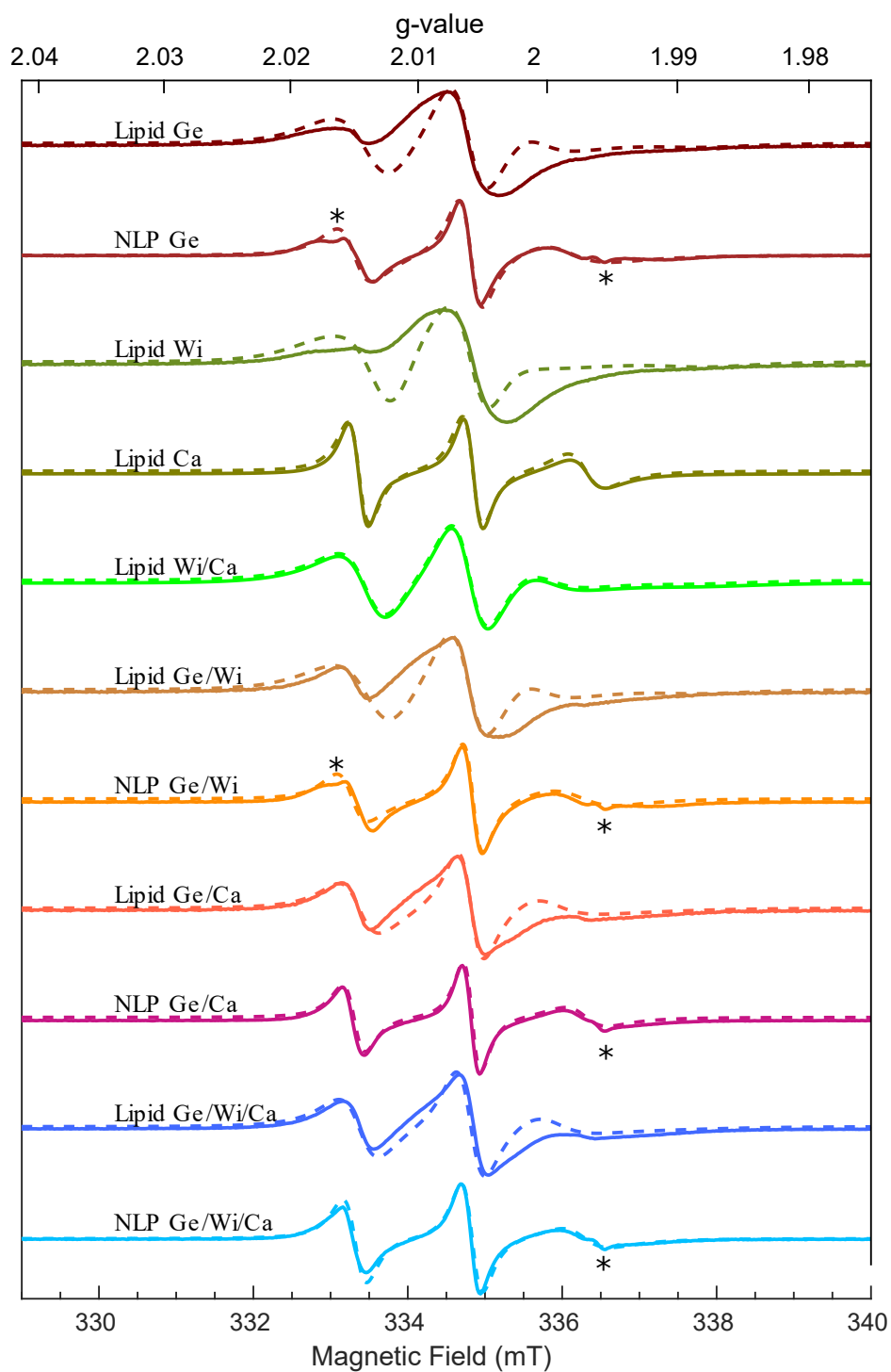
Figure 6.9: X-band EPR spectra of DxPCA dissolved in lipids and loaded to NLP at room temperature, microwave power for lipids is 1 mW and for NLPs is 6.5 mW and modulation for all spectra is 1 G.

Table 6.6: Rotational correlation time (τ_D) of DxPCA dissolved in lipids and loaded to NLPs (All anisotropic magnetic and dynamic parameters in tableA.4).

Composition	τ_D (ns)	g_{ave}	g_{ave} at 80 K	A_{ave} (MHz)	A_{ave} (MHz) at 80 K	Linewidth (mT)
Gelucire	4.7	2.0058	2.0058	39.6	40.7	0.200
NLP-Ge	2.5	2.0057	2.0057	41.3	41.3	0.005
Witepsol	5.0	2.0058	2.0058	39.1	41.0	0.100
Capryol	1.4	2.0056	2.0057	41.6	41.5	0.200
Witepsol/Capryol	3.2	2.0057	2.0057	40.3	41.3	0.200
Gelucire/Witepsol	4.7	2.0058	2.0058	39.3	39.3	0.200
NLP-Ge/Wi	2.3	2.0056	2.0056	42.2	42.0	0.010
Gelucire/Capryol	3.0	2.0057	2.0057	40.3	41.3	0.010
NLP-Ge/Ca	1.8	2.0057	2.0056	42.6	42.4	0.050
Gelucire/Witepsol/Capryol	3.5	2.0057	2.0057	41.0	41.2	0.100
NLP-Ge/Wi/Ca	2.2	2.0057	2.0056	42.0	42.0	0.100

A first estimate of the correlation times involved can be obtained by comparing the spectra of DxPCA in the lipid samples with figure 3.6 displaying the spectra dependence on the rotational correlation time. The spectrum of DxPCA in Capryol shows the most narrow lines and thus the fastest motion with a characteristic τ_{corr} of about 1 ns according to figure 3.6.

The spectra of DxPCA in the Gelucire/Capryol and Gelucire/Witepsol/Capryol NLP show similar spectra corresponding to τ_{corr} of around 2.5 ns. DxPCA in the NLP made of Gelucire and Gelucire/Witepsol correspond to slower motion than those for the Gelucire/Capryol and Gelucire/Witepsol/Capryol NLP but with a τ_{corr} clearly less than 5 ns. The spectra for DxPCA in the bulk lipid mixtures of Gelucire/Capryol and Gelucire/Witepsol/Capryol are again very similar to each other but it is difficult to estimate a τ_{corr} from their shape. This is also true for the bulk lipid samples.

As we mentioned earlier, the spectra of DxPCA in lipids and NLPs indicate a slow-motion regime. In this regime anisotropy of the motion has more severe consequences than for fast motion and we had to include anisotropic rotational correlation times to properly simulate the spectra. Besides broadening by slow motion additional residual broadening, e.g. from hfs, was represented by a Gaussian linewidth except for DxPCA in Capryol, which required a Lorentzian linewidth function. The magnetic parameters reported in table 6.6 agree in all cases well with those determined by low-temperature EPR. Further we discuss only the effective average rotational correlation time τ_D reported in table 6.6 and determined by $3\tau_D^{-1} = \tau_1^{-1} + \tau_2^{-1} + \tau_3^{-1}$ from the principal values τ_i given in table A.4.

The tumbling of DxPCA dissolved in the liquid lipid Capryol is slower ($\tau_D \approx 1.4$ ns) than in water ($\tau_{corr} \approx 80$ ps), but significantly faster than in the solid lipids (τ_D of Gelucire is 4.7 ns and Witepsol is 5 ns). The τ_D of DxPCA in the solid Gelucire/Witepsol mixture is similar to that seen in the individual lipids. DxPCA in the bulk lipid mixtures containing Capryol are not tumbling as fast as for pure Capryol (τ_D for lipid-Ge/Ca is 3 ns and for lipid-Ge/Wi/Ca 3.5 ns),

however much faster than in all solid lipids. For the NLP cases τ_D is fastest for NLP-Ge/Ca ($\tau_D \approx 1.8$ ns) and the magnetic parameters fitting to roughly to Capryol. Interestingly, the τ_D of DxPCA in NLP-Ge/Wi is closely similar τ_D to NLP-Ge/Wi/Ca, and is faster tumbling than bulk lipids. As a general trend, we find much higher mobility of DxPCA in NLPs than in the bulk lipids. However, the magnetic parameters and the correlation time clearly show that DxPCA is embedded in the NLP.

6.1.3 Investigation of spin probe environments in NLPs by relaxation time

The spin-lattice relaxation time (T_1) is a powerful indicator [144, 146] of differences in the environment of a spin probe, which reveals important properties of the micro-environment and we complement by T_1 experiments the information on polarity/proticity experienced by the spin probes and on their mobility gathered previously. Since the spin-lattice relaxation time can depend on the orientation of the molecule with respect to the direction of the static field [152] the observed relaxation time can strongly dependent upon the acquisition field position within the spectrum [172] and is reported in (Table A.5) for the canonical orientations of PCA, TEMPO DxPCA.

Here we compare T_1 values obtained from time traces of inversion recovery measurements at 80 K at the g_y field position of all three spin probes, which are reported in table 6.7. Additionally, the relaxation times of DxPCA in water and toluene, PCA in water and TEMPO in toluene also are reported in this table. The experimental data analyzed by a bi-exponential fit $f(t) = 1 - 2(A_1 e^{t/\tau_1} + A_2 e^{t/\tau_2})$ are shown in appendix A. The two time constants τ_1 and τ_2 have different interpretations. The shorter τ_2 is due to the spectral diffusion (see Section 3.3.3) and is not considered here. In contrast, the longer τ_1 can be identified with the spin-lattice relaxation time T_1 and will be discussed in the following for the three different spin probes.

PCA in lipids and NLPs

Inspection of the column with the fit results for PCA in the lipids and NLPs in table 6.7 shows that PCA dissolved in Gelucire has the shortest and in Witepsol the longest τ_1, i.e. T_1. The T_1 of PCA dissolved in the Witepsol/Capryol mixture and the Gelucire/Capryol mixture are rather close to the relaxation time for the Capryol sample while the T_1 of PCA dissolved in the Gelucire/Witepsol mixture is between the T_1 of both lipids, but closer to the T_1 of Witepsol. The T_1 of PCA dissolved in the Gelucire/Witepsol/Capryol mixture is comparable to that in the Gelucire/Capryol mixture, thus again close to that of the Capryol sample. However, it should be noted that the T_1 in the Gelucire/Capryol mixture is longer than in both individual lipids. Taken together, the relaxation data for PCA point towards a Capryol dominated PCA environment in the lipid mixtures except Ge/Wi, where Witepsol appears dominant. A longer T_1 is found in all NLP samples than for the corresponding lipids and mixtures, and the T_1 of all samples are quite similar in contrast to the different lipids and mixtures. Thus, even though the relaxation time is far shorter than in pure water, the aqueous surrounding of the NLP seems to play an important role for the spin lattice relaxation of the spin probes embedded

into NLP.

TEMPO in lipids and NLPs

The TEMPO T_1 is reversed compared to PCA with respect to the Gelucire and the Capryol samples with a faster T_1 in Capryol while in the Witepsol it is the slowest as for PCA. The two lipid mixtures Gelucire/Capryol and Gelucire/Witepsol show very similar TEMPO T_1 with again the surprising finding that the T_1 in the Gelucire/Capryol is much longer than for the individual lipids. Again similar to PCA, a T_1 close to the value of the Witepsol sample is found for the Witepsol/Capryol mixture. However, in clear contrast to the PCA case no consistent trend is found when moving from the bulk lipids to NLPs. While NLP-Ge show a longer T_1 than in bulk Gelucire, as seen for PCA in all NLP, the T_1 of NLP-Ge/Wi and NLP-Ge/Wi/Ca remain virtually unaltered from the bulk lipids. For NLP-Ge/Ca even s significant decrease of T_1 is found compared to the bulk.

DxPCA in lipids and NLPs

The findings for the T_1 of DxPCA in the different lipid samples again have little common with those for the other two spin probes. Here, the shortest T_1 for the bulk lipids is found for Gelucire, but with a value that is almost identical to that for Witepsol, which showed the significantly longest T_1 for PCA and TEMPO. Capryol, which leads to a fast T_1 for PCA and TEMPO yields the slowest T_1 for DxPCA.

Similar to PCA and TEMPO, the DxPCA T_1 is close to that for Capryol in the Witepsol/Capryol mixture. However, while PCA and TEMPO showed only in the Gelucire/Capryol mixture a T_1 longer than for the individual lipids this is the case for DxPCA all lipid mixtures except Witepsol/Capryol. When comparing the NLP samples with the corresponding bulk lipids a prolongation of T_1 is only found for NLP-Ge. The three other NLP samples give rise to virtually identical T_1 as the bulk lipids, respectively. However as for PCA, the T_1 of DxPCA in all NLP are very similar. Unfortunately, since these values are virtually identical to those of the bulk lipids except for Gelucire it is difficult to assign these similar T_1 to an influence of the surrounding aqueous except for NLP-Ge. The different results seen for the three different spin probes when comparing the T_1 data for bulk lipids and NLPs have to be seen in light of their different hydro- vs. lipophilicity. The hydrophilic/liphophilic PCA can be forced upon NLP fabrication towards the particle surface, thus strongly experiencing the aqueous surrounding of the NLP. The amphiphilic TEMPO can respond differently to the NLP fabrication dependent on the specific lipid composition, such that a T_1 prolongation can be observed by increased exposure to the aqueous phase as for PCA, but also unchanged T_1 if stay unaltered in the lipid core of the NLP. However, the T_1 reduction for TEMPO in NLP-Ge/Ca can not be explained. Apparently, the lipophilic/hydrophobic DxPCA remains in the lipidic NLP core and experiences an environment giving rise to T_1 as in the corresponding bulk lipids except for NLP-Ge in which also the lipophilic DxPCA seems to be pushed towards the surface.

Table 6.7: Spin-lattice relaxation time T_1 of spin probes (DxPCA, PCA and TEMPO) dissolved in lipids and loaded to NLPs have been obtained by bi-exponential fitting of inversion recovery time traces at field positions g_y.

$$f(t) = 1 - 2(A_1 e^{(-t/\tau_1)} + A_2 e^{(-t/\tau_2)})$$

Composition	A_1	τ_1 (us)	A_2	τ_2 (us)	A_1	τ_1 (us)	A_2	τ_2 (us)	A_1	τ_1 (us)	A_2	τ_2 (us)
	PCA				TEMPO				DxPCA			
Gelucire	0.51	84	0.49	9	0.56	74	0.44	8	0.58	154	0.42	28
NLP-Ge	0.67	167	0.33	28	0.63	124	0.37	18	0.66	240	0.34	31
Witepsol	0.59	183	0.41	25	0.57	109	0.43	17	0.51	157	0.49	18
Capryol	0.42	120	0.58	23	0.48	56	0.52	8	0.59	181	0.41	24
Witepsol/Capryol	0.52	128	0.48	15	0.58	105	0.42	14	0.59	176	0.41	23
Gelucire/Witepsol	0.50	141	0.50	19	0.62	170	0.38	21	0.69	218	0.31	34
NLP-Ge/Wi	0.65	183	0.35	27	0.63	176	0.37	22	0.62	218	0.38	27
Gelucire/Capryol	0.53	133	0.47	18	0.64	170	0.38	23	0.69	217	0.31	33
NLP-Ge/Ca	0.64	171	0.36	27	0.60	122	0.40	17	0.64	230	0.36	29
Gelucire/Witepsol/Capryol	0.52	130	0.48	17	0.59	122	0.41	17	0.63	210	0.37	26
NLP-Ge/Wi/Ca	0.62	175	0.38	26	0.57	125	0.43	17	0.63	230	0.37	28
Water	0.67	450	0.33	35	-	-	-	-	0.66	420	0.34	40
Toluene	-	-	-	-	0.63	190	0.37	17	0.70	240	0.30	41

6.2 Spin probe distribution in nanostructured lipid particles

In this section we summarize the EPR results on the three investigated spin probes in the bulk lipid and NLP samples. We relate the findings derived from low temperature measurements on the g_x and A_z parameters and the T_1 values with the rotational correlation time τ_{corr} and the average magnetic parameters g_{ave} and A_{ave} extracted from room temperature measurements.

PCA

The magnetic parameters g_x and A_z and the spin-lattice relaxation time T_1 of PCA show for all NLP samples a consistent change when changing from the bulk lipid to NLP samples. The g_x value decreases in all NLP samples while A_z increases concomitantly (Table 6.1) as observed for PCA in different solvents (Table A.1) when increasing the polarity/proticity of the solvent. Quantitatively, the parameters show only a small increase in proticity and an overall lipidic environment. The T_1 data corroborate this finding with a moderate increase of T_1 in the NLP samples compared to the bulk lipid samples, but still much shorter T_1 than in aqueous solution. Thus, the low-temperature experiments lead to the conclusion PCA stays in the NLP samples in an lipidic environment, but clearly experiences an influence of the aqueous phase surrounding the NLP. When moving to the room temperature experiments we see a quite different picture. Again both independent parameters sets, i.e. on one hand the average magnetic parameters g_{ave} and A_{ave} and on the other the rotational correlation time τ_{corr} provide a common trend, however contradicting the findings from the low-temperature experiments when comparing bulk lipid with NLP samples. The g_{ave} and A_{ave} parameters for the bulk lipid samples are in good agreement with those seen in the low-temperature experiments and the τ_{corr} are consistent with slow tumbling in the highly viscous lipid preparations. This is very different for the NLP samples were only a small decrease of g_{ave} and weak increase of A_{ave} was seen in the low-temperature experiments on the NLP samples. The g_{ave} and A_{ave} parameters for PCA in all NLP samples are almost identical to those found for PCA in aqueous solution and the τ_{corr} values also show fast tumbling as for free PCA in water. Thus, the room temperature lead to the conclusion PCA is expelled from the NLP into the aqueous phase, which contradicts the finding from the low temperature experiments. Unfortunately, we see no possibility to reconcile these contradicting observations. Apparently, the highly polar PCA probe is an unsuitable reporter for the lipidic NLP drug carriers and we have to exclude the PCA in NLPs data from further analysis.

TEMPO

Berner *et. al.* [193] showed that TEMPO, as an amphiphilic nitroxide, is soluble in water and lipid mixtures. We could reproduce this finding and made use of this fact for investigating the loading of TEMPO in NLP. The magnetic parameters g_x and A_z of TEMPO in the bulk lipids and NLPs obtained at low temperature indicate that two different interaction scenarios coexist for TEMPO with the lipids similar to the case of the solvent ethanol. Thereby, one part

corresponds to TEMPO in an apolar/aprotic micro-environment and the other represents an apolar fraction but with a hydrogen bond. In all solid lipid preparations the majority represents the apolar/aprotic part, while for the liquid lipid Capryol the apolar/protic part is dominant, and the lipid mixtures containing Capryol show variable fractions with large apolar/aprotic fraction in the binary mixtures and larger apolar/protic fraction in the ternary Ge/Wi/Ca mixture. The NLPs except NLP-Ge/Wi/Ca show an increase in the apolar/protic fraction compared to the bulk lipids. The ternary Ge/Wi/Ca lipid mixture with a slight predominance fraction of the polar/aprotic TEMPO environment in the bulk shows an inversion of this ratio in the NLP. Besides the ratio of the two different environments also the absolute TEMPO g_x and A_z values are interesting to compare. Witepsol gives rise to the largest g_x/smallest A_z, Gelucire to intermediate values, and Capryol to the smallest g_x/largest A_z. The Wi/Ca and the Ge/Ca mixtures show g_x and A_z very similar to Capryol while the Ge/Wi mixture shows an average of the individual lipids as does the ternary Ge/Wi/Ca mixture. This can be interpreted that TEMPO favors in the mixtures more the solid lipids than the liquid lipid Capryol. A similar trend as for g_x and A_z can be observed when looking at the T_1 relaxation times also obtained at low temperatures. Capryol leads there to the shortest T_1, Gelucire to an intermediate value, and Witepsol to the longest T_1. In none of the lipid mixtures the short T_1 caused by Capryol is seen. Instead all lipid mixtures show a T_1 larger than any of the individual lipids, with the shortest value in the ternary mixture. It remains unclear how these T_1 can be slower than those of the individual lipids arises by mixing. No common change is observed when comparing the NLPs and the respective lipid mixtures. Two NLP samples, NLP-Ge/Wi and NLP-Ge/Wi/Ca show virtually unchanged T_1, while the NLP-Ge sample shows a strong increase of T_1 while in NLP-Ge/Ca a similar decrease is found. The average magnetic parameters g_{ave} and A_{ave} and the rotational correlation time τ_{corr} extracted from the room temperature measurements report for the bulk lipids a highly viscous lipidic environment of TEMPO, with the g_{ave} and A_{ave} values being in agreement with the mean values of the two protonation states in the lipidic environment seen in the low-temperature experiments. The TEMPO spectra for the NLP samples clearly show two very different TEMPO environments. One environment is of lipidic character, the other is an aqueous environment. The fraction of the aqueous environment is largest for the NLP-Ge (35%), followed by NLP-Ge/Wi (20%), i.e. the NLP made of exclusively solid lipids, while the two NLP containing the liquid lipid Capryol, NLP-Ge/Ca and NLP-Ge/Wi/Ca show only small fractions (8% and 6%, respectively, see table 6.5). As in the case of PCA, no indication of TEMPO in an aqueous environment has been detected in the low-temperature data. However, important differences arise for the two probes. The room temperature experiments showed for PCA exclusively an aqueous environment, while the low-temperature data only show a lipidic environment. In constrast, for TEMPO both an aqueous and a lipidic environment is seen in the room temperature experiments. Furthermore, the absence of a signal from TEMPO in an aqueous environment in the low-temperature data can be reconciled with the observation at room temperature. An EPR signal for TEMPO could not be detected in frozen aqueous solution, which is the reason that no reference values for the g and A matrices nor for T_1 of TEMPO at low temperatures have been quoted in the corresponding (section 5.1.1). This argument is inexistent for the

case of PCA, which can be well observed at low temperatures as evidenced by the spectrum reported in figure 5.1. Therefore, we conclude that the EPR data discussed above give relevant information on the incorporation of TEMPO into NLP.

DxPCA

The magnetic parameters g_x and A_z of DxPCA in the bulk lipid and NLP samples obtained at W-band frequency and 80 K (Fig. 6.6, Table 6.3) show a homogeneous DxPCA environment in the two solid lipids Gelucire and Witepsol and their mixture reflecting an apolar/aprotic environment similar to toluene. For the liquid lipid Capryol these parameters indicate again a lipidic environment, however with likely two different hydrogen bonding scenarios, i.e. once the absence of hydrogen bonds and magnetic parameters as in the solid lipids and once presence of a hydrogen bond with g_x and A_z intermediate between the apolar/aprotic and the polar/protic extremes. Such a two component situation is also seen for all lipid mixtures containing Capryol and all NLP samples. Thereby, the parameters for the apolar/aprotic situation are virtually identical for all samples. The second parameter sets differ between the bulk lipid mixtures as well as all NLP samples with smaller g_x and a larger A_z for the NLPs compared to the respective bulk lipids. However, in all cases the magnetic parameters represent environments clearly distinct from water. This finding is corroborated by the T_1 measurements also performed at 80 K. All T_1 values are close to the values seen for DxPCA in toluene and about a factor of two or more faster than in water (see Table 5.5). Since the g_x and A_z parameters of DxPCA in the bulk mixtures of the solid lipids with Capryol are very similar to the values occurring for pure Capryol, this could lead to the conclusion of a partitioning of DxPCA in the NLP into a Capryol fraction. However, the T_1 contradict this interpretation. DxPCA shows the longest T_1 of all bulk lipids in Capryol, but even longer T_1 in all lipid mixtures and NLP arguing against a Capryol phase in the mixtures and NLP. It is important to note that for DxPCA loaded to NLP-Ge and NLP-Ge/Wi a second magnetic parameter set corresponding to a more polar/protic environment arises in addition to the apolar/aprotic environment present in the bulk lipids. This second more polar/protic environment reflects the presence of the aqueous phase surrounding of these NLPs. Thus, the fraction of DxPCA with unmodified magnetic parameters corresponding to an apolar/aprotic environment likely resides in the core of the NLP unaffected by the water around the NLP while the second fraction is in an outer shell of the NLP with properties modified by the aqueous phase. The interpretation of the magnetic parameters seen for the two Capryol containing NLPs is more difficult for several reasons. i) Two distinct apolar environments with likely different proticity are already seen in the pure liquid lipid Capryol, ii) the magnetic parameters observed in Capryol containing bulk lipids are very similar to the values seen for the pure Capryol, and iii) the second parameter sets representing a apolar/protic environment in the Capryol containing samples are very similar to those arising for the additional more polar/protic environment in the NLP-Ge and NLP-Ge/Wi samples. The DxPCA fraction in the NLP-Ge/Ca and NLP-Ge/Wi/Ca samples with g_x and A_z corresponding to an apolar/aprotic environment again clearly represents spin probes in the core of the NLPs unaffected by the aqueous phase. The second parameter

sets with slightly smaller g_x and slightly larger A_z than in the bulk samples likely represent a superposition of scenarios impossible to disentangle. A plausible interpretation is that it contains contributions from i) a fraction without hydrogen bond to lipids, but experiencing an influence from the aqueous surrounding, as in the case of NLP-Ge and NLP-Ge/Wi, i.e. from a surface layer of the NLP, ii) a fraction from an apolar environment with hydrogen bond to lipids, as in the cases the Capryol containing samples, i.e. from the core of the NLP, and iii) a fraction with hydrogen bond to lipids experiencing an influence from the aqueous surrounding, i.e. again from a surface layer of the NLP. The two components stemming from a NLP surface then cause the decrease of g_x and increase of A_z compared to the bulk lipids. Further information can be deduced from the DxPCA mobility in the lipid samples. The DxPCA mobility studies have been performed, in contrast to the other spin probes, not by W-band cw-EPR, but by X-band cw-EPR at room temperature, in response to the much slower rotational mobility of the much larger DxPCA molecule. Only a very small fraction ($\approx$ 2%) of DxPCA released to water was observed for the NLP samples, clearly identified by the rotational correlation time and the average magnetic parameters. This is in agreement with the results from low-temperature EPR where no indication of DxPCA in an aqueous environment was found for any sample. Furthermore, the rather good agreement between the average values g_{ave} and g_{ave} obtained by X-band EPR at room temperature for the vast majority species ($\approx$ 98%) with those from low-temperature W-band EPR indicate that both techniques report on DxPCA under identical environmental conditions, in contrast to the situation for PCA. The obtained rotational correlation times reported in table 6.6 clearly show a faster tumbling of DxPCA in Capryol than in all solid lipids, mixed lipids and in the NLPs, but significantly slower than in pure water. The slower tumbling in the Capryol containing mixtures and NLPs than in pure Capryol corroborates the conclusion from the T_1 data that no phase separation of DxPCA into a Capryol-only environment occurs in the mixed bulk lipids and NLPs even though the magnetic parameters would be consistent with this fact. However, a certain softening of the lipid mixtures by the liquid lipid Capryol might be the origin for the mobility increase compared to the solid lipids and mixtures without Capryol. A possible interpretation of the increase in DxPCA mobility in the NLP samples compared to the respective bulk lipids can be put forward when considering the explanation of the obtained magnetic parameters in the NLP. There, it was argued that an important fraction of the DxPCA signal stems from a NLP surface shell with properties modified by the aqueous environment. Taken together, the EPR studies presented so far lead to the conclusion that DxPCA is virtually completely loaded to NLPs in aqueous solution with a significant contribution of DxPCA in the core and outer shell of the NLP.

Summary

In summary, polarity and dynamics investigations of DxPCA by dual-frequency EPR shows that the DxPCA (logP = 1.89 [166]) is located at the core and outer shell of NLPs. TEMPO has a similar partition coefficient as DxPCA, both model drugs behave differently. DxPCA does not favor being buried in the lipid components, and it is associated within an micro-environment

of intermediate polarity. On the other hand, TEMPO does not like to stay in one environment; therefore, it is located in both lipid and aqueous environment but with different ratios. PCA does not like the lipid micro-environment and, during the preparation, it is transferred from the lipid compartment to the aqueous solution of NLPs.

6.3   Drug/NLPs association model

In the previous section, the magnetic and the dynamics parameters were investigated (see Section 6.1), and based on this information, spin probes location in NLPs was revealed (see Section 6.2). In this section, we comparatively utilized the aforementioned measurements to investigation how lipids associate with each other in mixed lipids and NLPs and then describe how each spinprobes are associated with them. A distinction between different lipids, with which the spin probes are surrounded in NLPs is not possible to be made only based on the polarity and the dynamics information. Therefore, the spin-lattice relaxation time T_1 was utilized as a complementary tool to study the surrounding environment of the spin probes in lipids and NLPs. Then, the information about the surrounding environments of a spin probe enables us to find nearby lipids to spinprobes. Thus, the structure of NLPs will be defined based on a comparative study of magnetic parameters, mobility, and relaxation time. The interaction of a spin probe with lipids and NLPs based on the different perspective was described previously (see Section 6.1), and the summary of polarity, mobility and relaxation time study of three spin probes dissolved in lipids and loaded to NLPs are summarized in table 6.8.

6.3.1   Lipids

PCA, TEMPO, and DxPCA are hydrophilic, amphiphilic, and hydrophobic probes, respectively. All spin probes were scattered in solid lipid Gelucire and Witepsol and liquid lipid Capryol. The rt measurement showed no aggregation of the spin probes in Capryol, unlike the ones in two solid lipids.
The weight of Capryol in this blend stays the same in the Gelucire/Capryol and the Witepsol/-Capryol mixtures. The weight of Witepsol is increased from 25% to 33%, and the weight of Gelucire is decreased from 75% to 55% in Gelucire/Witepsol/Capryol mixture. In this mixture, the solid lipids are the major and Capryol is the minor compartment. Thereby, studying how lipids arrange along with each other in NLPs is a key point to understand the drugs/NLP association model, as it will be investigated in this part.

Table 6.8: Comparative study of spin probes dissolved in lipids and loaded to NLPs.

Spin probes	Composition	Polarity	Mobility	Spin-lattice relaxation time
PCA				
	Gelucire	apolar/aprotic environment	slow-motion regime	an apolar environment
	Witepsol	apolar/aprotic environment	slow-motion regime	an apolar environment
	Capryol	more protic environment than solid lipids	fastest one	represent apolar/aprotic environment
	Witepsol/Capryol	apolar/aprotic environment, intermediate of pure lipids	intermediate of Wi and Ca	corresponds Capryol
	Gelucire/Witepsol	apolar/aprotic environment	corresponds Gelucire	approximately corresponds Witepsol
	Gelucire/Capryol	apolar/aprotic environment, corresponds Gelucire	intermediate of Ge and Ca	approximately corresponds Capryol
	Gelucire/Witepsol/Capryol	apolar/aprotic environment	corresponds Ge/Ca	similar to the lipid-Ge/Wi and lipid-Ge/Ca
TEMPO				
	Gelucire	almost an apolar/aprotic environment	slow-motion regime	an apolar environment
	NLP-Ge	the majority in an apolar/aprotic with a minority in a protic environment	faster than the bulk	an apolar environment
	Witepsol	almost an apolar/aprotic environment	slow-motion regime	an apolar environment
	Capryol	the majority in a protic with a minority in an apolar/aprotic environment	fastest one	an apolar environment
	Witepsol/Capryol	the majority in an apolar/aprotic with a minority in a protic environment, indicates Wi	intermediate of Wi and Ca	corresponds Witepsol
	Gelucire/Witepsol	almost an apolar/aprotic environment	slow-motion regime	an apolar environment and different from pure lipids
	NLP-Ge/Wi	the majority in a protic with a minority in an apolar/aprotic environment	similar to the bulk	corresponds Gelucire/Witepsol
	Gelucire/Capryol	the majority in an apolar/aprotic with a minority in a protic environment, indicates Ge	intermediate of Wi and Ca	an apolar environment and different from pure lipids
	NLP-Ge/Ca	the majority in a protic with a minority in an apolar/aprotic environment	similar to the bulk	an apolar environment and different from pure lipids
	Gelucire/Witepsol/Capryol	the majority in a protic with a minority in an apolar/aprotic environment	similar to lipid-Ge/Wi	an apolar environment and different from pure lipids
	NLP-Ge/Wi/Ca	the majority in a polar/aprotic with a minority in a protic environment	similar to the bulk	corresponds NLP-Ge/Ca
DxPCA				
	Gelucire	an apolar/aprotic environment	slow-motion regime	an apolar environment
	NLP Ge	an apolar/aprotic and a protic environments	faster than bulk lipid	an apolar environment
	Witepsol	an apolar/aprotic environment	slow-motion regime	an apolar environment
	Capryol	the majority in a protic with a minority in an apolar/aprotic environment	fastest one	an apolar environment
	Witepsol/Capryol	the majority in a protic with a minority in an apolar/aprotic environment	Intermediate of Wi and Ca	corresponds Capryol
	Gelucire/Witepsol	an apolar/aprotic environment	slow-motion regime	a new environment instead of pure lipids
	NLP-Ge/Wi	the majority in a protic with a minority in an apolar/aprotic environment	faster than the bulk	similar to the bulk lipid
	Gelucire/Capryol	an apolar/aprotic and a protic environments	intermediate of Ge and Ca	a new environment instead of pure lipids, similar to lipid-Ge/Wi
	NLP-Ge/Ca	the majority in a protic with a minority in an apolar/aprotic environment	faster than the bulk	similar to the bulk lipid
	Gelucire/Witepsol/Capryol	the majority in an apolar/aprotic with a minority in a protic environment	Intermediate of solid and liquid lipid	a new environment instead of pure lipids, similar to the lipid-Ge/Wi and -Ge/Ca
	NLP-Ge/Wi/Ca	an apolar/aprotic and a protic environments	faster than the bulk	similar to the bulk lipid

Witepsol/Capryol mixture

The comparison of the magnetic parameters of PCA in mixed lipid Wi/Ca with solid lipid Wi and liquid lipid Ca reveals an apolar/aprotic environment surrounding PCA in Wi/Ca mixture, which represents the intermediate environment of both pure lipids (Table 6.1). The mobility (Table 6.4) and the relaxation time (Table 6.7) of PCA dissolved in the Witepsol/Capryol mixture have similar behavior as magnetic parameters, and reveal intermediate mobility and also relaxation time. As a summary, PCA interacts with both lipids, but the measurement results lead us to conclude, PCA has a weaker interaction with Capryol as a more protic environment than Witepsol.

The magnetic parameters of TEMPO are mostly represented as an apolar regime in the Wil/Ca mixture (Table 6.2). The τ_{corr} stands somewhere in the middle of two lipids without showing any aggregation (Table 6.5). TEMPO has very fast relaxation time in Capryol but slower in Witepsol and the Witepsol/Capryol mixture and the T_1 of TEMPO dissolved in the Wi/Ca mixture was the same as in Witepsol. Thus, it can be concluded that the TEMPO is located outside of Capryol.

The polarity (Table 6.3), the mobility (Table 6.6) and the relaxation time (Table 6.7) of DxPCA dissolved in the Witepsol/Capryol mixture is mainly represent of Capryol micro-environment. Comparison of the spin probes dissolved in the Witepsol/Capryol mixture and properties of solid (Wi) and liquid (Ca) lipids lead us to the conclusion that it does not consist of two distinct micro-environments but rather Capryol is evenly distributed in lipid matrix of Witepsol.

Gelucire/Witepsol mixture

The magnetic parameters of PCA dissolved in the Gelucire/Witepsol mixture (Table 6.1) illustrate that it is located in an apolar regime, in the both solid lipids, and the mobility of PCA in Ge/Wi mostly represents Gelucire (Table 6.4). The T_1 has a value between the ones in two lipids (Table 6.7) but it represents more Witepsol than Gelucire. We can conclude, PCA is located on both two pure lipids in the Gelucire/Witepsol mixture.

The magnetic parameters of TEMPO dissolved in the Gelucire/Witepsol mixture demonstrate almost an apolar/aprotic environment (Table 6.2). The comparison between the magnetic parameters of TEMPO dissolved in Gelucire, Witepsol, and the Gelucire/Witepsol mixture, proves that TEMPO rather prefers to be surrounded by an aprotic environment. The mobility of TEMPO dissolved in the Gelucire/Witepsol mixture is also comparable to the one in Witepsol (Table 6.5). The T_1 value of the TEMPO dissolved in the Gelucire/Witepsol mixture is not similar to any relaxation time in pure solid lipids. The polar chains of lipids arrange towards each other and a new lipids configuration in the border of two solid lipids might influence the relaxation time. Thus, TEMPO is located in both pure solid lipids but it mainly seems to be more in the Witepsol environment.

DxPCA shows similar behavior as PCA in the Gelucire/Witepsol mixture. The similarity of the magnetic and dynamic parameters of DxPCA in both solid lipids (see Table 6.3, 6.6) made it difficult to characterize whether or not DxPCA associated with one or the other pure lipids in

the Gelucire/Witepsol mixture. The relaxation time indicates a new environment for DxPCA, and also the T_1 of DxPCA dissolved in the Gelucire/Witepsol mixture is different from the ones for each pure lipid (Table 6.7). Therefore, it can be concluded that DxPCA is located in both lipids but in a new arrangement for lipids which influences the relaxation time of DxPCA dissolved in the Gelucire/Witepsol mixture. The comparative results of spinprobes in Ge/Wi indicate that two distinguished and separated micro-environments are made of them when Gelucire and Witepsol are mixed.

Gelucire/Capryol mixture

The magnetic parameters of PCA dissolved in the Gelucire/Capryol mixture indicate that Gelucire is the surrounding environment of PCA (Table 6.1). The τ_{corr} value of PCA dissolved in the Gelucire/Capryol mixture indicates intermediate mobility (Table 6.4). But, the T_1 of PCA dissolved in the Gelucire/Capryol mixture is the same as the one for PCA in Capryol (Table 6.7). Therefore, based on the configuration of polar branches of Gelucire and Capryol along with each other in the mixture, one can conclude that PCA is mainly located in Gelucire and has interaction with Capryol.

The magnetic parameters of TEMPO dissolved in the Gelucire/Capryol mixture reveal a mainly aprotic regime similar to the one dissolved in Gelucire (Table 6.2). The mobility of TEMPO is in an intermediate range of Gelucire and Capryol (Table 6.5). The relaxation time of TEMPO dissolved in the Gelucire/Capryol mixture is higher than both individual lipids (Table 6.7). This shows that TEMPO is located in Gelucire and near to Capryol with an influence from it. According to the relaxation time of PCA and TEMPO in the Gelucire/Capryol mixture, it can be said that the interaction of two lipids (Gelucire and Capryol) is independent of the dissolved spin probes.

The magnetic parameters of DxPCA dissolved in the Gelucire/Capryol mixture reveal two micro-environments (Table 6.3). One micro-environment is an aprotic one very similar to Gelucire, and another one is a more protic micro-environment similar to Capryol. The mobility of DxPCA dissolved in the Gelucire/Capryol mixture is more similar to Gelucire (Table 6.6). The relaxation time does not show any sign of both two pure lipids (Table 6.7). The hydroxyl group of Capryol and Carboxyl group of Gelucire make a new arrangement along with each other which leads to a new environment for DxPCA and changes the relaxation time.

According to the results of spin probes incorporated into the Gelucire/Capryol mixture, the association of Capryol with Gelucire is the same as Witepsol and Capryol. Then, Capryol is spread inside the imperfect crystallization lipid matrix of Gelucire.

Gelucire/Witepsol/Capryol mixture

Evident from the data obtained from the models of lipid mixing the following conclusions can be drawn. The mixture of two solid lipids makes two separate phases. However, the mixing of a solid lipid and a liquid lipid results in only one phase.

The magnetic parameters of PCA dissolved in the Gelucire/Witepsol/Capryol mixture in-

dicate an apolar/aprotic regime. Both solid lipids of Gelucire and Witepsol are a possible candidate for the micro-environment of PCA (Table 6.1). The mobility of PCA dissolved in the Gelucire/Witepsol/Capryol mixture is similar to PCA dissolved in the Gelucire/Capryol mixture (Table 6.4). Likewise, is the relaxation time of PCA dissolved in the Gelucire/Witepsol/Capryol mixture introduced PCA dissolved in the Gelucire/Capryol mixture (Table 6.7). Therefore, it can be said that PCA is associated with Gelucire/Capryol.

According to the polarity investigations, TEMPO dissolved in the Gelucire/Witepsol/Capryol mixture associates with two environments, an apolar and a more polar media (Table 6.2) in which each medium equally contributes to the impact on proticity values extracted from TEMPO spectra. The mobility of TEMPO dissolved in the Gelucire/Witepsol/Capryol mixture is identical to the one dissolved in Gelucire/Witepsol (Table 6.5). Also, the T_1 represents a value for Witepsol (Table 6.7). According to the experimental parameters and how TEMPO is located in other pure and mixed lipids, one can conclude that TEMPO is situated within the two solid lipids, but not inside Capryol.

The magnetic parameters of DxPCA dissolved in the Gelucire/Witepsol/Capryol mixture again show two micro-environments, an apolar and a polar (Table 6.3). The apolar micro-environment is made by Gelucire or Witepsol or both lipids, and the polar micro-environment by Capryol. The mobility of DxPCA dissolved in the Gelucire/Witepsol/Capryol mixture is faster than the ones dissolved in Gelucire, Witepsol, and the Gelucire/Witepsol mixture (Table 6.6) but not as fast as the one in Capryol. However, the relaxation time is slower than all three individual lipids. The T_1 in this mixture is similar to the T_1 of DxPCA dissolved in the Gelucire/Witepsol and the Gelucire/Capryol mixtures (Table 6.7). Taking how DxPCA is associated with other lipid mixtures into account, as well as all magnetic and dynamic parameters, one can conclude that DxPCA is located in a micro-environment with all the three lipids in the vicinity.

Summary of the spin probe/lipid association model

In summary, the following model of the spin probes association with lipids is represented by the following statements:

- DxPCA has a tendency to associate with Capryol which is in agreement with lipophilic properties of DxPCA and lipophilicity of Capryol.

- PCA and TEMPO are mainly located in solid lipids instead of liquid lipids due to the fatty properties of solid lipids which are less than the ones from Capryol. This makes them a more favorable environment for hydrophilic and amphiphilic spin probes.

- The solid-solid lipid mixtures consist of two distinct phases and it makes the mixed as imperfect crystal. The comparison between the solid-solid and liquid-solid lipid mixtures reveals that the liquid lipid (Capryol) influences the crystallization of solid lipids and localizes in imperfection spots created by solid lipid crystals and changes incorporation model to multiple type model (see Section 2.2.2).

6.3.2 NLPs

The location of a spin probe in lipids is governed by the association tendency of lipids to each other. This also gives insights into the structure of NLPs. In NLPs systems, water is also present in the solution besides the environment created by lipids. On one end of the spectrum, PCA (logP=−1.7) prefers an aqueous solution and moves toward the environment created by water during NLP fabrication. However, TEMPO has an amphiphilic behavior despite its partition coefficient value (logP=1.8) and tends to interact with both lipid and aqueous environments. On the other end, DxPCA is a lipophilic molecule (logP=1.8) which prefers a lipid environment. Another point that needs to be considered is the conformation of lipids along with each other that changes when NLPs are fabricated. This is caused by polar properties of water which enforces the polar groups of lipids to be arranged near water leading to a new arrangement of lipids in NLPs. In the previous section how spinprobes localized in the NLPs was revealed (see Section 6.2), PCA is not loaded in NLPs and located outside of all NLPs, therefore, we eliminated it from further discussion in this section. TEMPO is buried in the core of NLPs without any interaction with water solution surrounding of them. DxPCA is dispersed within the entire lipid matrix of the NLPs, and it partially interacts with water solution surrounding NLPs.

NLP-Gelucire

The spin-lattice relaxation time of TEMPO loaded into NLP-Ge is about two times slower than TEMPO in Gelucire. Additionally, TEMPO was not affected by water according to the polarity investigation (Table 6.2) and the faster relaxation time for TEMPO loaded to NLP-Ge is caused by the new conformation of Gelucire. TEMPO is randomly distributed in the lipid matrix of Gelucire while it is buried in NLP-Ge, as was previously shown. TEMPO was found to be located in the core of NLP-Ge and had a non-aggregated distribution in NLP-Ge. The association model for TEMPO loaded to NLP-Ge is a drug-enriched model within the core, depicted in figure 2.4 III.

Two sets of magnetic parameters for DxPCA were obtained (Table 6.3). DxPCA is partially affected by lipid and aqueous solution according to the polarity investigations (Table 6.3) showing that DxPCA interacts with two micro-environments; lipid-water environment for the outer part and lipid environment for the inner part. DxPCA is dispersed within the entire lipid matrix, depicted in figure 2.4 I and any aggregation was not seen in this state and The relaxation time of DxPCA is shifted to slower values when micro-environment changes from Gelucire to NLP-Ge. Considering the mechanism DxPCA association to NLPs, one can conclude that the spin probe is affected by a new environment. This is also corroborated by the results of polarity and mobility investigations.

NLP-Gelucire/Witepsol

TEMPO dissolved in the Gelucire/Witepsol mixture is located in both lipids as found previously. Magnetic (Table 6.2) and dynamics (Table 6.5) parameters of TEMPO loaded into NLP-Ge/Wi mimic the ones for TEMPO dissolved in the Gelucire/Witepsol mixture. The T_1 is the only parameter of TEMPO into NLP-Ge/Wi which is different from TEMPO dissolved in the Gelucire/Witepsol mixture (Table 6.7). The water changes lipids conformation and when lipids turn into NLPs, TEMPO does not interact with the same surrounding environment as before. Therefore, TEMPO will be located in Witepsol, which is distributed in Gelucire. Witepsol, based on its properties, does not have any interactions with the aqueous solution surrounding the NLP. A fraction of TEMPO, as amphiphilic substance, dissolved in the Gelucire/Witepsol mixture is released from the solid lipids mixtures to water. However, the encapsulated fraction of TEMPO loaded into NLP-Ge/Wi is more than the one in NLP-Ge (Table 6.5). Thus, it can be said that imperfections in the crystallization of NLPs are increased in the presence of Witepsol [116].

The magnetic parameters of DxPCA loaded into NLP-Ge/Wi display a more polar medium than the one dissolved in the Gelucire/Witepsol mixture (Table 6.3). Also, DxPCA has higher mobility than the one in the Gelucire/Witepsol mixture (Table 6.6). The relaxation time of DxPCA loaded into NLP-Ge/Wi is still the same as the Gelucire/Witepsol mixture (Table 6.7). It can be suggested that DxPCA is located in both lipids when dissolved in Gelucire/Witepsol mixture. Gelucire functions as a surfactant in NLPs and Witepsol does not show properties that would enable it to interact with water directly. Thus, one can suggest that Witepsol is distributed as separate islands in Gelucire (see Fig. 2.5). It can also be said that DxPCA is dispersed within the entire lipid matrix of the NLPs. One can conclude that DxPCA is mainly associated with Gelucire in both core and outer shell, also, Witepsol reaches the outer position in the NLP, but it does not interact with the aqueous solution. Additionally, DxPCA in the core is located in both solid lipids.

NLP-Gelucire/Capryol

The magnetic parameters present an association of TEMPO with NLP-Ge/Ca, which is different than the one dissolved in the Gelucire/Capryol mixture (Table 6.2). The magnetic parameters of TEMPO represent a more protic medium in NLP-Ge/Ca than the one dissolved in the Gelucire/Capryol mixture. The carboxyl group of Gelucire and the hydroxyl group of Capryol show a tendency to interact with water. Then, in NLP-Ge/Ca, when this two hydroxyl and carboxyl groups interact with water, therefore TEMPO is positioned in the middle of the resulting conformation. The magnetic parameters of TEMPO loaded to NLP-Ge/Ca represent a rather protic micro-environment. The relaxation time is also faster due to the conformational change of lipids when going from a mixture of lipids to NLP (Table 6.7). Capryol, as a co-surfactant, mainly is localized in the outer shell of the NLP. TEMPO is restricted to two positions, first of which is in the inner part of Gelucire with interactions with Capryol. The second position is in the outer shell of Gelucire and again interacting with Capryol. In NLP-Ge/Ca, TEMPO is

mostly encapsulated within the NLP-Ge/Ca. The presence of Capryol causes a reduction in the release of TEMPO to water solution in NLP systems (Table 6.5).

The magnetic parameters of DxPCA loaded to NLP-Ge/Ca reveal two environments, first an apolar regime which is the same as Gelucire and the second regime indicates a more polar environment than Capryol (Table 6.3). DxPCA is located in an intermediate environment of Gelucire/Capryol in the lipid mixture in which Capryol functions as a co-surfactant and can interact with water. This is the reason why we obtained more protic magnetic parameters for DxPCA loaded to NLP-Ge/Ca compared to DxPCA dissolved in the Gelucire/Capryol mixture. DxPCA has a faster tumbling rate when loaded into NLP-Ge/Ca than when dissolved in the Gelucire/Capryol mixture (Table 6.4). The relaxation time of DxPCA loaded into NLP-Ge/Ca is slower than the one dissolved in the Gelucire/Capryol mixture (Table 6.7). DxPCA shows an interaction with water at the surface of NLP-Ge/Ca, reflected in the slower relaxation time compared to the one dissolved in the lipid mixture. Capryol droplets are located in the outer shell of Gelucire while DxPCA is scattered between Gelucire and Capryol. The location of Capryol modifies the surface of NLP-Ge/Ca and also the DxPCA is dispersed within the entire lipid matrix of which show a good agreement with our results obtained from EPR spectroscopy.

NLP-Gelucire/Witepsol/Capryol

The magnetic parameters of TEMPO loaded into the NLP-Ge/Wi/Ca also show a more polar micro-environment than the one dissolved in the Gelucire/Witepsol/Capryol mixture (Table 6.2). Additionally, the polar parts of Gelucire and Capryol are arranged toward the aqueous solution, based on the surfactant properties of both lipids. Therefore, TEMPO is located in the inner part of NLP and interacts with the apolar parts of lipids. The mobility value of TEMPO loaded to the NLP-Ge/Wi/Ca is between the values for NLP-Ge/Wi and NLP-Ge/Ca (Table 6.5). Also, the relaxation time of TEMPO loaded to NLP-Ge/Wi/Ca is very similar to the one dissolved in the Gelucire/Witepsol/Capryol mixture (Table 6.7). TEMPO loaded into NLP-Ge/Wi/Ca is located in an environment made by both solid lipids and also interacts with both, similar to what was observed for TEMPO dissolved in the Gelucire/Witepsol/Capryol mixture. Capryol is placed in the outer shell of Gelucire while Witepsol is located in the core of Gelucire.

The magnetic parameters of DxPCA loaded to NLP-Ge/Wi/Ca present an apolar and a polar regime with the same ratio (Table 6.3). The polarity of the micro-environment felt by DxPCA in the NLP-Ge/Wi/Ca is increased from the one seen in the Gelucire/Witepsol/Capryol. Capryol is the most favorable medium for DxPCA in all three lipids. From the released DxPCA from the solid lipids, the biggest fraction was seen to migrate from Witepsol to Capryol. The DxPCA loaded to the NLP-Ge/Wi/Ca shows more mobility than the one in the Gelucire/Witepsol/-Capryol mixture and is similar to the one loaded to the NLP-Ge/Ca (Table 6.6). The relaxation time of DxPCA loaded to the NLP-Ge/Wi/Ca also displays a similarity to the one loaded to NLP-Ge/Ca (Table 6.7). No influence of Witepsol on the magnetic and dynamic parameters of DxPCA loaded to the NLP-Ge/Wi/Ca was observed. Capryol is localized in the outer shell of NLPs, and Witepsol is placed in the inner part of NLPs. DxPCA is dispersed within the entire lipid matrix of the NLPs and is associated with both Gelucire and Capryol.

Summery of a drug/NLPs association model

A model of drug/NLP association has a strong dependence on the properties of the drug and its mode of interaction with lipids. The EPR spectroscopy provided unprecedented insights into this. The key points of this section and comparison with spinprobes distribution in NLPs (see Section 6.2) are summarized in the following:

- In mixtures of solid lipids, as a consequence of the high number of glycerides, an imperfect crystal is formed (Fig 2.5 I). Both solid lipids are highly crystallized, and the presence of liquid lipids in the mixture reduces the structure to a lower order crystal and increases the number of imperfections in the lattice of the crystal [111]. Mixing of one or both solid lipids with liquid lipids forms a multiple type model (Fig 2.5 II) because Capryol prevents high order crystallizations [29]. Also, Capryol as co-surfactant modifies the surface of the NLPs, then this enables Capryol to reach the surface of the NLP and interact with water.

- In the NLP-Ge/Wi, Witepsol is distributed in the inner part of Gelucire. In this case, Witepsol does not reach the surface of NLP and does not interact with water. As we represented previously, TEMPO located in the core of NLPs. Also, we found TEMPO has distributed mainly in Wi in Ge/Wi mixture. Furthermore, DxPCA has distributed in both lipids in mixed Ge/Wi, and additionally, DxPCA is dispersed within the entire lipid matrix of NLP-Ge/Wi.

- In the NLP-Ge/Ca, Capryol increases imperfections in the crystallization of Gelucire and gets distributed in the vacant space in the Gelucire crystal structure. Also, Capryol as co-surfactant modifies the surface of the NLPs, then this enables Capryol to reach the surface of the NLP and interact with water. According to experimental results and comparative study, TEMPO likes to locate in Gelucire. Gelucire is the main component of NLP-Ge/Ca and makes core of it. On the other hand, DxPCA locates in liquid lipid Capryol and it is dispersed within the entire lipid matrix of NLP-Ge/Ca.

- The structure of NLP-Ge/Wi/Ca is realized with overlaid sub-structures of the NLP-Ge/Wi and the NLP-Ge/Ca in which Witepsol is located in the core while Capryol is in and active interaction with water.

The information gathered here, along with the incorporation models which have been introduced in the section 2.2.2, allow us to set forth the spinprobes/NLP association model which in turn reveals precious information about the location of a spinprobe when loaded to the NLP, as well as its incorporation model for NLPs. PCA is not located inside NLPs, and then no localization model. TEMPO is buried inside the NLPs and the localization model is drug enrich with in core. DxPCA is dispersed within the entire lipid matrix of the NLPs.

7 Conclusion and outlook

The present investigation has shown that EPR spectroscopy is able to provide evidence for the association of a drug with CMS nanoparticles and NLPs as dermal drug delivery systems. The magnetic parameters, g- and A-matrices determined by EPR, strongly depend on the relative unpaired spin density at the nitrogen and oxygen atoms of the NO group of the spin probe and thereby, report on the polarity and proticity of the surrounding micro-environment of the spin probe. Furthermore, the study of the spin-lattice relaxation time T_1 can provide information on molecular vibrations and, thereby, provide information on the mechanical properties of the environment. Additionally, room temperature measurements are utilized to extract dynamic information, such as the rotational correlation time τ_{corr} of the spin probe and the viscosity of the spin probe's environment.

The CMS nanoparticles consist of a dendritic polyglycerol core with polar properties, which is surrounded by two layers of different chemical composition, a lipophilic inner shell, and a hydrophilic outer shell. The magnetic parameters of DxPCA have been studied in different solvents with a broad distribution in polarity and proticity, i.e., apolar/aprotic, polar/aprotic, apolar/protic, and polar/protic, as reference systems for studying the micro-environment of DxPCA in CMS nanocarriers. Thereby, a linear correlation was shown between the magnetic parameters of DxPCA and the polarity/proticity. It was demonstrated that when polarity and proticity of the solvent increase, the A_z value increases and the g_x value decreases. Then, the magnetic parameters of DxPCA in CMS nanocarriers were compared to the established correlation between g_x and A_z and the solvent polarity/proticity. This comparison shows DxPCA in CMS nanocarriers experiences an environment of intermediate polarity, i.e, significantly lower polarity than in water and higher than in toluene. Thus, the magnetic parameters clearly show that DxPCA is loaded within the CMS nanoparticles. In the next step, the location of DxPCA inside the CMS nanoparticles has been analyzed by relaxation time measurements. The T_1 of DxPCA in CMS nanoparticles is again significantly different from DxPCA in water and manifests an aprotic environment. According to the structure of CMS nanoparticles, their core is polar/protic and their outer shell is polar/aprotic. Since the linker between the apolar inner shell and the polar/protic core is a protic region it can be excluded as the environment of DxPCA. Thus, the T_1 reveals that DxPCA associates with neither the polar/protic core nor the polar/aprotic outer shell. Thus one can argue that DxPCA is neither located on the edge of CMS core nor in the inner shell. Therefore, DxPCA must be located at the interface between the hydrophobic inner and hydrophilic outer shell of the CMS nanoparticles (Fig. 7.1).

Based on the association model of DxPCA and CMS nanoparticles, its functionality has been investigated. Room temperature studies give useful evidence about the mobility of a drug loaded in CMS nanoparticles, and, thereby, helps to determine the functionality of CMS nanoparticles. The dynamics of DxPCA in aqueous solution is entirely different from DxPCA loaded into the CMS nanoparticles. DxPCA loaded into the CMS nanoparticles rotates slower than in water. At the same time, the analysis of the rotational correlation time of CMS, based on the Stokes-Einstein equation, shows that the rotation of DxPCA is much faster than that of the whole CMS nanoparticle. Thus, the mobility of DxPCA demonstrates that it is partially immobilized in CMS, and can not freely rotate. Moreover, this difference found in the dynamics between freely dissolved DxPCA and DxPCA loaded into CMS nanoparticles has been used to

analyze the drug/carrier penetration behavior into the skin. The penetration of the drug into the skin is facilitated only for DxPCA loaded into the CMS nanoparticles [166].
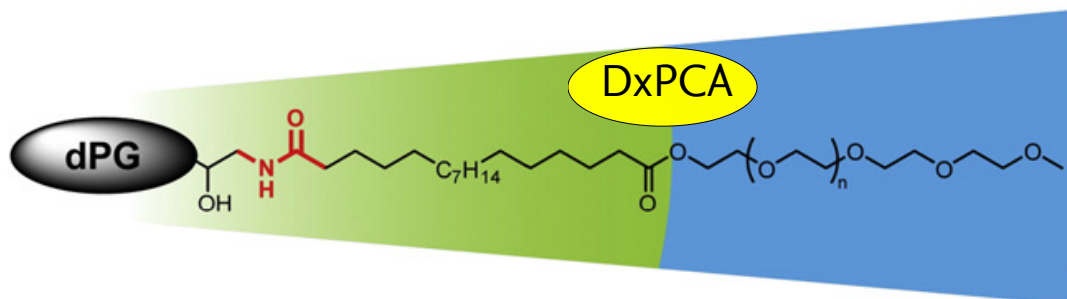

Figure 7.1: Localization of DxPCA in CMS nanoparticles

Using the same spectroscopic approach as for CMS nanoparticles, an association model of a drug to NLPs has been determined by EPR spectroscopy. The three different lipids, Gelucire® 50/13 (solid lipid), Witepsol® S55 (solid lipid) and Capryol® 90 (liquid lipid), have been chosen for fabrication of NLPs. Gelucire has been mainly used for the preparation of solid dispersions to improve the solubility/bioavailability of poorly water-soluble drugs and also has surfactant functionality. Capryol functions as a water-insoluble co-surfactant. Witepsol as hard fat is used for increasing the wettability of NLPs and improving the drug absorption. Firstly, the effective polarity of the surrounding micro-environment of the spin probes, PCA, TEMPO, and DxPCA, has been investigated in lipids, lipid mixtures, and NLPs. Additionally, reference systems for the polarity/proticity investigation of spin probes spanned from extremely polar/protic solvents (water) to apolar/aprotic solvents (toluene). The magnetic parameters of PCA loaded to NLPs have been found to be in an intermediate polarity regime between lipids and water. Likewise, the effective environment polarity experienced by DxPCA within the NLPs is in the intermediate polarity range between an apolar/aprotic environment of solid lipids and the polar/protic environment of the medium, water. On the other hand, the magnetic parameters of TEMPO in the NLPs and in the lipids are quite similar, i.e. they indicate an apolar/aprotic environment. Secondly, in rt EPR rather high mobility of the spin probes has been found in the liquid lipid Capryol while a strong immobilization occurs in the solid lipids. Additionally, the spin probes aggregate in the solid lipids and lipid mixtures, while they do not aggregate in NLPs. PCA in lipids is strongly immobilized, but the mobility of PCA in NLPs is in the fast motion regime. The magnetic and dynamic parameters at room temperature indicate PCA in water. TEMPO rotates slowly in lipids as well as in NLPs, indicating more constant mobility. DxPCA is strongly immobilized in the lipids but has slightly higher mobility in NLPs. Thirdly, the relaxation times of the spin probes in lipids and NLPs have been measured. The relaxation time of PCA in lipids is faster than in NLPs, which indicates the presence of an aqueous environment around PCA in NLPs. The T_1 of TEMPO in lipids and NLPs indicate an apolar/aprotic environment around TEMPO in both environments. The relaxation time of

DxPCA in lipids and NLPs are slightly different and reveals that DxPCA experiences a partially protic environment. The results of the polarity, mobility and relaxation time investigation together lead to drug/NLP association models. Based on the intermediate polarity, fast motion, and slow relaxation time of PCA, one can argue that it is located outside the lipid environment. PCA, as a hydrophilic probe, is in aqueous solution. In contrast, TEMPO is buried inside NLPs according to the identical magnetic and dynamic parameters as well as the relaxation time in the lipids and NLPs. Accordingly, a drug/NLP association model is suggested for TEMPO, which suggests its enrichment within the core. One can conclude that DxPCA is located at the lipid and lipid-water interface according to the difference of magnetic parameters, mobility and relaxation time of DxPCA in lipids and NLPs. Thus, the derived drug/NLP association model of the lipophilic drug DxPCA is dispersed within the entire lipid matrix of the NLPs. The structure of NLPs made exclusively of solid lipids consists of are imperfect crystals. When the liquid lipid Capryol is added to the NLPs composition, the NLP's structure turns to an amorphous state. The study of PCA does not reveal any information regarding the structure of NLPs, due to the fact that it out of NLPs. The rt measurements of TEMPO loaded to NLPs reveal partitioning between the NLP's lipid phase and the solvent's aqueous phase. The ratio of loaded and unloaded TEMPO depends on the amount of Capryol admixed to NLPs. Capryol increases the loading efficiency of TEMPO in NLPs. Accordingly, the imperfect crystal NLPs have less loading capacity than the amorphous NLPs. The high-pressure homogenization process for NLP formation does not introduce DxPCA into the lipid matrix, which indicates an ordered matrix and expulsion of DxPCA to the outer shell. Nevertheless, DxPCA is almost completely associated with the NLP and shows an NLP/water equilibrium distribution strongly balanced towards the nanoparticles. This is probably promoted by the lipophilic properties of Dx and its low solubility in water.

The result of this study can be used for improving the synthesis of CMS nanoparticles and NLPs to fabricate efficient DDS. The knowledge about the location of the drug inside the CMS nanoparticles could lead to an efficient strategy for the release mechanism [196]. In addition, the evidence for the location of DxPCA inside CMS nanoparticles could be used to synthesize the CMS nanoparticles with proper branching number [197] and help to improve their functionality for a new class of CMS nanoparticles such as the biodegradable and pH-sensitive CMS [93, 94].

The drug/NLP association models for different substances could help to fabricate efficient NLP as DDS with adequate size for optimal drug dosage and appropriate for a given dermal penetration strategy. The loading capacity for hydrophobic substances, such as DxPCA, is dependent on the surface area and volume of NLPs. A nanocarrier with a bigger diameter is a candidate for penetration along the hair follicle route, which can transport a drug to deeper layers of the skin, but with the cost of lower loading capacity. Moreover, NLPs can function as a reservoir for an amphiphilic substance, such as TEMPO, and prevent degradation of a drug by the skin's redox-active substances before arriving at the target.

The advantage of dual-frequency EPR spectroscopy was successfully utilized for investigation of thermal responsive nanogels [198, 199] and pH-sensitive nanoparticles [200] as well CMS nanoparticles and NLPs. Thus, it could be shown, that dual-frequency EPR spectroscopy is a

valuable approach for the investigation of different classes of nanocarriers.

When different species are present in a sample with slightly shifted g-values due to a heterogeneous micro-environment (as e.g. has been shown in section 6.1.1) for TEMPO and DxPCA, then the precise investigation of polarity and proticity of a spin probe in this complex situation can be achieved by measuring at even higher frequency than W-band [51]. Due to the higher spectral resolution, the g-matrix can be extracted unequivocally also in samples with complex solvent mixtures. Additionally, EPR techniques which can directly probe the hyperfine coupling (e.g., ENDOR and EDNMR) of ^{14}N is also a complementary technique for determining reliable values of the complete A-matrix, which is not resolved in the EPR spectra. This would be a prerequisite for more reliable simulations of the complex shaped g_x-peaks of spin-probes, where a varying number of H-bonds occurs [152, 201]. The performing hyperfine spectroscopy at high frequency would help to separate out the individual contributions of species in different solvent phases by a weighted simulation of the EPR spectrum. Complementary to the micro-environment investigations could be the usage of distance determination between spin-probes by pulsed EPR (e.g. Pulsed Electron-Electron Resonance, PELDOR). This could potentially give a picture of how the spin probe is distributed within a nanoparticular system. Additionally, it could be determined, how the conformation of a nanocarrier and the association of the drug with it are changed when drug release occurs [202, 203]. But the efficient labeling of the drug (analog), its loading efficiency and proper size of the nanocarriers are potential issues during drug analog synthesis and nanoparticle fabrication, which in turn could limit distance measurements by EPR. The information about the localization and association of a drug with a nanocarrier obtained via EPR spectroscopy is valuable to track a penetration route of a nanocarrier in the skin and to reveal release profiles of a drug from a DDS to the target organ [120]. The combination of EPR with other spectroscopic and microscopic techniques, such as time-resolved fluorescence microscopy [204], X-ray spectroscopy [205], and Raman microscopy [206], lead even reliable results about the penetration of the nanocarriers into the skin and the drug release profile. Additionally, the results can be used for modeling of the human skin and simulation of the penetration rate of a substance into the different layers [207].

A Supplementary data
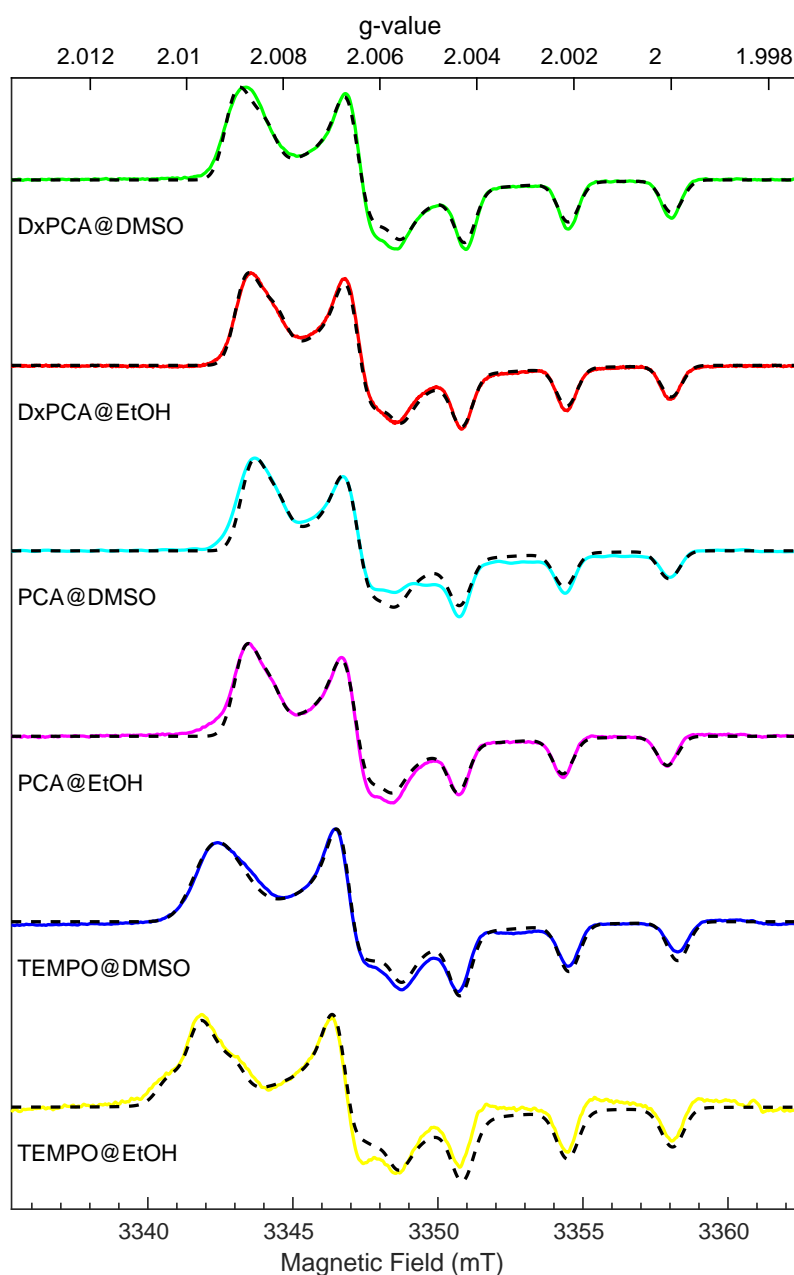
Figure A.1: The high field spectra of DxPCA, PCA and TEMPO in DMSO and EtOH solvents at 80 K, green is DxPCA in DMSO (microwave power: 20 nW, modulation amplitude: 5 G), red is DxPCA in EtOH (microwave power: 40 nW, modulation amplitude: 5 G), cyan is PCA in DMSO (field sweep echo. pseudo modulation 5 G) and magenta is PCA in EtOH (microwave power: 10 μW, modulation amplitude: 5 G), blue is TEMPO in DMSO (microwave power: 5 μW, modulation amplitude: 5 G) and yellow is TEMPO in EtOH (microwave power: 50 μW, modulation amplitude: 5 G), dashed black lines are the simulations corresponding to the experimental data.

Table A.1: Magnetic Parameters of PCA in different solvents (Error margins in the last digit given in parenthesis), together with polarities and relative dielectric permetivities of the used solvents; (p) protic, (a) is aprotic.

Solvent	g-matrix g_x, g_y, g_z	A-matrix (MHz) A_{xx}, A_{yy}, A_{zz}
CMS [104]	2.00890, 2.00600 , 2.0012	30, 35, 72
Water (p)	2.00805(3), 2.00596(2), 2.00212(2)	15, 15, 105(1)
Ethanol (p)	2.00850(3), 2.00615(3), 2.00222(2)	13, 13, 101(1)
1-propanol(p)	2.00848(3), 2.00611(1), 2.00210(2)	13, 13, 102(1)
1-decanol(p)	2.00865(1), 2.00621(1), 2.00220(2)	15, 10, 100(1)
DMSO(a)	2.00835(3), 2.00610(2), 2.00218(2)	13, 13, 101(1)
Acetone(a)	2.00850(5), 2.00595(5), 2.00210(2)	15, 15, 99(1)
methyl formate(a)	2.00850(2), 2.00604(4), 2.00211(1)	15, 15, 100(1)

Table A.2: Magnetic and dynamic parameters of PCA in Lipid and NLP at room temperature

Component	g-matrix g_x, g_y, g_z	A-matrix (MHz) A_x, A_y, A_z	Linewidth (mT) [Gaussian, Lorentzian]	τ_{corr} ps
Lipid-Ge	2.00901, 2.00610, 2.00214	13, 13, 96	[0,00, 1.80]	700
NLP-Ge	2.00807, 2.00618, 2.00218	13, 13, 113	[0.15, 0.00]	30
Lipid-Wi	2.00900, 2.00617, 2.00216	15, 13, 96	[0.00, 0.50]	1000
Lipid-Ca	2.00905, 2.00615, 2.00209	13, 13, 102	[0.00, 0.30]	250
Lipid-Wi/Ca	2.00895, 2.00622, 2.00216	13, 10, 97	[0.00, 1.00]	400
Lipid-Ge/Wi	2.00901, 2.00610, 2.00214	13, 13, 95	[0,00, 1.80]	700
NLP-Ge/Wi	2.00824, 2.00608, 2.00215	15, 15, 109	[0.15, 0.00]	30
Lipid-Ge/Ca	2.00910, 2.00623, 2.00217	15, 15, 96	[0.00, 0.80]	450
NLP-Ge/Ca	2.00825, 2.00608, 2.00215	15, 15, 109	[0.15, 0.00]	30
Lipid-Ge/Wi/Ca	2.00890, 2.00618, 2.00215	16, 16, 96	[0.00, 1.50]	450
NLP-Ge/Wi/Ca	2.00823, 2.00608, 2.00215	15, 15, 108	[0.15, 0.00]	30

Appendix A. Supplementary data

Table A.3: Magnetic and dynamic parameters of TEMPO in Lipid and NLP at room temperature

Solvent	g-matrix g_x, g_y, g_z	A-matrix (MHz) A_x, A_y, A_z	Linewidth (mT) [Gaussian, Lorentzian]	τ_{corr} (ps)
Lipid-Ge	2.01027, 2.00630, 2.00216	20 20 82	[0.40, 0.00]	200
NLP-Ge	2.00854, 2.00640, 2.00220	20, 20, 108	[0.16, 0.00]	10
	2.01027, 2.00630, 2.00216	20, 20, 97	[0.20, 0.00]	65
Lipid-Wi	2.00997, 2.00638, 2.00218	20, 20, 94	[0.00, 0.40]	125
Lipid-Ca	2.01013, 2.00610, 2.00200	20, 20, 97	[0.00, 0.35]	50
Lipid-Wi/Ca	2.00987, 2.00634, 2.00219	20, 20, 95	[0.00, 0.50]	80
Lipid-Ge/Wi	2.01025, 2.00638, 2.00218	20, 20, 91	[0.25, 0.00]	80
NLP-Ge/Wi	2.00870, 2.00628, 2.00214	20, 20, 108	[0.17, 0.00]	10
	2.01005, 2.00638, 2.00218	20, 20, 94	[0.20, 0.00]	80
Lipid-Ge/Ca	2.01005, 2.00629, 2.00215	20, 20, 95	[0.00, 0.20]	65
NLP-Ge/Ca	2.00881, 2.00623, 2.00212	20, 20, 108	[0.16, 0.00]	10
	2.01033, 2.00629, 2.00215	20, 20, 93	[0.00, 0.20]	65
Lipid-Ge/Wi/Ca	2.01015, 2.00624, 2.00212	20, 20, 92	[0.00, 0.20]	80
NLP-Ge/Wi/Ca	2.00856, 2.00632, 2.00220	20, 20, 108	[0.16, 0.00]	10
	2.01026, 2.00624, 2.00212	20, 20, 94	[0.00, 0.20]	80

Table A.4: Magnetic and dynamic parameters of DxPCA in lipids and NLPs.

Composition	g g_x, g_y, g_z	A (MHz) A_x, A_y, A_z	Linewidth (mT) [Gaussian, Lorentzian]	τ_{corr} (ns) τ_1, τ_2, τ_3
Gelucire	2.00900, 2.00617, 2.00211	12, 13, 94	[0.200, 0.000]	5.0, 3.0, 10.0
NLP-Ge	2.00875, 2.00623, 2.00220	13, 12, 99	[0.005, 0.000]	4.0, 1.2, 10.0
Witepsol	2.00900, 2.00620, 2.00213	12, 10, 96	[0.100, 0.000]	2.5, 10.0, 10.0
Capryol	2.00865, 2.00616, 2.00214	13, 14, 99	[0.000, 0.200]	1.0, 1.0, 5.0
Witepsol/Capryol	2.00870, 2.00620, 2.00212	13, 10, 98	[0.200, 0.000]	3.2, 3.2 3.2
Gelucire/Witepsol	2.00900, 2.00617, 2.00211	11, 13, 94	[0.200, 0.000]	5.0, 3.0, 10.0
NLP-Ge/Wi	2.00860, 2.00605, 2.00215	14, 15, 98	[0.010, 0.000]	5.0, 1.0, 10.0
Gelucire/Capryol	2.00875, 2.00616, 2.00214	11, 13, 97	[0.010, 0.000]	5.0, 1.5, 10.0
NLP-Ge/Ca	2.00863, 2.00620, 2.00218	15, 13, 100	[0.050, 0.000]	2.0, 1.0, 10.0
Gelucire/Witepsol/Capryol	2.00875, 2.00617, 2.00215	13, 13, 97	[0.100, 0.000]	4.0, 2.0, 10.0
NLP-Ge/wi/Ca	2.00865, 2.00615, 2.00218	14, 13, 102	[0.100, 0.000]	1.6, 1.6, 10.0
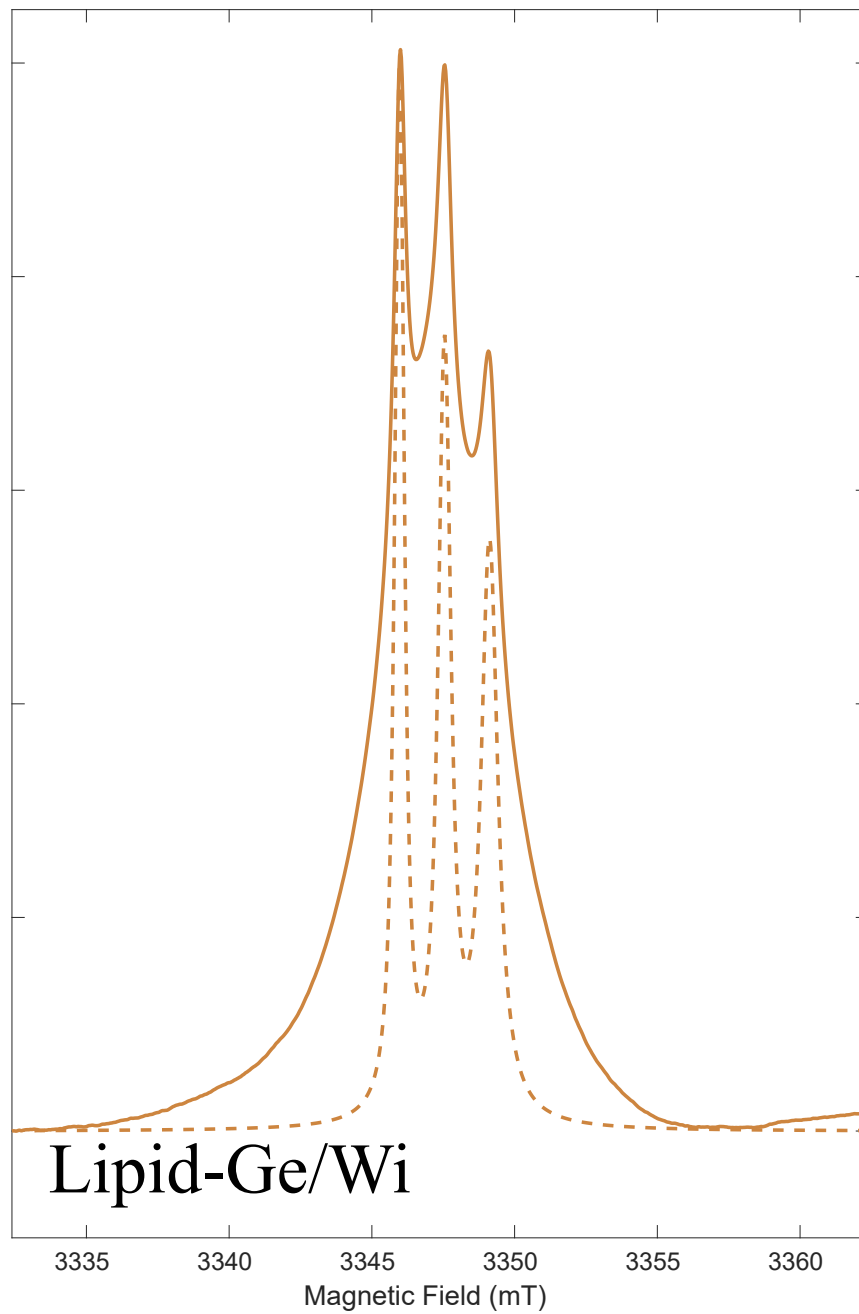
Figure A.2: Integral of the W-band spectrum of TEMPO dissolved in Gelucire/Witepsol at room temperature. The dashed lines correspond to a simulation of the spectrum with parameters given in table 6.5.
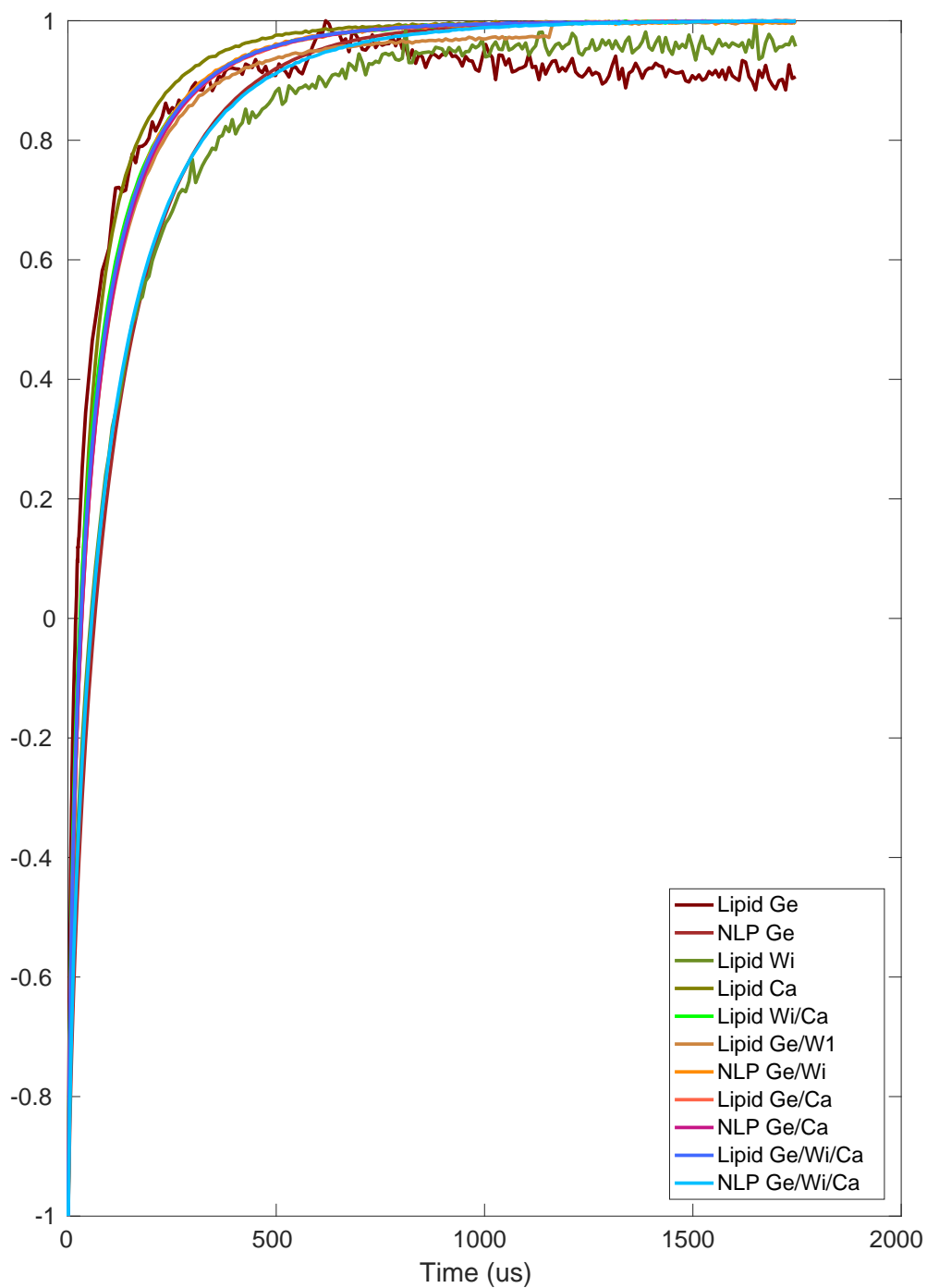
Figure A.3: Inversion recovery measurement of PCA loaded to lipids and NLPs measured at W-band at g_y magnetic field position at 80 K.
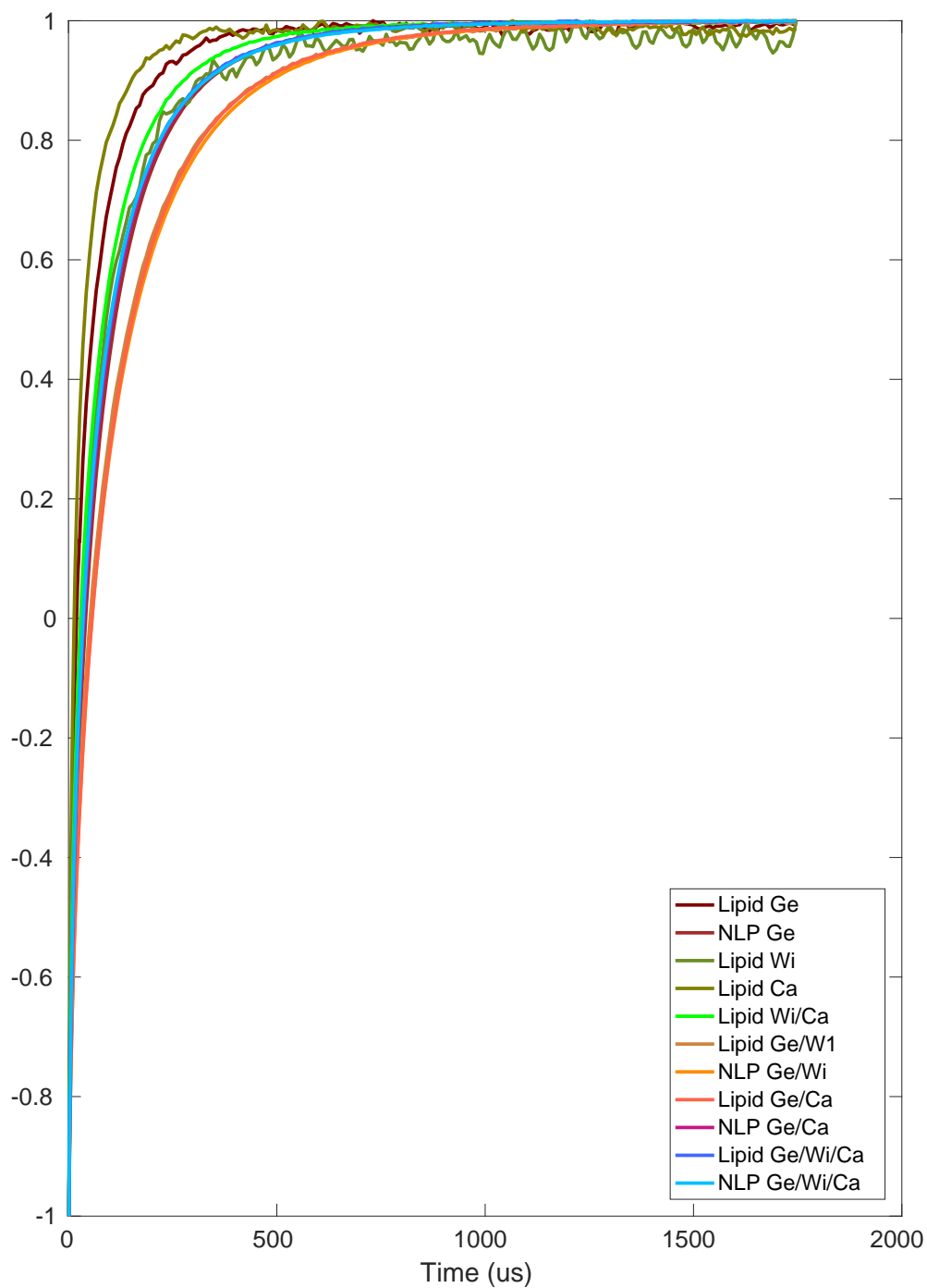
Figure A.4: Inversion recovery measurement of TEMPO loaded to lipids and NLPs measured at W-band at g_y magnetic field position at 80 K.
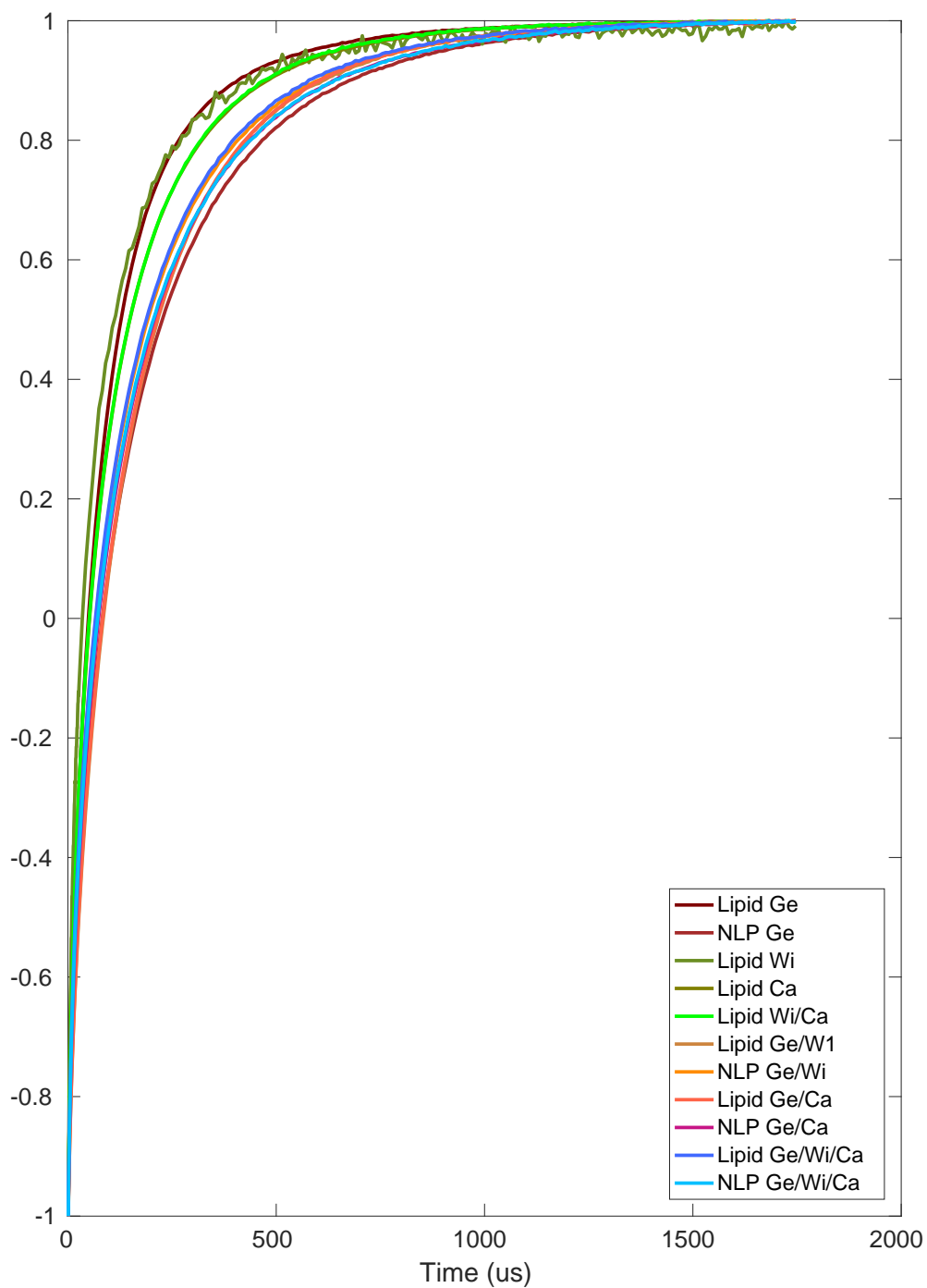
Figure A.5: Inversion recovery measurement of DxPCA loaded to lipids and NLPs measured at W-band at g_y magnetic field position at 80 K.

Table A.5: Spin lattice relaxation time T_1 of spin probes (DxPCA. PCA and TEMPO) obtained by bi-exponential fitting of inversion recovery time traces in for different lipids and NLPs at the different field positions (g_x, g_y and g_z).

$$f(t) = 1 - 2(A_1 e^{(-t/\tau_1)} + A_2 e^{(-t/\tau_2)})$$

| Composition	A_{1x}	τ_{1x} (us)	A_{2x}	τ_{2x} (us)	A_{1y}	τ_{1y} (us)	A_{2y}	τ_{2y} (us)	A_{1z}	τ_{1z} (us)	A_{2z}	τ_{2z} (us)
DxPCA@Lipid-Ge	0.62	195	0.38	28	0.58	154	0.42	28	0.63	366	0.37	32
DxPCA@NLP-Ge	0.66	244	0.34	32	0.66	240	0.34	31	0.65	414	0.35	35
DxPCA@Lipid-Wi	0.53	150	0.47	18	0.51	157	0.49	18	0.49	225	0.51	19
DxPCA@Lipid-Ca	0.62	195	0.38	25	0.59	181	0.41	24	0.61	331	0.39	28
DxPCA@Lipid-Wi/Ca	0.62	186	0.38	23	0.59	176	0.41	23	0.59	310	0.41	26
DxPCA@Lipid-Ge/Wi	0.68	210	0.32	35	0.69	218	0.31	34	0.65	352	0.35	40
DxPCA@NLP-Ge/Wi	0.62	221	0.38	28	0.62	218	0.38	27	0.60	376	0.40	32
DxPCA@Lipid-Ge/Ca	0.68	218	0.32	35	0.69	217	0.31	33	0.69	384	0.31	42
DxPCA@NLP-Ge/Ca	0.65	235	0.35	30	0.64	230	0.36	29	0.63	396	0.37	32
DxPCA@Lipid-Ge/Wi/Ca	0.64	211	0.36	26	0.63	210	0.37	26	0.61	350	0.39	28
DxPCA@NLP-Ge/wi/Ca	0.64	225	0.36	27	0.63	230	0.37	28	0.62	376	0.38	30
PCA@Lipid-Ge	0.57	78	0.43	8	0.51	84	0.49	9	0.44	192	0.56	16
PCA@NLP-Ge	0.68	187	0.32	30	0.67	167	0.33	28	0.68	341	0.32	37
PCA@Lipid-Wi	0.54	229	0.46	29	0.59	183	0.41	25	0.55	340	0.48	32
PCA@Lipid-Ca	0.50	140	0.50	28	0.42	120	0.58	23	0.61	251	0.39	30
PCA@Liid-Wi/Ca	0.53	126	0.47	15	0.52	128	0.48	15	0.47	196	0.53	17
PCA@Lipid-Ge/Wi	0.57	122	0.43	17	0.50	141	0.50	19	0.51	215	0.49	20
PCA@NLP-Ge/Wi	0.67	195	0.33	28	0.65	183	0.35	28	0.65	341	0.35	27
PCA@Lipid-Ge/Ca	0.54	114	0.46	14	0.53	133	0.47	18	0.52	211	0.48	19
PCA@NLP-Ge/Ca	0.66	186	0.33	28	0.64	171	0.36	27	0.65	322	0.35	28
PCA@Lipid-Ge/Wi/Ca	0.55	124	0.45	17	0.52	130	0.48	17	0.50	180	0.50	18
PCA@NLP-Ge/Wi/Ca	0.64	186	0.36	26	0.62	175	0.38	26	0.63	312	0.37	30
TEMPO@Lipid-Ge	0.54	94	0.46	11	0.56	74	0.44	8	0.49	201	0.51	18
TEMPO@NLP-Ge	0.62	132	0.38	20	0.63	124	0.37	18	0.62	257	0.38	27
TEMPO@Lipid-Wi	0.63	86	0.37	13	0.57	109	0.43	17	0.58	216	0.42	25
TEMPO@Lipid-Ca	0.55	73	0.45	10	0.48	56	0.52	8	0.50	127	0.50	13
TEMPO@Lipid-Wi/Ca	0.60	110	0.40	15	0.58	105	0.42	14	0.57	196	43	20
TEMPO@Lipid-Ge/Wi	0.62	152	38	20	0.62	170	0.38	21	0.65	303	0.35	27
TEMPO@NLP-Ge/Wi	0.63	175	0.37	25	0.63	176	0.37	22	0.65	330	0.35	31
TEMPO@Lipid-Ge/Ca	0.64	163	0.36	24	0.64	170	0.36	23	0.67	311	0.33	31
TEMPO@NLP-Ge/Ca	0.60	130	0.40	19	0.60	122	0.40	17	0.59	244	0.41	25
TEMPO@Lipid-Ge/Wi/Ca	0.59	115	0.41	17	0.59	122	0.41	17	0.58	226	0.42	23
TEMPO@NLP-Ge/Wi/Ca	0.57	128	0.43	18	0.57	125	0.43	17	0.56	240	0.44	23

B Thermoresponsive Nanogels

The highly hydrophilic nanocarriers are an attractive system for the topical drug delivery system. The thermal responsive nanogel (tNG) [199] is a potential system for efficient delivery of hydrophobic drugs. The tNG is fabricated from dendritic polyglycerol (dPG) as a crosslinker and linear thermoresponsive polyglycerol (tPG) inducing responsiveness to temperature changes. The β-cyclodextrin (βCD) could be successfully introduced into the drug carrier systems by exploiting its unique affinity toward dexamethasone as well as its role as topical penetration enhancer. dual-frequency EPR helps to find the localization of the drug within the hydrophobic cavity of βCD by differences in its mobility and environmental polarity.

EPR investigations pointed out different environments for DxPCA loaded to the Thermoresponsive Nanogels (tNGs) with and without βCD. For the aqueous dispersion of the tNG $-$ tPG loaded with the spin labeled drug the spectral shape is comparable, representing a freely tumbling molecule in solution. The EPR spectrum of DxPCA loaded to tNG $-$ tPG $-$ βCD differs remarkably recognizable by spectral broadening of the high-field line (at 336 mT) in comparison to tNG $-$ tPG. By comparison, the EPR spectra of DxPCA loaded to tNG $-$ tPG $-$ βCD and in an aqueous solution of βCD (Fig.B.1a) illustrate that the cyclic oligosaccharide seems to be responsible for the restricted mobility of DxPCA.

In general, the mobility of a spin label is encoded into the spectral shape of an EPR spectrum as incomplete time-averaging over the anisotropic magnetic interactions by the tumbling motion of the molecule. A measure for the mobility is the rotational correlation time τ_{corr}, which can be deduced by simulation of the EPR spectrum. For a consistent simulation of the EPR spectra at ambient temperature, the magnetic parameters (g- and ^{14}N hyperfine matrices) should be measured independently. Therefore EPR spectra at 94 GHz were acquired, from which by simulation the g- matrix and the ^{14}N hyperfine coupling could be estimated (TableB.1 and Fig.B.1b) The obtained magnetic parameters (g_{xx}, and A_{zz}, see Table B.1) illustrate the polarity of DxPCA's environment loaded to the various tNG dispersions and dissolved in aqueous solutions. DxPCA loaded to tNG $-$ tPG shows a similar EPR spectrum as in water. indicating a high mobility of DxPCA in this dispersion. A little tendency towards a more apolar environment for tNG $-$ tPG is given, recognizable by the slight upshift of g_{xx} and correspondingly downshift of A_{zz} (TableB.1). For DxPCA loaded to tNG $-$ tPG $-$ βCD and dissolved in the aqueous βCD

solution the change is noticeably higher reflecting a more apolar environment. Interestingly, for both βCD containing solutions the same magnetic as well as mobility parameters were obtained indicating a similar environment for DxPCA. Comparing the parameters obtained from EPR the following conclusions can be elucidated: for the tNG $-$ tPG $-$ βCD dispersion as well as the βCD solution DxPCA is located in a more apolar environment compared to the tNG $-$ tPG dispersion and also the rotational correlation time reports for the same partial immobilization of the drug in these βCD containing solutions

Taking these two facts together, the most probable location of DxPCA is within the hydrophobic pocket of βCD, leading to a more apolar environment and hindered rotation compared to the tNG $-$ tPG dispersion and aqueous solution. Electron paramagnetic resonance studies localized the drug within the hydrophobic cavity ofβCD by differences in its mobility and environmental polarity.

Table B.1: Magnetic parameters (g- and A-matrix) of DxPCA loaded in different tNG.

Composition	g-matrix	A-matrix, (MHz)	t_{corr}, (ps)
tNG$_t$PG + DxPCA	2.00840(5), 2.00603(2), 2.00215(1)	15, 15, 101(1)	80
tNGtPG $-$ βCD + DxPCA	2.00870(3), 2.00615(2), 2.00217(2)	15, 13, 99(1)	400
βCD + DxPCA	2.00870(3), 2.00610(2), 2.00214(1)	15, 14, 99(1)	400
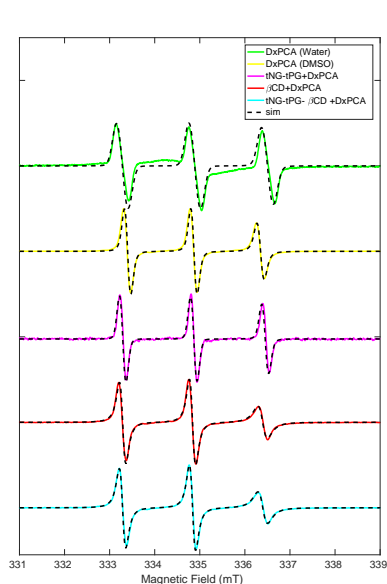
(a) X-band EPR spectra of DxPCA subjected to tNG $-$ tPG, tNG $-$ tPG $-$ βCD at ambinate temperature).
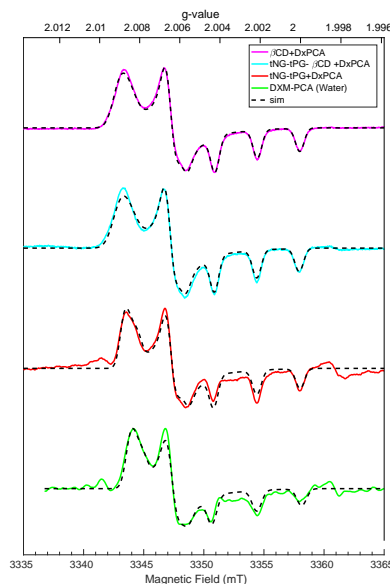
(b) W-band EPR spectra of DxPCA loaded to different tNGs at cryogenic temperature.

Figure B.1: X- and W-band spectra of tNG in the abominate and cryogenic temperature.

C Publications

Elements of this work that have been published:

- PART OF CHAPTER 5 HAVE BEEN PUBLISHED AS:
  S. Saeidpour, S.B. Lohan, M. Anske, M. Unbehauen, E. Fleige, R. Haag, M.C. Meinke, R. Bittl, C. Teutloff, "Localization of dexamethasone within dendritic core-multishell (CMS) nanoparticles and skin penetration properties studied by multi-frequency electron paramagnetic resonance spectroscopy (EPR)", *European Journal of Pharmaceutics and Biopharmaceutics*, **July 2017**, *116*, 94-101
  As well some text sections as some figures have been taken or adapted form this publication.
  https://doi.org/10.1016/j.ejpb.2016.10.001

- THE EXPERIMENT, RESULT AND DISCUSSION OF DXPCA LOADED IN NLPS IN CHAPTER 6 IS BASED ON:
  S. Saeidpour, S. B. Lohan, A. Solik, V. Paul, R. Bodmeier, G. Zoubari, M Unbehauen , R Haag, R. Bittl, M. C. Meinke, C. Teutloff, "Drug Distribution in Nanostructured Lipid Particles", *European Journal of Pharmaceutics and Biopharmaceutics*, **January 2017**, *100*, 19-23
  As well some text sections as some figures have been taken or adapted form this publication.
  https://doi.org/10.1016/j.ejpb.2016.10.008

Other publications related to this research:

- S.B. Lohan, N. Icken, C. Teutloff, S. Saeidpour, R. Bittl, J. Lademann, E. Fleige, R. Haag, S.F. Haag, M.C. Meinke,"Investigation of cutaneous penetration properties of stearic acid loaded to dendritic core-multi-shell (CMS) nanocarriers", *International Journal of Pharmaceutics*, **March 2016**, *501*, 271-277

Publication

- S.B. Lohan, S. Saeidpour, A. Solik, S. Schanzer, H. Richter, P. Dong, M.E. Darvin, R. Bodmeier, A. Patzelt, G. Zoubari, M. Unbehauen, R. Haag, J. Lademann, C. Teutloff, R. Bittl, M.C. Meinke, "Investigation of the cutaneous penetration behavior of dexamethasone loaded to nano-sized lipid particles by EPR spectroscopy, and confocal Raman and laser scanning microscopy", *European Journal of Pharmaceutics and Biopharmaceutics*, **July 2017**, *116*, 102-110

- THE EXPERIMENT, RESULT AND DISCUSSION OF APPENDIX B IS BASE ON:
  M. Giulbudagian, S. Hönzke, J. Bergueiro, D. Isık, F. Schumacher, S. Saeidpour, S. B. Lohan, M. C. Meinke, C. Teutloff, M. Schäfer-Korting, G. Yealland, B. Kleuser, S. Hedtrich, and M. Calderón, "Enhanced Topical Delivery of Dexamethasone by β-Cyclodextrin Decorated Thermoresponsive Nanogels, *Nanoscale* **January 2018**, *10 (1)*, 469-479
  As well as some text sections as same figures have been taken from this publication.

- K Walker, M Unbehauen, S. B. Lohan, S. Saeidpour, M. C. Meinke, R Zimmer and R Haag, "Spin-labeling of Dexamethasone: Radical Stability vs. Temporal Resolution of EPR-Spectroscopy on Biological Samples", *Zeitschrift für Physikalische Chemie*, **April 2018**

- P. Dong, F. F. Sahle, S. B. Lohan, S. Saeidpour, S Albrecht, C. Teutloff, R. Bodmeier, M. Unbehauen, C. Wolff; R. Haag, J. Lademann, A., M. Schäfer-Korting, M.C. Meinke, "pH-sensitive Eudragit® L 100 nanoparticles promote cutaneous penetration and drug release on the skin", *Journal of Controlled Release*, **February 2019**

Other publication not related to this research:

- M. Nagaraj, T. W. Franks, S. Saeidpour, T. Schubeis, H. Oschkinat, C. Ritter, B. J. Van Rossum, "Surface binding of TOTAPOL assists structural investigations of amyloid fibrils by dynamic nuclear polarization NMR", *ChemBioChem.*, **July 2016**, *17*,:1308-1311

Abbreviation

CMS	Dendritic Core MultiShell
cw	Continuous Wave
DDS	Drug Delivery System
dPG	denritic Poly-Glycerol
DxPCA	Dexamethasone labelled PCA
EPR	Electron Paramagnetic Resonance
FSE	Field Sweep Echo
hfs	hyperfine splitting
NLC	Nano Lipid Carrier
NLP	Nanostructured Lipid Particles
NLP-Ge	Nanostructured Lipid Particles Gelucire
NLP-Ge/Wi	Nanostructured Lipid Particles Gelucire/Witepsol
NLP-Ge/Ca	Nanostructured Lipid Particles Gelucire/Capryol
NLP-Ge/Wi/Ca	Nanostructured Lipid Particles Gelucire/Witepsol/Capryol
OHV	Hydroxyl Value
Lipid-Ge	Lipid Gelucire
Lipid-Ge/Wi	Lipid Gelucire/Witepsol
Lipid-Ge/Ca	Lipid Gelucire/Capryol
Lipid-Ge/Wi/Ca	Lipid Gelucire/Witepsol/Capryol
PCA	3-carboxy-2,2,5,5-tetramethyl-1-pyrrolidinyloxy
SC	Stratum Corneum
SLN	Solid Lipid Nanoparticle
TEMPO	2,2,6,6-Tetramethylpiperidin-1-yl oxyl
tNG	Thermoresponsive Nanogels

Bibliography

[1] T.-T. Zhang, W. Li, G. Meng, P. Wang, W. Liao, Strategies for transporting nanoparticles across the blood-brain barrier, Biomater. Sci. 4 (2016) 219–229.

[2] M. R. Prausnitz, R. Langer, Transdermal drug delivery, Nature Biotechnology 26 (2008) 1261.

[3] E. Amstad, E. Reimhult, Nanoparticle actuated hollow drug delivery vehicles, Nanomedicine 7 (1) (2012) 145–164, pMID: 22191783.

[4] G. Cevc, G. Blume, A. Schätzlein, D. Gebauer, A. Paul, The skin: a pathway for systemic treatment with patches and lipid-based agent carriers, Advanced Drug Delivery Reviews 18 (3) (1996) 349 – 378, the Skin as a Site for Drug Delivery: the Liposome Approach and its Alternatives.

[5] E. Proksch, R. Fölster-Holst, J.-M. Jensen, Skin barrier function, epidermal proliferation and differentiation in eczema, Journal of Dermatological Science 43 (3) (2006) 159 – 169.

[6] M. A. Kendall, Y.-F. Chong, A. Cock, The mechanical properties of the skin epidermis in relation to targeted gene and drug delivery, Biomaterials 28 (33) (2007) 4968 – 4977.

[7] D. S. Malik, N. Mital, G. Kaur, Topical drug delivery systems: a patent review, Expert Opinion on Therapeutic Patents 26 (2) (2016) 213–228.

[8] J. Lademann, H. Richter, A. Teichmann, N. Otberg, U. Blume-Peytavi, J. Luengo, B. Weiß, U. F. Schaefer, C.-M. Lehr, R. Wepf, W. Sterry, Nanoparticles – an efficient carrier for drug delivery into the hair follicles, European Journal of Pharmaceutics and Biopharmaceutics 66 (2) (2007) 159 – 164.

[9] I. Weitzman, R. C. Summerbell, The dermatophytes., Clinical Microbiology Reviews 8 (2) (1995) 240–59.

[10] T. Bieber, Atopic dermatitis, New England Journal of Medicine 358 (14) (2008) 1483–1494, pMID: 18385500.

[11] F. O. Nestle, D. H. Kaplan, J. Barker, Psoriasis, New England Journal of Medicine 361 (5) (2009) 496–509, pMID: 19641206.

[12] N. Barkalina, C. Charalambous, C. Jones, K. Coward, Nanotechnology in reproductive medicine: Emerging applications of nanomaterials, Nanomedicine: Nanotechnology, Biology and Medicine 10 (5) (2014) e921 – e938.

[13] J. Padmanabhan, T. R. Kyriakides, Nanomaterials, inflammation, and tissue engineering, Wiley Interdisciplinary Reviews: Nanomedicine and Nanobiotechnology 7 (3) (2015) 355–370.

[14] J. De Leeuw, H. De Vijlder, P. Bjerring, H. Neumann, Liposomes in dermatology today, Journal of the European Academy of Dermatology and Venereology 23 (5) (2009) 505–516.

[15] D. Papakostas, F. Rancan, W. Sterry, U. Blume-Peytavi, A. Vogt, Nanoparticles in dermatology, Archives of Dermatological Research 303 (8) (2011) 533.

[16] L. A. DeLouise, Applications of nanotechnology in dermatology, Journal of Investigative Dermatology 132 (3, Part 2) (2012) 964 – 975.

[17] M. Elsabahy, K. L. Wooley, Design of polymeric nanoparticles for biomedical delivery applications, Chem. Soc. Rev. 41 (2012) 2545–2561.

[18] P. P. Shah, P. R. Desai, A. R. Patel, M. S. Singh, Skin permeating nanogel for the cutaneous co-delivery of two anti-inflammatory drugs, Biomaterials 33 (5) (2012) 1607 – 1617.

[19] S. Arayachukeat, S. P. Wanichwecharungruang, T. Tree-Udom, Retinyl acetate-loaded nanoparticles: Dermal penetration and release of the retinyl acetate, International Journal of Pharmaceutics 404 (1) (2011) 281 – 288.

[20] M. Kim, B. Jung, J.-H. Park, Hydrogel swelling as a trigger to release biodegradable polymer microneedles in skin, Biomaterials 33 (2) (2012) 668 – 678.

[21] S. Barua, S. Mitragotri, Challenges associated with penetration of nanoparticles across cell and tissue barriers: A review of current status and future prospects, Nano Today 9 (2) (2014) 223 – 243.

[22] E. Carazo, A. Borrego-Sanchez, F. Garcia-Villen, R. Sanchez-Espejo, P. Cerezo, C. Aguzzi, C. Viseras, Advanced inorganic nanosystems for skin drug delivery, The Chemical Record 18 (7-8) 2018 891 – 899.

[23] R. Alvarez-Román, A. Naik, Y. Kalia, R. Guy, H. Fessi, Skin penetration and distribution of polymeric nanoparticles, Journal of Controlled Release 99 (1) (2004) 53 – 62.

[24] C. Zoschke, P. Schilrreff, E. L. Romero, J. M. Brandner, M. Schafer-Korting, Dendritic nanoparticles for cutaneous drug delivery - testing in human skin and reconstructed human skin, Current Pharmaceutical Design 21 (20) (2015) 2784–2800.

[25] A. Vogt, C. Wischke, A. T. Neffe, N. Ma, U. Alexiev, A. Lendlein, Nanocarriers for drug delivery into and through the skin — do existing technologies match clinical challenges?, Journal of Controlled Release 242 (2016) 3 – 15, international Conference on Dermal Drug Delivery by Nanocarriers, Berlin 14-16 March.

[26] A. F. Antunes, P. Pereira, C. Reis, P. Rijo, C. Reis, Nanosystems for skin delivery: From drugs to cosmetics, Current Drug Metabolism 18 (18) (2017) 412–425.

[27] M. Unbehauen, E. Fleige, F. Paulus, B. Schemmer, S. Mecking, S. Moré, R. Haag, Biodegradable core–multishell nanocarriers: Influence of inner shell structure on the encapsulation behavior of dexamethasone and tacrolimus, Polymers 9 (8) (2017) 316.

[28] V. P. Torchilin, Recent advances with liposomes as pharmaceutical carriers, Nat Rev Drug Discov 4.

[29] J. Pardeike, A. Hommoss, R. H. Müller, Lipid nanoparticles (SLN, NLC) in cosmetic and pharmaceutical dermal products, International Journal of Pharmaceutics 366 (1) (2009) 170 – 184.

[30] M. Schäfer-Korting, W. Mehnert, H.-C. Korting, Lipid nanoparticles for improved topical application of drugs for skin diseases, Advanced Drug Delivery Reviews 59 (6) (2007) 427 – 443, lipid Nanoparticles: Recent Advances.

[31] C. Dianzani, G. P. Zara, G. Maina, P. Pettazzoni, S. Pizzimenti, F. Rossi, C. L. Gigliotti, E. S. Ciamporcero, M. Daga, G. Barrera, Drug delivery nanoparticles in skin cancers, BioMed Research International 13.

[32] G. Martini, L. Ciani, Electron spin resonance spectroscopy in drug delivery, Phys. Chem. Chem. Phys. 11 (2009) 211–254.

[33] K. Pancholi, A review of imaging methods for measuring drug release at nanometre scale: a case for drug delivery systems, Expert Opinion on Drug Delivery 9 (2) (2012) 203–218.

[34] A. Schroeter, T. Engelbrecht, R. H. H. Neubert, A. S. B. Goebel, New nanosized technologies for dermal and transdermal drug delivery. a review, Journal of Biomedical Nanotechnology 6 (2010) 511–528.

[35] H. E. J. Hofland, J. A. Bouwstra, H. E. Bodde, F. Spies, H. E. Junginger, Interactions between liposomes and human stratum corneum in vitro: freeze fracture electron microscopical visualization and small angle x-ray scattering studies, British Journal of Dermatology 132 (6) (1995) 853–866.

[36] L. Montenegro, F. Lai, A. Offerta, M. G. Sarpietro, L. Micicchè, A. M. Maccioni, D. Valenti, A. M. Fadda, From nanoemulsions to nanostructured lipid carriers: A relevant development in dermal delivery of drugs and cosmetics, Journal of Drug Delivery Science and Technology 32 (Part B) (2016) 100 – 112.

Bibliography

[37] E. B. Souto, A. J. Almeida, R. H. Müller, Lipid nanoparticles (SLN, NLC) for cutaneous drug delivery:structure, protection and skin effects, Journal of Biomedical Nanotechnology 3 (2007) 317–331.

[38] S. Hoeller, A. Sperger, C. Valenta, Lecithin based nanoemulsions: A comparative study of the influence of non-ionic surfactants and the cationic phytosphingosine on physicochemical behaviour and skin permeation, International Journal of Pharmaceutics 370 (1) (2009) 181 – 186.

[39] V. Klang, C. Valenta, N. B. Matsko, Electron microscopy of pharmaceutical systems, Micron 44 (Supplement C) (2013) 45 – 74.

[40] J. Mérian, J. Gravier, F. Navarro, I. Texier, Fluorescent nanoprobes dedicated to in vivo imaging: From preclinical validations to clinical translation, Molecules 17 (5) (2012) 5564–5591.

[41] S. R. Pygall, J. Whetstone, P. Timmins, C. D. Melia, Pharmaceutical applications of confocal laser scanning microscopy: The physical characterisation of pharmaceutical systems, Advanced Drug Delivery Reviews 59 (14) (2007) 1434 – 1452, intersection of Nanoscience and Modern Surface Analytical Methodology.

[42] S. Wartewig, R. H. Neubert, Pharmaceutical applications of mid-ir and raman spectroscopy, Advanced Drug Delivery Reviews 57 (8) (2005) 1144 – 1170.

[43] P. Santos, A. C. Watkinson, J. Hadgraft, M. E. Lane, Application of microemulsions in dermal and transdermal drug delivery, Skin Pharmacol Physiol 28 (2008) 246–259.

[44] R. Singh, H. S. Nalwa, Medical applications of nanoparticles in biological imaging, cell labeling, antimicrobial agents, and anticancer nanodrugs, Journal of Biomedical Nanotechnology 7 (2011) 489–503.

[45] S. Kempe, H. Metz, K. Mäder, Application of electron paramagnetic resonance (EPR) spectroscopy and imaging in drug delivery research – chances and challenges, European Journal of Pharmaceutics and Biopharmaceutics 74 (1) (2010) 55 – 66, imaging Techniques in Drug Development.

[46] E. Bordignon, H. Brutlach, L. Urban, K. Hideg, A. Savitsky, A. Schnegg, P. Gast, M. Engelhard, E. Groenen, K. Möbius, H.-J. Steinhoff, Heterogeneity in the nitroxide microenvironment: Polarity and proticity effects in spin-labeled proteins studied by multifrequency EPR, Applied Magnetic Resonance 37 (1-4) (2010) 391–403.

[47] E. Yagi, K. Sakamoto, K. Nakagawa, Depth dependence of stratum corneum lipid ordering: A slow-tumbling simulation for electron paramagnetic resonance, Journal of Investigative Dermatology 127 (4) (2007) 895 – 899.

[48] K. A. Walker, M. L. Unbehauen, S. B. Lohan, S. Saeidpour, M. C. Meinke, R. Zimmer, , R. Haaga, Spin-labeling of dexamethasone: Radical stability vs. temporal resolution of

EPR-spectroscopy on biological samples, Zeitschrift für Physikalische Chemie submitted.

[49] J. P. Klare, H.-J. Steinhoff, Spin labeling EPR, Photosynthesis Research 102 (2) (2009) 377–390.

[50] J. A. Weil, J. R. Bolton, Basic Principles of Paramagnetic Resonance, John Wiley & Sons, Inc., 2006, Ch. 1, pp. 1–35.

[51] S. K. Misra, Multifrequency Aspects of EPR, Wiley-VCH Verlag GmbH & Co. KGaA, 2011, Ch. 2, pp. 23–55.

[52] J. Hadgraft, Skin, the final frontier, International Journal of Pharmaceutics 224 (1–2) (2001) 1 – 18.

[53] T. M. Suhonen, J. A. Bouwstra, A. Urtti, Chemical enhancement of percutaneous absorption in relation to stratum corneum structural alterations, Journal of Controlled Release 59 (2) (1999) 149 – 161.

[54] M. Boer, E. Duchnik, R. Maleszka, M. Marchlewicz, Structural and biophysical characteristics of human skin in maintaining proper epidermal barrier function, Advances in Dermatology and Allergology/Postępy Dermatologii i Alergologii 33 (1) (2016) 1–5.

[55] H. B. Allen, Dermatology Terminology, Springer-Verlag London, 2010.

[56] R. Agrawal, J. A. Woodfolk, Skin barrier defects in atopic dermatitis, Current Allergy and Asthma Reports 14 (5) (2014) 433.

[57] N. Y. Schürer, G. Plewig, P. M. Elias, Stratum corneum lipid function, Dermatology 183 (1991) 77–94.

[58] G. K. Menon, G. W. Cleary, M. E. Lane, The structure and function of the stratum corneum, International Journal of Pharmaceutics 435 (1) (2012) 3 – 9, advances in Topical Drug Delivery.

[59] B. Forslind, M. Lindberg (Eds.), Skin, Hair, and Nails Structure and Function, MARCEL DEKKEIR INC., 2004.

[60] J. McGrath, R. Eady, F. Pope, Rook's Textbook of Dermatology, 7th Edition, Vol. 1-4, Blackwell Science, 2004, ch.3.

[61] E. Christophers, A. M. Kligman, Visualization of the cell layers of the stratum corneum, Journal of Investigative Dermatology 42 (6) (1964) 407 – 409.

[62] J. A. Bouwstra, G. S. Gooris, J. A. van der Spek, W. Bras, Structural investigations of human stratum corneum by small-angle x-ray scattering, Journal of Investigative Dermatology 97 (6) (1991) 1005 – 1012.

Bibliography

[63] J. Welzel, Optical coherence tomography in dermatology: a review, Skin Research and Technology 7 (1) (2001) 1–9.

[64] P. Garidel, Mid-ftir-microspectroscopy of stratum corneum single cells and stratum corneum tissue, Phys. Chem. Chem. Phys. 4 (2002) 5671–5677.

[65] K. Cal, J. Stefanowska, D. Zakowiecki, Current tools for skin imaging and analysis, International Journal of Dermatology 48 (12) (2009) 1283–1289.

[66] M. Forster, M.-A. Bolzinger, G. Montagnac, S. Briancon, Confocal raman microspectroscopy of the skin, European Journal of Dermatology 21 (6) (2011) 851–863.

[67] C. R. Flach, D. J. Moore, Infrared and raman imaging spectroscopy of ex vivo skin, International Journal of Cosmetic Science 35 (2) (2013) 125–135.

[68] L. Norlén, Update of technologies for examining the stratum corneum at the molecular level, British Journal of Dermatology 171 (s3) (2014) 13–18.

[69] M. Ulrich, L. Themstrup, N. de Carvalho, M. Manfredi, C. Grana, S. Ciardo, R. Kästle, J. Holmes, R. Whitehead, G. B. E. Jemec, G. Pellacani, J. Welzel, Dynamic optical coherence tomography in dermatology, Dermatology 232 (2016) 298–311.

[70] P. M. Elias, Structure and function of the stratum corneum extracellular matrix, Journal of Investigative Dermatology 132 (9) (2012) 2131 – 2133.

[71] K. W. Ng, W. M. Lau, Skin Deep: The Basics of Human Skin Structure and Drug Penetration, Springer Berlin Heidelberg, Berlin, Heidelberg, 2015, pp. 3–11.

[72] M. D. A. van Logtestijn, E. Domínguez-Hüttinger, G. N. Stamatas, R. J. Tanaka, Resistance to water diffusion in the stratum corneum is depth-dependent, PLOS ONE 10 (2) (2015) 1–12.

[73] C. Archer, Rook's Textbook of Dermatology, 7th Edition, Vol. 1-4, Blackwell Science, 2004, ch.4.

[74] J. Fitzpatrick, J. Morelli, Dermatology Secrets Plus, Mosby, 2010.

[75] G. B. Kasting, N. D. Barai, T. Wang, J. M. Nitsche, Mobility of water in human stratum corneum, Journal of Pharmaceutical Sciences 92 (11) (2003) 2326 – 2340.

[76] T.-N. T. Tran, Cutaneous drug delivery: An update, Journal of Investigative Dermatology Symposium Proceedings 16 (1) (2013) S67 – S69.

[77] M.-A. Bolzinger, S. Briançon, J. Pelletier, Y. Chevalier, Penetration of drugs through skin, a complex rate-controlling membrane, Current Opinion in Colloid & Interface Science 17 (3) (2012) 156 – 165.

[78] A. M. Barbero, H. F. Frasch, Transcellular route of diffusion through stratum corneum: Results from finite element models, Journal of Pharmaceutical Sciences 95 (10) (2006) 2186–2194.

[79] R. Chourasia, S. k.Jain, Drug targeting through pilosebaceous route, Current Allergy ReportsDrug Targets 10 (10) (2009) 950–967.

[80] K. K. Jain (Ed.), Drug Delivery Systems, Springer, 2008.

[81] A. Z. Wilczewska, K. Niemirowicz, K. H. Markiewicz, H. Car, Nanoparticles as drug delivery systems, Pharmacological Reports 64 (5) (2012) 1020 – 1037.

[82] J. P. Atkinson, H. I. Maibach, N. Dragicevic, Targets in Dermal and Transdermal Delivery and Classification of Penetration Enhancement Methods, Springer Berlin Heidelberg, Berlin, Heidelberg, 2015, Ch. 8, pp. 93–108.

[83] I. A. Aljuffali, C.-H. Huang, J.-Y. Fang, Nanomedical strategies for targeting skin microbiomes, Current Drug Metabolism 16 (2015) 255–271.

[84] A. Gupta, R. Bansal, S. Gupta, N. Jindal, A. Jindal, A. nanocarriers and nanoparticles for skin care and dermatological treatments, Indian Dermatology Online Journal 4 (4) (2013) 267–272.

[85] M. Navya, K. H. Basavaraj, Siddaramaiah, G. Johnsy, R. Rashmi, Biopolymers as transdermal drug delivery systems in dermatology therapy, Critical Reviews™ in Therapeutic Drug Carrier Systems 27 (2) (2010) 155–185.

[86] M. Lawrence, G. D. Rees, Microemulsion-based media as novel drug delivery systems, Advanced Drug Delivery Reviews 45 (1) (2000) 89 – 121, emulsions for Drug Delivery.

[87] R. H. Müller, K. Mäder, S. Gohla, Solid lipid nanoparticles (SLN) for controlled drug delivery – a review of the state of the art, European Journal of Pharmaceutics and Biopharmaceutics 50 (1) (2000) 161 – 177.

[88] D. Thassu, M. Deleers, Y. Pathak (Eds.), Nanoparticulate Drug Delivery Systems, CRC Press, 2007.

[89] M. R. Radowski, A. Shukla, H. von Berlepsch, C. Böttcher, G. Pickaert, H. Rehage, R. Haag, Supramolecular aggregates of dendritic multishell architectures as universal nanocarriers, Angewandte Chemie International Edition 46 (2007) 1265–1269.

[90] C. Rabe, E. Fleige, K. Vogtt, N. Szekely, P. Lindner, W. Burchard, R. Haag, M. Ballauff, The multi-domain nanoparticle structure of a universal core-multi-shell nanocarrier, Polymer 55 (26) (2014) 6735 – 6742.

[91] S. Hönzke, C. Gerecke, A. Elpelt, N. Zhang, M. Unbehauen, V. Kral, E. Fleige, F. Paulus, R. Haag, M. Schäfer-Korting, B. Kleuser, S. Hedtrich, Tailored dendritic core-multishell nanocarriers for efficient dermal drug delivery: A systematic top-down approach from synthesis to preclinical testing, Journal of Controlled Release 242 (2016) 50 – 63.

Bibliography

[92] E. Fleige, K. Achazi, K. Schaletzki, T. Triemer, R. Haag, pH-responsive dendritic core–multishell nanocarriers, Journal of Controlled Release 185 (2014) 99 – 108.

[93] K. A. Walker, J.-F. Stumbé, R. Haag, Polyester-based, biodegradable core-multishell nanocarriers for the transport of hydrophobic drugs, Polymers 8 (5).

[94] F. Du, S. Hönzke, F. Neumann, J. Keilitz, W. Chen, N. Ma, S. Hedtrich, R. Haag, Development of biodegradable hyperbranched core-multishell nanocarriers for efficient topical drug delivery, Journal of Controlled Release 242 (2016) 42 – 49, international Conference on Dermal Drug Delivery by Nanocarriers, Berlin 14-16 March.

[95] E. Mohammadifar, F. Zabihi, Z. Tu, S. Hedtrich, A. Nemati Kharat, M. Adeli, R. Haag, One-pot and gram-scale synthesis of biodegradable polyglycerols under ambient conditions: nanocarriers for intradermal drug delivery, Polym. Chem. 8 (2017) 7375–7383.

[96] D. Mathias, S. Dirk, N. Falko, L. Yan, P. Florian, M. Nan, H. Rainer, Synthesis of ph-cleavable dpg-amines for gene delivery application, Macromolecular Bioscience 17 (1) 160 – 190.

[97] S. Stefani, S. K. Sharma, R. Haag, P. Servin, Core-shell nanocarriers based on pegylated hydrophobic hyperbranched polyesters, European Polymer Journal 80 (2016) 158 – 168.

[98] S. Stefani, I. N. Kurniasih, S. K. Sharma, C. Bottcher, P. Servin, R. Haag, Triglycerol-based hyperbranched polyesters with an amphiphilic branched shell as novel biodegradable drug delivery systems, Polym. Chem. 7 (2016) 887–898.

[99] R. Haag, Supramolecular drug-delivery systems based on polymeric core-shell architectures, Angew. Chem. Int. Ed. Engl. 43 (2004) 278–282.

[100] A. Boreham, M. Pfaff, E. Fleige, R. Haag, U. Alexiev, Nanodynamics of dendritic core-multishell nanocarriers, Langmuir 30 (2014) 1686–1695.

[101] S. Lohan, N. Icken, C. Teutloff, S. Saeidpour, R. Bittl, J. Lademann, E. Fleige, R. Haag, S. Haag, M. Meinke, Investigation of cutaneous penetration properties of stearic acid loaded to dendritic core-multi-shell (CMS) nanocarriers, International Journal of Pharmaceutics 501 (2016) 271–277.

[102] S. Küchler, M. R. Radowski, T. Blaschke, M. Dathe, J. Plendl, R. Haag, M. Schäfer-Korting, K. D. Kramer, Nanoparticles for skin penetration enhancement - a comparison of a dendritic core-multishell-nanotransporter and solid lipid nanoparticles, Eur. J. Pharm. Biopharm, 71 (2009) 243–50.

[103] M. A. Quadir, M. R. Radowski, F. Kratz, K. Licha, P. Hauff, R. Haag, Dendritic multishell architectures for drug and dye transport, Journal of Controlled Release 132 (3) (2008) 289 – 294, proceedings of the Tenth European Symposium on Controlled Drug Delivery.

[104] S. Haag, E. Fleige, M. Chen, A. Fahr, C. Teutloff, R. Bittl, J. Lademann, M. Schafer-Korting, R. Haag, M. Meinke, Skin penetration enhancement of core–multishell nanotransporters and invasomes measured by electron paramagnetic resonance spectroscopy, International Journal of Pharmaceutics 416 (2011) 223 – 228.

[105] G. Yoon, W. Park, I.-S. Yoon, Solid lipid nanoparticles (SLNs) and nanostructured lipid carriers (NLCs): Recent advances in drug delivery, Journal of Pharmaceutical Investigation 43 (5) (2013) 353–362.

[106] M. H. J. K. K. Westesen, H. Bunjes, Physicochemical characterization of lipid nanoparticles and evaluation of thier drug loading capacity and sustained release potatial, J. Control Release 20 (8) (1997) 223.

[107] K. Jores, W. Mehneert, K. Mäder, Physicochemical investigation on solid lipid nanoparticles and on oil-loaded solid lipid nanoparticles: a nuclear magnetic resonance and electron spin resonance study, Pharm. Res. 20 (8) (2003) 1274–1283.

[108] S. L. Borgia, M. Regehly, R. Sivaramakrishnan, W. Mehnert, H. Korting, K. Danker, B. Röder, K. Kramer, M. Schäfer-Korting, Lipid nanoparticles for skin penetration enhancement—correlation to drug localization within the particle matrix as determined by fluorescence and parelectric spectroscopy, Journal of Controlled Release 110 (1) (2005) 151 – 163.

[109] H. Bunjes, K. Westesen, M. H. Koch, Crystallization tendency and polymorphic transitions in triglyceride nanoparticles, International Journal of Pharmaceutics 129 (1) (1996) 159 – 173.

[110] S. Khan, S. Baboota, J. Ali, S. Khan, R. Narang, J. K. Narang, Nanostructured lipid carriers: An emerging platform for improving oral bioavailability of lipophilic drugs, International Journal of Pharmaceutical Investigation 5 (4) (2015) 182–191.

[111] R. Shah, D. Eldridge, E. Palombo, I. Harding, Lipid Nanoparticles Production, Characterization and Stability, Springer, 2015.

[112] S. Abbott, Surfactant Science: Principles and Practice, 2016.

[113] W. Griffin, Classification of the surface-active agents by hlb, J. Soc. Costa. Chem. 1 (1949) 311–326.

[114] J. T. Davies, A quantitative kinetic theory of the emulsion type: I. physical chemistry of the emulsifying agent., Proc. 2nd Int. Congr. Surface Activity 1 (1957) 426–438.

[115] A. Rabaron, G. Cavé, F. Puisieux, M. Seiller, Physical methods for measurement of the hlb of ether and ester non-ionic surface-active agents: H-nmr and dielectric constant, International Journal of Pharmaceutics 99 (1) (1993) 29 – 36.

Bibliography

[116] G. Zoubari, S. Staufenbiel, P. Volz, U. Alexiev, R. Bodmeier, Effect of drug solubility and lipid carrier on drug release from lipid nanoparticles for dermal delivery, European Journal of Pharmaceutics and Biopharmaceutics 110 (2017) 39 – 46.

[117] J. de Oliveira Eloy, J. Saraiva, S. de Albuquerque, J. M. Marchetti, Solid dispersion of ursolic acid in gelucire 50/13: a strategy to enhance drug release and trypanocidal activity, AAPS PharmSciTech 13 (4) (2012) 1436–1445.

[118] S. Ranjita, S. Kamalinder, In-vitro release of paracetamol from suppocire suppositories: Role of additives, Malaysian Journal of Pharmaceutical Sciences 8 (1) (2010) 57–71.

[119] J. Patel, A. Patel, M. Raval, N. Sheth, Formulation and development of a self-nanoemulsifying drug delivery system of irbesartan, Journal of Advanced Pharmaceutical Technology & Research 2 (1) (2011) 9 – 16.

[120] S. B. Lohan, S. Saeidpour, A. Solik, S. Schanzer, H. Richter, P. Dong, M. E. Darvin, R. Bodmeier, A. Patzelt, G. Zoubari, M. Unbehauen, R. Haag, J. Lademann, C. Teutloff, R. Bittl, M. C. Meinke, Investigation of the cutaneous penetration behavior of dexamethasone loaded to nano-sized lipid particles by EPR spectroscopy, and confocal raman and laser scanning microscopy, European Journal of Pharmaceutics and Biopharmaceutics 116 (2017) 102 – 110, nanocarriers: Architecture, Transport, and Topical Application of Drugs for Therapeutic Use.

[121] S. Saeidpour, S. B. Lohan, A. Solik, V. Paul, R. Bodmeier, G. Zoubari, M. Unbehauen, R. Haag, R. Bittl, M. C. Meinke, C. Teutloff, Drug distribution in nanostructured lipid particles, European Journal of Pharmaceutics and Biopharmaceutics 110 (2017) 19 – 23.

[122] M. Pinheiro, R. Ribeiro, A. Vieira, F. Andrade, S. Reis, Design of a nanostructured lipid carrier intended to improve the treatment of tuberculosis, Drug Des Devel Ther. 10 (2016) 2467–2475.

[123] A. E.-H. de Mendoza, M. Rayo, F. Mollinedo, M. J. Blanco-Prieto, Lipid nanoparticles for alkyl lysophospholipid edelfosine encapsulation: Development and in vitro characterization, European Journal of Pharmaceutics and Biopharmaceutics 68 (2) (2008) 207 – 213.

[124] M. Marchiori, G. Lubini, G. D. Nora, R. Friedrich, M. Fontana, A. Ourique, M. Bastos, L. Rigo, C. Silva, S. Tedesco, R. Beck, Hydrogel containing dexamethasone-loaded nanocapsules for cutaneous administration: preparation, characterization, and in vitro drug release study, Drug Development and Industrial Pharmacy 36 (8) (2010) 962–971.

[125] A. zur Mühlen, C. Schwarz, W. Mehnert, Solid lipid nanoparticles (SLN) for controlled drug delivery – drug release and release mechanism, European Journal of Pharmaceutics and Biopharmaceutics 45 (2) (1998) 149 – 155.

[126] J. J. Sakurai, S. F. Tuan, Modern Quantum Mechanics, Addison-Wesley Pub. Co., 1994.

142

[127] E. G. M. Brustolon (Ed.), Electron Paramagnetic Resonas A Practitioner's Toolkit, WILEY, 1999.

[128] J. A. Weil, J. R. Bolton, Zeeman Energy (g) Anisotropy, John Wiley & Sons, Inc., 2006, Ch. 4, pp. 85–117.

[129] J. A. Weil, J. R. Bolton, Magnetic Interaction between Particles, John Wiley & Sons, Inc., 2006, Ch. 2, pp. 36–57.

[130] J. A. Weil, J. R. Bolton, Isotropic Hyperfine Effects in EPR Spectra, John Wiley & Sons, Inc., 2006, Ch. 3, pp. 58–84.

[131] C. Engelhard, Correlating structure and function: An EPR study on cryptochroms, lov proteins and channelrhodopsin, Ph.D. thesis, Freie universität Berlin (2015).

[132] M. P. Eastman, R. G. Kooser, M. R. Das, J. H. Freed, Studies of heisenberg spin exchange in ESR spectra. i. linewidth and saturation effects, The Journal of Chemical Physics 51 (6) (1969) 2690–2709.

[133] Reichardt, Christian, Welton, Thomas, Empirical Parameters of Solvent Polarity, Wiley-VCH, 2010, Ch. 3, pp. 425–508.

[134] D. Marsh, C. Toniolo, Polarity dependence of EPR parameters for TOAC and MTSSL spin labels: Correlation with doxyl spin labels for membrane studies, Journal of Magnetic Resonance 190 (2) (2008) 211 – 221.

[135] M. Huber, Introduction to magnetic resonance methods in photosynthesis, Photosynth Res 102 (2009) 305–310.

[136] M. Plato, H. J. Rteinhoff, C. Wegener, J. T. Törring, A. Savitsky, K. Möbius, Molecular orbital study of polarity and hydrogen bonding effects on the g and hyperfine tensors of site directed no spin labelled bacteriorhodopsin, Molecular Physics 100 (2002) 3711–3721.

[137] H. M. McConnell, D. B. Chesnut, Negative spin densities in aromatic radicals, The Journal of Chemical Physics 27 (4) (1957) 984–985.

[138] A. H. Cohen, B. M. Hoffman, Hyperfine interactions in perturbed nitroxides, Journal of the American Chemical Society 95 (6) (1973) 2061–2062.

[139] E. Bordignon, EPR Spectroscopy of Nitroxide Spin Probes, American Cancer Society, 2017, pp. 235–254.

[140] H. Longuet-Higgins, A. Stone, The electronic structure and electron spin resonance of tricyclopentadienyl trinickel dicarbonyl, Molecular Physics 5 (5) (1962) 417–424.

[141] A. J. Stone, Gauge invariance of the g tensor, Proceedings of the Royal Society of London. Series A, Mathematical and Physical Sciences 271 (1346) (1963) 424–434.

Bibliography

[142] S. K. Misra, J. H. Freed, Molecular Motions, Wiley-Blackwell, 2011, Ch. 11, pp. 497–544.

[143] S. Shimada, ESR studies on molecular motion and chemical reactions in solid polymers in relation to structure, Progress in Polymer Science 17 (6) (1992) 1045 – 1106.

[144] S. K. Misra, Relaxation of Paramagnetic Spins, Wiley-VCH Verlag GmbH & Co. KGaA, 2011, Ch. 10, pp. 455–495.

[145] F. Bloch, Nuclear induction, Physical Review 70 (1946) 460.

[146] C. P. Poole, H. A. Farach, Relaxation in Magnetic Resonance, Academic press, 1971.

[147] A. Abragam, The Principles of Nuclear Magnetism, Oxford Univ. Press, 1961.

[148] Y. Zhou, B. E. Bowler, G. R. Eaton, S. S. Eaton, Electron spin lattice relaxation rates for s = 1/2 molecular species in glassy matrices or magnetically dilute solids at temperatures between 10 and 300 k, Journal of Magnetic Resonance 139 (1) (1999) 165 – 174.

[149] S. S. Eaton, G. R. Eaton, Relaxation Times of Organic Radicals and Transition Metal Ions, Springer US, 2002, Ch. 2, pp. 29–154.

[150] H. Sato, V. Kathirvelu, A. Fielding, J. P. Blinco, A. S. Micallef, S. E. Bottle, S. S. Eaton, G. R. Eaton, Impact of molecular size on electron spin relaxation rates of nitroxyl radicals in glassy solvents between 100 and 300 k, Molecular Physics 105 (15-16) (2007) 2137–2151.

[151] G. R. Eaton, S. S. Eaton, Frequency Dependence of Electron Spin Relaxation Times, Wiley-VCH Verlag GmbH & Co. KGaA, 2011, Ch. 17, pp. 719–753.

[152] A. Schwiger, G. Jeschke, Principles of Pulse Electron Paramagnetic Resonance, Oxford university press, 2001.

[153] A. Schnegg, M. Fuhs, M. Rohrer, W. Lubitz, T. F. Prisner, K. Möbius, Molecular dynamics of qa-• and qb-• in photosynthetic bacterial reaction centers studied by pulsed high-field EPR at 95 ghz, The Journal of Physical Chemistry B 106 (36) (2002) 9454–9462.

[154] E. Law, M. Leung, Corticosteroids in stevens-johnson syndrome/toxic epidermal necrolysis: current evidence and implications for future research, Ann. Pharmacother 49 (3) (2015) 335–342.

[155] G. I. Likhtenshtein, J. Yamauchi, S. Nakatsuji, A. I. Smirnov, R. Tamura, Nitroxide, Application in Chemistry, Biomedicine and Materilas Science, WILEY-VCH Verlag, 2008.

[156] A. Hoffmann, A. Henderson, A new stable free radical: Di-t-butyl-nitroxide., J. am. chem. soc 83 (1961) 4671–4672.

[157] A. I. Kokorin (Ed.), Nitroxides - Theory, Experiment and Applications, InTech, 2012.

[158] C. Altenbach, S. L. Flitsch, H. G. Khorana, W. L. Hubbell, Structural studies on transmembrane proteins. 2. spin labeling of bacteriorhodopsin mutants at unique cysteines, Biochemistry 28 (1989) 7806–7812.

[159] A. I. Smirnov, T. I. Smirnova, P. D. Morse, Very high frequency electron paramagnetic resonance of 2,2,6,6-tetramethyl-1-piperidinyloxy in 1,2-dipalmitoyl-sn-glycero-3-phosphatidylcholine liposomes: partitioning and molecular dynamics, BiophysicalJournal 68 (1995) 2350–2360.

[160] S. F. Haag, J. Lademann, M. C. Meinke, Application of EPR-spin Probes to Evaluate Penetration Efficiency, Storage Capacity of Nanotransporters, and Drug Release, Springer Berlin Heidelberg, Berlin, Heidelberg, 2017, pp. 215–228.

[161] D. Hinderberger, EPR Spectroscopy in Polymer Science, Springer Berlin Heidelberg, Berlin, Heidelberg, 2012, pp. 67–89.

[162] U. A. Nilsson, L. I. Olsson, G. Carlin, A. C. Bylund-Fellenius, Inhibition of lipid peroxidation by spin labels. relationships between structure and function., Journal of Biological Chemistry 264 (19) (1989) 11131–11135.

[163] G. M. Rosen, E. Finkelstein, E. J. Rauckman, A method for the detection of superoxide in biological systems, Archives of Biochemistry and Biophysics 215 (2) (1982) 367 – 378.

[164] N. Kocherginsky, H. M. Swartz, Nitroxide spin labels reactions in biology and chemistry, CRC press, 1998.

[165] S. H. Yalkowsky, Y. He, P. Jain, Handbook of Aqueous Solubility Data, Second Edition, CRC, 2010.

[166] S. Saeidpour, S. Lohan, M. Anske, M. Unbehauen, E. Fleige, R. Haag, M. Meinke, R. Bittl, C. Teutloff, Localization of dexamethasone within dendritic core-multishell (CMS) nanoparticles and skin penetration properties studied by multi-frequency electron paramagnetic resonance (EPR) spectroscopy, European Journal of Pharmaceutics and Biopharmaceutics 116 (2017) 94 – 101, nanocarriers: Architecture, Transport, and Topical Application of Drugs for Therapeutic Use.

[167] A. Weidinger, M. Waiblinger, B. Pietzak, T. A. Murphy, Atomic nitrogen in C60:N@C60, Applied Physics A 66 (1998) 287–292.

[168] L. dhar, S. Jalandra, Instrumentation of ESR spectroscopy, pharmatutor.

[169] G. R. Eaton, S. S. Eaton, D. P. Barr, R. T. Weber, Basics of Continuous Wave EPR, Springer Vienna, Vienna, 2010.

[170] E. L. Hahn, Spin echoes, Phys. Rev. 80 (1950) 580–594.

[171] J. S. Hyde, M. Pasenkiewicz-Gierula, A. Jesmanowicz, W. E. Antholine, Pseudo field modulation in EPR spectroscopy, Applied Magnetic Resonance 1 (1990) 483–496.

[172] J. Du, G. Eaton, S. Eaton, Temperature, orientation, and solvent dependence of electron spin-lattice relaxation rates for nitroxyl radicals in glassy solvents and doped solids, Journal of Magnetic Resonance, Series A 115 (2) (1995) 213 – 221.

[173] OECD GUIDELINE FOR THE TESTING OF CHEMICALS, Partition Coefficient (n-octanol/water): Shake Flask Method (July 1995).

[174] S. Stoll, A. Schweiger, Easyspin, a comprehensive software package for spectral simulation and analysis in EPR, Journal of Magnetic Resonance 178 (2006) 42 – 55.

[175] S. K. Misra, Simulation of EPR Spectra, Wiley-VCH Verlag GmbH & Co. KGaA, 2011, Ch. 9, pp. 417–454.

[176] K. A. Earle, D. E. Budil, Calculating Slow-Motion ESR Spectra of Spin-Labeled Polymers, John Wiley & Sons, Inc., 2006, Ch. 3, pp. 53–83.

[177] S. Stoll, Chapter six - cw-EPR spectral simulations: Solid state, in: P. Z. Qin, K. Warncke (Eds.), Electron Paramagnetic Resonance Investigations of Biological Systems by Using Spin Labels, Spin Probes, and Intrinsic Metal Ions, Part A, Vol. 563 of Methods in Enzymology, Academic Press, 2015, pp. 121 – 142.

[178] S. K. Misra, Simulation of slow-motion cw EPR spectrum using stochastic liouville equation for an electron spin coupled to two nuclei with arbitrary spins: Matrix elements of the liouville superoperator, Journal of Magnetic Resonance 189 (1) (2007) 59 – 77.

[179] A. Kh, Vorobiev, N. A. Chumakova, Simulation of Rigid-Limit and Slow-Motion EPR Spectra for Extraction of Quantitative Dynamic and Orientational Information, Nitroxides - Theory, Experiment and Applications, 2012, Ch. 3.

[180] R. P. Mason, C. F. Polnaszek, J. H. Freed, Interpretation of electron spin resonance spectra of spin labels undergoing very anisotropic rotational reorientation. comments, The Journal of Physical Chemistry 78 (13) (1974) 1324–1329.

[181] R. Owenius, M. Engstroem, M. Lindgren, M. Huber, Influence of solvent polarity and hydrogen bonding on the EPR parameters of a nitroxide spin label studied by 9-GHz and 95-GHz EPR spectroscopy and DFT calculations, The Journal of Physical Chemistry A 105 (2001) 10967–10977.

[182] O. N. Aleksandrova, Spin labeling ESR investigation of the molecular environment of soil interacting with chemical organic contaminants, Journal of Geochemical Exploration 129 (2013) 6 – 13, molecular Aspects of Humic Substances and Biological Functionality in Soil Ecosystems.

[183] U. Bhardwaj, D. J. Burgess, Physicochemical properties of extruded and non-extruded liposomes containing the hydrophobic drug dexamethasone, International Journal of Pharmaceutics 388 (2010) 181 – 189.

[184] L. J. Berliner (Ed.), Spin Labeling (Theory and Application), Academic Press, 1976.

[185] L. J. Berliner (Ed.), Spin Labeling II (Theory and Application), Academic Press, 1979.

[186] A. Zecevic, G. R. Eaton, S. S. Eaton, M. Lindgren, Dephasing of electron spin echoes for nitroxyl radicals in glassy solvents by non-methyl and methyl protons, Molecular Physics 95 (6) (1998) 1255–1263.

[187] D. Marsh, Spin-label EPR for determining polarity and proticity in biomolecular assemblies: Transmembrane profiles, Applied Magnetic Resonance 37 (2010) 435–454.

[188] T. Kamawamura, S. Matsunami, T. Yonezawa, Solvent effects on the g-value of di-t-butyl nitric oxide, Bulletin of the Chemical Society of Japan 40 (1967) 1111–1115.

[189] P. C. Database, 2-hydroxypropyl octanoate, National Center for Biotechnology Information (Feb. 2017).

[190] V. Ratsimbazafy, E. Bourret, R. Duclos, C. Brossard, Rheological behavior of drug suspensions in gelucire mixtures and proxyphylline release from matrix hard gelatin capsules, European Journal of Pharmaceutics and Biopharmaceutics 48 (3) (1999) 247 – 252.

[191] K. Satake, T. Nakajima, M. Iwata, Y. Fujikake, M. Kimura, Physicopharmaceutical characteristics of ulinastatin vaginal suppositories prepared in a hospital, YAKUGAKU ZASSHI 131 (11) (2011) 1639–1644.

[192] D.-H. Kim, D. C. Martin, Sustained release of dexamethasone from hydrophilic matrices using plga nanoparticles for neural drug delivery, Biomaterials 27 (15) (2006) 3031 – 3037.

[193] B. Berner, C. E. Blanco, G. W. Ellison, L. W. Myers, H. E. Hirsch, Partition coefficients of 2,2,6,6-tetramethylpiperidine-1-oxyl (tempo) in erythrocyte lipids in multiple sclerosis, Journal of Neuroscience Research 5 (3) (1980) 225–231.

[194] R. Sivaramakrishnan, C. Nakamura, W. Mehnert, H. Korting, K. Kramer, M. Schäfer-Korting, Glucocorticoid entrapment into lipid carriers characterisation by parelectric spectroscopy and influence on dermal uptake, Journal of Controlled Release 97 (3) (2004) 493 – 502.

[195] J. K. G. Lukowski, Energy dispersive x-ray analysis of loaded solid lipid nanoparticles„ in: J. Proceedings – 28th International Symposium on Controlled Release of Bioactive Materials and 4th Consumer & Diversified Controlled Release of Bioactive Materials and 4th Consumer & Diversified San Diego, CA, United Staes, 2001, p. 516–517.

[196] R. Schwarzl, F. Du, R. Haag, R. R. Netz, General method for the quantification of drug loading and release kinetics of nanocarriers, European Journal of Pharmaceutics and Biopharmaceutics 116 (2017) 131 – 137, nanocarriers: Architecture, Transport, and Topical Application of Drugs for Therapeutic Use.

[197] E. Mohammadifar, M. Adeli, A. N. Kharat, H. Namazi, R. Haag, Stimuli-responsive core multishell dendritic nanocarriers, Macromolecular Chemistry and Physics 218 (8) (2017) 1600525–n/a, 1600525.

[198] C. Gerecke, A. Edlich, M. Giulbudagian, F. Schumacher, N. Zhang, A. Said, G. Yealland, S. B. Lohan, F. Neumann, M. C. Meinke, N. Ma, M. Calderón, S. Hedtrich, M. Schäfer-Korting, B. Kleuser, Biocompatibility and characterization of polyglycerol-based thermoresponsive nanogels designed as novel drug-delivery systems and their intracellular localization in keratinocytes, Nanotoxicology 11 (2) (2017) 267–277, pMID: 28165853.

[199] M. Giulbudagian, S. Hönzke, J. Bergueiro, D. Işık, F. Schumacher, S. Saeidpour, S. B. Lohan, M. C. Meinke, C. Teutloff, M. Schäfer-Korting, G. Yealland, B. Kleuser, S. Hedtrich, M. Calderón, Enhanced topical delivery of dexamethasone by beta-cyclodextrin decorated thermoresponsive nanogels, Nanoscale 10 (2018) 469 – 479.

[200] P. Dong, F. F. Sahle, S. B. Lohan, S. Saeidpour, S. Albrecht, C. Teutloff, R. Bodmeier, M. Unbehauen, C. Wolff, R. Haag, J. Lademann, A. Patzelt, M. Schäfer-Korting, ph-sensitive eudragit l 100 nanoparticles promote cutaneous penetration and drug release on the skin, Journal of Controlled Release.

[201] A. Nalepa, K. Möbius, M. Plato, W. Lubitz, A. Savitsky, Nitroxide spin labels—magnetic parameters and hydrogen-bond formation: A high-field EPR and ednmr study, Applied Magnetic Resonance.

[202] G. Jeschke, Deer distance measurements on proteins, Annual Review of Physical Chemistry 63 (1) (2012) 419–446, pMID: 22404592.

[203] K. Ackermann, C. Pliotas, S. Valera, J. H. Naismith, B. E. Bode, Sparse labeling peldor spectroscopy on multimeric mechanosensitive membrane channels, Biophysical Journal 113 (9) (2017) 1968 – 1978.

[204] U. Alexiev, P. Volz, A. Boreham, R. Brodwolf, Time-resolved fluorescence microscopy (flim) as an analytical tool in skin nanomedicine, European Journal of Pharmaceutics and Biopharmaceutics 116 (2017) 111 – 124, nanocarriers: Architecture, Transport, and Topical Application of Drugs for Therapeutic Use.

[205] K. Yamamoto, A. Klossek, R. Flesch, F. Rancan, M. Weigand, I. Bykova, M. Bechtel, S. Ahlberg, A. Vogt, U. Blume-Peytavi, P. Schrade, S. Bachmann, S. Hedtrich, M. Schäfer-Korting, E. Rühl, Influence of the skin barrier on the penetration of topically-applied dexamethasone probed by soft x-ray spectromicroscopy, European Journal of Pharmaceutics and Biopharmaceutics 118 (2017) 30 – 37, biological Barriers – 11th International Conference and Workshop.

[206] A. Klossek, S. Thierbach, F. Rancan, A. Vogt, U. Blume-Peytavi, E. Rühl, Studies for improved understanding of lipid distributions in human skin by combining stimulated and spontaneous raman microscopy, European Journal of Pharmaceutics and Biopharmaceutics 116 (2017) 76 – 84, nanocarriers: Architecture, Transport, and Topical Application of Drugs for Therapeutic Use.

[207] R. Schulz, K. Yamamoto, A. Klossek, R. Flesch, S. Hönzke, F. Rancan, A. Vogt, U. Blume-Peytavi, S. Hedtrich, M. Schäfer-Korting, E. Rühl, R. R. Netz, Data-based modeling of drug penetration relates human skin barrier function to the interplay of diffusivity and free-energy profiles, Proceedings of the National Academy of Sciences.

Acknowledgements

Declaration

Selbstständigkeitserklärung

Hiermit erkläre ich, dass ich die vorliegende Arbeit selbständig und nur unter Verwendung der angegebenen Literatur und Hilfsmittel angefertigt habe. Zudem erkläre ich, dass diese Arbeit in keinem früheren Promotionsverfahren eingereicht und dort angenommen oder für ungenügend befunden wurde

Own Work Declaration

I hereby certify that the work presented here was accomplished by myself and without the use of illegitimate means or support, and that no sources and tools were used other than those cited.

13 March 2019, Berlin, Germany
_____

Signed:
_____